Efficient finite element strategies for solving the radiative transfer equation

Mohd Afeef Badri

THESE DE DOCTORAT DE

L'UNIVERSITE DE NANTES
COMUE UNIVERSITE BRETAGNE LOIRE

ECOLE DOCTORALE N° 602
Sciences pour l'Ingénieur
Spécialité : *Energétique-Thermique-Combustion*

Par

Mohd Afeef BADRI

Efficient finite element strategies for solving the radiative transfer equation

Thèse présentée et soutenue à Nantes, le 23-10-2018
Unité de recherche : LTeN CNRS UMR 6607

Rapporteurs avant soutenance :

Amélie LITMAN	Maître de Conférences, HDR, Aix Marseille Université, France.
Pedro J. M. COELHO	Professeur, University of Lisbon, Portugal.

Composition du Jury :

Amélie LITMAN	Maître de Conférences, HDR, Aix Marseille Université, France.
Pedro J. M. COELHO	Professeur, University of Lisbon, Portugal.
Richard FOURNIER	Professeur, Université Paul Sabatier, France.
Pierre JOLIVET	Chargé de Recherche, CNRS UMR 5505, France.
Mazen SAAD	Professeur, Centrale Nantes, France.
Directeur de thèse Benoit ROUSSEAU	Directeur de recherche, CNRS UMR 6607, France.
Co-directeur de thèse Steven LE CORRE	Professeur, Université de Nantes, France.
Encadrant de thèse Yann FAVENNEC	Maître de Conférences, Université de Nantes, France.

"If we knew what it was we were doing, it would not be called research, would it ?"

Albert Einstein

ACKNOWLEDGMENTS

Three years ago, I got the opportunity to pursue this Doctorate, and my decision was highly influenced by a strong desire of exploring the field of numerical science, parallel computing, and radiative transfer. Needless to say, the journey has been incredible because of the diligent contributions made by some of the very important people of my life. Today, through this acknowledgment note, it is time for me to express my gratitude to each one of them and let them know how they have helped me grow, not only as a professional but also as an individual.

First, I would like to thank Dr. Amélie Litman and Dr. Pedro Coelho who reviewed this manuscript and participated as jury members during my thesis defense. Further, my sincere gratitude to Dr Richard Forunier, Dr. Pierre Jolivet, and Dr. Mazen Saad who were also the members of my thesis defense jury.

I would like to acknowledge the support from the IRT-JV [1], Bouguenais for funding my thesis research. Without their support this thesis wouldn't have seen the days light.

My sincere gratitude to my thesis supervisors Dr. Benoit Rousseau, Dr. Steven Le Corre, and Dr. Yann Favennec, who not only backed me during my research but also showed their confidence and faith in me at all times. Each discussion with them, be it scientific or personal, has been incredibly insightful. Dr. Benoit Rousseau has certainly helped me understand some key aspects of radiation from a physicist's point of view. Discussing work with him was always exciting as well as inducive. It was equally fun to discuss the industrial aspects of this work with Dr. Steven Le Corre who has also been a source of motivation to me.

I fall short of words to explain how enriching the experience has been to work with Dr. Yann Favennec - My Guru. An inspirational man with a profound vision. No matter how complex my question was, he always had an answer. Discussing and learning from him about various techniques of mathematical modeling, finite elements, inverse problems was always fun and thrilling. His go-get-it approach always helped me to think out of the box. He has been my inspiration to many of my work pieces and I would like to dedicate my accolades to him.

---

[1]L'Institut de Recherche Technologique Jules Verne

I would like to acknowledge Dr. Pierre Jolivet for all his vision and wisdom in the area of high performance computing. Working with him has been one of the most enriching experiences and the collaboration with him not only made me achieve my results but also learn to explore new dimensions of my research.

I want to thank ICI[2] supercomputing unit, Centrale Nantes for letting me access and avail their supercomputers Liger. Certainly this cooperation has shaped my research work in a better way.

My host team at LTeN[3], the CeFopRam team – Benoit, Yann, Gilberto, Giorgia, Arnaud, David, Simon, Aubin, Tom, and Atin – has been so encouraging and supportive throughout my journey that my research wouldn't have been possible without their team spirit, and result-oriented approach. I want to thank each one of my team members for being so adjuvant. In particular my ex office mate, David Le Hardy (now Dr. David) who had started as a PhD student and his doctoral research became one of the building blocks of this thesis.

I would also like to thank my parents and my brother who supported me in all my pursuits, family (the Badri's and the Shah's) for having faith in me, and friends for being there, no matter what. Without their support, I wouldn't have reached this far.

Last, but not the least, whom I met during this doctorate, my lifeline, my lovely wife Samar. Before everything else, she became my best friend and made my journey balmier. She celebrates with me even when the smallest things go right and she has held my hand and stood there for me whenever I needed her.

I appreciate each one of you and want to thank you with all my heart for the efforts you all have made in helping me achieve my goals.

TABLE OF CONTENTS

Version française

La modélisation du transfert radiatif présente un intérêt pour de nombreux domaines de la science et de la technologie. Les problèmes de transfert radiatif existent en abondance en thermique, en astrophysique, en médecine, en physique de la combustion, en climatologie, etc. On trouve aussi des problèmes de transfert radiatif dans diverses applications d'ingénierie et de procédés industriels, comme la combustion dans les moteurs à turbine à gaz, dans les procédés de fabrication de matériaux utilisant le chauffage au laser, dans les systèmes thermo-solaire de synthèse chimique, ou encore dans le transport des particules dans les réacteurs nucléaires. Mathématiquement, les phénomènes de transfert radiatif macroscopique ou microscopique sont modélisés à l'aide de l'équation de transfert radiatif. Par nature, l'équation de transfert radiatif est une équation integro-différentielle contenant jusqu'à sept variables indépendantes : la fréquence de rayonnement, trois coordonnées d'espace, deux coordonnées angulaires décrivant la direction du rayonnement, et le temps. Cette grande dimensionnalité limite l'existence d'une solution analytique aux cas très simples. Malheureusement ces cas ne représentent que quelques problèmes rares de transfert radiatif. Par conséquent, pour des problèmes plus réalistes, des solutions approximatives de l'équation de transfert radiatif via une approche numérique doivent être recherchées.

La recherche menée dans cette thèse est financée par l'Institut de Recherche Technologique Jules Verne de Bouguenais, dans le cadre du projet SODA[4], qui regroupe des partenaires académiques (Laboratoire LTeN[5], Nantes et Laboratoire GEM[6], Nantes) et industriels (Airbus Innovation Group, Safran Composites, et Dassault Aviation).

---

[4] SimulatiOn du Drapage Automatisé
[5]Laboratoire de Thermique et d'Energie de Nantes
[6]Institut de Recherche en Génie Civil et Mécanique

Les partenaires industriels du projet utilisent des lasers modernes comme source de chauffage pour la fabrication avancée de matériaux composites. Ceci constitue leur motivation pour la résolution de l'équation de transfert radiatif dans les milieux absorbant, émettant et diffusant avec des sources laser collimatées. La modélisation de tels problèmes nécessite la production d'une méthode (solveur) capable de gérer le transfert radiatif tridimensionnel dans les milieux participants de topologie complexe. C'est en effet l'objectif principal de cette thèse. La recherche a été réalisée au sein de l'équipe $\mathbb{C}$éf$_\mathrm{o}$P$\mathcal{R}$am[7], au sein de l'axe TTMI[8] du LTeN, Nantes. L'un des objectifs de l'équipe $\mathbb{C}$éf$_\mathrm{o}$P$\mathcal{R}$am est la caractérisation avancée de matériaux réels incluant des géométries complexe.

Au cours des cinq chapitres fournis dans cette thèse, nous passons en revue la procédure complète pour résoudre numériquement l'équation de transfert radiatif, et proposons un solveur parallèle capable de gérer des topologies complexes et des milliards d'inconnus. Ce sont des échelles qui étaient inaccessibles par les solveurs de transfert radiatif standard.

Au chapitre 1, l'équation de transfert radiatif stationnaire est construite. Elle se lit

$$(\boldsymbol{s} \cdot \nabla + \beta)I(\boldsymbol{x}, \boldsymbol{s}) = \frac{\sigma_s}{4\pi} \oint_{\boldsymbol{s}'=4\pi} I(\boldsymbol{x}, \boldsymbol{s}')\Phi(\boldsymbol{s}, \boldsymbol{s}') \, \mathrm{d}\boldsymbol{s}' + \kappa I_b(T, \lambda)$$

où, κ, σ_s, Φ, and I_b sont les paramétres radiatifs connus, et $I(\boldsymbol{x}, \boldsymbol{s})$ est le champ d'intensité radiative dépendant des trois coordonnées spatiales $\boldsymbol{x} = \boldsymbol{x}(x, y, z)$ et des deux coordonnèes angulaires $\boldsymbol{s} = \boldsymbol{s}(\theta, \phi)$. Cette équation est construite selon l'aspect phénoménologique du transport à l'échelle du photons. Parmi la grande variété de méthodes numériques disponibles pour résoudre l'équation de transfert radiatif, une étude bibliographique non exhaustive et une brève description de certaines méthodes populaires sont fournies. Outre la description générale, les avantages et inconvénients de chaque méthode numérique sont mis en évidence. Ce premier chapitre se termine par l'identification des principales difficultés générales rencontrées lors de la résolution numérique de l'équation de transfert radiatif.

Pour résoudre numériquement l'équation de transfert radiatif, une double discrétisation est nécessaire (discrétisations spatiale et angulaire). L'un des choix populaires récents pour cette discrétisation spatio-angulaire est la méthode des éléments finis (FEM) couplée à la méthode des ordonnées discrètes (DOM). Ce processus partic-

---

[7]Caractérisation et Fonctionnalisation des Propriétés Radiatives de Matériaux
[8]transferts thermiques dans les matériaux et aux interfaces

ulier de discrétisation spatio-angulaire pour l'équation de transfert radiatif est le thème central du chapitre 2. La première étape, la discrétisation angulaire, convertit l'équation de transfert radiatif integro-différentielle en un ensemble fini d'équations aux dérivées partielles, toutes couplées entre elles. Ceci est fait en employant la méthode des ordonnées discrètes. La deuxième étape de discrétisation implique l'application de la méthode des éléments finis sur chaque équation aux dérivées partielles. Ceci conduit à un système de formulations variationnelles. En raison de la nature hyperbolique de l'équation de transfert radiatif, plutôt que la méthode éléments finis standard, sa version stabilisée Petrov-Galerkin (SUPG-FEM) est choisie.

Au cœur de cette thèse se trouve "la méthode des éléments finis vectoriels", une technique de discrétisation spatiale par laquelle nous tentons d'améliorer la procédure standard de la solution SUPG-FEM DOM pour l'équation de transfert radiatif. Plutôt que d'utiliser les éléments finis standards, nous reformulons l'équation de transfert radiatif à l'aide d'éléments finis vectoriels. Les éléments finis vectoriels, plus connus sous le nom d'éléments finis mixtes, sont parfois utilisés pour résoudre les problèmes couplés de Navier-Stokes, d'élasticité, ou d'électromagnétisme, etc. Le chapitre 2 détaille également la méthode des éléments finis vectoriels et montre comment mettre en place cette procédure couplant éléments finis vectoriel et ordonnés discrètes. On y met en évidence les principales différences entre l'approche standard et l'approche vectorielle. Notamment, l'approche vectorielle donne une équation vectorielle unique qui est résolue après introduction d'un unique espace fonctionnel vectoriel, alors que la formulation standard donne un ensemble d'équations. Les tests numériques révèlent que l'approche vectorielle produit des temps plus courts lors de l'assemblage des systèmes linéaires, ainsi que dans la phase de résolution, par rapport à la formulation éléments finis standard.

Le chapitre 3 concerne la parallélisation qui doit être compatible avec l'approche vectorielle. La double procédure de discrétisation du schéma vectoriel permet de paramétrer la parallélisation via deux techniques différentes de décomposition du domaine (DD) et de décomposition angulaire (AD). Ces deux techniques de parallélisations dont considérées. Autant la mise en place de la décomposition de domaine sur le solveur éléments finis standard aurait été fastidieux, autant l'approche vectorielle en facilite la mise en place. Il est montré comment configurer la décomposition angulaire avec l'approche vectorielle. Notamment, une nouvelle technique algébrique permettant de redistribuer efficacement la matrice obtenue avec la méthode de décomposition angulaire a été mise en place. Un avantage direct de cette nouvelle approche est que

la méthode de décomposition angulaire peut être étendue sur des milliers d'unités de traitement en parallèle, ce qui n'est pas possible par l'approche standard. Afin d'évaluer l'efficacité de la parallélisation des méthodes DD et AD proposées, des analyses de performance ont été réalisés pour des problèmes de transfert radiatif à grande échelle comportant des millions d'inconnues. On montre que les méthodes AD et DD proposées possèdent des capacités de mise à l'échelle quasi-linéaires, et que la mise à l'échelle de la méthode DD est quasi-indépendante des propriétés radiatives. D'un point de vue global, on observe que la méthode AD est légèrement plus efficace que la méthode DD.

Le chapitre 4 est ensuite consacré à l'analyse des préconditionneurs pour les méthodes de Krylov, afin d'accélérer la procédure de résolution des système linéaires. Sur la base de la physique du rayonnement, différents problèmes de transfert radiatif dans des milieux transparents, absorbants, diffusants et réfléchissants sont analysés. Une analyse spectrale est effectuée sur ces différents problèmes afin d'étudier l'effet de chaque opérateur sur le nombre de conditionnement du système linéaire global. Il est conclu, entre autres, que les problèmes impliquant un milieu absorbant seul ou transparent sont bien conditionnés, l'ajout de la diffusion augmente le nombre de conditionnement du système linéaire et que ce conditionnement se détériore fortement encore lorsque la physique de la réflexion est ajoutée. Deux solveurs de Krylov, le GMRES et le BiCGSTAB, avec ou sans préconditionnement, sont étudiés. Il en ressort que le BiCGSTAB est plus efficace que le GMRES dans tous les cas, avec son nombre inférieur d'itérations, son temps de résolution plus faible, et ses besoins mémoire plus faibles également. Concernant le préconditionnement, il est établi que les systèmes de préconditionnement avec la méthode de Jacobi par bloc (avec des factorisations LU incomplètes) conduisent à des convergences plus rapides encore.

Le cinquième chapitre est enfin consacré aux applications numériques pour l'analyse de certains problèmes de transfert radiatif à grande échelle. Pour construire la confiance dans la fiabilité des résultats obtenus, ce chapitre est d'abord dédié à la vérification, la validation et la qualification des différentes méthodes proposées. L'approche vectorielle est testée sur la base de différents benchmarks, et atteste de la fiabilité de la méthode proposée. En particulier, la méthode des solutions manufacturées est utilisée pour la vérification. On y compare aussi les solutions obtenues avec certaines solutions de référence disponibles dans la littérature ou de Monte–Carlo. Après validation et vérification des schémas proposés, nous montrons ensuite les capacités du solveur à gérer des milliards d'inconnues, pour des géométries complexes et pour des milieux

anisotropes, avec prise en compte de la spécularité. L'application traitée concerne la propagation du rayonnement dans des mousses à pores ouvertes. L'analyse des champs volumétriques d'intensité radiative apporte une connaissance plus précise de l'atténuation de l'énergie radiative localisée et globale dans le volume des mousses.

Enfin, une conclusion est présentée et complétée par des perspectives d'études.

English version

Modeling radiative transfer is of interest to many fields of science and technology. The problems of radiative transfer exist in abundance in thermal science, astrophysics, medicine, optical tomography, combustion physics, climatology, etc. One also finds radiative transfer problems in diverse engineering applications and industrial processes, such as combustion in gas turbine engines or in rocket nozzles, laser heating material manufacturing, solar thermo-chemical synthesis, and particle transport in nuclear reactors. Mathematically, mesoscopic and macroscopic scale radiative transfer is modeled using the radiative transfer equation. By nature, the radiative transfer equation is a complex integro-differential equation with up to seven independent variables: the frequency of radiation, three space coordinates, two angular coordinates describing the direction of radiation, and time. Such mathematical complexities limit the existence of an analytical solution only for simplified cases. Unfortunately these simplified cases only account for handful of radiative transfer problems. Hence, for more realistic problems of radiative transfer, the approximate solutions of the radiative transfer equation via a numerical approach are used.

The research conducted in this thesis is funded by Institut de Recherche Technologique Jules Verne, Bouguenais, France under the project SODA[9], that brings together academic partners (LTeN[10] Laboratory, Nantes, and GEM[11] Laboratory, Nantes, France) and industrial partners (Airbus Innovation Group, Safran Composites, and Dassault Aviation). Industrial partners on the project utilize the modern-day lasers as heating source for advance composite-material manufacturing. They find their motivation to solve the radiative transfer equation in absorbing, emitting, and scattering media with collimated laser sources. Modeling such problems in an efficient way demands a method (solver) that can handle three-dimensional radiative transfer problems efficiently within complex topology participating media, hence this thesis. This research was handled by the $\mathbb{C}\acute{e}f_0\mathcal{P}\mathcal{R}$am[12] team which is a sub part of TTMI[13] team at LTeN Laboratory. One of the goals of the $\mathbb{C}\acute{e}f_0\mathcal{P}\mathcal{R}$am team is advanced characterization of real materials which include complex geometries. Development of an advanced numerical technique to solve the radiative transfer equation via this thesis

---

[9]SimulatiOn du Drapage Automatisé

[10]Laboratoire de Thermique et d'Energie de Nantes

[11]Institut de Recherche en Génie Civil et Mécanique

[12]Caractérisation et Fonctionnalisation des Propriétés Radiatives des Matériaux

[13]Transferts Thermiques dans les Matériaux et aux Interfaces

hence also has scientific motives attached.

Over the course of five chapters provided in this thesis, we review the full solution procedure for solving the radiative transfer equation, and by the end we propose a parallel radiative transfer solver capable of handling complex topology participating media problems of radiation with billions of unknowns. These are scales that were previously unattainable by standard radiative transfer solvers.

In chapter 1, the reader is exposed to the monochromatic steady-state radiative transfer equation which reads

$$(s \cdot \nabla + \beta)I(x, s) = \frac{\sigma_s}{4\pi} \oint_{s'=4\pi} I(x, s')\Phi(s, s') \, \mathrm{d}s' + \kappa I_b(T, \lambda),$$

where, κ, σ_s, Φ, and I_b are the known radiative parameters for a given participating medium. $I(x, s)$ is the unknown radiative intensity field dependent on three spatial coordinates $x = x(x, y, z)$ and two angular coordinates $s = s(\theta, \phi)$. Following the phenomenological way of treating the radiation energy based on the photon framework, the radiative transfer equation has been derived in section 1.2. Among the vast variety of numerical methods available for solving the radiative transfer equation, a non-exhaustive bibliographical survey and a brief description for some of the popular methods have been provided in section 1.4. Besides their general description, pros and cons of each numerical method have been highlighted. Chapter 1 ends in section 1.5 which identifies general difficulties faced while solving the radiative transfer equation numerically.

In order to solve the radiative transfer equation numerically, dual discretization in space and angles is needed (spatio-angular discretization) as $I = I(x, s)$. One of the recent popular choices for this spatio-angular discretization is the finite element method (FEM) coupled to the discrete ordinates method (DOM). Detailing such a spatio-angular discretization process is the theme for chapter 2. The first step of dual discretization procedure, called the angular discretization, converts the integro-differential radiative transfer equation into a finite set of coupled partial differential equations. This is done by employing the discrete ordinates method, which has been explained in section 2.1.1.1. The second discretization step, which has been detailed in section 2.1.1.2, involves applying the finite element method on each partial differential equation leading to a system of variational formulations. In particular, due to the convection-dominant nature of radiative transfer problems, rather than the Galerkin finite element method, the Petrov–Galerkin FEM (SUPG-FEM) is chosen for spatially

discretizing each partial differential equation. Elaborated explanations and mathematical expressions for the full SUPG–FEM discretization procedure for the discrete ordinates radiative transfer equation are provided in section 2.1.1.

At the heart of this thesis is "the vectorial finite element method", a novel spatial discretization technique via which we attempt to improve upon the standard FEM solution procedure for the radiative transfer equation. Rather than using the standard finite elements, we reformulate the radiative transfer equation using vectorial finite elements. The vectorial FEM which is more commonly known as the mixed FEM is popular for solving the coupled problems of Navier–Stokes, elasticity, electromagnetism, etc. Chapter 2 also discusses the vectorial finite element method in details and shows how to set up such discretization procedure for the RTE. Sections 2.2.1 and 2.2.2, highlight the main differences between standard and vectorial FEM. A major difference comes from the fact that the vectorial FEM leads to a variational formulation which is a single vectorial equation solved in vectorial functional space, while, the standard FEM leads to a set of variational formulations which are solved over a single functional space. Contrary to blocked linear system structure from the standard FEM, the matrices derived from the vectorial FEM are banded. The advantages of using the vectorial FEM are made clear via numerical tests performed in section 2.3. The tests reveal that the vectorial FEM formulations yield faster timings for the linear system assemblies, as well as for the solution phase when compared to the standard FEM formulations for the RTE.

An efficient numerical method is the one which apart from qualities like accuracy, stability, generality, etc., is also easy to parallelize. Thankfully, one added advantage of using the vectorial FEM formulations is its straightforward parallelization. The main intention of chapter 3 is to review different approaches of parallelization compatible with the vectorial FEM. Depending on spatial and angular discretizations, the dual discretization procedure of the vectorial FEM allows us to set up parallelization via two different techniques of domain decomposition (DD) and angular decomposition (AD). Section 3.2 elaborates both of these parallelization techniques. While setting up DD with the standard FEM solver would have been a tedious task, the single vectorial equation makes it easier to set up DD with the vectorial FEM. The section 3.2.1 details why. Next, it is shown in section 3.2.2 how to set up AD with the vectorial FEM. The chapter further presents the extended AD in section 3.2.2.1. A new algebraic technique for efficiently redistributing the matrix obtained with the AD method has been implemented. A direct advantage of this new approach is that

the AD method can be extended on thousands of parallel processing units, which is not possible for standard AD techniques introduced in the literature. In order to assess the parallelization efficiency of the proposed DD and AD methods, scalability measurements have been performed. Section 3.3, provides results from the strong scaling performance analysis that was conducted for large scale radiative transfer problems with millions of unknowns. The proposed AD and DD methods are shown to possess quasi-linear scaling capabilities. Further, property independent scaling quality of DD is highlighted in section 3.3.2. Time-wise, the AD method is observed to perform better in comparison to DD method.

In order to speedup and tune the solving procedure further, the next chapter 4 is dedicated to the analysis of preconditioners for the Krylov subspace methods for solving different multi-dimensional radiative transfer problems. Based on the physics of radiation, different radiative transfer problems within transparent, absorbing, scattering, and reflecting media are analyzed. In section 4.2 an eigenspectrum analysis is performed on these different problems of radiation in order to study the effect of each physics on the condition number of the problem. It is concluded that: absorbing/transparent media problems are well conditioned; including the physics of scattering decreases the condition number of the discretized system; the condition numbers for an absorbing media does not change if reflection is added at the borders of problems; and the conditioning deteriorates heavily when the physics of reflection is involved in transparent/scattering media problems. Two Krylov subspace solvers, the GMRES and the BiCGSTAB, with or without preconditioning, are investigated in section 4.3.2 for solving the above mentioned radiative transfer problems. In conclusion, the BiCGSTAB outruns the GMRES for all cases, showing lower iteration count, solving times, and memory requirements. Via different numerical experiments on complex topology radiative transfer problems, it is established that preconditioning systems with the block Jacobi method (with incomplete LU factorizations with zero level of fill-in as block solvers) leads to faster convergence.

The fifth chapter is devoted to numerical experiments for analyzing some large scale problems of radiative transfer. To build trust in the reliability of results obtained from the vectorial FEM to predict unforeseen situations in radiative transfer, section 5.1 is dedicated to method verification, validation, and qualification. A thorough testing of the vectorial FEM against different benchmarks vouches for the reliability of the proposed method. In particular, the method of manufactured solutions is used in section 5.1.1 for verification of the vectorial FEM. Sections 5.1.2 and

5.1.3 compare the solutions obtained via the vectorial FEM against some reference solutions available in the literature and against the Monte–Carlo solutions, respectively. In addition, a transient conduction radiation problem that involves high temperatures has been solved in section 5.2. The aim of the problem is to reproduce a thermogram (temperature vs. time curve) obtained in a laser flash experiments for participating media by coupling conductive and radiative heat transfers. It is shown that experimental thermograms can be reproduced numerically with the vectorial FEM approach. After validating and verifying the vectorial FEM, finally, we show the capabilities of the solver to handle billions of unknowns, complex geometries, anisotropic media, specular reflections within some application cases of open-cell foam radiation. The volumetric radiation fields presented in section 5.2 bring into picture a more accurate and comprehensive knowledge about the localized and overall radiative energy attenuation within foams volume.

Finally the thesis ends with some conclusive remarks on the studies performed during the three years of this research.

Authors publications and presentations

This thesis led to the following publications, and presentations.

- **Peer reviewed journal publications**

  M. A. Badri, P. Jolivet, B. Rousseau, S. Le Corre, H. Digonnet, and Y. Favennec, "Vectorial finite elements for solving the radiative transfer equation," *Journal of Quantitative Spectroscopy and Radiative Transfer*, vol. 212, pp. 59–74, 2018.

  M. A. Badri, P. Jolivet, B. Rousseau, and Y. Favennec, "High performance computation of radiative transfer equation using the finite element method," *Journal of Computational Physics*, vol. 360, pp. 74–92, 2018.

  M. A. Badri, P. Jolivet, B. Rousseau, and Y. Favennec, "Preconditioned Krylov subspace methods for solving radiative transfer problems with scattering and reflection," *Computers and Mathematics with Applications*, 2018.

  D. Le Hardy, M. A. Badri, B. Rousseau, S. Chupin, D. Rochais, and Y. Favennec, "3D numerical modelling of the propagation of radiative intensity through a X-ray tomographied ligament," *Journal of Quantitative Spectroscopy and Radiative Transfer*, vol. 194, pp. 86–97, 2017.

- **Peer reviewed international conference proceedings**

  M. A. Badri, A. Biallais, G. Domingues, Y. Favennec, G. Fugallo, A. M. Monthe, and B. Rousseau, "Combining micro- meso- and macro-scopic numerical methods for multiscale radiative transfer modeling of sic-based foams up to very high temperatures," in *Proceedings of the 16th International Heat Transfer Conference*, IHTC 16. Beijing, China, August 10–15, 2018.

  M. A. Badri, Y. Favennec, P. Jolivet, S. Le Corre, and B. Rousseau, "A parallel implicit mixed-fem solution for complex domain radiative trasfer problems using immersed meshes," in *Proceedings of Computational Thermal Radiation in Participating Media VI Eurotherm Seminar No. 110*, CTRPM VI, Lisbon, Portugal, April 11–13, 2018.

  Y. Favennec, M. A. Badri, T. Mathew, and B. Rousseau, "Angular adaptivity with finite elements on ball-triangulation for efficient numerical solutions of radiative transfer equation," in *Proceedings of Computational Thermal Radiation in Participating Media VI Eurotherm Seminar No. 110*, CTRPM VI, Lisbon, Portugal, April 11–13, 2018.

  M. A. Badri, Y. Favennec, P. Jolivet, D. Le Hardy, S. Le Corre, and B. Rousseau, "Spatial versus angular parallelization for solution of radiative transfer equation in participating media," in *ICHMT DIGITAL LIBRARY ONLINE*, Begel House Inc., 2017.

- **National/international conferences with presentation or poster**

M. A. Badri, Y. Favennec, P. Jolivet, S. Le Corre, A. Biallais, and B. Rousseau, "Discrete-scale numerical radiative transfer analysis of porous participating medias," in *French Interpore Conference on Porous Media*, JEMP 2018, Nantes, France, Oct. 8–10, 2018 (Presentation).

B. Rousseau, A. Biallais, M. A. Badri, Y. Favennec, T. Fey, M. Stumpf, and J. Vicente, "Numerical design of cellular ceramics with prescribed effective thermal radiative properties," in *Computational Thermal Radiation in Participating Media VI Eurotherm Seminar No. 110*, CTRPM VI, Lisbon, Portugal, April 11–13, 2018 (Poster).

S. Lal, M. A. Badri, Y. Favennec, and B. Rousseau, "Towards development of a robust 3D numerical method to interpret thermograms of cellular ceramics acquired by the Laser Flash method," in *42nd International Conference and Expo on Advanced Ceramics and Composites*, ICACC2018, Daytona Beach, USA, Jan. 21–26, 2018 (Presentation).

M. A. Badri, Y. Favennec, S. Le Corre, and B. Rousseau, "Implicit parallel radiative transfer equation solver with application to complex semi-transparent media," in *11émes Journées d'Etudes en Rayonnement Thermique*, JERT2017, Orléans, France, Nov. 23–24, 2017 (Presentation).

M. A. Badri, Y. Favennec, H. Digionnet, S. Le Corre, and B. Rousseau, "Mixed finite element solution of radiative transfer equation ," in *7th International Conference on Advanced COmputational Methods in ENgineering*, ACOMEN2017, Ghent, Belgium, Sept. 18–22, 2017 (Presentation).

Acronyms

AD	angular decomposition
CFD	computational fluid dynamics
DD	domain decomposition
DOM	discrete ordinates method
FE	finite element
FEM	finite element method
FVM	finite volume method
MPI	Message Passing Interface
PDE	partial differential equation
RTE	radiative transfer equation
SUPG	streamline upwind Petrov Galerkin

Symbols

β	extinction coefficient
$\boldsymbol{n}$	outward unit normal vector
$\boldsymbol{s}$	direction vector
$\boldsymbol{s}_m$	discrete direction vector
$\boldsymbol{x}$	cartesian space coordinates
κ	absorption coefficient
λ	wavelength
$\mathrm{d}\omega$	solid angle
N_d	number of directions
ν	frequency
Ω	spatial domain
Ω^h	spatial mesh
ω_m	discrete weight
$\partial\Omega$	boundary
Φ	scattering phase function
ϕ	azimuthal angle
ρ^d	diffused reflectivity coefficient
ρ^s	specular reflectivity coefficient

σ_s	scattering coefficient
$\mathcal{S}$	unit sphere
$\mathcal{S}^{N_d}$	discretized unit sphere
θ	zenith angle
ε	emissivity
$\widehat{G}$	manufactured radiative density
$\widehat{I}$	manufactured radiative intensity
G	radiative density
$h_{\boldsymbol{s}}$	angular mesh size
$h_{\boldsymbol{x}}$	spatial mesh size
I	radiative intensity
I_b	blackbody emission
n	refractive index
N_e	number of mesh elements
N_v	number of mesh nodes
N_P	number of MPI processes
T	temperature
t	time

Subscripts and superscripts

λ	frequency dependence
c	collimated
s	specular
w	wall

Constants

|	
c_0	speed of light in vacuum $2.99792458\,10^8\ \mathrm{m\,s^{-1}}$
c_1	SUPG algorithimic constant $\quad$ 2
h	Planks constant $6.626068\,10^{-34}\ \mathrm{J\,s}$
k	Boltzmann constant $1.3806503\,10^{-23}\ \mathrm{J\,K^{-1}}$

THE RADIATIVE TRANSFER EQUATION

Radiation is simply energy in the form of waves or particles that travels through space or other media. Radiative transfer is the physical phenomenon of energy transport caused due to these waves or particles. Sunshine is the most familiar forms of radiation. Radiation is important to many fields of science and technology. For thermal engineering or scientific applications that involve high temperatures, characterizing radiation is vital. This is because, at elevated temperatures energy transfer due to radiation can dominate the other two modes of heat transfer namely conduction and convection. A modernistic radiative transfer application is found within the material manufacturing industry. Many material manufacturers, nowadays, use radiation emitted by sophisticated lasers as heating sources for materials. The Automated Tape Placement process is one such example where composite forming is accomplished by using a laser. Some manufacturers also use lasers for melting, cutting, and welding materials. Naturally, for these applications, knowledge of radiative field and its propagation is crucial. Other examples where the energy transfer due to radiation plays a propitious role involve: combustion systems, optical tomography, rocket nozzles, porous gas burners, solar collectors, etc. While all the previously cited examples are man-made, natural radiative transfer problems exist more commonly in the fields of astrophysics and climatology. Some examples of radiative transfer that were mentioned are shown in figure 1.1.

Examples provided in the previous paragraph belong to diverse scientific communities that are involved in solving radiative transfer: thermal science, astro-
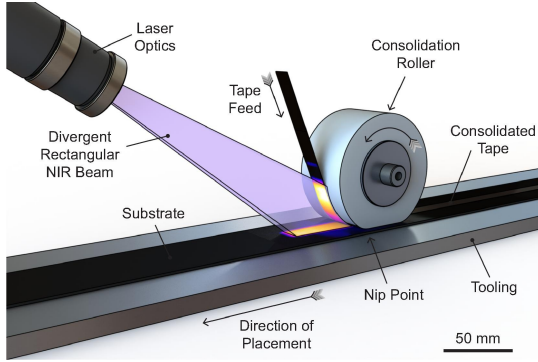
(a) Automated Tape Placement [14].
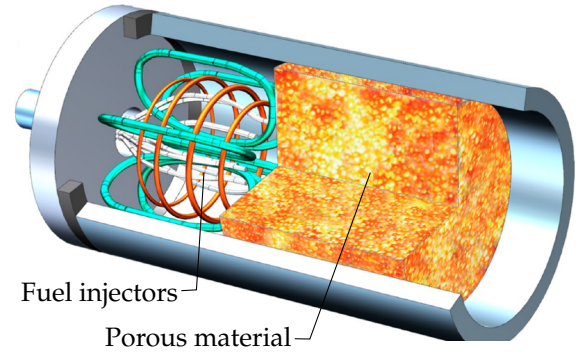
(b) Porous material radiation [15].
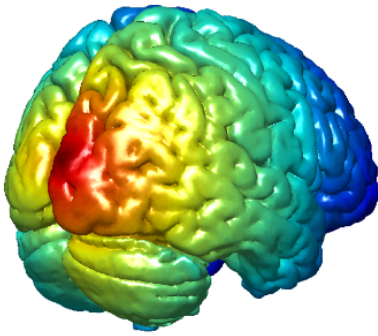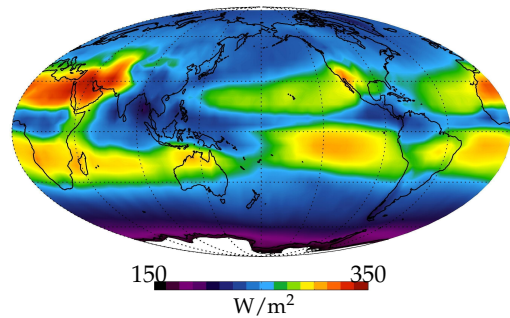

(c) Optical tomography [16].

(d) Rocket nozzles [17].

(e) Parabolic trough solar collector [18].

(f) Climatology radiation mesurements [19].

Figure 1.1: Radiative transfer examples from different application domains.

physics, medicine, optical tomography, climatology, combustion science, to cite but a few. Previous research has established that radiative transfer can be characterized mathematically by the radiative transfer equation (RTE) at mesoscopic and macroscopic scales, and by the Maxwell equations at microscopic scales. Publication metric data available over the Internet shows that the RTE has been growing in popularity since the early 1900's. Trends plotted[1] in figure 1.2, confirm that even at present the equation is a hot topic within different scientific communities. It can be observed from the figure that there is an exponential growth in research concerning the radiative transfer equation till date. Hence, one can say that, solving the radiative transfer equation efficiently and accurately is of paramount importance for many fields of science.
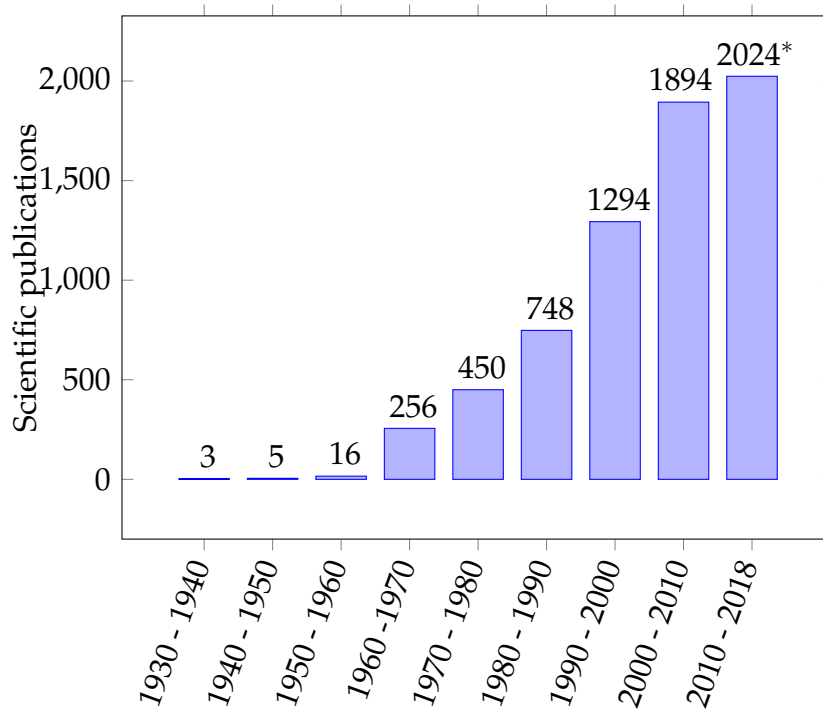
Figure 1.2: Scientific publication metrics for the radiative transfer equation. The superscript * stands for incomplete data, because the metric for the final decade requires data till the year 2020.

Although solving radiative transfer was taken up as a challenge by many sects of science, radiative transfer, probably was, amongst the last modes of energy transport to be widely taken into account by the numerical scientists. The main reason is notorious nature of the RTE, which will be introduced in the forthcoming section 1.2.

---

[1]Data was acquired from https://app.dimensions.ai/discover/publication with keyword search on "radiative transfer equation".

In its general form, the RTE involves both differential and integral operators, therefore complicating its solution process.

In the following sections in this chapter, the reader is exposed to the radiative transfer equation and how to solve it numerically. These sections are inspired by the book "Radiative heat transfer" written by M. F. Modest [20], the book "Numerical methods in multidimensional radiative transfer" written by G. Kanschat, E. Meinköhn, R. Rannacher, and R. Wehrse [21], the thesis of D. Le Hardy [22], and the ETR2017[2] school lecture "Solution methods of the radiative transfer equation" by P. J. M. Coelho [23].

1.1   Preliminary description of radiation

Radiative transfer can be defined as the change in energy of any system due to absorption and emission of electromagnetic waves. Physically, these electromagnetic waves can be pictured as a group of massless (sub-atomic) particles propagating at the speed of light c. Each particle carries some amount of energy, inversely proportional to the wavelength λ of its associated wave. These massless particles are called photons. Each photon can be associated with a plane wave, which when interacts with an atomic system either leads to energy loss by emission of photons, or to energy gain by absorption of photons. Photon absorption causes energy gain, this is due to the excitation of electrons from the lower energy states to the higher ones. Contrarily, emission of photons causes energy loss, this is due to jump of electrons from the higher energy states to the lower ones. The energy gained, and equivalently the energy lost, are quantified by $\Delta E_p = h\nu$, where $h = 6.626068\ 10^{-34}$ J s is the Plank's constant and ν frequency of the photon: $\nu = c/\lambda$. Pictorial representations of the emission and the absorption processes are presented in figure 1.3.

In order to accurately account for radiative transfer of a system, solving the Maxwell's equations for obtaining the electromagnetic field is inevitable. This equation is quite frequently solved in microscopic regimes, however the approach seems too detailed for mesoscopic and macroscopic considerations. Fortunately, the Maxwell's equations are linear by nature, hence any solution to the equation can also be represented as superposition of plane waves, or in other words, by a set of photons. For this reason, to quantify radiative transfer at mesoscopic and macroscopic scales,

---

[2]Summer school Ecole Transferts Radiatif en milieux semitransparents, 13-19 May 2017, Piriac-sur-Mer, France
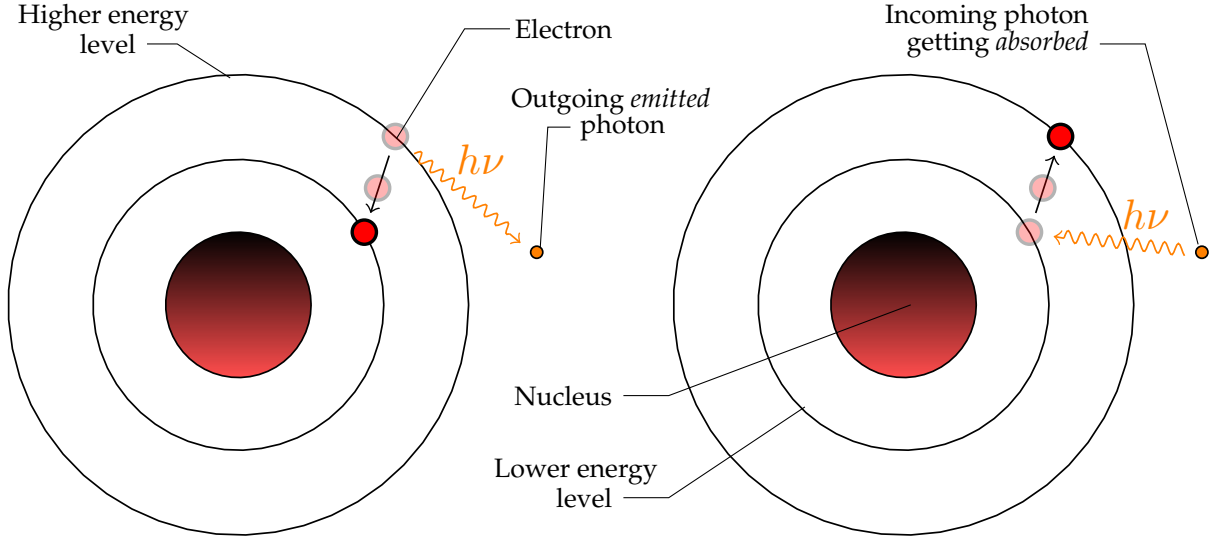
Figure 1.3: Pictorial representation of emission (left) and absorption (right) processes at atomic level.

one can concentrate on number of photons present at any spatial location $x(x, y, z)$, and its energy distribution. The photon density defines the number of photons at any location x traveling in direction s, crossing an infinitesimal area dA perpendicular to s, within a solid angle $d\omega$, and within wavelength and time intervals of λ to $\lambda + d\lambda$ and t to $t + dt$, respectively. Further, if the number of photons is multiplied by the energy that each photon carries, photon energy density or more commonly known as radiative intensity I is obtained. Hence, radiative intensity I can be physically defined as,

$$I_\lambda(x, s, t) = \frac{\text{photon energy at } \lambda \text{ through an area normal to } s}{dA \ d\omega \ d\lambda \ dt}, \quad (1.1)$$

where, the subscript λ denotes the wavelength dependence. Denoting this photon energy by $dQ_{r\lambda}$, we can write,

$$I_\lambda(x, s, t) = \frac{dQ_{r\lambda} \cdot n}{s \cdot n \ dA \ d\omega \ d\lambda \ dt}, \quad (1.2)$$

here, n is the normal vector of dA. The discussed nomenclature of the equation is made clear in figure 1.4. Equation (1.2) makes it clear that the radiative intensity is neither a vector nor a scalar quantity. This is due to that fact that radiative intensity is a function of directions s which are defined over the unit sphere. Equation (1.2) can further be used to derive the total radiative energy Q_r (also known as radiative heat flux) that crosses the surface perpendicular to the normal n, per unit area and time

$$Q_{r\lambda}(x) = \int_{\lambda=0}^{\infty} \int_{\omega(s)=4\pi} I_\lambda(x, s, t) s \ d\omega \ d\lambda. \quad (1.3)$$

5

Using the radiative intensity one could also derive other quantities of interest, like:

- the monochromatic radiative heat flux,

$$Q_r(\boldsymbol{x}) = \int_{\omega(\boldsymbol{s})=4\pi} I_\lambda(\boldsymbol{x},\boldsymbol{s},t)\boldsymbol{s}\,\mathrm{d}\omega, \tag{1.4}$$

- the monochromatic radiative density (incident radiation),

$$G(\boldsymbol{x}) = \int_{\omega(\boldsymbol{s})=4\pi} I_\lambda(\boldsymbol{x},\boldsymbol{s},t)\,\mathrm{d}\omega, \tag{1.5}$$

- the monochromatic radiative heat influx $Q_r^+(\boldsymbol{x})$, defined on a surface with normal vector $\boldsymbol{n}$, given by

$$Q_r^+(\boldsymbol{x}) = \int_{\substack{\omega(\boldsymbol{s})=4\pi \\ \boldsymbol{s}\cdot\boldsymbol{n}<0}} I_\lambda(\boldsymbol{x},\boldsymbol{s},t)|\boldsymbol{s}\cdot\boldsymbol{n}|\,\mathrm{d}\omega, \tag{1.6}$$

- the monochromatic radiative heat efflux $Q_r^-(\boldsymbol{x})$, defined on a surface with normal vector $\boldsymbol{n}$, given by

$$Q_r^-(\boldsymbol{x}) = \int_{\substack{\omega(\boldsymbol{s})=4\pi \\ \boldsymbol{s}\cdot\boldsymbol{n}>0}} I_\lambda(\boldsymbol{x},\boldsymbol{s},t)|\boldsymbol{s}\cdot\boldsymbol{n}|\,\mathrm{d}\omega. \tag{1.7}$$

Apart from the knowledge of radiative intensity $I_\lambda(\boldsymbol{x},\boldsymbol{s},t)$ and radiative energy $Q_{r\lambda}$, it is also necessary to quantify how much a system emits at different physical conditions. For this, the concept of black body was introduced. By definition, any body which can absorb all the photons that it interacts with, is called a black body. Further, it is established that such bodies, under thermal equilibrium, emit equivalent amount of energy that it had absorbed. This statement is dubbed as the Kirchhoff's law. To quantify the energy emitted by a black body $I_{b\lambda}$, the Plank's black body distribution law can be used. It reads,

$$I_{b\lambda}(T,\lambda) = \frac{2\pi hc_0^2}{n^2\lambda^5}\frac{1}{\left[\exp(hc_0/n\lambda kT)-1\right]}, \tag{1.8}$$

where, $c_0 = 2.99792458\ 10^8\ \mathrm{m\,s^{-1}}$ is the speed of light in vacuum, $n = c_0/c$ is the refractive index of the medium, T denotes the temperature of the medium, and $k = 1.3806503\ 10^{-23}\ \mathrm{J\,K^{-1}}$ is the Boltzmann constant. The black body emits photons isotropically, equally in all directions, hence does not depend on $\boldsymbol{s}$, and is a scalar variable within a medium.
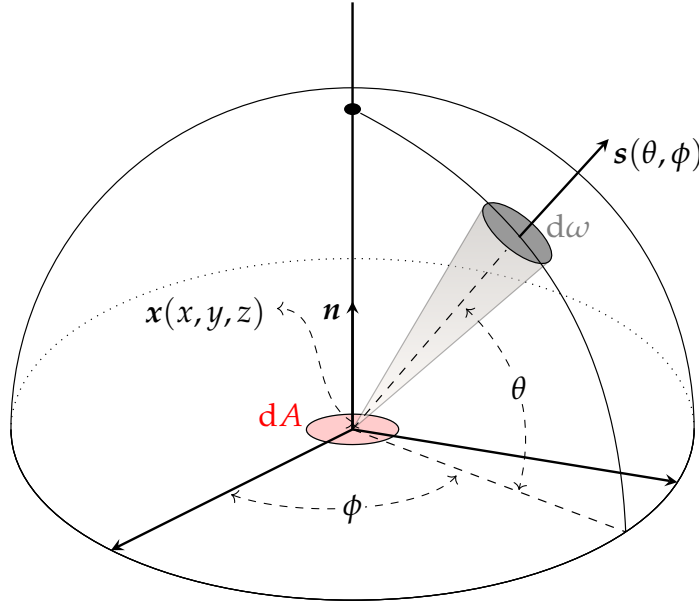
Figure 1.4: Infinitesimal area dA surrounded by the unit hemisphere. The propagation direction s and its corresponding solid angle $d\omega$ have also been shown.

1.2 The radiative transfer equation

Once all the mathematical tools for describing radiation are settled, the RTE can now be introduced. The RTE can be derived in several different ways. In this thesis, the phenomenological way of treating the radiation energy based on the photon framework will be followed, and the other ways to derive the equation will be briefly discussed at the end of this section.

As it was established in the previous paragraph, the radiative energy at macro- and meso-scales can be characterized by its specific intensity or simply the radiative intensity $I_\lambda(x, s, t)$ which is a function of the position x, the wavelength λ, the direction $s = [\cos\phi\sin\theta, \sin\phi\sin\theta, \cos\theta]^\top$, and the time t. The azimuthal angle θ and the zenith angle ϕ are used to characterize s. Figure 1.4 shows these two angles. It follows that, the radiative intensity $I_\lambda(x, s, t)$ along its path is subjected to the following three processes: (a) absorption characterized by the absorption coefficient $\kappa_\lambda(x)$, (b) scattering characterized by the scattering coefficient $\sigma_{s\lambda}(x)$ and the scattering phase function $\Phi_\lambda(s, s')$, and (c) emission characterized by the absorption coefficient $\kappa_\lambda(x)$ and the Plankian black body function $I_{b\lambda}(T, \lambda)$. The addition of the absorption and the scattering coefficients is called the extinction coefficient $\beta_\lambda(x)$. The inverse of the

7

(a) Absorption process $(\,\mathrm{d}I/\,\mathrm{d}s)_-$.

(b) Emission process $(\,\mathrm{d}I/\,\mathrm{d}s)_+$.

(c) In-scattering process $(\,\mathrm{d}I/\,\mathrm{d}s)_+$.

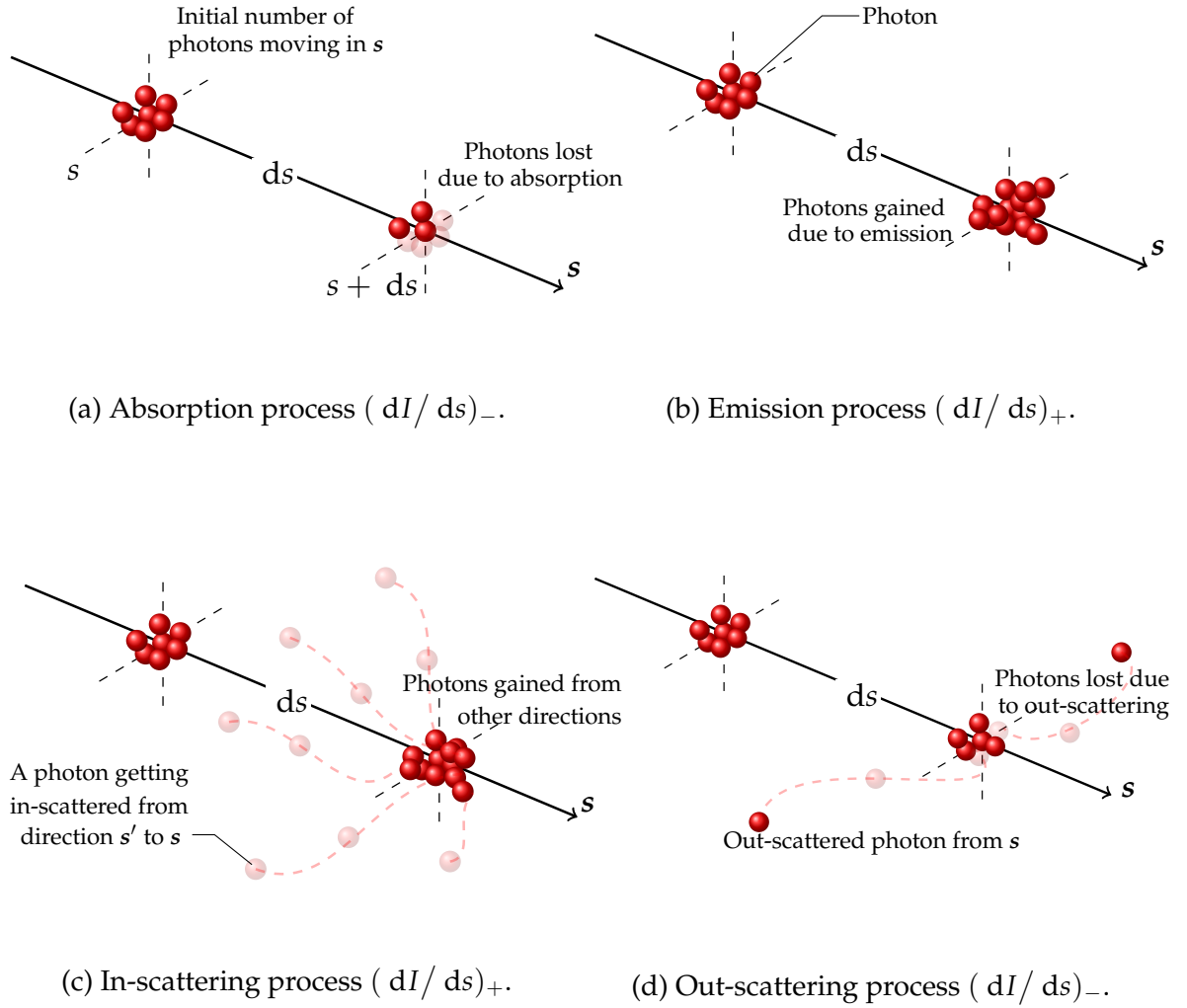(d) Out-scattering process $(\,\mathrm{d}I/\,\mathrm{d}s)_-$.

Figure 1.5: Pictorial representation of absorption, emission, in-scattering, and out-scattering: processes that affect the net loss or gain of photons in the direction s.

extinction coefficient is the mean free path $m_\lambda = 1/\beta_\lambda$. Before continuing further with the derivation, the process of scattering can be stated as the redirection of any photon from its original direction s to some other direction s'. If a photon is joined by other scattered photons, this leads to rise in radiative energy (as the photon count increases). This subprocess of scattering is known as in-scattering. Contrarily, if a photon scatters away from its main propagating direction, this leads to a loss in the radiative energy (as photon count decreases). This subprocess of scattering is known as out-scattering. The probability of how a photon propagating in s can be redirected to s' is defined by the scattering phase function $\Phi_\lambda(s, s')$.

As mentioned, the radiative intensity I propagating in s, once it traverses

infinitesimal distance $ds(\ll m_\lambda)$, is reduced by the process of extinction. In the photon framework, this reduction accounts for the decrease in the number of photons, either by absorption of photon by the medium (see figure 1.5a) or by out-scattering of photons to other directions (see figure 1.5d). Mathematically this is given by

$$\left(\frac{dI}{ds}\right)_{-} = -\left[\kappa_\lambda(\boldsymbol{x}) + \sigma_{s\lambda}(\boldsymbol{x})\right] I_\lambda(\boldsymbol{x}, \boldsymbol{s}, t) = -\beta_\lambda(\boldsymbol{x}) I_\lambda(\boldsymbol{x}, \boldsymbol{s}, t). \tag{1.9}$$

Further I is increased by the process of emission. In photon framework, this gain accounts for the increase in number of photons due to emission (see figure 1.5b). Mathematically this is given by

$$\left(\frac{dI}{ds}\right)_{+} = \kappa_\lambda(\boldsymbol{x}) I_{b\lambda}(T, \lambda). \tag{1.10}$$

Finally I is further increased by in-scattering. As in-scattering has contribution from all directions, hence, it must be calculated by integration over all solid angles. In the photon framework, the gain in radiative intensity due to in-scattering accounts for the increase of the number of photons that are redirected to the current direction by the process of in-scattering (see figure 1.5c). Mathematically this is given by

$$\left(\frac{dI}{ds}\right)_{+} = \frac{\sigma_{s\lambda}(\boldsymbol{x})}{4\pi} \oint_{s'=4\pi} I_\lambda(\boldsymbol{x}, \boldsymbol{s}') \Phi_\lambda(\boldsymbol{s}, \boldsymbol{s}') \, d\boldsymbol{s}'. \tag{1.11}$$
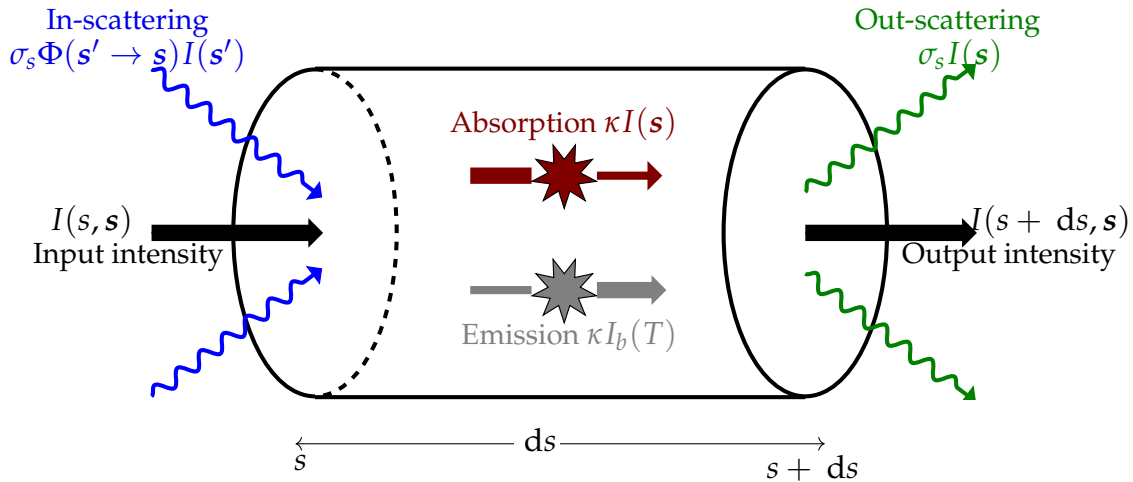

Figure 1.6: Attenuation of the radiative intensity by absorption, scattering, and emission processes. Note, for conciseness, time, wavelength, and spatial dependence for all the functions in the figure are not used.

The variation of the radiative intensity by the processes of emission, absorption, in-scattering and out-scattering has been pictorially shown in figure 1.6. Since we

are interested in the net balance of the total number of photons, this can be achieved by combining the three equations (1.9) to (1.11),

$$\frac{\mathrm{d}I}{\mathrm{d}s} = -\beta_\lambda(\boldsymbol{x})I_\lambda(\boldsymbol{x},\boldsymbol{s},t) + \kappa_\lambda(\boldsymbol{x})I_{b\lambda}(T,\lambda) + \frac{\sigma_{s\lambda}(\boldsymbol{x})}{4\pi} \oint_{s'=4\pi} I_\lambda(\boldsymbol{x},\boldsymbol{s}')\Phi_\lambda(\boldsymbol{s},\boldsymbol{s}')\,\mathrm{d}\boldsymbol{s}'. \quad (1.12)$$

Note, for readability, $I_\lambda(\boldsymbol{x},\boldsymbol{s},t)$ is simply presented as I on the left hand side of the equations above. This will be followed until the full radiative transfer equation (1.18) is derived. Since the variation of radiative intensity $\mathrm{d}I$ along a direction $\boldsymbol{s}$ depends both on distance $\mathrm{d}s$ in this direction, and on traversal time $\mathrm{d}t$. Therefore we could write,

$$\mathrm{d}I = I(s+\mathrm{d}s, t+\mathrm{d}t) - I(s,t) = \frac{\partial I}{\partial s}\,\mathrm{d}s + \frac{\partial I}{\partial t}\,\mathrm{d}t. \quad (1.13)$$

Recall that photons travel at the speed of light c, hence $\mathrm{d}s = c\,\mathrm{d}t$. This changes the equation to,

$$\frac{\mathrm{d}I}{\mathrm{d}s} = \frac{\partial I}{\partial s} + \frac{1}{c}\frac{\partial I}{\partial t}. \quad (1.14)$$

Substituting equation (1.14) in equation (1.12), the equation now reads,

$$\begin{aligned}
\frac{\partial I}{\partial s} + \frac{1}{c}\frac{\partial I}{\partial t} = & -\beta_\lambda(\boldsymbol{x})I_\lambda(\boldsymbol{x},\boldsymbol{s},t) + \kappa_\lambda(\boldsymbol{x})I_{b\lambda}(T,\lambda) \\
& + \frac{\sigma_{s\lambda}(\boldsymbol{x})}{4\pi} \oint_{s'=4\pi} I_\lambda(\boldsymbol{x},\boldsymbol{s}')\Phi_\lambda(\boldsymbol{s},\boldsymbol{s}')\,\mathrm{d}\boldsymbol{s}'.
\end{aligned} \quad (1.15)$$

Since the derivative along the photon traversal distance $\partial/\partial s$ is independent of the coordinate system, therefore, in terms of Cartesian coordinates, we may express this as

$$\frac{\partial I}{\partial s} = \frac{\partial x}{\partial s}\frac{\partial I}{\partial x} + \frac{\partial y}{\partial s}\frac{\partial I}{\partial y} + \frac{\partial z}{\partial s}\frac{\partial I}{\partial z}. \quad (1.16)$$

Notice that the three partial differentials $\partial x/\partial s$, $\partial y/\partial s$, and $\partial z/\partial s$ are simply the three components s_x, s_y, and s_z of the direction $\boldsymbol{s}$ (see figure 1.4). Hence one could replace $\partial I/\partial s$ in equation (1.15) simply by $\boldsymbol{s} \cdot \nabla I$, the equation then reads

$$\begin{aligned}
\boldsymbol{s} \cdot \nabla I_\lambda(\boldsymbol{x},\boldsymbol{s},t) + \frac{1}{c}\frac{\partial I_\lambda(\boldsymbol{x},\boldsymbol{s},t)}{\partial t} = & -\beta_\lambda(\boldsymbol{x})I_\lambda(\boldsymbol{x},\boldsymbol{s},t) + \kappa_\lambda(\boldsymbol{x})I_{b\lambda}(T) \\
& + \frac{\sigma_{s\lambda}(\boldsymbol{x})}{4\pi} \oint_{s'=4\pi} I_\lambda(\boldsymbol{x},\boldsymbol{s}')\Phi_\lambda(\boldsymbol{s},\boldsymbol{s}')\,\mathrm{d}\boldsymbol{s}'.
\end{aligned} \quad (1.17)$$

Equation (1.17) is the radiative transfer equation in its comprehensive form. One could also do the exercise of deriving the RTE by another phenomenological approach, i.e, by employing Einstein's concept of photons. Then, the radiative intensity field is described in terms of photon gas which satisfies the linear Boltzmann

equation (see [24] for more details). The Boltzmann equation is capable of describing the transport of general particles irrespective of the physics followed by them. Another approach to derive the RTE is by using a stochastic model (see [25] for more details). The stochastic nature of the radiation was implicitly included within the classical derivation of the RTE [26]. This approach connects radiation with Markov processes. Further, under some assumptions, the RTE can also be derived directly by reducing the Maxwell's equation. The analytical wave theory starts with the Maxwell's equations and takes ensemble averages based on statistics of the position, sizes, and concentration of the scatterers [27]. This results in Bethe–Salpeter equation [28]. The Bethe–Salpeter equation can then be used to derive the RTE [29].

The full RTE is presented in equation (1.17). However, for this thesis, the following three assumptions to the equation will be considered. First, since the speed of the light is very high, for many practical cases, one can consider that the radiative intensity field instantly reacts to any changes of the physical conditions that determine it. Hence, from here forth, the partial derivative of I with respect to time t, in equation (1.17), will be ignored. Second, all the test cases presented in this thesis deal with radiation within solid materials. In most of these cases the radiative intensity is monochromatic by nature. Following this, the wavelength dependence from equation (1.17) will be dropped. However, the monochromatic wavelength ($\lambda \to \mathbb{R}$) is still required for calculating the black body intensity $I_b(\boldsymbol{x}, \lambda)$ by using equation (1.8). Finally, we assume that the medium of interest is stationary (compared to c). This means that non-polarized radiation can be considered. The monochromatic steady-state radiative transfer equation within any homogenized medium reads

$$(\boldsymbol{s} \cdot \nabla + \beta)I(\boldsymbol{x}, \boldsymbol{s}) = \frac{\sigma_s}{4\pi} \oint_{\boldsymbol{s}'=4\pi} I(\boldsymbol{x}, \boldsymbol{s}')\Phi(\boldsymbol{s}, \boldsymbol{s}')\,\mathrm{d}\boldsymbol{s}' + \kappa I_b(T, \lambda) \quad \forall \boldsymbol{x} \in \mathbb{R}^d, \boldsymbol{s} \in \mathcal{S}. \quad (1.18)$$

Here d is the dimension of the problem, and $\mathcal{S}$ is the unit sphere within which solid angles $\mathrm{d}\omega$ and directions $\boldsymbol{s}$ lie (the half unit sphere was shown in figure 1.4).

1.3 Boundary conditions for solving the radiative transfer equation

The RTE described in the previous section, in its monochromatic steady form (1.18), contains the first order transport operator for the radiative intensities. Assuming that the RTE is to be solved for any domain Ω such that $\boldsymbol{x} \in \Omega \subset \mathbb{R}^d$, and that the domain is enclosed by a surface $\partial\Omega$, solving the RTE within the domain Ω then becomes a

boundary value problem which can be solved with the help of radiative intensities specified on the surface (wall) $\partial\Omega$ of the medium. In fact, how radiation behaves at the surfaces is a crucial piece of knowledge that is needed alongside the RTE for solving it.

Any surface $\partial\Omega$ which is not at absolute 0 K temperature, will emit certain amount of radiation. This emitted energy or the emitted intensity I_{emitted}, depends on the surface temperature, the direction of emission, etc. Generally, the black body intensity $I_b(T_w, \lambda)$ is used as a reference to define the surface properties of any enclosed medium. For $\partial\Omega$ which is at temperature T, we define the emissivity ε as

$$\varepsilon = I_{\text{emitted}}(T_w, \boldsymbol{s})\big/I_b(T_w, \lambda), \tag{1.19}$$

where the subscript w denotes wall affiliation. Since, at a given temperature, no body is capable of emitting more radiation than the black body (Kirchhoff law), ε will always be between 0 and 1. Hence, using this equation (1.19), we can write a simple boundary condition for the RTE for a problem with emitting walls,

$$I_w(\boldsymbol{x}_w, \boldsymbol{s}) = I_{\text{emitted}}(\boldsymbol{x}_w, \boldsymbol{s}, T) = \varepsilon I_b(T_w, \lambda) \qquad \forall \boldsymbol{x}_w \in \partial\Omega. \tag{1.20}$$

Note that this kind of boundary condition is also known as *diffused boundary condition*.

Another type of boundary conditions arise when the surface emits radiation but only in a single direction $\boldsymbol{s}_c$. This is called the *collimated boundary condition*. One way to treat such boundary condition is to assume $\varepsilon = 1$ for the collimated direction $\boldsymbol{s}_c$, while $\varepsilon = 0$ for other directions $\boldsymbol{s}_c'$. Mathematically, equation (1.20) can be adapted for the collimated case:

$$I_w(\boldsymbol{x}_w, \boldsymbol{s}) = I_{\text{collimated}} = \begin{cases} I_0 & \forall \boldsymbol{x}_w \in \partial\Omega \quad \text{if } \boldsymbol{s} = \boldsymbol{s}_c, \\ 0 & \forall \boldsymbol{x}_w \in \partial\Omega \quad \text{if } \boldsymbol{s} \neq \boldsymbol{s}_c. \end{cases} \tag{1.21}$$

Here, I_0 is the radiative intensity strength of the collimated beam. Such type of boundary condition arises in solar collector applications, laser radiation problems, etc.

Further, other type of boundary conditions arise due to property of the surface known as reflectivity ρ. Such boundary conditions are needed when radiations reach surfaces with different refractive indices on either side of the surface. Certain cases exist where reflectivity of the surface is neglected and radiation is allowed to freely pass through. This type of boundary condition is called *vacuum boundary condition*.

For cases where the phenomena of reflections cannot be ignored, based on the topology of the surface (optically rough or smooth), reflectivity ρ is divided into a
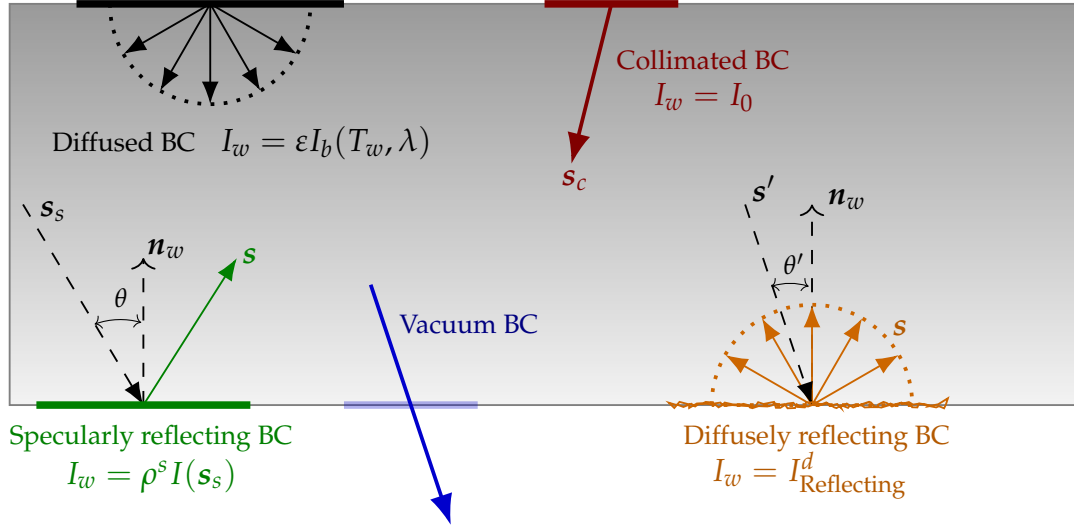
Figure 1.7: Different kinds of boundary conditions for the radiative transfer equation. In the figure, BC denotes boundary condition.

diffuse component ρ^d (rough surfaces), and a specular component ρ^s (smooth surfaces). This gives rise to two types of boundary conditions: *diffusely reflecting boundary condition* and *specularly reflecting boundary condition*. Note that the superscripts *d* and *s* stand for diffusely and specularly, respectively.

A surface is considered to be diffusely reflecting if it is capable of distributing the incident radiative intensity traveling in s' to all the directions s contained in the hemisphere. The hemisphere exists with a conditional $n_w \cdot s' < 0$. Mathematically this boundary condition reads

$$I_w(x_w, s) = I^d_{\text{Reflecting}} = \frac{\rho^d}{\pi} \int_{n_w \cdot s' < 0} I_w(x_w, s') |n_w \cdot s'| \, ds', \qquad (1.22)$$

here, n_w is the local outward normal to surface $\partial\Omega$ and $n_w \cdot s' = \cos\theta'$ is cosine of angle between any incoming direction s' and the surface normal n_w.

Next, a surface is considered to be specularly reflecting if it is capable of redirecting the incident radiative intensity traveling in specular direction s_s to another direction s. These directions are governed by $s_s = s - 2(\cos\theta)n_w$, here $\cos\theta = s \cdot n_w$. Mathematically, the boundary condition reads

$$I_w(x_w, s) = I^s_{\text{Reflecting}} = \rho^s I(x_w, s_s). \qquad (1.23)$$

Reflections are considered to be idealized for the diffusely or specularly

reflecting surfaces. For non-ideal surfaces, one could build the bidirectional reflection function ρ^{BRDF} (either by theory or experiments), and use it to model such surfaces. While both ρ^d and ρ^s are scalar values, the bidirectional reflection function ρ^{BRDF} on the other hand is a full map of how all incoming directions $\boldsymbol{s}$ are reflected to corresponding directions $\boldsymbol{s}'$. One could see such functions as special kinds of phase functions valid only at the boundaries. Mathematically, the *non-ideally reflecting boundary condition* can be stated as,

$$I_w(\boldsymbol{x}_w, \boldsymbol{s}) = I_{\text{Reflecting}}^{\text{BRDF}} = \int_{\boldsymbol{n}_w \cdot \boldsymbol{s}' < 0} \rho^{\text{BRDF}} I(\boldsymbol{x}_w, \boldsymbol{s}', \boldsymbol{s}) I_w(\boldsymbol{x}_w, \boldsymbol{s}') |\boldsymbol{n}_w \cdot \boldsymbol{s}'| \, \mathrm{d}\boldsymbol{s}'. \qquad (1.24)$$

All the boundary conditions discussed in previous paragraphs have been pictorially represented in figure 1.7. There are other types of boundary conditions that exist, for instance, refraction at the surfaces, opaque surfaces with arbitrary emittance, etc. These will not be discussed here, but [20] can be referred for a detailed knowledge on these types of boundary conditions.

1.4 Bibliographical survey of solution methods for radiative transfer problems

To solve the radiative transfer problems many solution techniques have been developed during the past years. Textbooks [20, 30] present detailed explanations of many solution methods, applicable to the radiative heat transfer problems. In this section, a brief description and a non-exhaustive bibliographical survey of some popular techniques for solving the radiative transfer problems is presented. The survey is not exhaustive considering the huge amount of developments and research in this area. Further, we would also overview some analytical methods for which solving the RTE may not be required.

Until the early 1960's main focus of numerical scientists solving the RTE was to solve the equation for simple cases that involved spherically symmetric or on plane-parallel systems. For these idealized cases the analytical solutions were readily amiable at the time [26, 31]. We know now that many formal solutions exist for the RTE, e.g., for a non-scattering medium, or for a purely scattering medium, or for a cold medium. The analytical expressions which govern radiation for such cases are provided in [20]. It was post 1960's that many scientific sects such as the radiative transfer community [20, 30, 32, 33, 34, 35, 36], the neutron transport community [37,

38, 39, 40, 41], the optical imaging community [42, 43, 44, 45], etc., aimed towards
numerically solving the radiative transfer phenomena for real world applications,
considering multidimensional and anisotropically scattering media. This consequently
led to development of many new numerical schemes for solving the RTE. Each newly
developed method claimed to have some or the other advantages over other methods.

Broadly, the numerical schemes that have been developed for solving the RTE
can be divided into two major categories. The first group consists of the physics-based
particle tracing approaches which are based on probabilistic concepts to simulate
elementary radiation events of absorption, emission, scattering, and reflection. The
second group consists of the deterministic approaches. Here, the integro-differential
RTE, is solved by the process of mathematical discretizations.

1.4.1 Stochastic approach (Monte–Carlo method)

Huge amount of work has been performed concerning the solution of radiative transfer
with Monte–Carlo methods. A non-exhaustive list of published literature include [46,
47, 48, 49, 50, 51]. Undoubtedly, the Monte–Carlo method is one of the most commonly
used and the most powerful numerical tool available for solving the RTE. The method
allows for simulating diverse range of radiative transfer problems with complex
geometries, heterogeneous media, anisotropically scattering media, etc. The method
is generally considered as a reference method, which can be used for benchmarking
purposes.

A Monte–Carlo radiative transfer simulation, based on probability theory,
simulates the stochastic events of absorption, emission, scattering, and reflection.
This is accomplished by firing a large number of photons from random positions
in random directions into the computational domain. The paths of the photons are
tracked throughout the medium. After a random distance depending on the mean free
path m, photons are scattered, absorbed, or reflected randomly. The process is iterated
for each photon until it has either escaped from the domain or has been absorbed
completely. From a computational view point, the algorithm becomes time consuming
in two scenarios: when a huge number of photons are needed to be tracked, or when
the photons are needed to be scattered several thousand times. The former case exists
when one considers a large computational domain and the latter case exists when
optically thick media (very short mean free paths) are considered.

Due to the mentioned limitations, several improvements to the classical

Monte–Carlo method have been made. For example, photons could be replaced by photon bundles (intensity packets) which are not completely absorbed at random distances but their strength (intensity) decreases according to κ, see [46]. Certain acceleration schemes exist to speed up the Monte–Carlo simulations, for instance see [52, 53, 54]. Moreover, to build a computationally fast Monte–Carlo method, parallelization comes in handy [55, 56]. It should be mentioned that these methods are easy to parallelize, as each photon or an intensity packet can be handled separately by a parallel processing unit.

With all the advantages of the Monte–Carlo method enlisted in the previous paragraphs, what motivated numerical scientists to solve the RTE deterministically is that, the Monte–Carlo method is computationally expensive when compared to the deterministic methods, particularly for relatively simple problems. As mentioned earlier, a large number of photons or intensity packets are needed to obtain statistically accurate results. Moreover, the Monte–Carlo solution algorithm is entirely different from the ones used in Computational Fluid Dynamics (CFD) for solving heat equation, fluid flow, etc. Hence it is difficult to couple a Monte–Carlo based solver to a deterministic CFD solver.

1.4.2 Deterministic approaches: angular discretization techniques

The steady-state monochromatic radiative transfer equation is a five dimensional problem by its nature since it depends both on space $x = x(x, y, z)$ (three unknowns) and angles $s = s(\theta, \phi)$ (two unknowns). Hence, for deterministic approaches, two kinds of discretizations can be looked at separately: angular discretization and spatial discretizations. In this subsection, the angular discretization techniques will be discussed.

1.4.2.1 Spherical harmonics method

This spherical harmonics method is also popularly known as the P_N method or the differential moment method. Introduced in [57], the spherical harmonics method transforms the RTE into a set of simultaneous partial differential equations. To briefly explain the method, first the radiative intensity $I(x, s)$ is expressed as a truncated series expansion in terms of directionally dependent spherical harmonics. Further, the phase function is expressed as a truncated series of Legendre polynomials. Next, these approximations are substituted in the RTE, which is then multiplied by the spherical harmonics of the series expansion and integrated over all directions. The method is

called the P_1 method when the spherical harmonics of the series is truncated only after one term, this yields one partial differential equation. Higher order variant, the P_3 method, truncates the spherical harmonics of the series after the first three terms, this yields 16 partial differential equations. However, only a few works reported in the past use the P_3 method [58, 59, 60]. In other words the P_1 method is more popularly used [61, 62, 63, 64]. Without attempting for completely describing the method, the reader is referred to textbooks such as [20, 30] which contain the detailed derivation and analysis of the method.

The main advantage of P_1 method is its simplicity and low computational cost. However, reasonable solutions can only be computed for problems where the radiative intensity field is nearly isotropic. In general, the method performs the best for optically thick media, while its accuracy depletes for optically thin media and for strongly anisotropic radiation intensities (collimated boundary conditions), particularly in multi-dimensional geometries with large aspect ratios [20]. Further, for problems with dominant emission from boundaries, the spherical harmonics method performs poorly.

The modified version of P_N method, known as the simplified P_N or SP_N method [65, 66, 67], is also used to discretize the RTE in the angular space. Note that after applying these methods, the spatial discretization of the problem is still required.

1.4.2.2 Discrete transfer method

The discrete transfer method [68, 69, 70, 71] solves the radiative transfer equation along representative rays (directions) between two boundaries. Each representative ray is contained within a solid angle, and it is assumed that the radiative intensity is constant within the solid angle. These representative rays are specified on the hemispheres centered about the points located on the boundary of the computational domain. These boundary points are determined from the computation grid. The method, so far, has been applied on radiative transfer problems either with non-scattering media or with isotropically scattering media. The method was originally built for structured grids, however, later it was expanded for unstructured grids [72], and for curvilinear grids [73].

This method originated in the combustion science community, and was specifically designed to accurately predict the boundary heat flux. This is due to the fact that the boundary heat flux is important for combustion applications. However, for satisfactorily predicting the radiative field (source needed for coupling radiation to CFD)

within the medium, the method requires a fine computational grid. This is a major drawback of the method, as the computational cost increases rapidly. Moreover, the method is non-conservative by nature, which may be disadvantageous if coupling of a discrete transfer radiative solver is required to other solvers that employ conservative discretization for other physics.

Another disadvantage of the discrete transfer method is the ray effect, which leads to a loss in accuracy. Ray effects arise for cases with sharp temperature gradients either on the boundary or within the medium. Whenever radiative intensity is assumed to be constant within a solid angle (non-physical assumption), ray effects are prone to happen. In order to rectify ray effects, the remedy is to use fine number of representative rays, but this implies a drastic increase in computational resources.

1.4.2.3 Discrete ordinates method

The discrete ordinates method (DOM) handles the angular discretizations by using the collocation method, i.e., replacing the integral over the unit sphere (first term on the right hand side of equation (1.18)) by a quadrature rule or a weighted summation. Consequently, one solves the RTE for a set of discrete directions, which span the total solid angle 4π around any spatial location. Following the DOM, one needs to solve simultaneous partial differential equations that replace the integro-differential RTE. The scheme was first introduced by Chandrasekhar [26] in 1950. However, it became a popular method to solve the RTE after a significant contribution from Fiveland [32] in 1984. Ever since, it has been widely used and developed [34, 35, 74, 75, 76, 77, 78]. The review paper [79] summarizes the recent advances in the discrete ordinates method for solving the radiative transfer equation. This method is the chosen angular discretization technique in this manuscript, hence the method will be explained in details in the following chapters.

For the DOM, the sets of discrete directions and their associated weights (solid angles) can be either calculated based on Gaussian quadrature rules [80, 81, 82], or constructed based on the angular mesh chosen to discretize the unit sphere [77, 83, 21], or constructed by using the finite element method [34, 84, 85, 86]. The degree of accuracy for the DOM depends on the choice of angular and spatial discretization procedures. For example, the discrete ordinates method coupled to the piecewise linear finite element method was reported to be second order accurate [35, 21].

The DOM is well suited for evaluating angular integrals of the radiative in-

tensity fields, such as the radiative density (equation 1.5), the radiative heat flux (equations 1.6 and 1.7), etc. However, the method is poorly suited to follow the paths of a particular photon. The reason being, that the DOM approximates the integral term of RTE either by a quadrature or by a weighted summation. Therefore, the method will be well suited for calculating integral quantities. This means, if we are interested in knowing how a particular directional intensity field changes within the medium, this method is not the most appropriate.

The ray effect, which was previously discussed in the context of discrete transfer method, is also a disadvantage of the DOM. The reason for occurrence of ray effect within the DOM being the same as before, i.e., the radiative intensity is assumed to be constant within a solid angle (non-physical assumption). Another bias for the DOM comes from false scattering. False scattering appears within numerical solutions of the RTE, and these appear due to application of upwinding techniques which are applied for handling the convective dominant RTE. However, it was proven that these two sources of errors (false scattering and ray effects) are opposing each other and tend to compensate the total error [87, 88]. The opposing effect comes from the fact, that when ray effects tend to enhance discontinuities or gradients of the radiative intensity field, false scattering tends to smooth the radiative intensity field. A simple remedy to mitigate these effects is to refine both angular and spatial meshes simultaneously. Further, one may also choose to use the modified DOM [89] which helps to eliminate these biases.

The DOM, at present has become the most widely used radiation model (discretization based) since it provides accurate results for a vast range of problems at moderate computational requirements. Complex geometries, heterogeneous media, reflections, anisotropic scattering, etc., can be easily handled by the method. Many preconditioning strategies [90, 91, 92, 93] and parallelization techniques [94, 95, 93, 96] have been developed for the method to enhance the algorithm. The method is also easily coupled with available CFD solvers, hence coupled conduction-convection-radiation problems have also been solved using such method.

1.4.2.4 Finite volume method

The finite volume method for angular discretization is much similar to the previously discussed DOM. The difference comes from the fact that the RTE is integrated over every control angle (solid angle) from the angular discretization. These control angles are constructed by intersecting parallel lines of constant latitude and constant meridian

lines. Like the DOM, the value of radiative intensity is constant within a control angle, however its direction is allowed to vary within the angle. The method is widely used with the finite volume discretization for the spatial domain. The finite volume method is known to model radiation with relatively good accuracy, and is becoming widely popular [97, 98, 99].

One advantage of the method is that it is fully conservative. By using analytical phase functions, an exact evaluation of the average phase function can be guaranteed. This is due to the fact that one can guarantee integral of the phase function over the unit sphere yields 4π. Disadvantages of the DOM, namely, ray effect and false scattering remain valid for the finite volume method as well. And like the DOM, the finite volume method is easily coupled with other CFD solvers and can be parallelized [100]. Raithby [101] compares the finite volume method to the DOM.

1.4.2.5   Other methods

In addition to the discussed methods for the angular discretization, several other methods are available. The flux methods (t2-flux method [102, 103], modified 2-flux method [104], 4-flux method [105], and 6-flux method [106]) were very popular in the past, because these were computationally cheap and easy to set up. Later, with the development of more accurate and flexible methods like the DOM, the spherical harmonics, etc., the flux methods are now rarely used. Another method, the Hotell's zonal method [107] was often used in the past to calculate radiative transfer in furnaces. The method was originally developed for non-scattering media and later expanded for scattering media. The zonal method like the Monte–Carlo method is considered as a reference method. However, its application to complex geometries significantly increases the computational time. Moreover, like the Monte–Carlo method, it remains decoupled from CFD solvers.

Another approach, the diffusion approximation, which is also dubbed as the Rosselands approximation [108, 109] is applicable to media with optical thickness much larger than unity. Physically, in such a medium, radiation travels very short distances before being absorbed. Mathematically, one gets an equation similar to the Fourier law for conduction, which is easy to solve analytically or numerically. A serious limitation comes from the fact that the model is not generalized and only applies to optically thick problems, as such the method is case specific. While a medium may be considered optical thick for a specified wavelength, the same media may behave semi-transparent or even optically thin for other wavelengths.

Another case specific method is the optically thin approximation [30], contrary to the Rosselands approximation the medium is consider to have optical thickness of much less than unity. Physically, for such scenarios, radiation escapes from the medium to the surroundings without being self absorbed or scattered. This is indeed the most dramatic simplification that can be considered for a radiative transfer problem. Even in cases with weak radiation, the method does not perform well [110]. One advantage of the method is that the method is computationally cheap. However, it is not preferred if an accurate calculation is required. The method also shares the same limitation as Rosselands approximation, i.e, a medium may not be optically thin for different wavelengths.

1.4.3 Deterministic approaches: spatial discretization techniques

In this subsection, the methods available for discretizing the RTE spatially (after angular discretization) are discussed. If angular discretization of the RTE leads to a partial differential equation(s) that cannot be solved analytically, spatial discretization becomes inevitable. For example, the DOM, the finite volume method, and the spherical harmonics methods, all need the spatial discretization. One could say that spatial discretization if it exists, is the second step of the full discretization process for numerically solving the RTE. Some of the used spatial discretization techniques include the finite difference method, the finite volume method, the finite element method, the method of short characteristics, etc.

1.4.3.1 Finite difference method and the method of short characteristics

Simplest among the spatial discretization schemes are the finite difference method [44, 111, 112] and the method of short characteristics [113, 114]. These methods are applied upon regular structured grids. Hence, in most cases, these can be only used with fairly simple geometries. Within diffuse optical tomography community, to solve an inverse radiative transfer problem, the finite difference method was coupled to the discrete ordinates method [115]. On the other hand, the method of short characteristics was also coupled to the discrete ordinates method to solve few two-dimensional astrophysics problems [116].

Both these methods yield an algebraic system of equations which can be rapidly solved for homogeneous media and smooth data. Regardless of their simplicity, the mathematical structure of these methods is weak, mathematical theories such as posterior error estimate (a powerful tool for mesh adaption) cannot be realized in such

methods. In addition, such methods fail when dealing with complex geometries, large optical depths, highly scattering media, and steep solution gradients [117]. Perhaps, these two methods are the two rarely used methods for spatial discretization of the RTE.

1.4.3.2   Finite volume method

The finite volume method is based on conservative properties of the partial differential equation(s) derived after angular discretization process of the RTE. Indeed, it is the most frequently used method for spatially discretizing the radiative transfer equation [33, 97, 118, 119, 120]. Mostly, the finite volume method is coupled with discrete ordinates method in order to give full solution of the radiative transfer equation [77, 121, 120]. However, the method has also been coupled to other angular discretization methods like, the finite element method [84], the finite volume method [97, 99], and the spherical harmonics method (P_1 and P_3) [60, 122, 123].

The finite volume method for spatial discretization works best with structured grids, because it is easy to handle transport sweeps that are needed during iterative solution phase. However, the method has also been extended for handling unstructured grids [99]. The radiative intensity field solution is constructed as a function of properties that are assumed to be constant inside small control volumes which depend on the grid. In regions where the solution exhibits discontinuities or steep gradients, the solution profile may produce spurious extrema due to convection dominance from the RTE. Such effects can lead to loss in robustness of the solution methodology in an iterative solution procedure like finite volumes, hence reconstruction techniques or use of slope limiters (the Venkatakrishnan limiter, the Van Leer limiter, the Barth–Jespersen limiter, the min-max limiter) have been developed in order to achieve higher order method [120]. Recently the review paper [121] listed the advances in use of the finite volume coupled to the discrete ordinates methods and the finite volume in space coupled to finite volume in angles for solving radiative transfer problems.

1.4.3.3   Finite element method

The finite element method (FEM) was first introduced in 1978 by Reddy et al. [124] to solve the radiative transfer for a 1D geometry. At present, not only has the method been extended to two- and three-dimensional problems, it has also become a popular choice for spatial discretization of the RTE [35, 21, 85, 125, 126, 127, 128, 129, 130]. Like the finite volume method (for space), the FEM has also been coupled to different

angular discretization schemes: the discrete ordinates method [35, 130, 131], the finite element method [34, 85, 86], and the spherical harmonics method [132]. The finite element method for spatial discretization coupled to the discrete ordinates method for angular discretization (FEM-DOM) are the methods chosen for fully discretizing the RTE in this thesis. In the chapters to follow the FEM-DOM will be discussed in detail.

The FEM is based on weak formulation of the main equation of radiation, and the solution field is constructed based on projection of these weak formulations on piecewise polynomial space functions. Due to its strong mathematical developments, the FEM allows theoretical studies such as uniqueness, consistency, existence, and stability of solution to be performed. Further, being of higher order, mesh requirements for the FEM are lower when compared to other methods. For a radiation field test of plane parallel medium, a comparison between the FEM and the finite difference method was published in [117].

Due to convective dominant nature of the RTE the classical FEM (Galerkin) cannot be used. For this reason, the discontinuous Galerkin FEM [35, 130, 133] or the streamline upwind Petrov–Galerkin FEM (SUPG-FEM) [130, 134, 135] or the least square FEM [136, 137, 138] are the FEM variants used instead.

Adaptive mesh refinement, unstructured grids, and dealing with complex geometries is exceptionally suited to the FEM. References [34, 43, 78, 117, 128, 130] would support this statement. Preconditioning and parallelization are two techniques which use the modern day computers to its full capacity for obtaining results quickly. These techniques have also been developed for enhancing the FEM discretization technique for the RTE [34, 90, 132]. The FEM is also popular for solving the radiative transfer problems dealing with graded media index (semi-transparent) materials [36, 125, 126, 138]. Once the weak formulations are set, a change in the geometry, or a change in the boundary conditions can be performed in an easy and straight forward manner. Freely available mathematical libraries (finite element kernels) [139, 140, 141] make it easy to implement finite element methods with these formulations. These methods have greater compatibility with existing software based on the FEM. As the FEM method is capable of sharing the computational grid with the control-volume CFD grids [128, 129], this makes FEM suitable for the multi-physics applications of radiative heat-transfer.

1.5   Difficulties while solving the radiative transfer equation

The problems of interest in this thesis, involve solving the radiative transfer phenomenon described by the monochromatic steady-state radiative transfer equation in an absorbing, emitting, and scattering medium. For determining radiative intensity fields by solving the RTE in such cases may be difficult on accounts of the following complications:

- The presence of in-scattering term (integral term in equation (1.18)), means that the RTE remains in its integro-differential form. Such rare equations which have both an integral and a differential operator prevent explicit application of standard numerical methods. Moreover, constructing analytical solutions is not generally possible and is restricted to fairly simple cases.

- The RTE under consideration is a boundary value problem and in-scattering tightly couples the solution at different spatial locations and different directions together. As a consequence, solving a large and not so sparse linear system after discretization is inevitable, causing problems of computational resource management.

- The discretization size of the radiative transfer problems is enormous, while in other areas of numerical computation, 3 is considered higher dimensional, the steady-state monochromatic RTE leads to a 5 dimensional problem. Hence, formulation of a numerical scheme that suits the equation is just the fist step to get the solution. In order to compute the solution efficiently high performance computing, preconditioning, mesh adaption, etc., may be required for large geometries.

- Due to the huge size of matrices, it is rather standard practice to use iterative solution schemes like the Gauss–Seidel or the source iteration method to solve such systems. However, for highly scattering or highly reflecting or optically thick media, such methods converge slowly or may even fail to converge.

- The RTE being a boundary value problem, any inaccurate numerical formulation for the boundary may lead to destabilization in terms of spurious oscillations. It further demands higher order upwinding solution schemes. This comes from

the fact that the equation contains the first order transport operator for radiative intensities.

- Adequate numerical solution for solving the RTE with reflecting boundary conditions still remains challenging in complex domain scenarios. This is true in particular for the specular reflections.

- Lastly, for solving the RTE numerically, radiative properties like κ, σ_s, Φ, ε, etc., are required. For a particular medium these properties are a function of x, s, λ, T, t. Such radiative properties are mostly calculated using inverse methods applied to experimental data. Because of the complexities in performing precisely such experiments, data available in the literature is scarce. Many researches also use stochastic methods like the Monte–Carlo method for obtaining the pseudo-experimental data for a particular medium and then predict the radiative properties via an inverse method.

Considering all the challenges to be met while modeling the phenomena of radiation, in this thesis the SUPG-FEM coupled to the DOM will be used for solving the RTE. Resolving the second last difficulty which was enlisted above, a previous doctoral thesis by David Le Hardy [22] (also conducted in my host laboratory LTeN, CNRS, Nantes) developed some advance techniques to accurately model reflections [78] within the SUPG-FEM framework for the RTE discretization. This doctoral work by David Le Hardy became one of the building blocks of the current thesis. One of the main motives of the current thesis is to improve the spatio-angular discretization process of the SUPG-FEM coupled to the DOM that was used in [22] . This is done by introducing the concept of the vectorial finite elements, the primary novelty of this thesis. It will be shown how to facilitate techniques like parallelization and preconditioning with the vectorial finite element approach for solving the discrete ordinates RTE. Overall, it will be shown how the vectorial finite elements lead to a radiative transfer equation solver that is capable of handling radiative problems with billions of unknowns within complex geometries and heterogeneous media. Over the course of upcoming chapters, the vectorial finite element method will be explained and discussed in detail.

2

THE VECTORIAL FINITE ELEMENT METHOD

This chapter introduces the vectorial finite element approach for solving the discrete ordinates radiative transfer equation. Building block for the vectorial finite element method is the standard finite element method. Hence, in order to lay groundwork for detailing the vectorial finite element scheme, the standard finite element method for solving the discrete ordinates radiative transfer equation is described in the next section section.

2.1 Introduction to the standard finite element method

Presently, the finite element method (FEM) is considered among the most popular and versatile numerical methods for solving diverse scientific problems within solid mechanics, fluid mechanics, electromagnetics, heat transfer, etc. In the context of radiative transfer problems, the FEM has been used for the full RTE discretization, i.e., finite elements are used for both angular and spatial discretizations. For example, in a recent work from Castro et al. [85], the piece wise constant finite elements were used for discretizing the angular space, and the piece wise linear finite elements were used to discretize the spatial domain. Besides this full discretization approach for the RTE, the coupled FEM-DOM, where only the spatial discretization is performed using the FEM, is also gaining popularity, cf. [128, 35, 117, 135, 78]. A pioneering work from Fiveland et al. [75] in 1994, used the FEM-DOM for solving the multi-dimensional radiative problems in participating media. Ever since, the FEM for solving radiative

transfer problems has been advancing and became an important class of method among other available methods for numerical solution of the RTE.

It is well known that the standard Galerkin FEM, when applied for solving a convection-dominated equation, does not perform well: it either produces excessive numerical diffusion, or non-physical oscillations. This remains true for the RTE as well, the reason being that a first order differential operator appears for the radiative intensity within the RTE (1.18). In addition, the equation does not have any diffusion-like operator. As such, the RTE demands an upwinding schemes. Since the standard Galerkin FEM is not upwinding by nature, the Discontinuous Galerkin FEM (DG-FEM) [35], the Least Square FEM (LS-FEM) [137], and the Streamline Upwind Petrov–Galerkin FEM (SUPG-FEM) [135], are the three FEM variants used for spatial discretization of the RTE.

With the DG-FEM, the spatial domain is discretized into non-overlapping discontinuous elements, which is in contrast to the continuous elements used in the standard Galerkin FEM. Within these discontinuous elements, the complete solution is constructed by element-wise modeling of numerical radiative flux between the boundaries of adjacent elements. In fact, the DG-FEM combines salient features of both FVM and FEM. The SUPG-FEM and the LS-FEM, on the other hand, tend to provide stable solutions to the convection-dominated RTE by adding artificial diffusion.

The novel vectorial FEM that is introduced later in this chapter is simply an advancement of the SUPG-FEM being used for the spatial discretization for the discrete ordinates RTE. In the next few lines the superiority of the SUPG-FEM over the DG-FEM and the LS-FEM is highlighted. A research article by Le Hardy et al. [130] compares the SUPG-FEM and the DG-FEM. Considering factors like the convergence rate and the number of degrees of freedom, the authors proved the SUPG-FEM was more efficient than the DG-FEM. In radiative transfer problems involving specularly reflecting boundary conditions, the number of terms in the variational formulation can be high for the LS-FEM compared to the SUPG-FEM. In addition, the streamline parameter used in the SUPG-FEM can be finely tuned to reduce numerical errors (both artificial diffusion and spurious oscillations), making the SUPG-FEM slightly superior to the LS-FEM.

Figure 2.1 shows the standard Galerkin FEM in comparison to the SUPG-FEM applied to a radiative transfer problem with no scattering. In the considered test, the RTE is solved within a centimeteric square domain with a top-hat collimated

irradiation of unit intensity. The medium was assumed to be non scattering, non emitting, absorbing with $\kappa = 10 \text{ cm}^{-1}$, and enclosed within transparent cold walls. For this particular case, the exact solution is readily available cf. [20]. Clearly, it can be seen in the figure that the SUPG-FEM, indeed, is able to capture the physics without any spurious oscillations and the standard Galerkin FEM fails to do so. The RTE discretization with the discrete ordinates method coupled to the SUPG-finite element method will be discussed in detail in the upcoming sections.
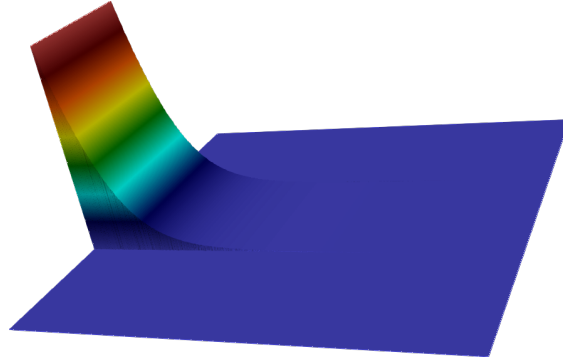
(a) Exact solution.
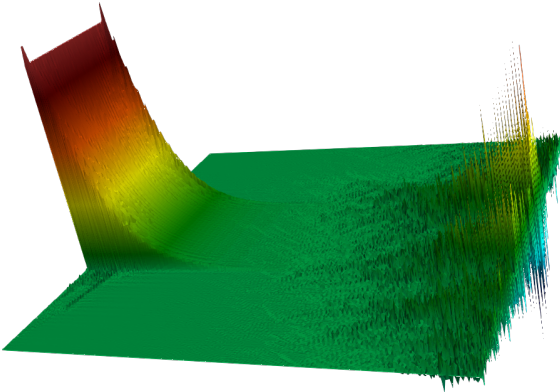
(b) Standard FEM solution.
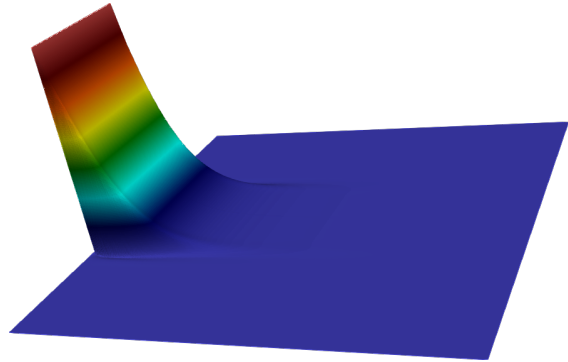
(c) SUPG-FEM solution.

Figure 2.1: Warped radiative intensity fields for a two-dimensional absorbing radiative transfer problem with a top-hat collimated irradiation impinging partly on its left wall.

2.1.1 Discretization of the RTE with the FEM-DOM

In this section, the focus is on the monochromatic steady-state radiative transfer equation, which can be rewritten from equation (1.18):

$$\mathcal{R}(I) = (\boldsymbol{s} \cdot \nabla + \beta) \, I(\boldsymbol{x}, \boldsymbol{s}) - \frac{\sigma_s}{4\pi} \oint_{\mathcal{S}} I(\boldsymbol{x}, \boldsymbol{s}') \Phi(\boldsymbol{s}, \boldsymbol{s}') \, \mathrm{d}\boldsymbol{s}' - \kappa I_b(\boldsymbol{x}) = 0 \qquad \forall \boldsymbol{x} \in \Omega, \forall \boldsymbol{s} \in \mathcal{S}. \tag{2.1}$$

In this equation, $I(\boldsymbol{x}, \boldsymbol{s})$ denotes the monochromatic steady-state radiative intensity for the spatial location $\boldsymbol{x} = (x, y, z)$, and along the direction vector $\boldsymbol{s} \in \mathcal{S}$. Further, if d is the dimension of the problem, $\Omega \subset \mathbb{R}^d$ denotes the spatial domain of interest.

Let us also define $\Gamma = \partial\Omega \times \mathcal{S}$ to be the boundary of the spatio-angular domain $\Omega \times \mathcal{S}$. Further, Γ can be divided into the inflow Γ^- and the outflow Γ^+ boundaries, defined as

$$\Gamma^- = \{(\boldsymbol{x}, \boldsymbol{s}) \mid \boldsymbol{x} \in \partial\Omega, \boldsymbol{s} \cdot \boldsymbol{n} < 0\}, \ \Gamma^+ = \{(\boldsymbol{x}, \boldsymbol{s}) \mid \boldsymbol{x} \in \partial\Omega, \boldsymbol{s} \cdot \boldsymbol{n} > 0\},$$

where $\boldsymbol{n}$ is the outward unit normal vector on the spatial boundary $\partial\Omega$ at $\boldsymbol{x}$.

To provide closure to the model, let us introduce the inflow boundary condition on Γ^-:

$$I = I_{\text{in}} \quad \forall (\boldsymbol{x}, \boldsymbol{s}) \in \Gamma^-. \tag{2.2}$$

Although other types of boundary conditions that include reflections can also be used (previously discussed in section 1.3), for the sake of simplicity we shall restrict the scope of this chapter to the mentioned inflow boundary condition. Given the boundary conditions (2.2), the monochromatic steady-state radiative transfer problem is a boundary value problem that can be formally written as

$$\text{find } I : \Omega \times \mathcal{S} \to \mathbb{R} \text{ such that}$$
$$\mathcal{R}(I) = 0. \tag{2.3}$$

To compute the numerical solution of problem (2.3) with the FEM-DOM, two steps discretization process is followed:

1. First, the continuous angular space ($\mathcal{S}$) is discretized with the DOM. This converts the continuous (in space and angles) RTE into a set of coupled partial differential equations (PDE), where each PDE is continuous in space. By negating the angular dependence from the RTE, the five-dimensional RTE containing $I = I(x, y, z, \theta, \phi)$ transforms into a coupled set of three-dimensional PDE's containing $I = I(x, y, z)$.

2. Next, the spatial discretization (Ω) using the SUPG-FEM is carried out for each PDE obtained from step 1. This leads to a system of equations known as the weak form equations. These weak form equations then lead to a linear system of equations which is then solved for obtaining the radiative intensities.

2.1.1.1 Step 1: angular discretization using the DOM

The DOM consists in replacing the continuous angular space $\mathcal{S}$ by a set of N_d discrete directions $(s_1, s_2, \ldots, s_{N_d}) \in \mathcal{S}^{N_d}$. Here, $\mathcal{S}$ represents the continuous unit sphere, while $\mathcal{S}^{N_d}$ is the discretized unit sphere. The RTE is then solved for these finite representative directions. For discretizing the unit sphere we follow the quasi-uniform angular discretization procedure. The discrete directions s_m are obtained by a successive division of an icosahedron, or an octahedron, also used by [34, 4, 142].

Figure 2.2 presents the quasi-uniform angular discretizations of the unit sphere by using the octahedral and the icosahedral refinements. To brief these angular discretizations procedure, each triangle within the principal octahedron (figure 2.2a) or within the principal icosahedron (figure 2.2b), is subdivided into four equally sized smaller triangles. From the principal octahedron with $N_d = 8$ each refinement leads to $N_d = 4^r \times 8$, where r is the refinement number. Similarly, from the principal icosahedron with $N_d = 20$, each refinement leads to $N_d = 4^r \times 20$. Next, the triangles and their corresponding barycenters are then projected onto the surface of the unit sphere. The location of these projected barycenters form the direction vector s_m, while the area of spherical triangles correspond to the weights w_m. The calculation of w_m is based on Huilier's theorem which is detailed in [78]. Using these quasi-uniform angular discretizations, it is guaranteed that, all the weights are positive and are approximately equal in value, $w_m \approx 4\pi/N_d$. Note, for two-dimensional problems, by exploiting the symmetry of the mentioned angular discretizations, only half the number of discrete directions are considered with double weights [20].

The followed quasi-uniform angular discretizations guarantee almost uniform quadratures. In comparison to other numerical quadrature methods, additional symmetry conditions are redundant and discretization artifacts at the poles are avoided [34]. The octahedral refinement scheme can be seen as a subset of the Thurgood quadrature (T_N), [83], i.e, the principal octahedron (figure 2.2a) is indeed T_1, its first refinement (figure 2.2c) is T_2, the second refinement (figure 2.2d) is T_4, and so on. Although, in the current thesis all developments and discussions are based on the quasi-linear angular discretization approach, one could easily extend these to other kinds of angular discretization, for example, the S_N quadrature.
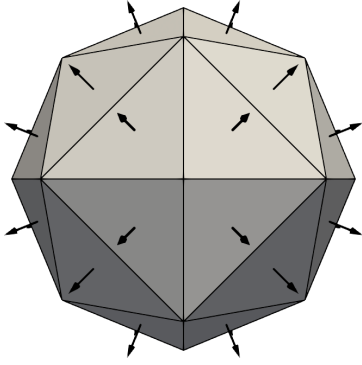
After obtaining the discretized directions $\{s_m\}_{m=1}^{N_d}$ and their corresponding weights $\{\omega_m\}_{m=1}^{N_d}$, the integral over the angular space that appears in the RTE (2.1)
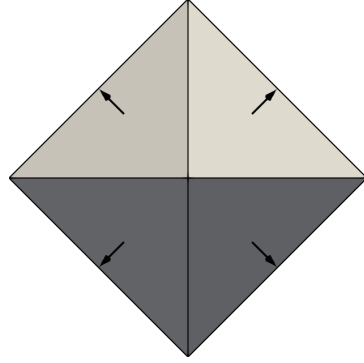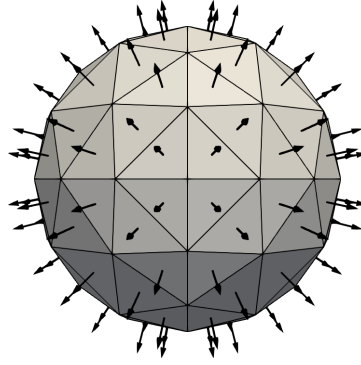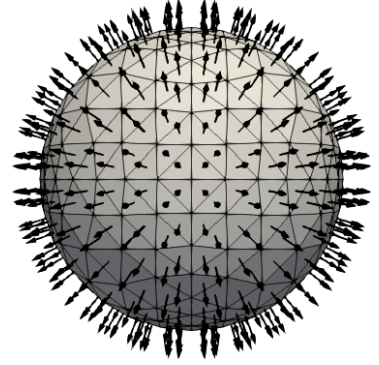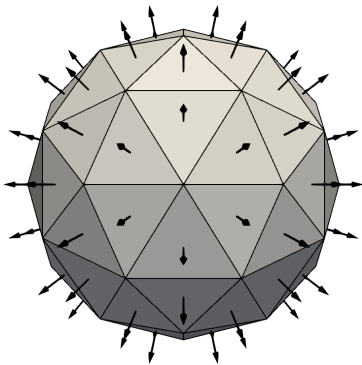
(a) Octahedron $N_d = 8$.
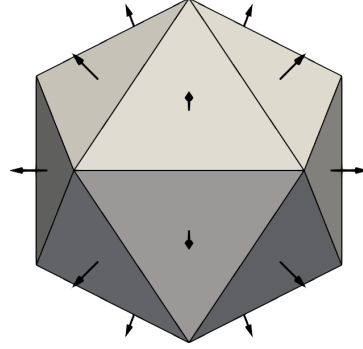
(b) Icosahedron $N_d = 20$.
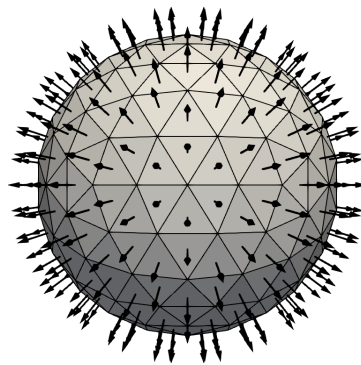
(c) First octahedral refinement $N_d = 32$.
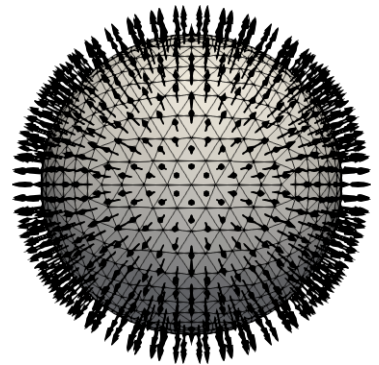
(d) Second octahedral refinement $N_d = 128$.

(e) Third octahedral refinement $N_d = 512$.

(f) First icosahedral refinement $N_d = 80$.

(g) Second icosahedral refinement $N_d = 320$.

(h) Third icosahedral refinement $N_d = 1280$.

Figure 2.2: Angular discretization meshes for the DOM using the octahedral and the icosahedral refinements of the unit sphere.

can now be replaced by a weighted summation:

$$\int_{s=4\pi} I(\boldsymbol{x}, \boldsymbol{s}) \, \mathrm{d}\boldsymbol{s} = \sum_{m=1}^{N_d} I_m(\boldsymbol{x}) w_m, \tag{2.4}$$

where $I_m(\boldsymbol{x}) = I(\boldsymbol{x}, \boldsymbol{s}_m)$ is the space-dependent radiative intensity associated to the discrete direction $\boldsymbol{s}_m$. Physically, the equation (2.4) is used to approximate the in-scattering process. Naturally, higher number of N_d would result in higher accuracy solutions to the RTE as the number of terms for the summation operation increases.

Now, using equation (2.4), the RTE (2.1) is replaced by a discrete set of N_d coupled partial differential equations that describes the radiation intensity fields along the N_d directions. The mth equation in the set of N_d equations reads

$$\mathcal{R}_m\left(\{I_n\}_{n=1}^{N_d}\right) = (\boldsymbol{s}_m \cdot \nabla + \beta) \, I_m(\boldsymbol{x}) - \sigma_s \sum_{n=1}^{N_d} \omega_n I_n(\boldsymbol{x}) \Phi_{m,n} - \kappa I_b(\boldsymbol{x}) = 0. \tag{2.5}$$

Similarly, the continuous boundary condition (2.2) is to be rewritten for all discrete directions, the inflow and outflow boundaries being redefined as

$$\partial\Omega_m^\pm = \{\boldsymbol{x} \in \partial\Omega \,|\, \boldsymbol{s}_m \cdot \boldsymbol{n} \gtrless 0\}.$$

In cases considered in this chapter, a collimated beam of intensity I_{in} may impinge parts of the boundary only along the specific entrant direction $\boldsymbol{s}_{\text{in}}$. For such a case, the discrete boundary condition then reads

$$I_m = \begin{cases} I_{\text{in}} & \forall \boldsymbol{x} \in \partial\Omega_m^- & \text{if } \boldsymbol{s}_m = \boldsymbol{s}_{\text{in}}, \\ 0 & \forall \boldsymbol{x} \in \partial\Omega_m^- & \text{if } \boldsymbol{s}_m \neq \boldsymbol{s}_{\text{in}}. \end{cases} \tag{2.6}$$

These discretized conditions are to be taken into account to form the set of N_d discrete boundary value problems, which reads

$$\begin{aligned} &\text{find } \{I_m : \Omega \to \mathbb{R}\}_{m=1}^{N_d} \text{ such that} \\ &\mathcal{R}_m\left(\{I_n\}_{n=1}^{N_d}\right) = 0. \end{aligned} \tag{2.7}$$

2.1.1.2 Step 2: spatial discretization using the SUPG-FEM

In this subsection, step 2 of the two steps discretization process for the RTE is discussed, i.e., the spatial discretization process. As discussed earlier in section 2.1, the standard Galerkin FEM lacks stability while solving the RTE, see figure 2.1. Hence, the SUPG-FEM is chosen to carry out the task of spatial discretization for solving the equation

set (2.7). The SUPG-FEM was developed for convection dominated equations by Huges et al. [143] in 1989. The SUPG-FEM stabilizes the streamline derivative by adding a controlled artificial diffusion term. The RTE in its discrete form, equation set (2.7), is convection dominant and by adding the artificial diffusion from the SUPG-FEM, the convection dominance can be negated.

The finite element method set out from variational formulations of a PDE, these are also referred as weak formulations. In order to derive this variational formulation, we multiply the PDE with a suitable test function and integrate the product over the computation domain. To do so, one considers the spatial domain Ω as N_e disjoint tetrahedra ($\Omega \subset \mathbb{R}^3$) or triangles ($\Omega \subset \mathbb{R}^2$) given by $\{\mathcal{C}_i\}_{i=1}^{N_e}$:

$$\Omega \simeq \Omega^h = \bigcup_{i=1}^{N_e} \mathcal{C}_i,$$

where the local element size for each $\mathcal{C}_i$ is defined by its diameter h_i. The process of splitting (approximating) the domain Ω by Ω^h, if often termed as meshing in numerical science terminology. Further, each spatial mesh Ω^h is usually labeled by its mesh size $h = \max(h_i)$.

For defining the variational formulation of the problem (2.7), the following Sobolev functional space is introduced:

$$\mathcal{V}_m^h = \{v \in L^2(\Omega^h) \text{ and } \boldsymbol{s}_m \cdot \nabla v \in L^2(\Omega^h)\}.$$

In a given $\boldsymbol{s}_m$, this functional space $\mathcal{V}_m^h$ is used to define the test function $w^h \in \mathcal{V}_m^h$ and the trial function $I_m^h \in \mathcal{V}_m^h$. In order to write the SUPG finite-dimensional variational form for the coupled system (2.7), each $\mathcal{R}_m(\{I_n\}_{n=1}^{N_d})$ is multiplied by the SUPG test function $w^h + \gamma \boldsymbol{s}_m \cdot \nabla w^h$, and then integrated over the whole computational domain Ω^h. The difference between the RTE variational formulations derived from the standard Galerkin FEM and the SUPG-FEM can be realized by the following equation:

$$\forall m = 1, 2, \ldots, N_d :$$
$$\begin{cases} \int_{\Omega^h} \mathcal{R}_m(\{I_n\}_{n=1}^{N_d}) \times (w^h) \, \mathrm{d}\boldsymbol{x} = 0 & \text{if Galerkin FEM} \\ \int_{\Omega^h} \mathcal{R}_m(\{I_n\}_{n=1}^{N_d}) \times (w^h + \gamma \boldsymbol{s}_m \cdot \nabla w^h) \, \mathrm{d}\boldsymbol{x} = 0 & \text{if SUPG-FEM.} \end{cases} \tag{2.8}$$

Note, the SUPG test function contains an additional term $\gamma \boldsymbol{s}_m \cdot \nabla w^h$, which is indeed the added artificial diffusion. The artificial diffusion is controlled using the stabilizing

coefficient $\gamma(\boldsymbol{x}) : \Omega^h \to \mathbb{R}^+$. Following the recommendations in [135], $\gamma(\boldsymbol{x})$ can be expressed as:

$$\gamma = \left(\frac{c_1^2}{h_x^2} + \beta^2 + 2\frac{c_1\sigma_s}{N_d h_x} \right)^{-\frac{1}{2}}, \tag{2.9}$$

where c_1 is an algorithmic constant. From experience and as per suggestion made in [135], the constant is chosen as $c_1 = 2$. Further, γ is a function of h_i, N_d, κ, and σ_s, hence it will adapt automatically for different media, spatial meshes sizes, and the number of DOM directions. Apart from this, [21] recommended choosing $\gamma = 0.3h_i$ if $\beta < 1$ and $\gamma = 0$ if $\beta \gg 1$. The former choice of γ given by the equation (2.9) will be default throughout this thesis.

The mathematical tools for writing the SUPG variational formulation are now settled. We can now define the SUPG finite-dimensional variational form as

$\forall m = 1, 2, \ldots, N_d :$

$$\int_{\Omega^h} [\boldsymbol{s} \cdot \nabla I_m + \beta I_m] \left(w^h + \gamma \boldsymbol{s}_m \cdot \nabla w^h \right) \mathrm{d}\boldsymbol{x} - \int_{\Omega^h} \sum_{n=1}^{N_d} \left[\omega_n \Phi_{m,n} \sigma_s I_n^h \right] \left(w^h + \gamma \boldsymbol{s}_m \cdot \nabla w^h \right) \mathrm{d}\boldsymbol{x}$$

$$- \int_{\Omega^h} [\kappa I_b] \left(w^h + \gamma \boldsymbol{s}_m \cdot \nabla w^h \right) \mathrm{d}\boldsymbol{x} = 0 \qquad \forall w^h \in \mathcal{V}_m^h. \tag{2.10}$$

The first term of the equation is now expanded, the equation then reads,

$\forall m = 1, 2, \ldots, N_d :$

$$\int_{\Omega^h} [\boldsymbol{s} \cdot \nabla I_m] \left(w^h \right) \mathrm{d}\boldsymbol{x} + \int_{\Omega^h} [\boldsymbol{s} \cdot \nabla I_m] \left(\gamma \boldsymbol{s}_m \cdot \nabla w^h \right) \mathrm{d}\boldsymbol{x} + \int_{\Omega^h} \left[\beta I_m^h \right] \left(w^h + \gamma \boldsymbol{s}_m \cdot \nabla w^h \right) \mathrm{d}\boldsymbol{x}$$

$$- \int_{\Omega^h} \sum_{n=1}^{N_d} \left[\omega_n \Phi_{m,n} \sigma_s I_n^h \right] \left(w^h + \gamma \boldsymbol{s}_m \cdot \nabla w^h \right) \mathrm{d}\boldsymbol{x}$$

$$- \int_{\Omega^h} [\kappa I_b] \left(w^h + \gamma \boldsymbol{s}_m \cdot \nabla w^h \right) \mathrm{d}\boldsymbol{x} = 0 \qquad \forall w^h \in \mathcal{V}_m^h. \tag{2.11}$$

Further, to introduce the boundary conditions, an integration by parts is performed on the main advection term, i.e., on the first term of the equation (2.11).

The equation then reads

$$
\begin{aligned}
\forall m = 1, 2, \ldots, N_d : & \\
- \int_{\Omega^h} s_m \cdot \nabla w^h I_m^h \, \mathrm{d}x \quad & + \quad \int_{\partial\Omega_m^-} s_m \cdot n \, w^h I_{\mathrm{in}} \, \mathrm{d}x \quad + \quad \int_{\partial\Omega_m^+} s_m \cdot n \, w^h I_m^h \, \mathrm{d}x \\
+ \int_{\Omega^h} \gamma s_m \cdot \nabla I_m^h \, s_m \cdot \nabla w^h \, \mathrm{d}x \quad & + \quad \int_{\Omega^h} \beta I_m^h (w^h + \gamma s_m \cdot \nabla w^h) \, \mathrm{d}x \\
- \int_{\Omega^h} \sum_{n=1}^{N_d} \omega_n \Phi_{m,n} \sigma_s I_n^h (w^h + \gamma s_m \cdot \nabla w^h) \, \mathrm{d}x & \\
- \int_{\Omega^h} \kappa I_b (w^h + \gamma s_m \cdot \nabla w^h) \, \mathrm{d}x = 0 & \qquad \forall w^h \in \mathcal{V}_m^h.
\end{aligned}
\tag{2.12}
$$

Equation (2.12) is the general SUPG-FEM variational form for solving the monochromatic steady-state RTE. It can be written in the following canonical form

$$
\begin{aligned}
& \forall m = 1, 2, \ldots, N_d : \\
& \text{find } I_m^h \in \mathcal{V}_m^h \text{ such that} \\
& a_{m,m}(I_m^h, w^h) \quad + \quad \sum_{\substack{n=1 \\ n \neq m}}^{N_d} a_{m,n}(I_n^h, w^h) = l_m(w^h) \qquad \forall w^h \in \mathcal{V}_n^h.
\end{aligned}
\tag{2.13}
$$

Here $a_{m,n} : \mathcal{V}_m^h \times \mathcal{V}_n^h \to \mathbb{R}$ and $l_m : \mathcal{V}_m^h \to \mathbb{R}$ are the bilinear and linear functionals:

$$
\begin{aligned}
a_{m,m}(I_m^h, w^h) = & -\int_{\Omega^h} s_m \cdot \nabla w^h (I_m^h - \gamma s_m \cdot \nabla I_m^h) \, \mathrm{d}x + \int_{\partial\Omega_m^+} s_m \cdot n \, w^h I_m^h \, \mathrm{d}x \\
& + \int_{\Omega^h} (\beta I_m^h - \omega_m \Phi_{m,m} \sigma_s I_m^h)(w^h + \gamma s_m \cdot \nabla w^h) \, \mathrm{d}x,
\end{aligned}
\tag{2.14}
$$

$$
a_{m,n \neq m}(I_n^h, w^h) = -\int_{\Omega^h} \omega_n \Phi_{m,n} \sigma_s I_n^h (w^h + \gamma s_m \cdot \nabla w^h) \, \mathrm{d}x,
\tag{2.15}
$$

$$
l_m(w^h) = -\int_{\partial\Omega_m^-} s_m \cdot n \, w^h I_{\mathrm{in}} \, \mathrm{d}x + \int_{\Omega^h} \kappa I_b (w^h + \gamma s_m \cdot \nabla w^h) \, \mathrm{d}x.
\tag{2.16}
$$

In order to assemble the matrix system from the variational formulation (2.13), one considers an approximation of the finite element functional space by a kth order polynomial space $\mathbb{P}_k(\mathcal{C}_i)$, for all $\mathcal{C}_i \in \Omega^h$. This leads to a family of polynomial basis functions $\{\varphi_i \in \mathcal{V}_m^h\}_{i=1}^{N_v}$ which in-turn formulates the solution $I_m^h(x) = \sum_{i=1}^{N_v} I_m^h(x_i) \varphi_i(x)$. In a similar fashion $w^h(x) = \sum_{j=1}^{N_v} w^h(x_j) \varphi_j(x)$. N_v is the number of degrees of freedom associated to the spatial mesh Ω^h. Such a discretization now yields

---

Algorithm 1: building the global FEM matrix A and vector b

---

    input N_d, κ, σ_s, and β
    load the spatial mesh Ω^h and the angular mesh $\{s_m\}_{m=1}^{N_d}$
    define functional spaces $\mathcal{V}_m^h$ and polynomial order k
    while $m < N_d$ **do**
        while $n < N_d$ **do**
            if $m = n$ **then**
                assemble $A_{m,n}$ by discretizing $a_{m,m}$ using equation (2.14)
            else
                assemble $A_{m,n}$ by discretizing $a_{m,n}$ using equation (2.15)
            end
        end
        assemble b_m by discretizing l_m using equation (2.16)
    end
    build matrix A by blocking all $\{A_{m,n}\}_{(m,n)\in[\![1;N_d]\!]^2}$
    build vector b by assembling all $\{b_m\}_{m\in[\![1;N_d]\!]}$

---

a linear system $AI = b$ that may be written using blocks of matrices or vectors as

$$
\begin{pmatrix}
A_{1,1} & A_{1,2} & \cdots & A_{1,N_d} \\
A_{2,1} & A_{2,2} & \cdots & A_{2,N_d} \\
\vdots & \vdots & \ddots & \vdots \\
A_{N_d,1} & A_{N_d,2} & \cdots & A_{N_d,N_d}
\end{pmatrix}
\begin{pmatrix}
I_1 \\ I_2 \\ \vdots \\ I_{N_d}
\end{pmatrix}
=
\begin{pmatrix}
b_1 \\ b_2 \\ \vdots \\ b_{N_d}
\end{pmatrix}.
$$

The diagonal terms $A_{m,m}$ and the off-diagonal terms $A_{m,n\neq m}$ of the block matrix A are themselves sparse matrices. These are built using the bilinear forms $a_{m,m}$ and $a_{m,n\neq m}$, given by equations (2.14) and (2.15), respectively. The right-hand side vector b is the row-wise concatenation of the b_m vectors built using the linear forms l_m, equation (2.16). Note that, in this chapter, the finite element functional spaces are approximated using the first order Lagrange polynomial space $\mathbb{P}_1(\mathcal{C}_i)$. Hence, the matrix A has $(N_v \times N_d)$ rows and columns, and both b and I are vectors of size $(N_v \times N_d)$.

In this standard SUPG-FEM strategy, only a single block $A_{m,n}$ or a single vector b_m can be constructed at a given time. In order to completely build the linear system, an iterative procedure for assembling the matrix A block by block needs to be adapted. Such a strategy is commonly being used for the linear system assembly process with the SUPG-FEM approach for the RTE, see [35, 130]. The vector b has to be
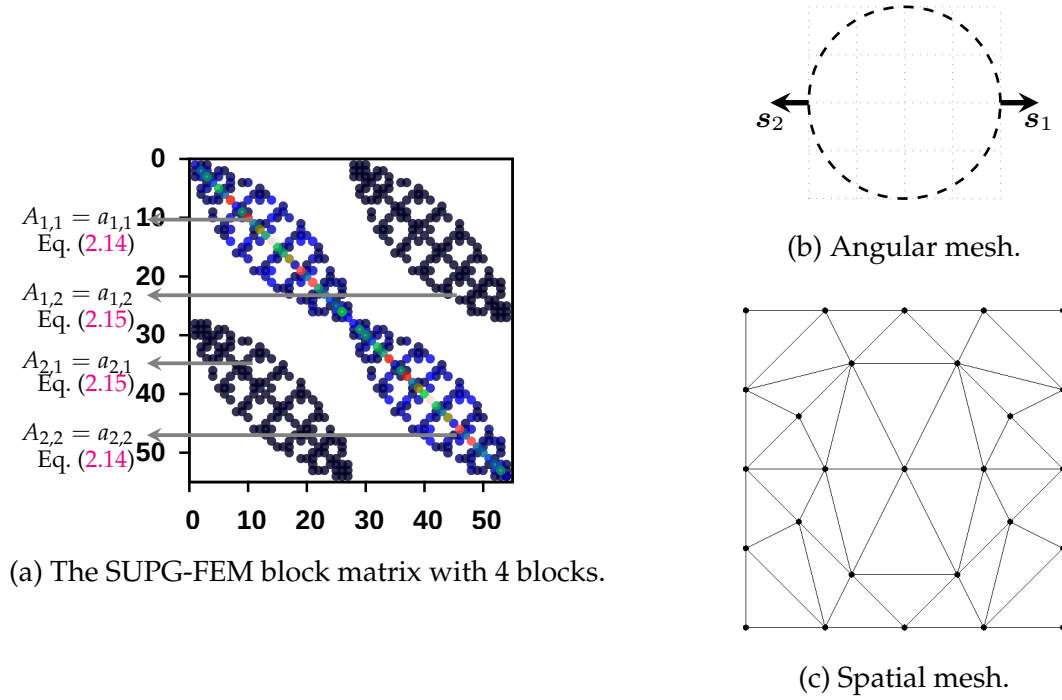
(a) The SUPG-FEM block matrix with 4 blocks.

(b) Angular mesh.

(c) Spatial mesh.

Figure 2.3: Assembly process for the SUPG-FEM matrix. Left: the assembled matrix, and right: the angular and the spatial meshes used ($N_d = 2$ and $N_v = 27$).

assembled in a similar fashion. Hence, the matrix assembly routine of the used finite element kernel needs to be called N_d^2 times, and the vector assembly routine is called N_d times. Such a process of matrix and vector assembly is presented in algorithm 1, and schematically shown in figure 2.3. A coarse spatial mesh with $N_v = 27$ vertices (figure 2.3c), and a coarse angular discretization with $N_d = 2$ directions (figure 2.3b), were used to construct A. Notice that in the figure 2.3a, $N_d^2 = 4$ sparse blocks exist within A and its global order is $N_d \times N_v = 54$.

2.1.2 Solving the discretized standard FEM-DOM system

As a consequence of the FEM-DOM discretization, a linear system of the form $AI = b$ has to be solved. The assembled matrix A, is large, sparse, and non-symmetric. Traditionally, iterative solution approaches (transport sweeps algorithm) like the source iteration method, the Gauss–Seidel method, and the successive over relaxation method, are used for solving the FEM-DOM linear systems. These three methods have been compared in [130]. In such methods, a sequence of transport sweeps (direction by direction) are performed and repeated until convergence. During each transport sweep, block matrices $A_{i,j}$ from A are constructed and erased to save memory. If it takes k

iterations for the solver to converge, each $A_{i,j}$ has to be constructed and then destroyed k times. Naturally, poor convergence will result in extremely long solving times. For more details, please refer [144].

These methods are popular due to their straightforward implementation and high memory efficiency. However, as reported in [91], the transport sweeps algorithms become inefficient (due to slow or unreached convergences) for high scattering media. The same is true for highly reflecting media. Within a highly scattering or reflecting media, the DOM directions are tightly coupled to one another, under such scenarios it is natural for any transport sweeps algorithm to become inefficient. Alternatively, the Krylov subspace methods like the generalized minimum residual method (GM-RES) [145] and the biconjugate gradient stabilized method (BiCGSTAB) [146], are known to overcome the shortcomings of the transport sweep algorithms. Many arguments supporting the superiority of the Krylov subspace methods over the traditional solving methods can be found in [77]. Though, it should be noted that contrary to the sweep algorithms, such methods require complete assembly of the linear system A, hence requiring much more memory. For such cases, parallelization comes in handy, in [34, 4, 147], a parallelized GMRES method has been used for solving the FEM-DOM linear systems.

2.2 Introduction to the vectorial finite element method

The previous section presented the spatio-angular discretization process for RTE by using the standard SUPG-FEM coupled to the DOM. In the current section, to improve such spatio-angular discretization, the RTE is reformulated using vectorial finite elements. This is one of the major novelties introduced via this thesis. It will be shown later in this section that reformulating the RTE using vectorial finite elements yields better timings when it comes to linear system assembly and solving.

Currently, with finite element methods, coupled problems can be solved by using two different approaches. The first involves a primal, 1-field formulation, i.e., finite elements are used iteratively to solve the coupled systems. This was the case in the preceding section where the FEM was used iteratively for building and solving the coupled discrete ordinates equations. Another finite element strategy to solve the coupled problems involves a vectorial (mixed) m-field formulation in which m number of fields are solved simultaneously. Such finite element strategy is dubbed as the vectorial FEM.

The vectorial FEM is more commonly known as the mixed FEM. However, in the context of solving RTE, the name vectorial FEM seems more appropriate than mixed FEM, the reason for which will be given in section 2.2.1. Introduced as a variational theorem for solving structural mechanics problems, the concept of the vectorial FEM was first proposed by Herrmann [148] in 1967: both displacement and stress fields were solved simultaneously for the system of incompressible and nearly incompressible elasticity. In fact, it was established that the vectorial FEM was the first effective FEM for such cases. Prior to this development many other 1-field FEM formulations were applied to this two-field problem of elasticity, and each resounded in failure. The vectorial FEM methods have subsequently been applied to many coupled problems in engineering and have been especially successful in constrained problems, e.g., in porous media physics [149], the Navier–Stokes equations [150], electromagnetism [151], multiphase flows [152], flows with heat transfer [153], to cite but a few. For further details about this method, a monograph written by Boffi et al. [154] may be referred. We propose in this section to take advantage of the vectorial FEM for the solution of the radiative transfer equation. While in preceding cited applications the number of equations is limited to only a few, the RTE demands hundreds of coupled equations to be solved simultaneously. Application of the vectorial FEM for solving the discrete ordinates RTE pushes the limits of the vectorial FEM.

The vectorial FEM is only applicable to physics which demands solving multiple coupled fields, or simply coupled problems. Indeed the method is applicable for the RTE in its discrete ordinates form, which presents a challenging case of N_d coupled equations. One of the advantages of using vectorial finite elements is that multiple unknown fields may be considered in the same discrete space, so that it is easier to couple them in the variational formulations. Being in the same discrete space, all m unknowns are solved simultaneously to the same level of accuracy. This may not be the case when employing the standard finite elements. Within the standard FEM (1-field formulations), as multiple fields are being solved iteratively, different fields can be of different level of accuracy, which may affect the overall solution process. Another advantage of the vectorial finite elements over the standard ones is that the former leads to faster matrix building process. However, there are at least two disadvantages while using the vectorial finite elements. First, the auxiliary field of the vectorial method engenders additional computational expense, and, second, the generalization to nonlinear problems is not always apparent [155].

2.2.1 Discretization of the RTE with the vectorial FEM

When setting up the RTE with the vectorial FEM[1], the first discretization step, i.e, the angular discretization remains the same, as was the case for the standard FEM-DOM, section 2.1.1.1. We rewrite the N_d coupled PDEs obtained from the DOM:

$$\forall m = 1, 2, \ldots, N_d :$$

$$\mathcal{R}_m \left(\{I_n\}_{n=1}^{N_d} \right) = (s_m \cdot \nabla + \beta) I_m(x) - \sigma_s \sum_{n=1}^{N_d} \omega_n I_n(x) \Phi_{m,n} - \kappa I_b(x) = 0. \tag{2.17}$$

The standard finite element method from section 2.1.1.2 dealt with this coupled problem of searching a set of N_d discrete radiative intensities I_m, by utilizing the N_d variational formulations (2.13). The vectorial finite element method looks at the problem in a different perspective. It defines the coupled set of equations (2.17) with a single equation. This problem consists in searching a vector of radiative intensities $\mathbb{I}^h$ (vectorial trial function) using a vectorial test function $\mathbb{W}^h$ which lies in the corresponding vectorial functional space $\mathbf{V}^h$:

$$\mathbf{V}^h = \prod_{i=1}^{N_d} \mathcal{V}_i^h.$$

In order to derive the vectorial FEM variational formulations for equation (2.17), the first step is to convert coupled set of equations (2.17) into its equivalent vectorial form. To do that, let us first define the radiative intensities vector $\mathbb{I}$, the collective direction vector $\mathbb{S}$ collecting all individual directions vectors s_m, and a matrix Θ of size $N_d \times N_d$ that combines scattering coefficient σ_s, weights ω_m, and scattering phase function $\Phi_{m,n}$. These quantities are expressed as,

$$\mathbb{I} = \begin{pmatrix} I_1 \\ I_2 \\ \vdots \\ I_{N_d} \end{pmatrix}, \quad \mathbb{S} = \begin{pmatrix} s_1 \\ s_2 \\ \vdots \\ s_{N_d} \end{pmatrix}, \quad \Theta = \begin{pmatrix} \sigma_s \omega_1 \phi_{1,1} & \sigma_s \omega_2 \phi_{1,2} & \cdots & \sigma_s \omega_{N_d} \phi_{1,N_d} \\ \sigma_s \omega_1 \phi_{2,1} & \sigma_s \omega_2 \phi_{2,2} & \cdots & \sigma_s \omega_{N_d} \phi_{2,N_d} \\ \vdots & \vdots & \ddots & \vdots \\ \sigma_s \omega_1 \phi_{N_d,1} & \sigma_s \omega_2 \phi_{N_d,2} & \cdots & \sigma_s \omega_{N_d} \phi_{N_d,N_d} \end{pmatrix}. \tag{2.18}$$

Using these notations, the coupled equations for the monochromatic steady-state RTE in its discrete ordinates form, equation (2.17) can now be reformulated in its equivalent vectorial form. The vectorial equation reads,

$$\mathbb{S} \cdot \nabla \mathbb{I} + \beta(x)\mathbb{I} - \Theta\mathbb{I} = \kappa(x)I_b\mathbb{1}, \tag{2.19}$$

---

[1]Note that, from here onwards, for the sake of conciseness, we shall call the vectorial SUPG-FEM DOM approach simply as the vectorial FEM. Further, the SUPG-FEM DOM will be simply called as the standard FEM or the FEM.

with $\mathbb{1}$ being the identity vector of same order as $\mathbb{I}$. Here, $\mathbb{S} \cdot \nabla \mathbb{I}$ would give a vector, the ith component of which will be given by $(\mathbb{S} \cdot \nabla \mathbb{I})_i = \boldsymbol{s}_i \cdot \nabla I_i$. Let us also introduce the following notations: $\mathbb{A}^\top \mathbb{B} = \sum_i \mathbb{A}_i \mathbb{B}_i$ and $(\mathbb{A} : \mathbb{B})_i = \mathbb{A}_i \mathbb{B}_i$, for the sake of conciseness.

We further define the vectorial trial and test functions $\mathbb{I}^h$ and $\mathbb{W}^h$ as,

$$\mathbb{I}^h = \begin{pmatrix} I_1^h \\ I_2^h \\ \vdots \\ I_{N_d}^h \end{pmatrix} \quad \text{and} \quad \mathbb{W}^h = \begin{pmatrix} w_1^h \\ w_2^h \\ \vdots \\ w_{N_d}^h \end{pmatrix} \in \mathbf{V}^h = \mathcal{V}_1^h \times \mathcal{V}_2^h \times \cdots \times \mathcal{V}_{N_d}^h. \tag{2.20}$$

Each component functional space $\mathcal{V}_m^h$ can be built using a polynomial basis $\mathbb{P}_k(\mathcal{C})$ with different orders k. All these spaces are crossed in order to define the space $\mathbf{V}^h$, hence the name mixed FEM. However, in the context of solving the RTE, all the component functional spaces $\mathcal{V}_m^h$ are built using the same polynomial basis. For example $\mathbb{P}_1(\mathcal{C})$ spaces have been used for most of the test cases that will appear in this thesis. Thereby, it seems more appropriate to call this method the vectorial FEM rather than the mixed FEM.

With all the test and trial functions available at a given time the vectorial FEM weak formulation can now be built by multiplying the vectorial equation (2.19) with the SUPG vectorial test function $\mathbb{W}^h + \gamma \mathbb{S} \cdot \nabla \mathbb{W}^h$, then integrating over the domain of interest Ω^h. Based on that, the problem now reads:

search $\mathbb{I}^h \in \mathbf{V}^h$ that satisfies:

$$\int_{\Omega^h} (\mathbb{S} \cdot \nabla \mathbb{I}^h + \beta \mathbb{I}^h)^\top (\mathbb{W}^h + \gamma \mathbb{S} \cdot \nabla \mathbb{W}^h) \, \mathrm{d}\boldsymbol{x} - \int_{\Omega^h} (\Theta \mathbb{I}^h)^\top (\mathbb{W}^h + \gamma \mathbb{S} \cdot \nabla \mathbb{W}^h) \, \mathrm{d}\boldsymbol{x}$$
$$= \int_{\Omega^h} (\kappa I_b \mathbb{1})^\top (\mathbb{W}^h + \gamma \mathbb{S} \cdot \nabla \mathbb{W}^h) \, \mathrm{d}\boldsymbol{x} \qquad \forall \mathbb{W} \in \mathbf{V}^h. \tag{2.21}$$

The Greens theorem is then applied for introducing the inflow boundary conditions, so that the problem becomes:

search $\mathbb{I}^h \in \mathbf{V}^h$ that satisfies:

$$-\int_{\Omega^h} (\mathbb{S} \cdot \nabla \mathbb{W}^h)^\top \mathbb{I}^h \, \mathrm{d}\boldsymbol{x} + \int_{\partial\Omega^h} (\mathbb{S} \cdot \boldsymbol{n} : \mathbb{H}_{[\mathbb{S} \cdot \boldsymbol{n} > 0]} : \mathbb{I}^h)^\top \mathbb{W}^h \, \mathrm{d}\boldsymbol{x}$$
$$+\int_{\partial\Omega^h} (\mathbb{S} \cdot \boldsymbol{n} : \mathbb{H}_{[\mathbb{S} \cdot \boldsymbol{n} < 0]} : \mathbb{I}_{\mathrm{in}}^h)^\top \mathbb{W}^h \, \mathrm{d}\boldsymbol{x} + \int_{\Omega^h} (\mathbb{S} \cdot \nabla \mathbb{I}^h)^\top (\gamma \mathbb{S} \cdot \nabla \mathbb{W}^h) \, \mathrm{d}\boldsymbol{x} \tag{2.22}$$
$$+\int_{\Omega^h} (\beta \mathbb{I}^h)^\top (\mathbb{W}^h + \gamma \mathbb{S} \cdot \nabla \mathbb{W}^h) \, \mathrm{d}\boldsymbol{x} - \int_{\Omega^h} (\Theta \mathbb{I}^h)^\top (\mathbb{W}^h + \gamma \mathbb{S} \cdot \nabla \mathbb{W}^h) \, \mathrm{d}\boldsymbol{x}$$
$$= \int_{\Omega^h} (\kappa I_b \mathbb{1})^\top (\mathbb{W}^h + \gamma \mathbb{S} \cdot \nabla \mathbb{W}^h) \, \mathrm{d}\boldsymbol{x} \qquad \forall \mathbb{W}^h \in \mathbf{V}^h.$$

Note that the vectorial indicator (Heaviside) function $\mathbb{H}_{[\mathbb{S}\cdot\boldsymbol{n}>0]}$ has been introduced. This function results in zeros and ones depending on Boolean operations, e.g., $\left(\mathbb{H}_{[\mathbb{S}\cdot\boldsymbol{n}>0]}\right)_i$ equals one if and only if $\boldsymbol{s}_i \cdot \boldsymbol{n} > 0$, and zero elsewhere.

Equation (2.22) is indeed the vectorial FEM variational form for solving the monochromatic steady-state RTE with prescribed boundary condition I_{in}. This vectorial FEM variational formulation can be written in the following canonical form:

$$
\begin{aligned}
&\text{find } \mathbb{I}^h(\boldsymbol{x}) \in \mathbf{V}^h \text{ such that} \\
&\mathbf{a}(\mathbb{I}^h, \mathbb{W}^h) = \mathbf{l}(\mathbb{W}^h) \quad \forall \mathbb{W}^h \in \mathbf{V}^h,
\end{aligned}
\tag{2.23}
$$

where $\mathbf{a} : \mathbf{V}^h \times \mathbf{V}^h \to \mathbb{R}$ and $\mathbf{l} : \mathbf{V}^h \to \mathbb{R}$ are the vectorial bilinear and linear functionals, respectively:

$$
\begin{aligned}
\mathbf{a}(\mathbb{I}^h, \mathbb{W}^h) = &\int_{\Omega^h} \left[\left((\mathbb{S} \cdot \nabla \mathbb{W}^h)^\top \mathbb{I}^h\right) + \left((\mathbb{S} \cdot \nabla \mathbb{I}^h)^\top (\gamma \mathbb{S} \cdot \nabla \mathbb{W}^h)\right) \right. \\
&\left. + \left((\beta \mathbb{I}^h)^\top (\mathbb{W}^h + \gamma \mathbb{S} \cdot \nabla \mathbb{W}^h)\right) - \left((\Theta \mathbb{I}^h)^\top (\mathbb{W}^h + \gamma \mathbb{S} \cdot \nabla \mathbb{W}^h)\right) \right] \mathrm{d}\boldsymbol{x} \\
&+ \int_{\partial\Omega} \left[\left((\mathbb{S} \cdot \boldsymbol{n} : \mathbb{H}_{[\mathbb{S}\cdot\boldsymbol{n}>0]} : \mathbb{I}^h)^\top \mathbb{W}^h\right) \right] \mathrm{d}\boldsymbol{x},
\end{aligned}
\tag{2.24}
$$

$$
\begin{aligned}
\mathbf{l}(\mathbb{W}^h) = &\int_{\Omega^h} \left[\left((\kappa I_b \mathbb{1})^\top (\mathbb{W}^h + \gamma \mathbb{S} \cdot \nabla \mathbb{W}^h)\right) \right] \mathrm{d}\boldsymbol{x} \\
&+ \int_{\partial\Omega} \left[\left(\mathbb{S} \cdot \boldsymbol{n} : \mathbb{H}_{[\mathbb{S}\cdot\boldsymbol{n}<0]} : \mathbb{I}^h_{\text{in}})^\top \mathbb{W}^h\right) \right] \mathrm{d}\boldsymbol{x}.
\end{aligned}
\tag{2.25}
$$

Note that, in contrast to the standard FEM variational formulation (2.13), which was a system of N_d equations, the vectorial FEM variational formulation (2.23) is a single equation. In other words, the equation (2.23) is simply the combination of N_d equations involved in the system (2.13).

In order to solve the vectorial FEM variational formulation one first needs to assemble the vectorial matrix system $\mathbb{A}\mathbb{I} = \mathbb{b}$ from the equation (2.22). This is done by approximating all the N_d components $(\mathcal{V}_m^h)$ of the vectorial finite element functional space $\mathbf{V}^h$ by a kth order polynomial space $\mathbb{P}_k(\mathcal{C}_i)$, for all $\mathcal{C}_i \in \Omega^h$. This leads to a family

of polynomial basis functions $\{\varphi_i \in \mathcal{V}_m^h\}_{i=1}^{N_v}$ which in-turn formulates the solution $\mathbb{I}^h(x) = \sum_{i=1}^{N_v} \mathbb{I}^h(x_i)\varphi_i(x)$. In a similar fashion $\mathbb{W}^h(x) = \sum_{j=1}^{N_v} \mathbb{W}^h(x_j)\varphi_j(x)$. N_v is the number of degrees of freedom associated to the spatial mesh Ω^h. The vectorial finite elements leads to a matrix system $\mathbb{A}\mathbb{I} = \mathbb{b}$ has its coefficients differently arranged than the standard FEM matrix system $AI = b$. For the standard and the vectorial FEM approach, the two equations given blow show the arrangement of matrix coefficient $(a_{i,j})_{k,l}$, where indices i, j represent to the spatial degrees of freedom with $i, j \in [1, N_v]$ and k, l represent the angular degrees of freedom with $k, l \in [1, N_d]$, and the arrangement to right hand side vector with coefficients $b_{i,j}$ where i, j represent the spatial and angular degrees of freedom, respectively, with $i \in [1, N_v]$ and $j \in [1, N_d]$.

The vectorial FEM linear system $\mathbb{A}\mathbb{I} = \mathbb{b}$ reads

$$
\begin{pmatrix}
(a_{1,1})_{1,1} & \cdots & (a_{1,1})_{1,N_d} & \cdots\cdots\cdots & (a_{1,N_v})_{1,1} & \cdots & (a_{1,N_v})_{1,N_d} \\
\vdots & \ddots & \vdots & \cdots\cdots\cdots & \vdots & \ddots & \vdots \\
(a_{N_v,1})_{1,1} & \cdots & (a_{N_v,1})_{1,N_d} & \cdots\cdots\cdots & (a_{N_v,N_v})_{1,1} & \cdots & (a_{N_v,N_v})_{1,N_d} \\
\vdots & & \vdots & & \vdots & & \vdots \\
\vdots & & \vdots & & \vdots & & \vdots \\
\vdots & & \vdots & & \vdots & & \vdots \\
(a_{1,1})_{N_d,1} & \cdots & (a_{1,1})_{N_d,N_d} & \cdots\cdots\cdots & (a_{1,N_v})_{N_d,1} & \cdots & (a_{1,N_v})_{N_d,N_d} \\
\vdots & \ddots & \vdots & \cdots\cdots\cdots & \vdots & \ddots & \vdots \\
(a_{N_v,1})_{N_d,1} & \cdots & (a_{N_v,1})_{N_d,N_d} & \cdots\cdots\cdots & (a_{N_v,N_v})_{N_d,1} & \cdots & (a_{N_v,N_v})_{N_d,N_d}
\end{pmatrix}
\begin{pmatrix}
i_{1,1} \\ \vdots \\ i_{1,N_d} \\ \vdots \\ \vdots \\ \vdots \\ i_{N_v,1} \\ \vdots \\ i_{N_v,N_d}
\end{pmatrix}
=
\begin{pmatrix}
b_{1,1} \\ \vdots \\ b_{1,N_d} \\ \vdots \\ \vdots \\ \vdots \\ b_{N_v,1} \\ \vdots \\ b_{N_v,N_d}
\end{pmatrix}
$$

The standard FEM linear system $AI = b$ reads

$$
\begin{pmatrix}
(a_{1,1})_{1,1} & \cdots & (a_{1,N_v})_{1,1} & \cdots\cdots\cdots & (a_{1,1})_{1,N_d} & \cdots & (a_{1,N_v})_{1,N_d} \\
\vdots & \ddots & \vdots & \cdots\cdots\cdots & \vdots & \ddots & \vdots \\
(a_{N_v,1})_{1,1} & \cdots & (a_{N_v,N_v})_{1,1} & \cdots\cdots\cdots & (a_{N_v,1})_{1,N_d} & \cdots & (a_{N_v,N_v})_{1,N_d} \\
\vdots & & \vdots & & \vdots & & \vdots \\
\vdots & & \vdots & & \vdots & & \vdots \\
\vdots & & \vdots & & \vdots & & \vdots \\
(a_{1,1})_{N_d,1} & \cdots & (a_{1,N_v})_{N_d,1} & \cdots\cdots\cdots & (a_{1,1})_{N_d,N_d} & \cdots & (a_{1,N_v})_{N_d,N_d} \\
\vdots & \ddots & \vdots & \cdots\cdots\cdots & \vdots & \ddots & \vdots \\
(a_{N_v,1})_{N_d,1} & \cdots & (a_{N_v,N_v})_{N_d,1} & \cdots\cdots\cdots & (a_{N_v,1})_{N_d,N_d} & \cdots & (a_{N_v,N_v})_{N_d,N_d}
\end{pmatrix}
\begin{pmatrix}
i_{1,1} \\ \vdots \\ i_{N_v,1} \\ \vdots \\ \vdots \\ \vdots \\ i_{1,N_d} \\ \vdots \\ i_{N_v,N_d}
\end{pmatrix}
=
\begin{pmatrix}
b_{1,1} \\ \vdots \\ b_{N_v,1} \\ \vdots \\ \vdots \\ \vdots \\ b_{1,N_d} \\ \vdots \\ b_{N_v,N_d}
\end{pmatrix}
$$

Notice, the linear system that arises from the vectorial FEM discretization is equivalent to the one that arises from the standard FEM discretization: the coefficients

for the two matrices are equal in number and value. However, the two matrices have different sparsity pattern, i.e., the vectorial FEM matrices are banded compared to the block matrix structure with standard FEM, see figure 2.4.
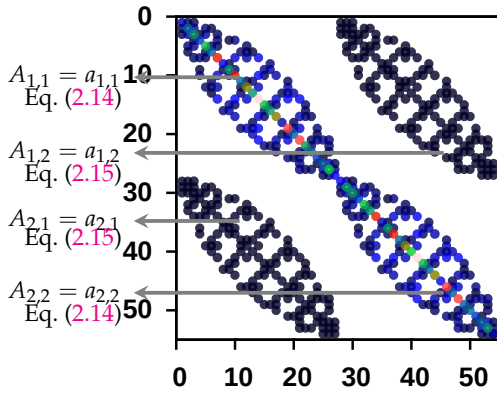

Algorithm 2: building the global vectorial FEM matrix $\mathbb{A}$ and vector $\mathbb{b}$
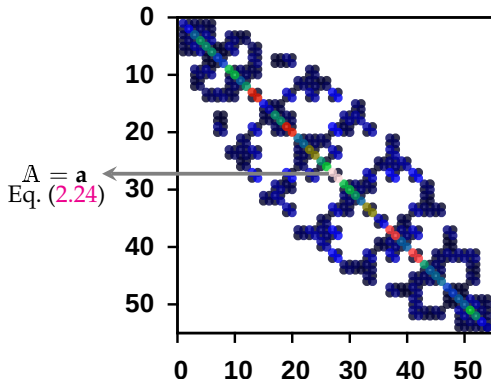
---

    input N_d, κ, σ_s, and β
    load the spatial mesh Ω^h and the angular mesh $\mathbb{S}$
    define vectorial functional space $\mathbf{V}^h$
    build matrix $\mathbb{A}$ using equation (2.24)
    build vector $\mathbb{b}$ using equation (2.25)

$A_{1,1} = a_{1,1}$
Eq. (2.14)

$A_{1,2} = a_{1,2}$
Eq. (2.15)

$A_{2,1} = a_{2,1}$
Eq. (2.15)

$A_{2,2} = a_{2,2}$
Eq. (2.14)

(a) Standard FEM block matrix with 4 blocks.

$\mathbb{A} = \mathbf{a}$
Eq. (2.24)

(b) Vectorial FEM banded matrix.
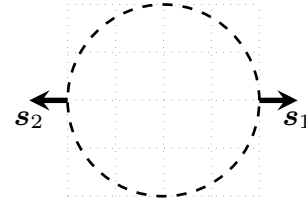
(c) Angular mesh.
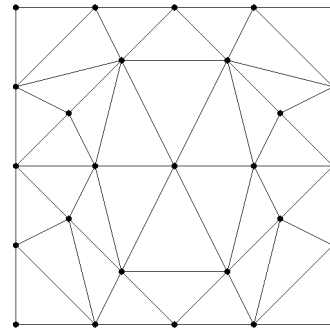
(d) Spatial mesh.

Figure 2.4: Assembly process for the standard and the vectorial FEM matrices. Left: the assembled matrices, and right: the angular and the spatial mesh used ($N_d = 2$ and $N_v = 27$).

      The vectorial FEM matrix $\mathbb{A}$ being built using the single equation (2.24), the matrix assembly routine of the used finite element kernel is called just once. Hence,

the assembly routine is being called $N_d{}^2 - 1$ times less than with the standard FEM discretization. However, it should be noted that a single block matrix assembly with the standard FEM (for computing $A_{m,n}$) is cheaper than the full vectorial FEM assembly (for computing $\mathbb{A}$). Overall, we will show further that it is more costly to assemble the full standard FEM system A, as the assembly routine has to be called $N_d{}^2$ times. A similar argument holds for the assembly of the vector $\boldsymbol{b}$, with the vectorial $\mathbb{b}$ is faster to assemble than the standard $\boldsymbol{b}$. Further, by taking out common factors and operations within the expressions (like mesh traversal or function interpolations), the vectorial FEM equations (2.24) and (2.25) involve less arithmetic operations than their counterpart standard FEM equations (2.14), (2.15), and (2.16). Observe that only two equations (2.24) and (2.25) exist for building $\mathbb{A}\mathbb{I} = \mathbb{b}$, in comparison to three equations (2.14), (2.15), and (2.16) for building $\boldsymbol{A}\boldsymbol{I} = \boldsymbol{b}$. The difference comes from the fact that the standard FEM had two equations (2.14) and (2.15), for building the matrix A, as the diagonal and off-diagonal parts are separately built. However, this is not possible with the vectorial FEM, which has a single equation for building $\mathbb{A}$.

Algorithm 2 describes the procedure followed for assembling the vectorial FEM matrix $\mathbb{A}$ and vector $\mathbb{b}$. In comparison to the standard FEM assembling procedure, given in algorithm 1, we find the iterative loops to be absent within the vectorial FEM assembling procedure. In addition, figure 2.4 represents schematically the building procedures followed for building the vectorial and standard FEM stiffness matrices. We chose the same example as in the preceding section 2.1.1.2: a coarse spatial mesh with $N_v = 27$, and a coarse angular discretization with $N_d = 2$. From this figure, it can be seen that the vectorial FEM leads to a short banded stiffness matrix. Notice the different sparsity pattern compared to the block FEM matrix in figure 2.4a. Moreover, we also see that the standard FEM requires 4 equations to build the full matrix, and on the other hand, the vectorial FEM matrix is built using a single equation.

2.2.2   Solving the discretized vectorial FEM system

The assembled matrices $\mathbb{A}$, are large, sparse, non-symmetric, and banded. The resulting linear systems can be efficiently solved using a Krylov subspace method such as the restarted GMRES from Saad and Schultz [145]. With such an approach, the solution for all the discrete intensities I_m are computed simultaneously (inevitable for the vectorial approach). Advantages of solving a full matrix system via Krylov subspace iterative method over other conventional methods like space-marching and source iteration can be found in [77, 156, 157]. For example, when dealing with ill-conditioned matrices,

which generally arise in radiation problems with heterogeneities, complex topologies, high scattering, and reflections, implicit schemes are necessary as conventional ones seize to perform. Since, we intend to build a method that is able to handle such complexities, this motivates the choice of implicit strategy over other traditional approaches.

The convergence for the restarted GMRES is established when the relative residual r_k is lower than a given tolerance ε. At the kth GMRES iteration, the residual norm r_k is given by

$$r_k = ||\mathbb{A}\mathbb{I}_k - \mathbb{b}||_2,$$

where $\mathbb{I}_k$ is the solution vector.

(a) $(N_d, N_v) = (2, 27)$ (b) $(N_d, N_v) = (2, 57)$ (c) $(N_d, N_v) = (4, 27)$

(d) $(N_d, N_v) = (2, 27)$ (e) $(N_d, N_v) = (2, 57)$ (f) $(N_d, N_v) = (4, 27)$
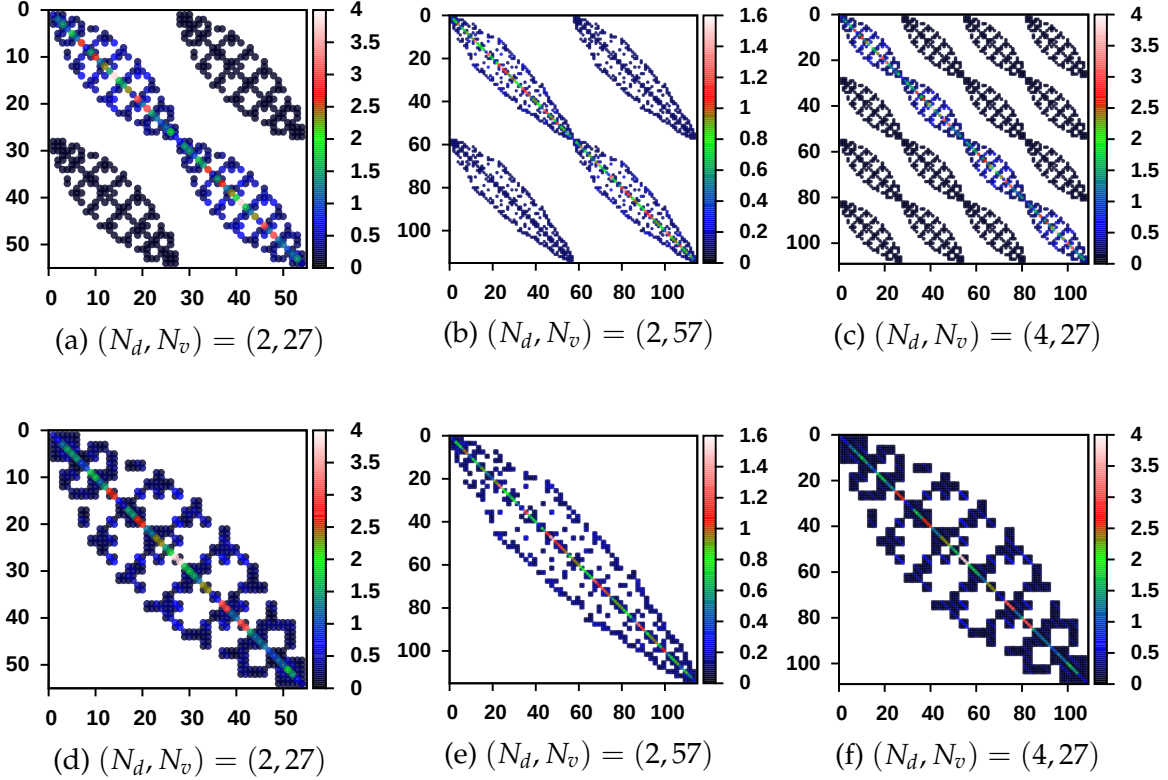
Figure 2.5: Matrix structures for the standard FEM stiffness matrix (top row) and the vectorial FEM stiffness matrix (bottom row). The effect of increase in mesh size and direction count has been shown in the different matrices.

Matrix structures express coupling between the problem unknowns. A banded matrix structure corresponds to unknowns that are coupled over short distances in the matrix. From a computational point of view, working with narrow banded matrices is most often preferable: certain operations, such as exact *LU* factorizations, perform

better with such structures [158]. Moreover, narrow banded matrices are better suited for modern computers and memory hierarchies, for example by reducing cache misses. It would be possible to renumber the matrices yielded by the standard FEM discretization using classical algorithm like Reverse Cuthill–McKee [159], but this implies an extra computational step, and it is also not trivial to do this in a distributed fashion. For these reasons, the GMRES is expected to converge faster for the vectorial FEM than for the standard FEM. However, we should also note that off-diagonal blocks vanish for non-scattering media ($\sigma_s = 0$). For such cases, the calculation time with vectorial FEM and standard FEM will be approximately equal.

In figure 2.5, we compare the matrix structures of both vectorial and standard FEM for some simple RTE systems. For the standard case, refining the mesh size (or the polynomial order) leads to an increase in the size of all matrices within the global stiffness matrix. And, increasing the total number of directions leads to an increase in block numbers. On the contrary, with vectorial finite elements, we always end up with a single banded matrix.

2.3   Comparing the vectorial to the standard FEM for solving RTE

In this section we provide results from a series of different numerical tests that compare the vectorial and standard FEM. All the tests were performed using the following open-source mathematical libraries: Gmsh [160] for the unstructured mesh generation, FreeFem++ [139] for writing the variational problems and assembling the linear systems, PETSc [161] for setting up the GMRES solver, and ParaView [162] for post-processing the results. All tests were performed on an ordinary laptop (Intel Core i7 with 16 GB of RAM).

Previously, the matrix structure, the system assembly process, and the solving strategy for the vectorial and the standard FEM were compared in theory. The theory suggests speed-ups for both system assembly and solution phase for the vectorial FEM compared to the standard FEM. In this section, numerical tests 2A, 2B, 2C, and 2D are designed to numerically investigate on these behaviors.

For all the tests in this section, a two-dimensional square geometry with a homogeneous participating medium is considered. The medium is assumed to be anisotropically scattering, which is modeled using the Henyey–Greenstein phase

Name	κ (cm^{-1})	σ_s (cm^{-1})	g	Medium
Test 2A	0	10	0.8	pure scattering
Test 2B	10	10	0.5	semi-transparent
Test 2C	0	0	-	transparent
Test 2D	10	0	-	pure absorbing

Table 2.1: Test case descriptions.

function [163]. Such a scattering phase function for two-dimensional cases reads

$$\Phi_{m,n} = \frac{1}{2\pi} \frac{1 - g^2}{[1 + g^2 - 2g\cos\theta]}, \tag{2.26}$$

where g is the anisotropy factor such that $g \in]-1, 1[$, and $\cos\theta = \boldsymbol{s}_m \cdot \boldsymbol{s}_n$. According to the value of g, one could say

$$\text{medium is} \begin{cases} \text{backward scattering} & \text{if } -1 \leq g < 0, \\ \text{isotropically scattering} & \text{if } g = 0, \\ \text{forward scattering} & \text{if } 1 \geq g > 0. \end{cases}$$

The four tests 2A, 2B, 2C, and 2D are differentiated by the values of radiative properties given in table 2.1. Each test has been solved twice, first using the standard FEM and second time using the vectorial FEM. In all these tests, the number of directions N_d used for discretizing the angular space is varied between 8 and 80. The four different angular discretizations used are the ones that were presented in the figures 2.2a, 2.2b, 2.2c, and 2.2f. Further, these angular discretizations are used alongside a fine spatial mesh with 21,000 nodes. For the boundary condition, we assume a top-hat type collimated radiation beam I_{in} entering the medium towards the direction $\boldsymbol{s}_{\text{in}} = [1, 0, 0]^T$ on some part of the left wall. This inflow boundary condition is defined by

$$I_{\text{in}}(\boldsymbol{x}, \boldsymbol{s}) = I_0 \mathbb{1}_{\left[\frac{2}{3} > y > \frac{1}{3}, \, x=0, \text{ and } \boldsymbol{s}=\boldsymbol{s}_{\text{in}}\right]},$$

where $I_0 = 1 \, \text{W} \, \text{cm}^{-2} \, \text{sr}^{-1}$ represents the beam strength, and $\mathbb{1}$ is the Heaviside step function such that $\mathbb{1}_{[\text{condition}]} = 1$ if the condition is true, and 0 otherwise.

All the tests in this section were carried out without any preconditioner. As the matrix structures for the standard FEM cases differ from the vectorial FEM cases, it is not easy to define an equivalent preconditioner. Moreover, we are mostly concerned here by the performance of the matrix–vector products without renumbering.

49
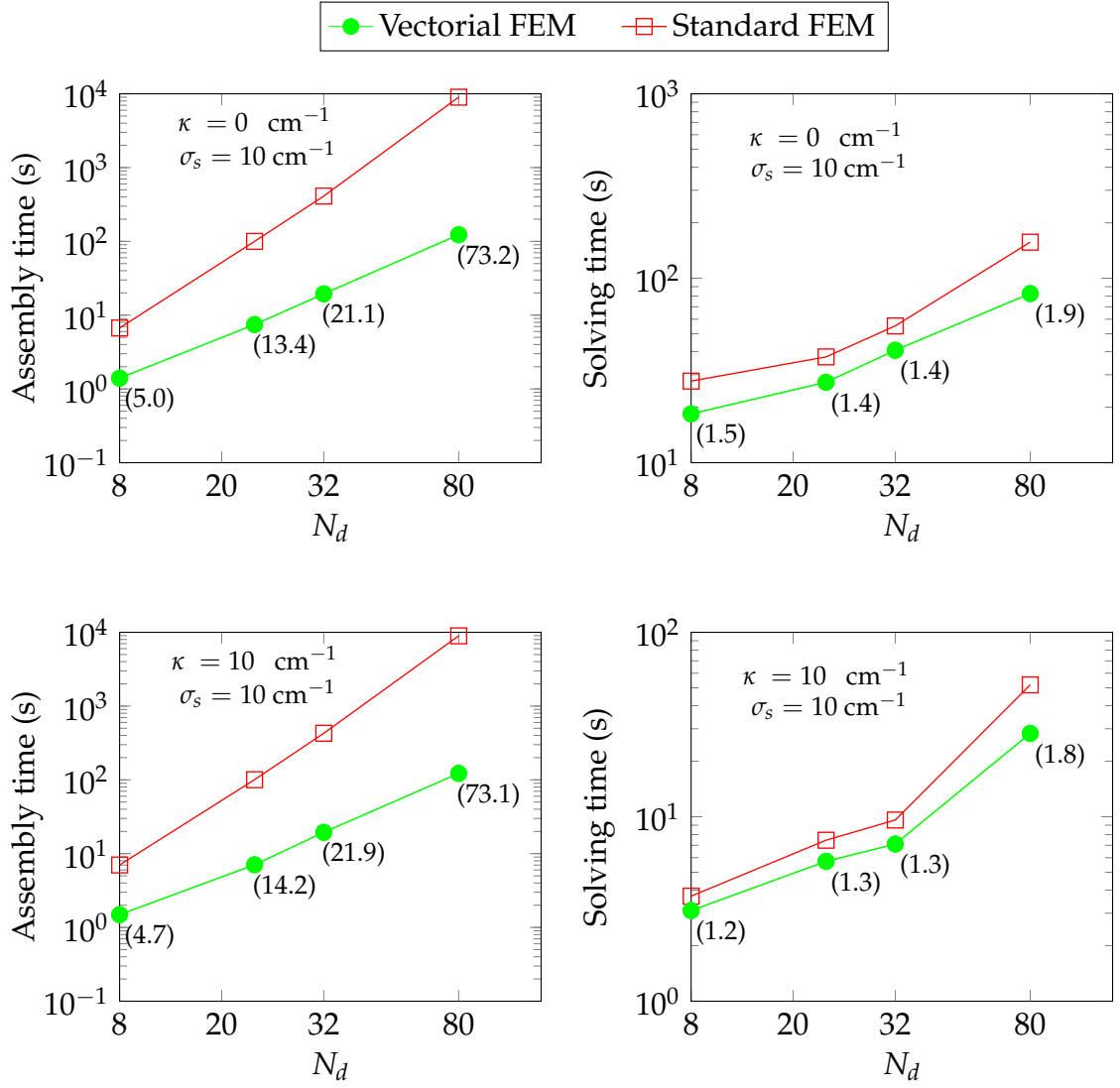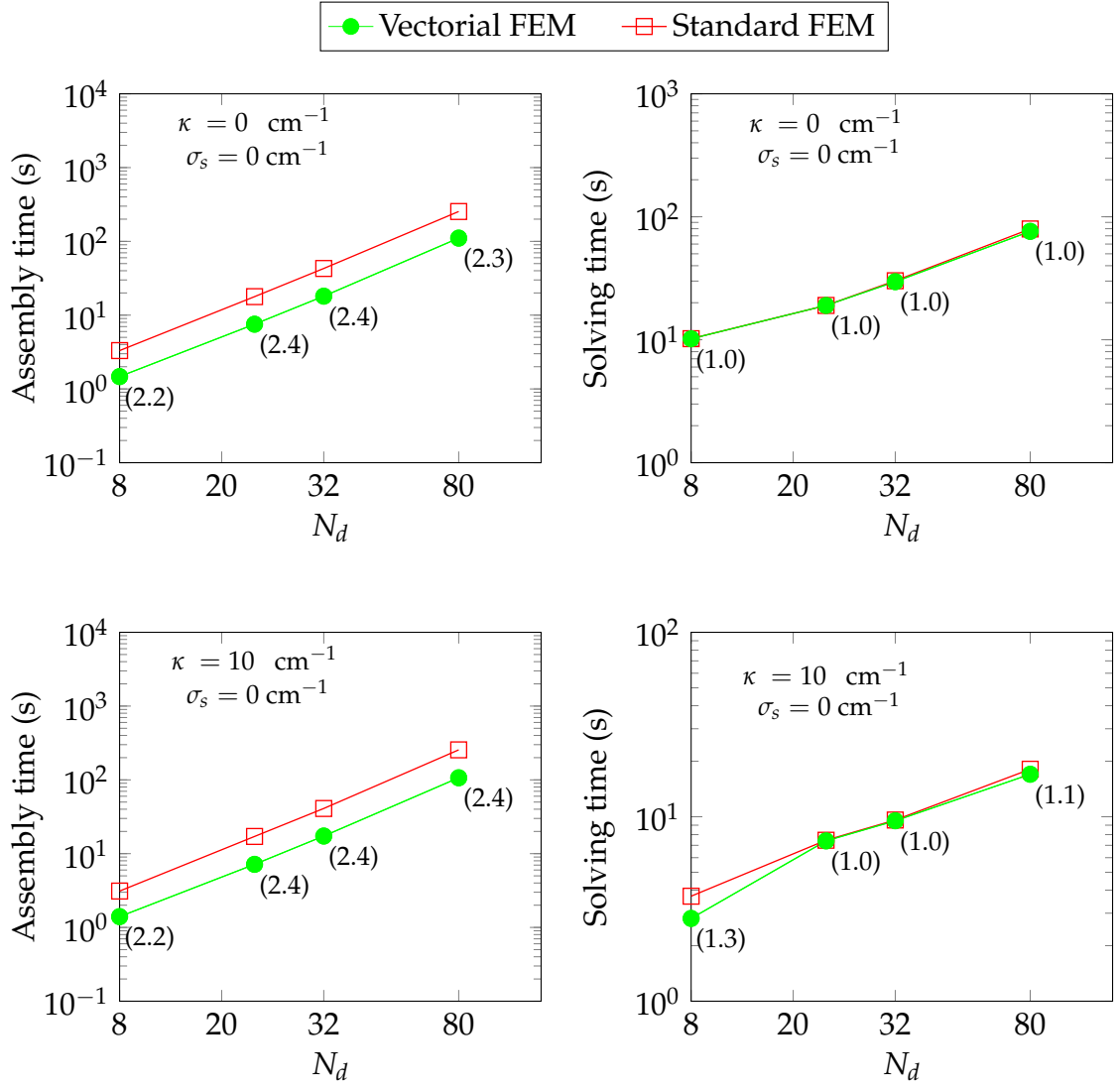
Figure 2.6: System assembly (left column) and solving (right column) times for scattering test cases. Top row: test 2A and bottom row: test 2B. The numbers in braces represent the speed-ups of the vectorial FEM over the standard FEM.

For the scattering tests 2A and 2B ($\sigma_s \neq 0$), the linear system assembly and solution times are reported in figure 2.6. The figure also reports the corresponding speed-up for the vectorial FEM compared to the standard FEM. As expected, the speed-ups for both system assembly and time to solution are observed for all simulations. When the number of directions is increased, the linear system assembly performance of vectorial FEM is even better relative to standard FEM, see figure 2.6 (left column). The reason for such a speed-up was pointed out in section 2.2.1. For the first simulation case with 8 directions, the vectorial FEM was approximately 5 times faster in assembly. While, for simulation case with 80 directions the vectorial FEM assembled the system approximately 73 times faster. This shows growth in speed-up with increase in directions. Concerning the solution phase, the vectorial FEM was 1.2 to 1.9 times faster than the standard FEM, see figure 2.6 (right column). The speed-up can be attributed to the matrix structure difference that we highlighted in section 2.2.2.

N_d	k_{GMRES}	cond(A)	Matrix–vector product timings	
			Standard FE	Vectorial FE
Semi-transparent case: test 2A				
8	117	63.02	2.9×10^0	2.0×10^0
20	103	38.07	6.3×10^0	4.5×10^0
32	105	40.49	1.2×10^1	8.8×10^0
80	106	33.04	4.2×10^1	2.1×10^1
Pure scattering case: test 2B				
8	539	223.20	1.6×10^1	9.4×10^0
20	426	75.58	2.7×10^1	1.8×10^1
32	360	28.50	4.3×10^1	3.1×10^1
80	250	45.97	1.1×10^2	6.1×10^1

Table 2.2: Scattering test cases (2A and 2B) solving phase data: vectorial FEM vs. standard FEM. The matrix–vector product timings reported within the table are in seconds.

To further investigate on the speed-ups for the solution phase for the scattering tests 2A and 2B, table 2.2 provides the matrix–vector product timings for the two methods. Notice, the matrix–vector product timings for the vectorial FEM are always lower compared to the standard FEM. Though the matrices have different structures (vectorial FEM vs. standard FEM), they are equivalent and thus have the same condition numbers for a given N_d. As a consequence, with both vectorial FEM and standard FEM, the number of iterations needed for the GMRES to reach convergence is identical. The condition numbers cond(A) and the number of GMRES iterations to converge k_{GMRES} have also been reported in table 2.2.

Figure 2.7: System assembly (left column) and solving (right column) times for non-scattering test cases. Top row: test 2C and bottom row: test 2D. The numbers in braces represent the speed-ups of vectorial FEM over standard FEM.

A similar comparison for the non-scattering ($\sigma_s = 0$) case, tests 2C and 2D, was also performed. The system assembly timings and solution times are reported in figure 2.7. Concerning the linear system assemblies, we observe the vectorial FEM to be more than two times faster than the standard FEM. However, now the speed-ups are not as high as what was observed in the scattering cases (tests 2A and 2B). The reason is simply that, as a non-scattering medium is considered, the off-diagonal blocks, that appeared in figure 2.3a for example, do not exist. Although the speed-ups between scattering and non-scattering cases are different, it can clearly be concluded that assembling discretized operators of the RTE is always faster with vectorial FEM than with standard FEM. Moreover, the speed-up increases as one uses more directions.

Referring to figure 2.7, plots comparing the times to solution for the non-scattering cases (tests 2C and 2D) have been provided. Adhering to the discussion from section 2.2.2, both vectorial and standard FEM exhibit similar performances, reporting no speed-up.

Note that for all problems involved in this section, reflecting boundary conditions are not considered. However, if one were to use reflecting boundary conditions, this means more integral terms should be evaluated in the variational formulation, cf. [78]. Following the assembly phase timings obtained for tests 2A and 2B, an additional speed up for the vectorial FEM assembly compared to the standard FEM assembly should be expected for reflecting problems. Concerning the solving phase, reflecting problems yield linear systems with off-diagonal blocks (direction s coupling to direction s'). Our results for tests 2A and 2B (also dealing with off-diagonal blocked matrices) indicate that the matrix–vector operation of vectorial FEM should be faster, in comparison to standard FEM, for solving the problems involving reflections. Although, it should be noted that reflecting problems, due to their arbitrary coupling between directions, are in general more difficult to solve compared to non reflecting problems, this means more solving iterations and time required for convergence of such problems. However, in general, the vectorial FEM should also be of interest for solving the reflecting problems of radiative transfer.

In a nutshell, results obtained in this section are in accordance with the previous discussions from sections 2.2.1 and 2.2.2. Overall, for solving the RTE using the FEM-DOM approach, vectorial finite elements are more computationally efficient than standard finite elements.

2.4   Conclusions

In this chapter, we proposed and implemented novel deterministic solution methodology for solving the multi-dimensional steady-state monochromatic radiative transfer equation. The DOM was used for angular discretization of the RTE. And for its spatial discretization, we used the vectorial FEM.

It was shown that the vectorial FEM for solving RTE leads to a linear system with banded matrices, conversely to the block matrix structure obtained with the standard FEM. We also reviewed how such matrix structures can be assembled and solved in an efficient manner. Being banded the vectorial FEM matrices lead to faster matrix–vector multiplications, which plays a key role in reducing solution timings when one uses Krylov subspace solvers.

As expected, the vectorial structure of the finite element spaces yields faster timings for the system assemblies, as well as for the solution phase when using scattering media. This claim was proven using some numerical experiments that compared the standard FEM to the vectorial FEM. Overall we proved that the vectorial FEM certainly has the potential to outrun the standard FEM when it comes to numerically solving the monochromatic steady-state RTE. This remains true for scattering or non-scattering problems of radiative transfer.

PARALLELIZED VECTORIAL FINITE ELEMENT METHOD

3.1   Introduction

Although devising the correct angular and spatial discretizations are crucial for numerically solving the RTE, parallelization is still needed for obtaining time- and memory-efficient solutions. Further, parallel computing becomes inevitable for many challenging numerical simulations, for example simulating radiative transfer within complex geometries that demands for a fine angular and spatial mesh. Another example is when the radiative intensity fields change drastically over short distances in the spatial domain; again for this case, a very fine spatial mesh is needed to capture the sharp solution field variations. Ray effects and false scattering if present again demands for a fine spatial and angular meshes. In all of these scenarios and many more, parallelization can definitely come in handy. Moreover, at current times an efficient numerical method is the one which apart from qualities likes accuracy, stability, generality, etc., is also easy to parallelize. Via this chapter it will be shown that straightforward scalable parallelization is one of the big advantages of using the vectorial FEM method for solving the RTE.

It was previously explained that, the commonly used, fixed point iteration methods (the source iteration method or the Gauss–Jacobi method, etc.) solve the FEM linear system by using operator split strategy. Hence these do not require to explicitly store the full matrix system. However, with the vectorial FEM, we explicitly assemble

the full linear systems from the coupled spatio-angular discretization, and then solve it using a Krylov subspace iterative method. For such an explicit assembly of the full linear system, parallelization becomes inevitable for the matrix system building and for solving, if large angular and spatial meshes are considered.

Several studies have shown the advantages of using parallel computing for the solution of RTE. Using a domain decomposition method and solving the preconditioned system using Krylov subspace methods, Krishnamoorthy et al. presented parallelization of the DOM-FVM for emitting-absorbing medium in [164]. Using up to 125 processes, scaling efficiency was assessed using SSD_{3b} quadrature with 80 directions and a fine spatial mesh with 121^3 cells. Radiative intensities were sequentially solved for each direction and it was observed that increasing the number of processes was not always beneficial. The authors also extended the work for the P_1-FVM [122]. Parallelization of a space-marching algorithm for the DOM-FVM using angular and spatial decomposition methods for emitting-absorbing media was presented in [165]. Afterwards, the work was extended in [166]. The authors reported higher efficiencies and speed-ups for the angular decomposition method than the domain decomposition method, within the scalability limits of the angular decomposition method, bounded by the size of the angular discretization. Scalability was evaluated using up to 80 processes. In [167], Howell presented the parallel space-marching algorithm along with adaptive mesh refinement for the DOM-FVM.

An implicit parallel algorithm based on pseudo-time marching using the domain decomposition method for the DOM-FVM was recently presented in [168]. Using the S_6 quadrature (80 directions) and a two-dimensional spatial mesh with 512^2 nodes, a strong scaling efficiency greater than 85 % with 256 processes was observed. The DOM-FVM for solving the neutron transport equation, an equation similar to the radiative transfer equation, has also been parallelized using the angular and spatial decomposition methods, cf. [169]. In a recent technical report by Adams et al. [170], the scaling performance of sweeps algorithm (space-marching on domain decomposition) using the DOM-FVM was proven to scale on more than a million of processes.

While most of the work on parallelization within the deterministic methods has been performed using the FVM, Kanschat [147] presented the domain and angular decomposition methods for the solution of RTE using the DOM-FEM. The advantages of ordinate parallelism (angular decomposition) over the domain decomposition method were highlighted. The work also combined adaptive mesh refinement along-

side parallelization. Parallel efficiency of ordinate parallelization was established for examples mimicking real astrophysical data. As an extension of this work, Richling et al. [34] efficiently computed solutions using the ordinate parallelism technique in other astrophysics applications. Combing parallelization and adaptive mesh refinement authors could solve problems with high number of ordinates. Pautz et al. [131] presented a modified space-marching method using the domain decomposition method for a DOM-FEM. By adding pipelining and prioritization strategy, a parallel efficiency of approximately 60 % was achieved on 128 processes. A domain decomposition method for P_N-FEM modeling of neutron transport was studied in [132]. The performance of the parallelization method was assessed using 125 processes. While storing multiple domains on a single processing element, the authors observed accelerating potential of the domain decomposition method.

Based on the studies conducted in the past, one could give an edge to parallelization based on spatial domain decomposition (DD) over parallelization based on angular decomposition (AD). Since in practice, one uses small number of ordinates, at most few hundreds for the largest applications, this sets in the most serious limitation of the AD method [171]. Indeed, its achievable speed-up is limited by the number of ordinates used to solve the problem. Following these facts, AD has been considered apt for parallel machines with low number of processing elements (threads, cores, etc.) while DD can be used on massively parallel machines. Although, the DD method has higher limits (order of spatial grid) for parallelization than the AD method, problems of efficiency degradation for participating media while increasing the level of parallelism has been reported, cf. [165, 172].

Contrary to most previous studies, in this chapter, parallelization studies are based on the solution of RTE in an absorbing-emitting-scattering heterogeneous medium. We would review the process of AD and DD parallelism applied onto the vectorial FEM formulations that were introduced in the previous chapter. To add to it, test cases with anisotropic scattering within complex geometries have been considered to test the performance of the proposed parallelization methods. Due to the presence of anisotropic scattering, the discrete intensities become tightly coupled, making the solution procedure challenging. Previously, [4] showed the requirement of a fine angular discretization for accurate solutions of anisotropic scattering cases. Adhering to it, simulation runs with up to 320 directions for 3D and 80 directions for 2D will be considered. While in most of the other parallelization studies a maximum of 80 directions for 3D cases have been used, cf. [164, 166, 168], we show scalability of

57

the newly proposed parallelization methods considering a fine 320 direction angular discretization alongside a fine spatial mesh.

3.2 Parallelization strategies for solving the RTE

Conventionally, in the serial computing framework which was adapted for the previous chapter, in order to solve the vectorial FEM variational formulation we first assembled the matrix system $\mathbb{A}\mathbb{I} = \mathbb{b}$ from the equation (2.22). Then the Krylov subspace based GMRES was employed in order to iteratively solve the system $\mathbb{A}\mathbb{I} = \mathbb{b}$. Parallelization strategies are however different than this conventional approach. Both assembly and solving phase for the linear system $\mathbb{A}\mathbb{I} = \mathbb{b}$ is handled in a different manner, i.e, multiple processes (computer cores) work on bits and pieces of the problem to speed up the assembly and solving routines. After parallelization, the work is distributed among multiple processes, naturally one can expect speed-up provided concurrency of the tasks is optimally handled. Two parallelization strategies are compatible with the introduced vectorial FEM: domain decomposition method (DD) and angular decomposition method (AD).

Numerically, solving the monochromatic steady-state radiative intensity $I(\boldsymbol{x}, \boldsymbol{s})$ depends on two discretization processes: the angular discretization applied on $\mathcal{S}$ and the spatial discretization applied on Ω. One can imagine two completely different strategies of parallelization. The first distributes the spatial discretization task among different processes. Such a method is more classical to other physics as well, and is known as domain decomposition method. The second method, which is native to radiative transfer, is called as the angular decomposition method. AD distributes the angular discretization task among different processes. In the following subsections we shall discuss DD and AD in detail.

3.2.1 Domain decomposition

The basic idea behind domain decomposition methods consists of dividing the spatial mesh into several smaller meshes, which can either be overlapping or non-overlapping. This introduces an implicit distribution of the workload on multiple processing units. After such a decomposition of the spatial mesh, a solution to the global problem is seeked iteratively while performing local solves in each subdomain. For each local solve inside a subdomain, virtual boundary conditions are provided, usually depending on the previous iterate from the neighboring subdomains. This approach was

first proposed by Schwarz in 1869 [173]. Because the local subdomain solves may be done concurrently, these methods are suited for parallel computing when different subdomains are assigned to different processing elements.
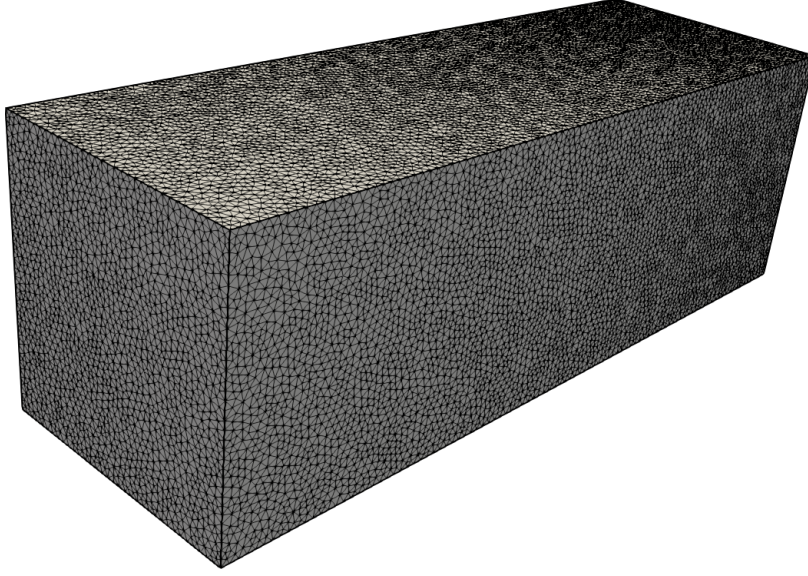
(a) Full mesh of a parallelepiped domain Ω^h.
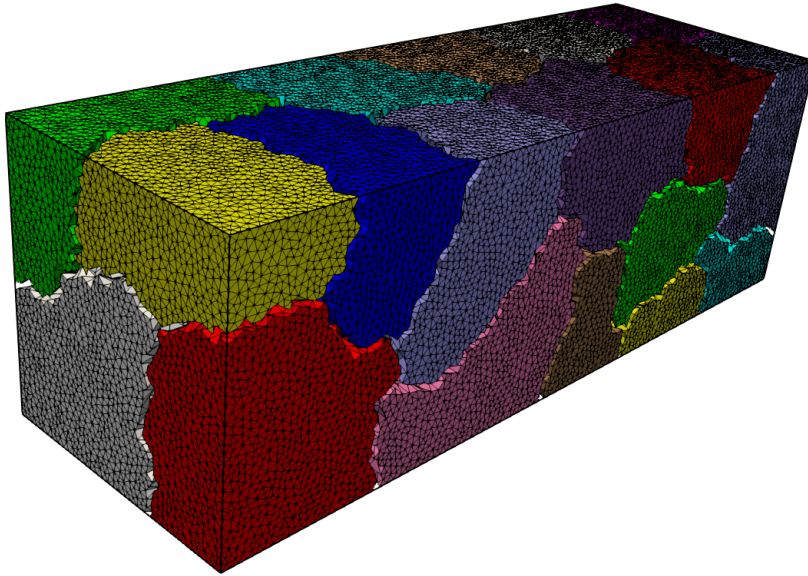
(b) Decomposed mesh of a parallelepiped domain $\{\Omega_i^h\}_{i=1}^{20}$.

Figure 3.1: Mesh partitioning for a parallelepiped domain using METIS.

To apply this method to the vectorial FEM solution procedure, the spatial mesh Ω^h is first split into N_p smaller partitions $\{\Omega_i^h\}_{i=1}^{N_p}$ known as subdomains. Each, mesh partition $\{\Omega_i^h\}_{i=1}^{N_p}$ is then assigned to N_p MPI processes. Partitioning can

be accomplished by using a freely available mesh partitioner such as METIS [174], PARMETIS [175], SCOTCH [176], etc. By using such packages for mesh partitioning, an equal distribution of the mesh between different partitions can be almost guaranteed. An example of mesh partitioning performed using the METIS package has been shown in figure 3.1. In the figure, a parallelepiped mesh being decomposed into 20 small subdomain meshes has been presented. Throughout this thesis METIS has been used for partitioning the meshes. Note that for DD method, only the spatial mesh Ω^h is decomposed, while the full angular mesh $s_m \in \mathcal{S}^{N_d}$ is still needed by all processes to assemble all local systems.

The local vectorial variational formulation on the local meshes $\{\Omega_i^h\}_{i=1}^{N_p}$ is used by each MPI process to assemble the local matrices. Such formulation can be written by reformulating equation (2.22):

$$\forall i = 1, 2, \ldots, N_p :$$
$$\text{search } \mathbb{I}^h \in \mathbf{V}^h \text{ that satisfies:}$$
$$- \int_{\Omega_i^h} (\mathbb{S} \cdot \nabla \mathbb{W}^h)^\top \mathbb{I}^h \, \mathrm{d}\boldsymbol{x} + \int_{\partial \Omega_i^h} (\mathbb{S} \cdot \boldsymbol{n} : \mathbb{H}_{[\mathbb{S} \cdot \boldsymbol{n} > 0]} : \mathbb{I}^h)^\top \mathbb{W}^h \, \mathrm{d}\boldsymbol{x}$$
$$+ \int_{\partial \Omega_i^h} (\mathbb{S} \cdot \boldsymbol{n} : \mathbb{H}_{[\mathbb{S} \cdot \boldsymbol{n} < 0]} : \mathbb{I}_{\text{in}}^h)^\top \mathbb{W}^h \, \mathrm{d}\boldsymbol{x} + \int_{\Omega_i^h} (\mathbb{S} \cdot \nabla \mathbb{I}^h)^\top (\gamma \mathbb{S} \cdot \nabla \mathbb{W}^h) \, \mathrm{d}\boldsymbol{x} \qquad (3.1)$$
$$+ \int_{\Omega_i^h} (\beta \mathbb{I}^h)^\top (\mathbb{W}^h + \gamma \mathbb{S} \cdot \nabla \mathbb{W}^h) \, \mathrm{d}\boldsymbol{x} - \int_{\Omega_i^h} (\Theta \mathbb{I}^h)^\top (\mathbb{W}^h + \gamma \mathbb{S} \cdot \nabla \mathbb{W}^h) \, \mathrm{d}\boldsymbol{x}$$
$$= \int_{\Omega_i^h} (\kappa I_b \mathbb{1})^\top (\mathbb{W}^h + \gamma \mathbb{S} \cdot \nabla \mathbb{W}^h) \, \mathrm{d}\boldsymbol{x} \qquad \forall \mathbb{W}^h \in \mathbf{V}^h \quad \forall \boldsymbol{x} \in \Omega_i^h.$$

Since all Ω_i^h are N_p times smaller in size than Ω^h, if $i > 1$, therefore, smaller sparse matrices with sizes $N_d \times N_v^i$ are assembled concurrently. Here, we use $\mathbb{P}_1$ (piecewise linear) finite elements for the spatial discretization, thus N_v^i is the number of local mesh nodes held by the MPI process i. This implies, smaller local systems are then individually assembled concurrently using equation (3.1). It is thus possible to expect a near-linear speedup of the matrix assembly with this approach.

In order to obtain satisfactory parallel scaling, both the assembly and the solution phases need to be efficient and scalable. The Portable Extensible Toolkit for Scientific Computation (PETSc) [161] has been used for defining suitable preconditioners and to carry out the solution phase at scale for the distributed linear systems. PETSc offers a collection of parallelized Krylov subspace solvers, like the GMRES, the BICGSTAB, the CG, etc. Among these the GMRES method has been chosen for carry-

(a) Decompositions with one process.

(b) Decompositions with two processes.
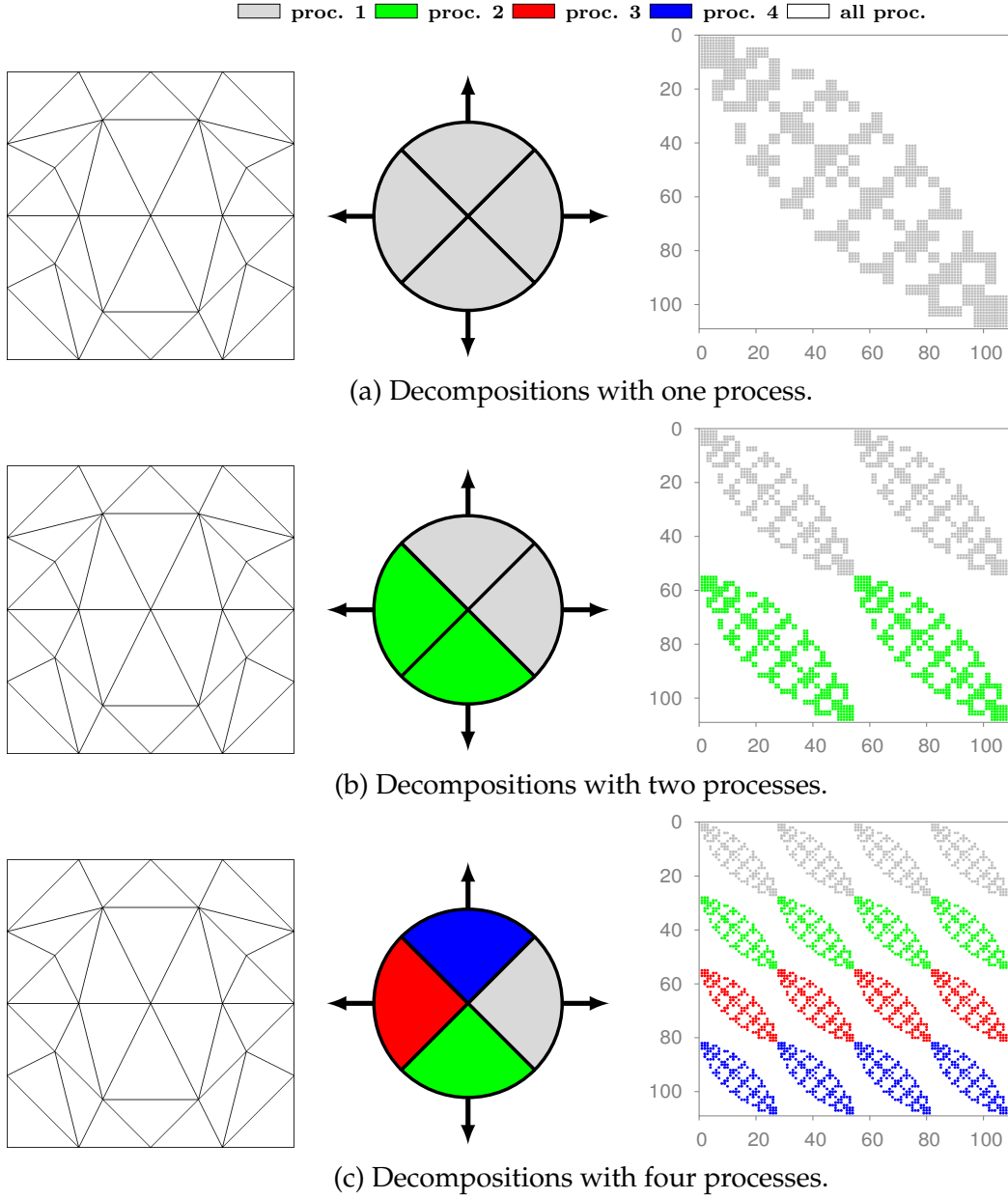
(c) Decompositions with four processes.
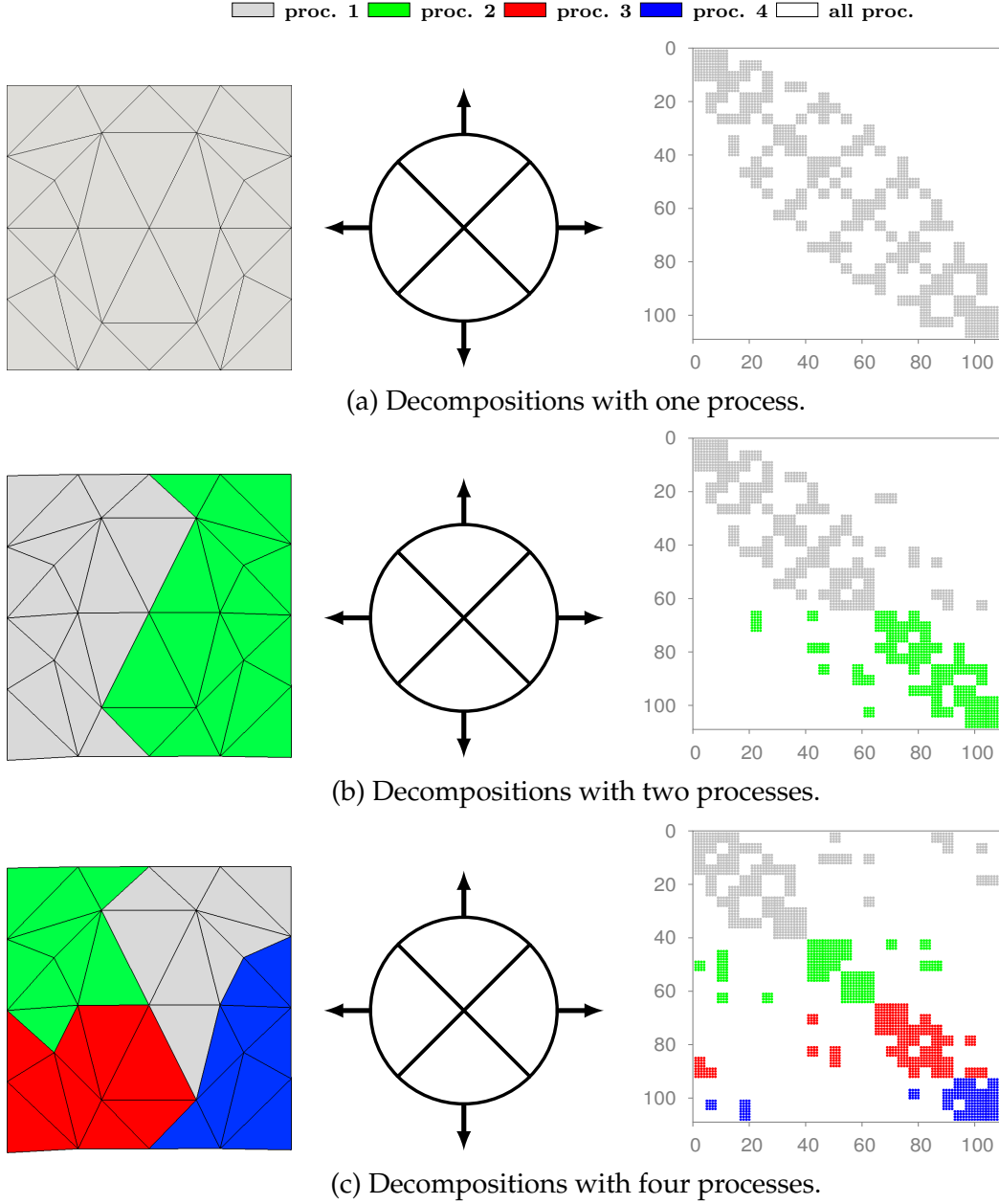
Figure 3.2: Domain decomposition strategy. Left subfigures: spatial mesh decomposition, middle subfigures: angular mesh decomposition, right subfigures: resulting distributed linear system.

ing out the parallel solving phase once done with assembly. The GMRES iteratively solves the global problem. As a main ingredient, the GMRES converges to a solution by repeatedly performing matrix–vector multiplications. We have thus to distribute the global matrix according to a one-dimensional row-wise partitioning. Vectors are distributed using the same partitioning. Matrix–vector products then imply some neighbor-to-neighbor communications, depending on the domain decomposition of the spatial mesh, and local computations.

Figure 3.2 presents pictorially the strategy of DD for RTE. Given a spatial mesh with 27 vertices, we decompose the assembly task in one, two, and four subdomains (subfigures a, b, and c respectively). For clarity, we consider here a coarse angular mesh with four directions. Observe how in all cases the local angular mesh remains the same while the spatial mesh Ω^h is split into N_p smaller local subdomains $\{\Omega_i^h\}_{i=1}^{N_p}$. The color coded matrix shows how the global matrix is distributed using smaller dimension matrices. Also observe the creation of off-diagonal elements within these matrices, corresponding to the coupling of one subdomain to its neighbors. For DD, the quality of the load balance is directly linked with the quality of the mesh partitioner.

3.2.2 Angular decomposition

In order to parallelize the vectorial FEM RTE solving process via angular decomposition, the discretized angular space (unit-sphere) $\mathcal{S}^{N_d}$ is split into N_p smaller angular meshes $\{\mathcal{S}_i^{N_d}\}_{i=1}^{N_p}$ and then assigned to N_p MPI processes. In other words each MPI process contains some number of directions from the total number of directions N_d. An example of angular mesh partitioning has been shown in figure 3.3. In the figure we show the third refinement octahedral mesh ($N_d = 512$) being partitioned into 8 small meshes. In other words, each MPI process will contain $512/8 = 64$ directions. To obtain the angular subdomain matrices, each MPI process i assembles them using the complete spatial mesh Ω^h and the local angular mesh $\{\mathcal{S}_i^{N_d}\}_{i=1}^{N_p}$. Because of this strategy, each MPI process is required to hold the full spatial mesh Ω^h (contrary to the DD approach), memory requirements for the AD approach are thus greater than for DD.

For such a decomposition, the subset angles that one MPI process handles is N_d/N_p, hence the vectorial variation formulation is based on N_d/N_p vectorial components. At the global level, this yields N_p vectorial variational formulations of RTE with each processor holding a single equation. For the ith MPI process one uses
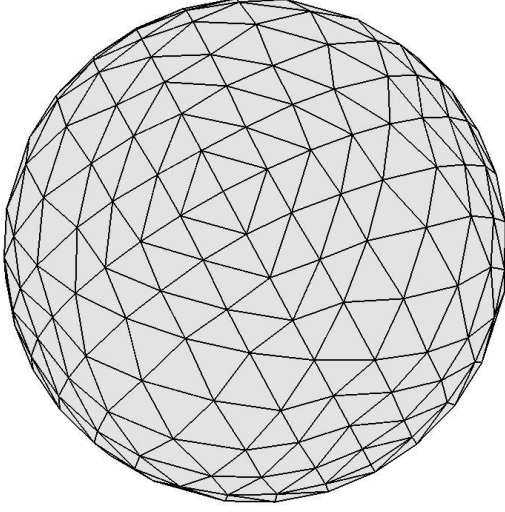
(a) Full angular discretization $\mathcal{S}^{N_d}$: third refinement octahedron $N_d = 512$.
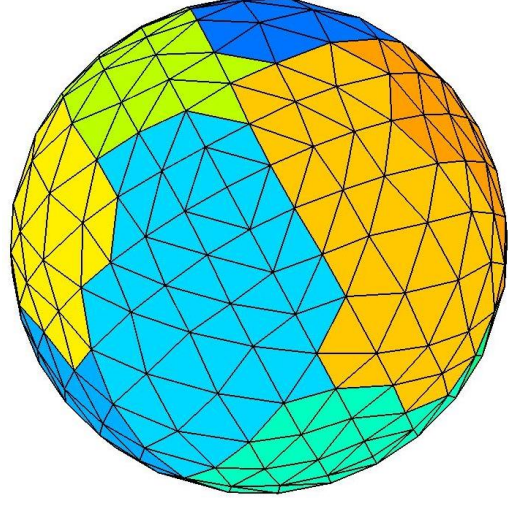
(b) Partitioned angular discretization of third octahedron refinement $\{\mathcal{S}^{N_d}\}_{i=1}^8$.

Figure 3.3: Angular mesh partitioning process using 8 processes.

the local radiative intensity trial function vectors $\mathbb{I}_i^h = [I_{(i-1)N_d/N_p+1}, \dots, I_{iN_d/N_p}]^\top$ and similar construction for local vectorial directions $\mathbb{S}_i$, and local test function vectors $\mathbb{W}_i^h$, for all $i = 1, \dots, N_p$. The phase–weight scattering matrix is split in the same fashion, using a row-wise distribution, such that the MPI process i holds N_d/N_p rows:

$$
\Theta_i = \begin{pmatrix}
\sigma_s\omega_1\phi_{(i-1)N_d/N_p+1,1} & \sigma_s\omega_2\phi_{(i-1)N_d/N_p+1,2} & \cdots & \sigma_s\omega_{N_d}\phi_{(i-1)N_d/N_p+1,N_d} \\
\sigma_s\omega_1\phi_{(i-1)N_d/N_p+2,1} & \sigma_s\omega_2\phi_{(i-1)N_d/N_p+2,2} & \cdots & \sigma_s\omega_{N_d}\phi_{(i-1)N_d/N_p+2,N_d} \\
\vdots & \vdots & \ddots & \vdots \\
\sigma_s\omega_1\phi_{iN_d/N_p,1} & \sigma_s\omega_2\phi_{iN_d/N_p,2} & \cdots & \sigma_s\omega_{N_d}\phi_{iN_d/N_p,N_d}
\end{pmatrix}.
\tag{3.2}
$$

To go one step further, in order to assemble the corresponding block matrix locally, we split the weighted phase function matrix as $\Theta_i = \tilde{\Theta}_i + \Theta_i^d$, in which Θ^d and $\tilde{\Theta}$ are the diagonal and the off-diagonal parts of Θ, respectively. Doing so, the

variational problems to be solved, in this case of angular decomposition, read:

$\forall i = 1, 2, \ldots, N_p :$

search $\mathbb{I}_i^h \in \mathbf{V}^{h\prime}$ that satisfies:

$$
\begin{aligned}
&- \int_{\Omega^h} (\mathbb{S}_i \cdot \nabla \mathbb{W}_i^h)^\top \mathbb{I}_i^h \, \mathrm{d}\boldsymbol{x} + \int_{\partial\Omega^h} (\mathbb{S}_i \cdot \boldsymbol{n} : \mathbb{H}_{[\mathbb{S}_i \cdot \boldsymbol{n} > 0]} : \mathbb{I}_i^h)^\top \mathbb{W}_i^h \, \mathrm{d}\boldsymbol{x} \\
&+ \int_{\Omega^h} (\mathbb{S}_i \cdot \nabla \mathbb{I}_i^h)^\top (\gamma \mathbb{S}_i \cdot \nabla \mathbb{W}_i^h) \, \mathrm{d}\boldsymbol{x} + \int_{\Omega^h} (\beta \mathbb{I}_i^h)^\top (\mathbb{W}_i^h + \gamma \mathbb{S}_i \cdot \nabla \mathbb{W}_i^h) \, \mathrm{d}\boldsymbol{x} \\
&- \int_{\Omega^h} (\Theta_i^d \mathbb{I}_i^h)^\top (\mathbb{W}_i^h + \gamma \mathbb{S}_i \cdot \nabla \mathbb{W}_i^h) \, \mathrm{d}\boldsymbol{x} - \int_{\Omega^h} (\tilde{\Theta}_i \mathbb{I}_i^h)^\top (\mathbb{W}_i^h + \gamma \mathbb{S}_i \cdot \nabla \mathbb{W}_i^h) \, \mathrm{d}\boldsymbol{x} \\
&= \int_{\Omega^h} (\kappa I_b \mathbb{1})^\top (\mathbb{W}_i^h + \gamma \mathbb{S}_i \cdot \nabla \mathbb{W}_i^h) \, \mathrm{d}\boldsymbol{x} - \int_{\partial\Omega^h} (\mathbb{S}_i \cdot \boldsymbol{n} : \mathbb{H}_{[\mathbb{S}_i \cdot \boldsymbol{n} < 0]} : \mathbb{I}_{\mathrm{in}}^h)^\top \mathbb{W}_i^h \, \mathrm{d}\boldsymbol{x} \\
&\qquad \forall \mathbb{W}_i^h \in \mathbf{V}^{h\prime}.
\end{aligned}
\tag{3.3}
$$

In this equation $\mathbf{V}^{h\prime}$ is the vectorial functional space but with reduced dimensions, i.e., $\mathbf{V}^{h\prime} = \mathcal{V}_1^h \times \mathcal{V}_2^h \times \cdots \times \mathcal{V}_{N_d/N_p}^h$.

Each MPI process may now assemble concurrently a diagonal block $\mathbb{A}_{i,i}$, of the global system $\mathbb{A}$, first five terms of equation (3.3). Coupling between different angles (off-diagonal block $\mathbb{A}_{i,j}$) is taken into account in the only term of the variational formulation involving $\tilde{\Theta}_i$, i.e., the sixth term of equation (3.3).

In current strategies being used in the literature to assemble the linear system in parallel, the number of processing units used cannot exceed the number of angles N_d, cf. [169, 171]. We will propose in the next section a way to efficiently alleviate this limitation.

Note the correspondence of the vectorial variational formulation equation (3.3) and the traditional finite element variational formulation equation (2.12). The main difference between the two being that here, we consider N_d/N_p vectorial equations while in the traditional formulation, N_d equations were considered. It would be fair to say that if $N_p = N_d$ the equation (3.3) is indeed the equation (2.12). However, the equation (3.3) introduces an explicit distribution of the workload on N_p MPI processes, which is thus easy to use in a distributed fashion.

Figure 3.4 presents pictorially the strategy of AD method for solving the RTE. Given an angular mesh with four directions, we decompose it in one, two, and four angular subdomains (subfigures a, b, and c respectively). For clarity, we consider a coarse spatial mesh with 27 nodes. Observe how in all the cases the local spatial mesh remains the same while the angular mesh $\mathcal{S}^{N_d=4}$ is split into N_p smaller local

(a) Decompositions with one process.

(b) Decompositions with two processes.

(c) Decompositions with four processes.

Figure 3.4: Angular decomposition strategy. Left subfigures: spatial mesh decomposition, middle subfigures: angular mesh decomposition, right subfigures: resulting distributed linear system.

subdomains $\{\mathcal{S}_i^{N_d}\}_{i=1}^{N_p}$. The matrix is color-coded so that it is straightforward to see how it is decomposed over an increasing number of MPI processes. With this technique it is possible to achieve perfect load balance since all local matrices are of the same dimensions, whereas this might not be the case with DD. However, it is also clear that it is not straightforward to derive a parallel method that will work for a number of processes N_p greater than the number of angles N_d. That is also linked to the fact that for AD, the explicit partitioning is done at the continuous level in equation (3.3), while for DD, the implicit partitioning is done at the discrete level when distributing the spatial mesh before assembling the coefficient matrix of equation (3.1). The global linear systems of both approaches are equivalent but not distributed in the same way. As such, special care must be taken to define appropriate preconditioner for the two types of distribution.

3.2.2.1   Extended angular discretization

In this paragraph, we will show how to raise the limit of angular decomposition method. In practice, one can locally build the diagonal blocks $\mathbb{A}_{i,i}$ and the off-diagonal blocks $\mathbb{A}_{i,j\neq i}$ of the global matrix $\mathbb{A}$. We take advantage of this in order to build these blocks concurrently on different MPI processes. Once all the matrices are built, each process handles N_p/N_d local matrices out of the complete row made of N_d blocks. This means that each block of rows for the global matrix, is built by multiple processes, cf. figure 3.5c. For each block of rows we use $N_{p_\text{row}} \geqslant 1$ processes. Hence, $N_p = N_{p_\text{row}} \times N_d$ processes are used for building the global matrix, with N_{p_row} going from 1 to N_d. We thus push the maximum number of processes that can be used efficiently with angular decomposition from $N_p = N_d$ to $N_p = N_d^2$. As an example, for a three-dimensional test case with $N_d = 320$, this means using up to 102,400 processes instead of only 320. We can thus use this new extended approach of angular decomposition to solve the RTE on massively parallel architectures.

Unfortunately, for the solution phase, PETSc only supports a row-wise distribution of the global matrix. As is, for a single block of rows, multiple processes may be in charge of different columns. So we have implemented a mechanism to redistribute the matrix accordingly to PETSc matrix layout. This step is carried out after all diagonal and off-diagonal blocks have been assembled.

This process of redistribution is explained briefly in figure 3.5, on a test case with four angles and eight MPI processes ($N_p > N_d$). This is a configuration for which it is not trivial to efficiently parallelize current RTE solvers using the angular

(a) Spatial mesh.

(b) Angular mesh decomposition.

(c) Concurrent assembly phase.

(d) Row-wise distribution after communications.
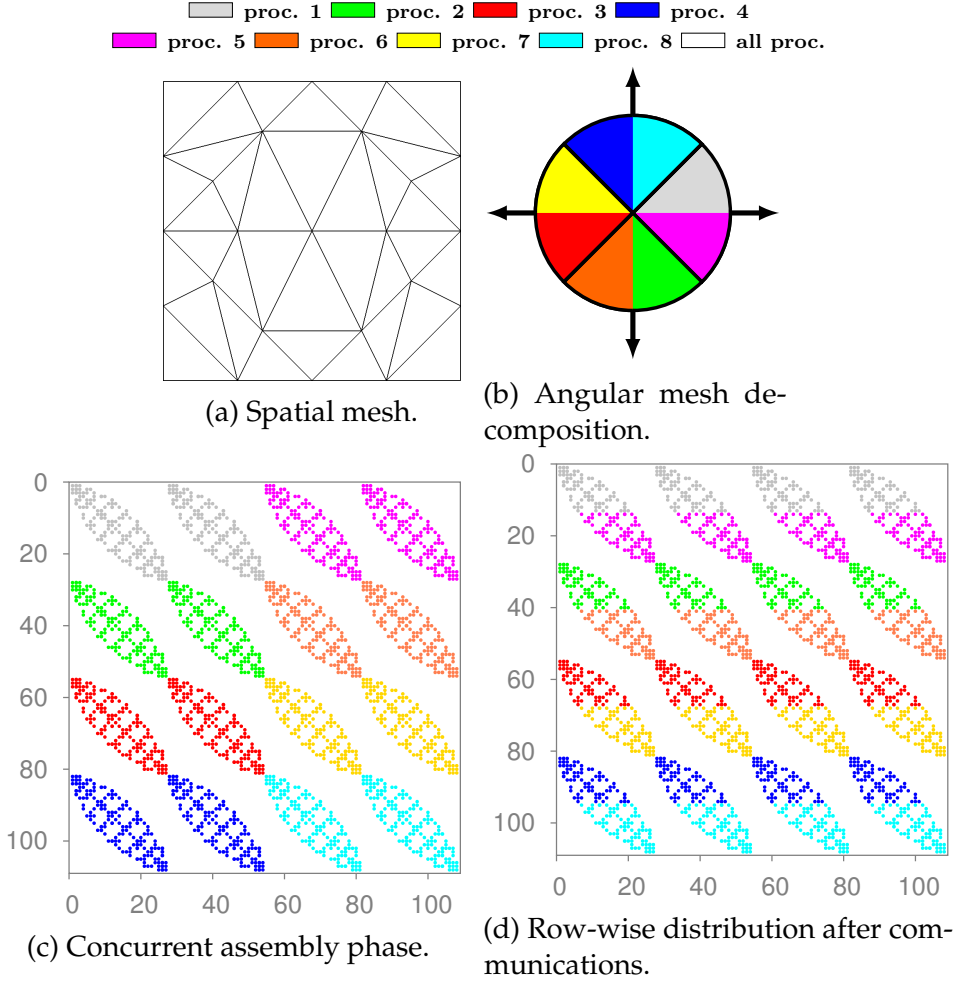
Figure 3.5: Redistribution scheme when $N_p > N_d$ $(8 > 4)$.

decomposition method. In the first step, figure 3.5c, all processes are in charge of assembling concurrently the same number of matrices. In this case, there are two local matrices (either one diagonal matrix plus one off-diagonal matrix, or two off-diagonal matrices), since $N_p / N_d = 2$. At this point, the global matrix does not follow a row-wise distribution. Using asynchronous point-to-point communications, we can redistribute the local matrices so that the assembled system can be supplied to a linear algebra backend such as PETSc, cf. figure 3.5d.

This redistribution mechanism may be seen as an additional level of algebraic decomposition in $N_{p_{\text{row}}}$ partitions on top of the angular decomposition in N_d partitions. However, since this algebraic decomposition is done directly on the matrices and not on the spatial mesh, there is no direct link with domain decomposition.

3.3   Analyzing the parallelization schemes

To make the best possible use of computational resources it is common in the high performance computation community to measure the scalability (also called as the scaling efficiency) of a parallelized solver. Scalability measurements indicate how efficient a solver is when one increases the numbers of parallel processing elements (CPUs / cores / processes / threads / etc.). Two basic kinds of scalability tests can be performed: the strong scaling test and the weak scaling test. The strong scaling tests are used to justify solvers that take a long run-times (process-bound). In other words by increasing the numbers of parallel processing elements one should be able to decrease the computational time linearly provided the solver scales strongly. The weak scaling tests, on the other hand, are used to justify solvers that take a lot of computational storage (memory-bound). In other words, the weak scaling measures how large a problem size, one can efficiently compute with a given parallel solver and system.

In strong scaling experiments, we try to fit the largest problem (workload) possible on a moderate number of parallel processing elements (MPI processes), and then we increase the number of parallel processing elements but keep the size of global problem constant (same spatial and angular meshes). A solver is considered to (strong) scale linearly if the N times increasing the parallel processing elements leads to N times decrease in problem solving time. In weak scaling experiments, the problem size (workload) assigned to each processing element stays constant and additional processing elements are used to solve a larger total problem. In case of weak scaling, linear scaling is achieved if the run time stays constant while the problem size is increased in direct proportion to the number of processing elements.

In the upcoming subsections strong scaling measurements have been performed for the proposed DD and extended AD (with redistribution) methods. Unfortunately, it is not possible to set up weak scaling experiments with the proposed parallel approaches, since the main criteria of increasing the problem size in direct proportions to the increasing number of processing elements cannot be met.

3.3.1   Parallel performance tests for AD and DD

In order to assess the performance of the two devised parallel methods, angular decomposition and domain decomposition, strong scaling test problems for solving the RTE within a heterogeneous participating medium are performed. Parallelization

performances are analyzed for both two- and three-dimensional radiative transfer problems. For the two-dimensional case, we use the unit square composed of a semi-transparent material (albedo $\omega = 0.9$) with circular inclusions (heterogeneities) of an absorbing material ($\omega = 0.09$). For the three-dimensional case, we use the unit cube composed of a semi-transparent material ($\omega = 0.9$) with cylindrical inclusions (heterogeneities) of an absorbing material ($\omega = 0.09$). Such cases may be seen as a model for anisotropic porous media with inclusions of solid opaque phase (rod bundles), cf. [177]. These tests were performed on supercomputer Liger, a 6,384 core machine at ICI[1] supercomputing facility, in Central Nantes, France.

(a) Three-dimensional case.   (b) Two-dimensional case.
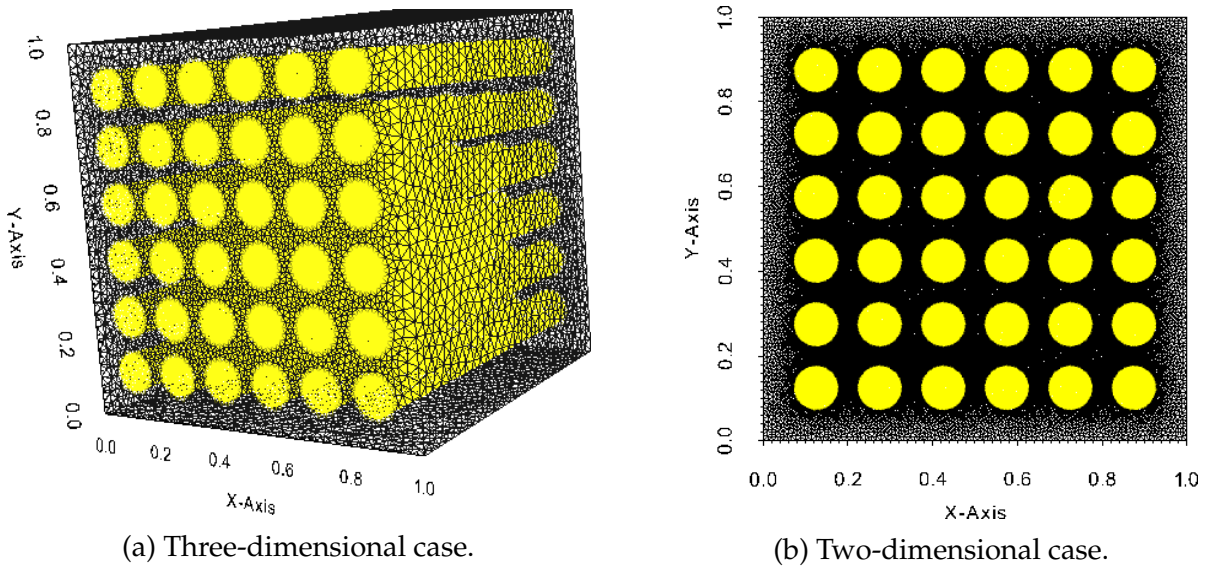
Figure 3.6: Test case meshes and geometry. The radiative properties $(\sigma_s, \kappa) = (0.1, 10.0)$ for inclusions (denoted by yellow color), and $(\sigma_s, \kappa) = (10.0, 0.1)$ for the semi-transparent host material (denoted by black color). Both σ_s, and κ are given in cm^{-1}.

Figure 3.6 presents the meshes considered for the two problems. Along with this figure, the numerical solution in terms of radiative density is presented in figure 3.7. Data concerning the two tests has been given in table 3.1. Such a heterogeneous test case, which has presence of both highly absorbing and highly scattering media, is designed to check robustness of the RTE solver, because such cases are generally more difficult to solve compared to homogeneous media cases with structured grids.

For both cases we assume that an external source laser (I_{in}) of unit power impinges the left-hand side of the domain towards the direction $s_{\mathrm{in}} = [1, 0, 0]^T$. The

[1]Institut de Calcul Intensif (High Performance Computing Center)

in-scattering effects are modeled using the Henyey–Greenstein phase function Φ,

$$\Phi_{m,n} = \frac{1}{4\pi} \frac{1 - g^2}{[1 + g^2 - 2gs_m \cdot s_n]^{\frac{3}{2}}},\tag{3.4}$$

with the anisotropic coefficient $g = 0.8$.

Characteristics	2D-case	3D-case
Spatial mesh Ω^h		
N_v	53,945	107,484
N_e	107,572	642,599
Angular mesh $\mathcal{S}^{N_d}$		
N_d	80	320
Global matrix $\mathbb{A}$		
d.o.f.	4.3×10^6	35×10^6
nnz	31×10^8	17×10^{10}

Table 3.1: Spatial mesh, angular mesh, and global matrix properties of the two test cases. nnz and d.o.f. abbreviate number of non zeros and degrees of freedom, respectively.

As stated in section 3.2, while the linear systems of both AD and DD are equivalent, they are not distributed in the same fashion, see figure 3.2c vs. figure 3.4c. Defining efficient schemes (preconditioner plus iterative method) for implicitly solving distributed sparse linear systems is a task that vastly depends on the distribution of said systems. On one hand, matrices obtained with AD imply costly matrix–vector operations because of their sparsity pattern (all-to-all communications). On the other hand, matrices obtained with DD imply cheap matrix–vector operations (neighboring subdomain-to-neighboring subdomain communications), but are much harder to precondition because of the small dense blocks of size $N_d \times N_d$ in the matrices, due to the use of vectorial finite elements in equation (3.1). After a careful study, we found out that for AD, left block Jacobi preconditioning with complete LU factorization performed by MUMPS [178] for the subdomain solver performed best among other preconditioners available in PETSc. For DD, symmetric point Jacobi preconditioning performed best. The topic of preconditioning will be discussed in detail in the next chapter.

The GMRES is stopped when the relative (to r_0) unpreconditioned residual r_k is lower than 10^{-8}. At the kth iteration, the unpreconditioned residual r_k is given by:

$$r_k = \|\mathbb{A}\mathbb{I}_k - \mathbb{b}\|_2,$$

where $\mathbb{I}_k$ is the solution vector.

Results concerning iteration counts and residuals for AD and DD methods are given in table 3.2. We observe higher iteration counts with DD. While AD converged in 14 (resp. 13) iterations for the two- (resp. three-) dimensional case, DD converged in 1217 (resp. 283) iterations. Such high differences in iteration counts between the two methods suggest that the condition numbers of the preconditioned systems from AD are lower than for DD. This problem of condition numbers for DD could have been handled by designing a more efficient preconditioner, as what was done for AD. However, due to the large dense blocks of size $N_d \times N_d$ in the global system because of the use of vectorial finite elements, the setup phase for cheap yet more robust preconditioners, e.g., incomplete LU factorization, becomes costly. Thus, the overall solution phase timings do not improve. On the other hand, the regular sparse matrix structure of diagonal blocks in AD are well suited for LU factorizations, making block Jacobi preconditioning with exact factorization a good choice of preconditioner for AD.

(a) Three-dimensional case.　　　　　(b) Two-dimensional case.
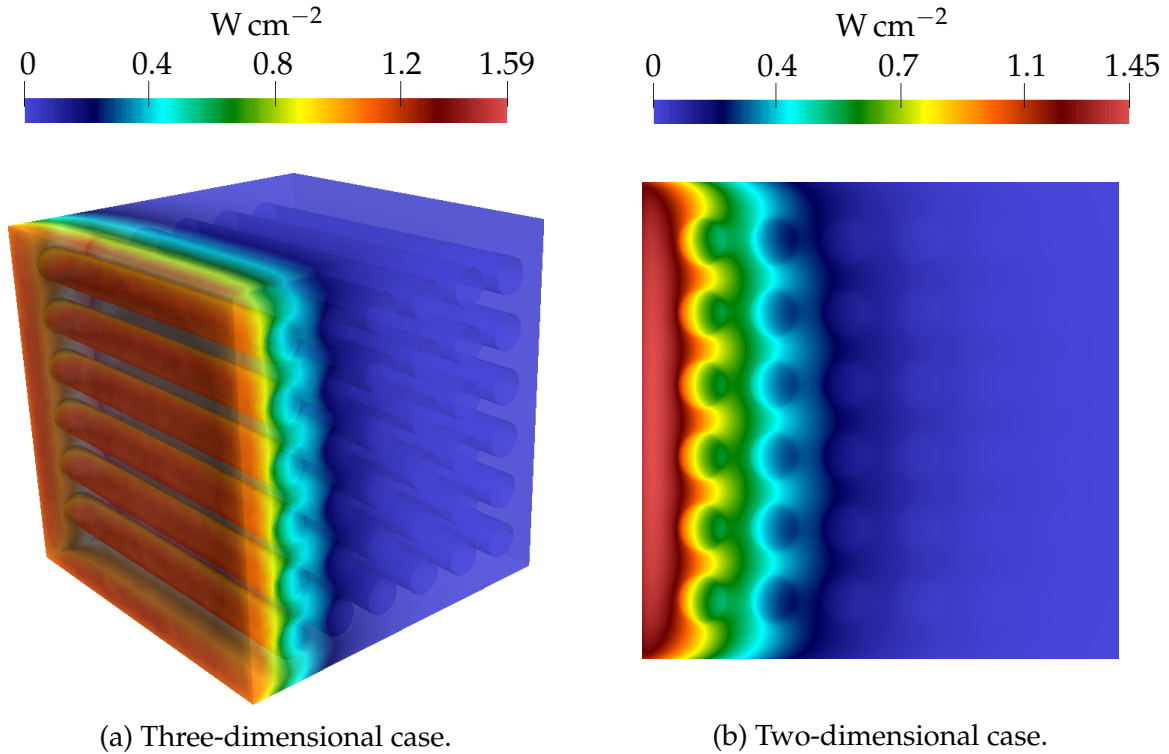
Figure 3.7: Radiative density field inside the medium.

The comparative performance of the two methods for two-dimensional and three-dimensional test cases are presented in figures 3.8 and 3.9, respectively. The

N_p	Angular Decomposition		Domain Decomposition	
	Iterations (k)	Residual (r_k)	Iterations (k)	Residual (r_k)
2D test case				
20	14	5.9×10^{-10}	1217	1.0×10^{-8}
40	14	7.6×10^{-10}	1217	1.0×10^{-8}
80	14	8.4×10^{-10}	1217	1.0×10^{-8}
160	14	8.4×10^{-10}	1217	1.0×10^{-8}
320	14	8.4×10^{-10}	1217	1.0×10^{-8}
3D test case				
160	13	2.4×10^{-6}	283	9.0×10^{-4}
320	14	1.5×10^{-6}	283	9.0×10^{-4}
640	14	1.2×10^{-6}	283	9.0×10^{-4}
1,280	14	1.7×10^{-6}	283	1.0×10^{-4}

Table 3.2: Iteration counts and residuals for both AD and DD methods.

figures reveals that both AD and DD scale strongly well: by increasing the number of processors, the global linear system is built faster. We notice that we quickly reach the maximum achievable speedup in three dimensions, for both AD and DD, because the local matrices become too small. The overall linear system assembly timings are greater for the AD method. The reason is that AD involves assembling multiple local sparse matrices, while for the DD method only one local sparse matrix is computed. Thus, for AD, more quadrature formulae needed by the finite element method have to be evaluated, making it more expensive. Also, for DD, each MPI process holds a portion of the spatial mesh along with the full angular mesh. The roles are switched for AD. Since the spatial mesh is much larger than the angular mesh, AD requires more memory per process than DD.

In figures 3.8b and 3.9b,the wall-clock timings for the solution phase of both AD and DD methods are shown for the two- and three-dimensional test cases. These timings can be split in two phases: construction of the preconditioner and solution phase by a Krylov subspace method. It is clear that we achieve quasi-optimal scaling both for AD and DD methods. The overall wall-clock timings for the solution phase in AD remains lower than DD. This difference is even more pronounced for the two-dimensional test case. Notice that for the AD method, the proposed matrix redistribution is needed as soon as N_p becomes greater than the number of directions, i.e., 80 (resp. 320) for the two- (resp. three-) dimensional test case. On the one hand, AD requires all processes to communicate at each iteration because of the matrix

(a) Assembly phase scaling.

(b) Solution phase scaling.
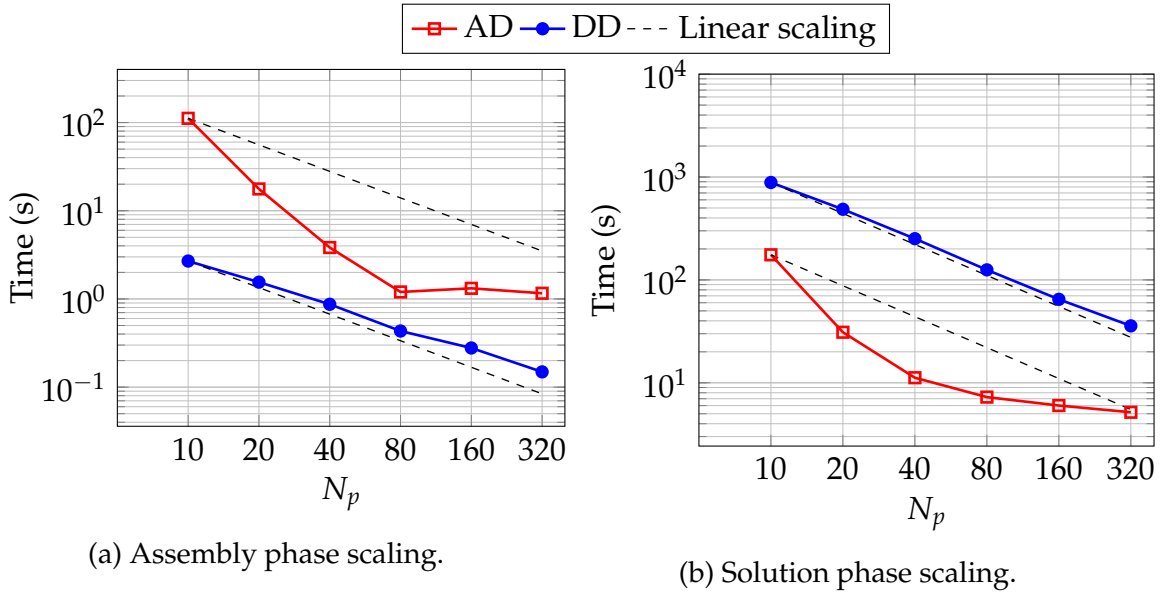
Figure 3.8: Scaling comparison between AD and DD for the two-dimensional test.

structure. On other hand, for DD, one process only communicates with its neighboring subdomains. Although much more communications are required by the AD method, it still outperformed the DD method in the solution phase.

In figure 3.9d, we display timings for construction of the different preconditioners (Jacobi for DD and block Jacobi for AD), as well as the time spent in the GMRES to reach convergence. Since Jacobi preconditioning only involves inverting the diagonal coefficients of the matrices, the time spent setting up the DD method preconditioner is negligible. It is also cheap to apply at each iteration. For the AD method, since we use exact LU factorizations as subdomain solvers, it is costlier to build. Once the factorizations have been computed, they may be used in successive backward eliminations/forward substitutions. This is of course costlier than applying the simpler Jacobi preconditioning. But, as clearly displayed in table 3.2, it yields a much more robust preconditioner. All in all, the AD method still reaches convergence quicker than the DD method.

Finally, we compare the overall speedup and efficiency of both AD and DD methods for the two- and three-dimensional test cases. This data is reported in table 3.3. The speedups (S_{N_p}) and the efficiencies (E_{N_p}) are proportional to the timings obtained with the lowest number of processes needed to run these simulations (10 and 160

(a) Assembly phase scaling.

(b) Solution phase scaling.

(c) Assembly timing breakdown.

(d) Solution timing breakdown.
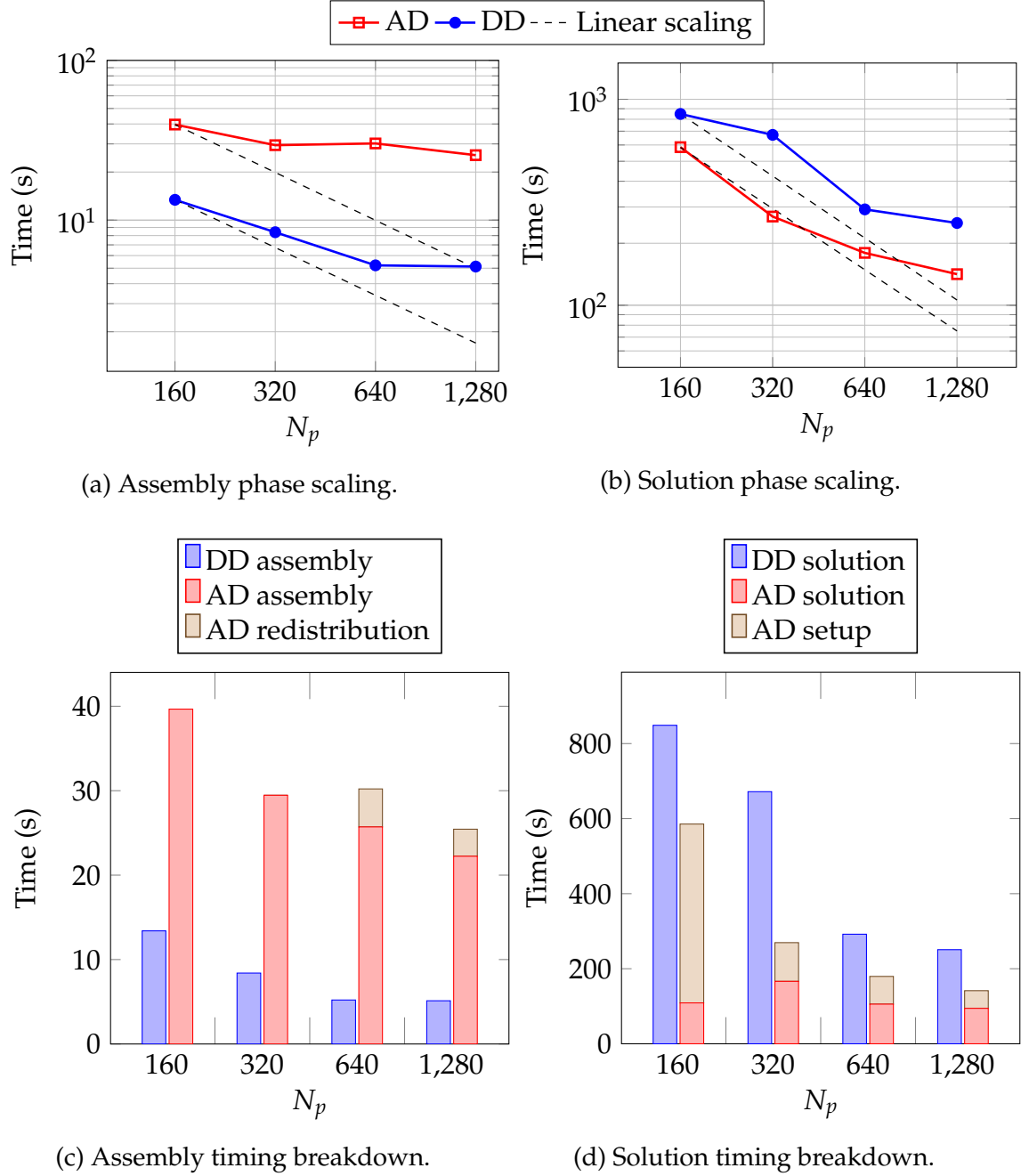
Figure 3.9: Scaling comparison between AD and DD for the three-dimensional test.

N_p	Angular Decomposition			Domain Decomposition		
	t	speedup	efficiency	t	speedup	efficiency
2D test case (4×10^6 d.o.f.)						
10	287.1	–	–	887.4	–	–
20	48.6	5.91	2.95	487.3	1.82	0.91
40	15.0	19.14	4.78	252.5	3.51	0.87
80	8.5	33.78	4.23	125.6	7.06	0.88
160	7.3	39.33	2.45	65.0	13.65	0.85
320	6.3	45.57	1.42	35.9	13.31	0.77
3D test case (35×10^6 d.o.f.)						
160	625.1	–	–	862.1	–	–
320	298.9	2.1	1.05	680.2	1.27	0.64
640	209.7	3.0	0.75	297.2	2.90	0.73
1,280	166.9	3.75	0.46	255.9	3.37	0.42

Table 3.3: Speedup analysis of AD and DD.

respectively). They read as:

$$S_{N_p} = \frac{t_{N_0}}{t_{N_p}} \quad \text{and} \quad E_{N_p} = \frac{t_{N_0} \times N_0}{t_{N_p} \times N_p},$$

where t_{N_0} corresponds to the total time (assembly and solution phase) for runs with 10 processes in 2D, or 160 processes in 3D. Similarly, t_{N_p} corresponds to the total time for the runs with N_p processes. Table 3.3 confirms that both methods scale with decent efficiencies. Overall, the efficiency is slightly better for AD than for DD.

3.3.2 DD parallel efficiency test

Previous subsections show that the angular decomposition method outruns the domain decomposition method when one considers overall solution timings. Despite that, another fact is that the domain decomposition method needs way less memory than the angular decomposition method. Angular decomposition demands to store copies of spatial meshes on each MPI process. Naturally, for problems with very large mesh size memory limitations would most certainly limit AD method. On the other side, domain decomposition demands to store copies of angular meshes on each MPI process. Angular mesh size and its corresponding memory allocation is almost negligible when one compares it to the mesh size and memory allocation for the spatial mesh. This reason makes domain decomposition method a good contender for simulations involving a large spatial mesh. With domain decomposition one can use the memory

allocated to a single MPI process (or node) for storing a portion of the spatial mesh (partition). This means, contrary to AD approach memory allocation required for each MPI process reduces as N_p is increased. For AD the memory gets N_p folds higher as N_p is increased.

Certainly, memory requirements and higher scalability limit are the two big advantages of DD over the standard AD (not extended AD). Literature, however reports that parallel efficiency of DD method depletes when using media with lower optical thickness, see for example [166, 179]. In this section, via numerical experiments we prove that this is not true for the DD set up with the vectorial FEM method and solved with a parallel GMRES.

In order to study the efficiency of the proposed domain decomposition algorithm, two three-dimensional numerical tests are considered. Test 3A: a highly absorbing medium with $\kappa = 10$ cm^{-1} and $\sigma_s = 0.1$ cm^{-1}, and test 3B: a highly scattering medium with $\kappa = 0.1$ cm^{-1} and $\sigma_s = 10$ cm^{-1} . Via these tests the aim is to demonstrate the quality of property-invariant efficiency of the proposed DD. In other words, contrary to the literature, it will be shown that the proposed DD does not suffer loss in efficiency when dealing with different media.

The problems consist of a cubic geometry (1 cm^3) impinged with a small circular collimated radiation beam I_{in} with radius r_b on a part of its left wall. This inflow boundary condition is defined by

$$I_{\text{in}}(\boldsymbol{x}, \boldsymbol{s}) = I_0 \mathbb{1}_{\left[(y-y_0)^2 + (z-z_0)^2 < r_b^2, \ x=0, \text{ and } \boldsymbol{s}=[1,0,0]^\top \right]},$$

where $I_0 = 1$ Wcm^{-2}sr^{-1}, $y_0 = 0.5$ cm, $z_0 = 0.5$ cm, and $r_b = 0.15$ cm represent the beam strength, the beam center coordinates, and the beam radius, respectively.

The spatial domain is triangulated with a fine tetrahedral mesh containing 251,000 nodes. For the angular domain, the first icosahedron refinement with 80 directions was used. The performances of the proposed domain decomposition method are assessed here in the strong scaling regime (the size of the global problem is fixed). The problems were solved using $N_p = 40$, 80, 160, 320, 640, and 1,280 MPI processes.

Although banded, the matrices obtained with vectorial FE domain decomposition are difficult to precondition because of their dense sub-blocks of size $N_d \times N_d$. Hence, like the previous subsection, the standard Jacobi preconditioner applied on the right was used with GMRES to improve the convergence rate and obtain efficient

(a) Scattering case density contours.

(b) Absorbing case density contours.
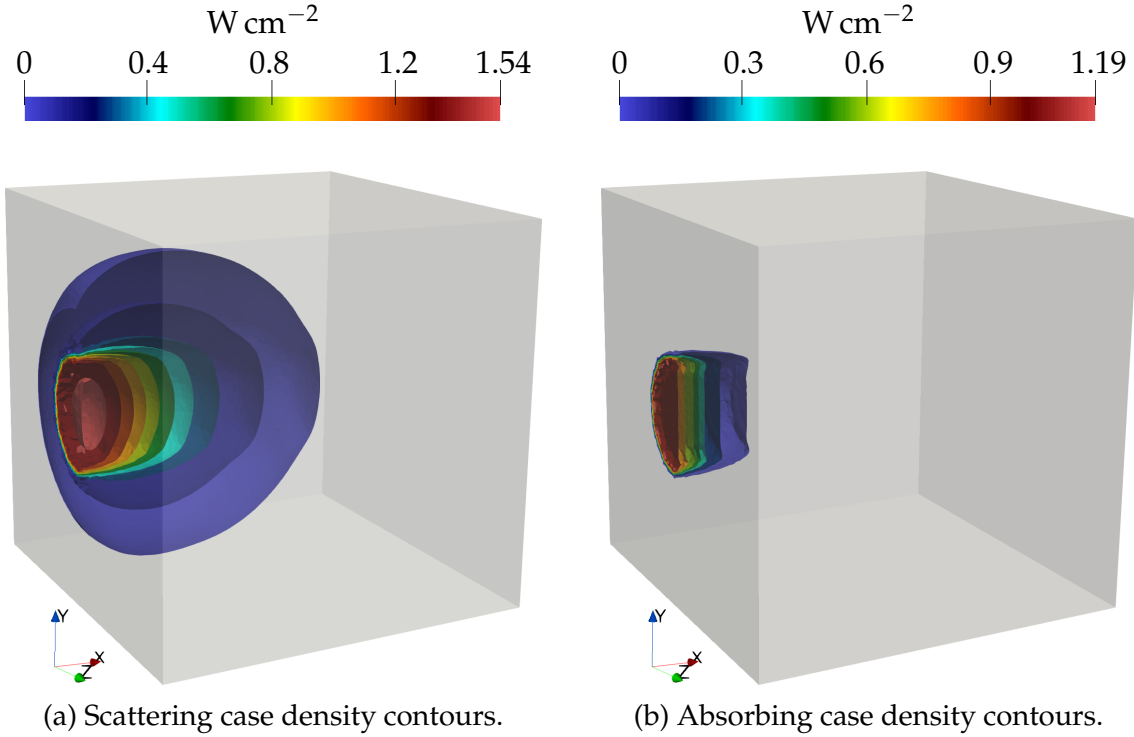
Figure 3.10: Scattering and absorbing test case results.

parallelization. The Jacobi preconditioning involves only the diagonal coefficients of the linear system, so it is relatively cheap, even when increasing the number of angles. The same cannot be said for slightly more advanced preconditioners, such as point block incomplete LU factorizations (which have to deal with the dense sub-blocks that increase in size as N_d).

The sliced density contours pertaining the two test cases are presented in figure 3.10. These contours show the change in radiation propagation volumes for the two tests. Adhering to the physics, the figure shows that the radiation propagation volume in the scattering test 3A is much higher than in the absorbing test 3B.

In figure 3.11, we present the parallel scaling and efficiency for the two test cases. The scaling is based on elapsed wall-clock time for the two major subroutines previously studied: system assembly and solution phase. We do not consider the pre- and post-processing times (for mesh decomposition and solution saving on disk). For both cases, the timings are shown to decrease quasi-linearly when the number of MPI processes are increased. In particular, nearly 60% efficiency was observed for both cases when 1,280 processes were used (see right-hand side figure 3.11). Overall, the timings observed for the absorbing cases are lower than for the scattering cases.
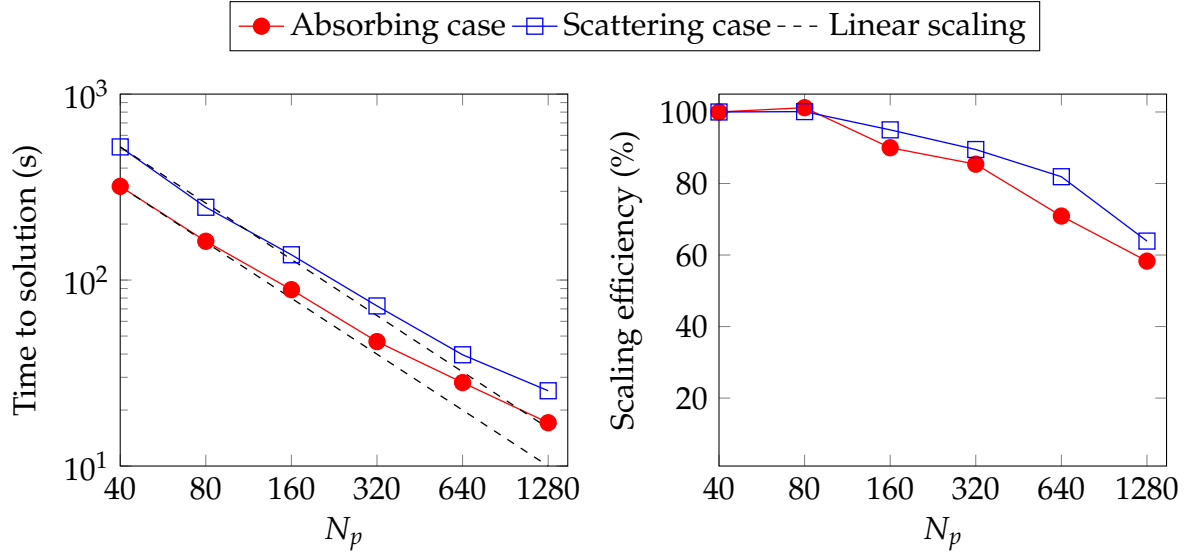
Figure 3.11: 3D parallel scaling analysis for the DD method within different media.

However, it seems that the parallel efficiencies are independent of the optical thickness of the medium (see figure 3.11, right). This result is in contrast with previous works of [166, 179]. Note that the BiCGSTAB solver from PETSc has also been shown to posses quasi-linear scaling capabilities (with marginally better timings than the GMRES), see [164]. Although, the results in this subsection were obtained using the GMRES solver from PETSc, one could expect nearly same performance if the BiCGSTAB solver were used, cf. next chapter.

3.4   Conclusions

Two different approaches of parallelization, angular decomposition and domain decomposition, were applied to solve the steady-state monochromatic radiative transfer equation. As a key ingredient, the vectorial finite element method, was used to facilitate parallelism by allowing us to work with sparse banded matrices.

A new algebraic technique for efficiently redistributing the matrix obtained with the angular decomposition method has been implemented. The new method can be used with up to N_d^2 processing elements, while previous methods were limited to N_d processing elements. A direct advantage of this new approach is that the angular decomposition method can be extended on more than one thousand MPI processes.

A scalability analysis was performed to ensure that the proposed approaches are appropriate. Using fine angular and spatial meshes, both angular and domain decomposition methods set up with vectorial finite elements possess near-linear (strong) scaling characteristics in two dimensions, as well as decent (strong) scaling efficiencies in three dimensions. Overall, the angular decomposition method performs better than the domain decomposition method. Due to important memory needs for discretizing the RTE, making implicit solvers strong scale (for a fixed-size global problem) on a large range of number of MPI processes is a challenge. It was also revealed that the proposed domain decomposition algorithm possess near-linear scaling characteristics which remained unaffected with change in radiative properties.

Proper preconditioning for both methods leads to a solution phase with numbers of GMRES iterations remaining constant with respect to the process count. The angular decomposition method left-preconditioned with block Jacobi and LU factorization for the subdomain solves proved to converge more rapidly than the domain decomposition method preconditioned with the Jacobi method.

To conclude, with the new redistribution scheme and thanks to low iteration counts, the angular decomposition method performs better than the domain decomposition method. Using both of these methods we could perform at scale radiative transfer simulation of a heterogeneous absorbing-emitting-scattering medium with very fine angular and spatial discretizations. Such scales were previously unattainable using standard radiative transfer equation solvers.

Preconditioned Krylov subspace methods

4.1 Introduction

When the discrete ordinates method is applied for solving the radiative transfer equation, the final task in the complete solution process is to solve a large linear system. Traditionally, solution strategies of such linear systems have been developed using the operator-split strategy which reduces the coupled system problem of discrete ordinates RTE to the solution of a series of linear problems. As stated earlier, this method is more commonly known as the source iteration method [180]. However, when one considers radiative transfer problems with dominant scattering, reflection, and heterogeneities, such a solution technique leads to unacceptably slow convergence rates, or may even fail to converge [91]. As a remedy to the slow convergence rates for the scattering dominant problems, the diffusion synthetic acceleration method may be used, cf. [181]. Such a method can be seen as a preconditioned source iteration method, and helps in accelerating the convergence rate for most highly scattering problems.

In the recent years, many researches have used the Krylov subspace methods [182] as an alternative to the traditional source iteration method or to the diffusion synthetic acceleration method. These Krylov subspace methods guarantee fast convergence for the non-trivial radiative transfer problems, without any need for deriving sophisticated acceleration techniques [77, 157, 183, 184, 185]. Furthermore, recent

advancements in parallelism of the Krylov subspace methods have provided the computational community with open-source mathematical libraries that scale well, and can handle large linear systems, cf. [161, 186]. Such tools provide easy access to a collection of Krylov subspace solvers and preconditioners that can be suitably selected depending on the system to be solved. In this chapter, again we use such an open-source mathematical library, PETSc [161], to solve the linear systems that arise while discretizing the RTE.

This chapter discusses two Krylov subspace methods, the BiCGSTAB [146] and the GMRES [145], with and without preconditioning, for the radiative transfer problems with specular reflection at the boundaries. To argue in favor of the Krylov subspace solvers for solving such radiative problems, an eigenvalue spectrum analysis (based on the Arnoldi iteration algorithm [187]) has been performed for different transparent, absorbing, scattering, and reflecting radiation problems. By computing the condition number based on this eigenvalue analysis, we show its degradation when reflection phenomena are involved.

4.2 Analyzing the FEM linear system for the RTE

In this chapter, let us again start by stating the discrete form of the monochromatic steady-state RTE,

$$
\forall m = 1, 2, \ldots, N_d :
$$
$$
\mathcal{R}_m \left(\{ I_n \}_{n=1}^{N_d} \right) = (\boldsymbol{s}_m \cdot \nabla + \beta) I_m(\boldsymbol{x}) - \sigma_s \sum_{n=1}^{N_d} \omega_n I_n(\boldsymbol{x}) \Phi_{m,n} - \kappa I_b(\boldsymbol{x}) = 0 \quad \forall \boldsymbol{x} \in \Omega.
$$
(4.1)

By now we know that the equation set (4.1) statistically describes the interaction of radiation using discrete radiative intensities I_m. And for each $\mathcal{R}_m$, there occurs: radiation loss due to extinction $\beta I_m(\boldsymbol{x})$, radiation gain due to in-scattering $\sigma_s \sum_{n=1}^{N_d} \omega_n I_n(\boldsymbol{x})$, and radiation gain due to black-body emission $\kappa I_b(\boldsymbol{x})$.

To complete the problem definition, boundary conditions containing external sources and reflections at the domain boundary $\partial\Omega \cap (\boldsymbol{s}_m \cdot \boldsymbol{n} < 0)$ (with $\boldsymbol{n}$ being the outward unit normal vector), are given by,

$$
I_m(\boldsymbol{x}) = \hat{I}_m(\boldsymbol{x}) + (1-\alpha) I_m^{\uplus}(\boldsymbol{x}) + \alpha I_m^{\vee}(\boldsymbol{x}) \quad \forall \boldsymbol{x} \in \partial\Omega.
$$
(4.2)

Here, $\hat{I}_m(\boldsymbol{x})$ is the inflow contribution due to external sources or diffused loading, $I_m^{\uplus}(\boldsymbol{x})$ quantifies the diffused contribution of reflection, $I_m^{\vee}(\boldsymbol{x})$ is the specular contribution of the reflection, and $\alpha \in [0,1]$ is a coefficient weighting the two reflection contributions. The diffused and the specular reflections are further expanded as,

$$I_m^{\uplus}(\boldsymbol{x}) = \frac{\rho^d}{\pi} \sum_{\boldsymbol{s}_j \cdot \boldsymbol{n} > 0} \omega_j I_j(\boldsymbol{x}) \boldsymbol{s}_j \cdot \boldsymbol{n} \quad \text{and} \quad I_m^{\vee}(\boldsymbol{x}) = \rho^s(\boldsymbol{s}_m, \boldsymbol{n}) \sum_{\boldsymbol{s}_j \cdot \boldsymbol{n} > 0} \delta_{m,j}(\boldsymbol{n}) I_j(\boldsymbol{x}).$$

The symbols ρ^s and ρ^d are the specular and the diffuse reflectivity coefficients, respectively, and $\delta_{m,j}$, for all $(m,j) \in [\![1; N_d]\!]^2$, are the partition-ratio coefficients. The way these coefficients are calculated in a very accurate manner for specular reflection is presented for two- and three-dimensional problems in [130] and [78], respectively. In particular, $\delta_{m,j}$ is calculated using the so-called "partitioning method" [78]. Developing an advanced finite element technique for the partition-ratio calculations, for complex geometry radiative transfer problems, was one of the primary researches conducted by a previous PhD scholar David Le Hardy from the LTeN Laboratory. His thesis [22] introduced the partitioning method. Here, we shall simply use these previously developed tools in the vectorial FEM framework. The partitioning method shall not be explained in this thesis. Readers who wish to know more about the method may refer to articles [130, 78] or thesis [22]. Note, further, that the weighting coefficient α is assumed to be equal to 1 in this chapter, i.e., only specular reflection is considered.

In the previous chapters, we introduced the vectorial finite element method for solving the discrete ordinates RTE (4.1). The method was then parallelized using two different techniques: domain decomposition and angular decomposition. In these previous chapters, the reflection phenomena was not integrated with the vectorial FEM. However, in the current chapter, the equation set (4.1) is solved using the previously developed (parallel) vectorial finite element method, with the added capabilities of modeling specular reflection using the partitioning method.

4.2.1 Assembling the linear system

As mentioned earlier, the linear system arising from the finite element discretization of the discrete ordinates RTE is sparse and non-symmetric by nature. It has the form:

$$\mathbb{A}\mathbb{I} = \mathbb{b}, \tag{4.3}$$

with the matrix $\mathbb{A} \in \mathbb{R}^{m \times m}$ and the vectors $\mathbb{I} \in \mathbb{R}^m$ and $\boldsymbol{b} \in \mathbb{R}^m$. The symbol $m = N_d \times N_v$, N_v being the number of degrees of freedom associated with the spatial

discretization. From previous numerical experiments conducted in this thesis, we know that both $\mathbb{A}$ and $\boldsymbol{A}$ have same condition number. In other words the standard and the vectorial FEM matrix structures lead to same convergence. This means analyzing conditioning of $\boldsymbol{A}$ means we are in-turn analyzing conditioning of $\mathbb{A}$. This theory shall be used in this section and we shall analyze $\boldsymbol{A}$ for different radiative scenarios.

To analyze thoroughly the linear system $\boldsymbol{AI} = \boldsymbol{b}$, we derive the following block matrix splitting for the linear system (4.3).

$$\boldsymbol{AI} \triangleq \left[A^T + A^E + A^S + A^R \right] \boldsymbol{I} = \boldsymbol{b}, \tag{4.4}$$

with, A^T, A^E, A^S, and A^R representing, respectively, the contributions from transport, extinction, scattering, and reflection processes embedded within the RTE (4.1). These are further expanded as,

$$A^T = \begin{pmatrix} A_1^T & 0 & 0 \\ 0 & \ddots & 0 \\ 0 & 0 & A_{N_d}^T \end{pmatrix}, \quad A^E = \begin{pmatrix} A_1^E & 0 & 0 \\ 0 & \ddots & 0 \\ 0 & 0 & A_{N_d}^E \end{pmatrix}, \tag{4.5}$$

$$A^S = \begin{pmatrix} A_{1,1}^S & \cdots & A_{1,N_d}^S \\ \vdots & \ddots & \vdots \\ A_{N_d,1}^S & \cdots & A_{N_d,N_d}^S \end{pmatrix}, \text{ and } A^R = \begin{pmatrix} 0 & A_{1,2}^R & \cdots & A_{2,N_d}^R \\ A_{2,1}^R & 0 & \cdots & A_{1,N_d}^R \\ \vdots & \vdots & \ddots & \vdots \\ A_{N_d,1}^R & A_{N_d,2}^R & \cdots & 0 \end{pmatrix}. \tag{4.6}$$

Similarly, the vector $\boldsymbol{b}$ expands to $\boldsymbol{b} = [b_1 \; \cdots \; b_{N_d}]$. The mth block of rows of the linear system is related to the finite element discretization of a single $\mathcal{R}_m$. It also includes, due to the integration by parts, the boundary condition terms. The entries of these matrices and the vector $\boldsymbol{b}$ are defined by,

$$\left[A_m^T \right]_{k,l} = - \int_\Omega \boldsymbol{s}_m \cdot \nabla \varphi_k (\varphi_l - \gamma \boldsymbol{s}_m \cdot \nabla \varphi_l) \, \mathrm{d}\boldsymbol{x} + \int_{\substack{\partial\Omega \\ \boldsymbol{s}_m \cdot \boldsymbol{n} > 0}} \boldsymbol{s}_m \cdot \boldsymbol{n} \; \varphi_k \varphi_l \, \mathrm{d}\boldsymbol{x}, \tag{4.7}$$

$$\left[A_m^E \right]_{k,l} = \int_\Omega \beta \varphi_l (\varphi_k + \gamma \boldsymbol{s}_m \cdot \nabla \varphi_k) \, \mathrm{d}\boldsymbol{x}, \tag{4.8}$$

$$\left[A_{m,n}^S \right]_{k,l} = - \int_\Omega \sigma_s \omega_n \Phi(\boldsymbol{s}_m, \boldsymbol{s}_n) \varphi_l (\varphi_k + \gamma \boldsymbol{s}_m \cdot \nabla \varphi_k) \, \mathrm{d}\boldsymbol{x}, \tag{4.9}$$

$$\left[A_{m,n}^R \right]_{k,l} = \int_{\substack{\partial\Omega \\ \boldsymbol{s}_n \cdot \boldsymbol{n} < 0 \cap \boldsymbol{s}_m \cdot \boldsymbol{n} > 0}} \rho^s(\boldsymbol{s}_m, \boldsymbol{n}) \delta_{m,n}(\boldsymbol{n}) \varphi_l \varphi_k \boldsymbol{s}_m \cdot \boldsymbol{n} \, \mathrm{d}\boldsymbol{x}, \tag{4.10}$$

$$[b_m]_k = - \int\limits_{\substack{\partial\Omega \\ s_m \cdot n < 0}} \hat{I}_m \varphi_k s_m \cdot n \, \mathrm{d}x + \int_\Omega \kappa I_b(\varphi_k + \gamma s_m \cdot \nabla \varphi_k) \, \mathrm{d}x. \qquad (4.11)$$

Again, in this chapter, the finite element basis functions φ_k, $k = 1, \ldots, N_v$ are the first-order Lagrange polynomials. Equations (4.7) to (4.11) combined together, correspond to the discrete formulation of equation (4.1) solved with the boundary conditions (4.2). More detailed derivations of the variational formulation may be found in previous chapters, and for the added reflection terms in [78].

4.2.2 Solution methods for the linear system

The most common iterative solving techniques for the discrete ordinates RTE linear system (4.3), belong to the fixed-point iteration schemes given by,

$$I_{k+1} = I_k + C^{-1}(b - AI_k), \qquad (4.12)$$

where the subscript k stands for the iteration index, and C^{-1} is the preconditioner. The source iteration method, which is the most widely used method for solving the linear systems that arise from the discrete ordinates RTE, uses $C^{-1} = (A^T + A^E)^{-1}$. In fact, the source iteration scheme can be seen as a Richardson method with "nearly" block Jacobi preconditioning (because the diagonal blocks from A^S are not used in C^{-1}). For absorption-dominant, or purely absorbing radiative transfer problems, this preconditioner forms a good approximation of A^{-1}, thereby the linear system (4.3) solved iteratively with the source iteration method undoubtedly performs well. In other situations, for example if the radiative transfer problem is scattering-dominant, or if it involves reflection, the source iteration, or other fixed-point methods do not perform well.

Since the source iteration method is a fixed-point iteration scheme, its convergence rate heavily relies on the spectral radius of the matrix $C^{-1}A$. In 1971, Reed [188] carried out the Fourier analysis for the source iteration method, and proved that the spectral radius c_s of $C^{-1}A$ is independent of the spatial mesh and is equal to the ratio σ_s/κ. Hence, when $\sigma_s \gg \kappa$, the source iteration method exhibits slow convergence. In Reed's paper it was also proved that, for the improved source iteration scheme, namely the diffusion synthetic acceleration method, the spectral radius of $C^{-1}A$ was dependent on the spatial mesh size, which was characterized by the size h of the mesh elements. It was seen that meshes with h greater than the mean free path lead to divergence of such solvers.

Krylov subspace solvers, as alternatives to fixed-point methods, usually have better convergence rates. In practice, a Krylov subspace solver, from a guess I_0 and an initial residual $r_0 = b - AI_0$, computes a more accurate approximation of the solution vector I_k by using the Krylov subspace $\mathcal{K}_k$ given by:

$$\mathcal{K}_k(A, r_0) = \text{span}\{r_0, Ar_0, A^2 r_0, \ldots, A^{k-1} r_0\}.$$

In other words, Krylov subspace methods solve $AI = b$ by repeatedly performing matrix–vector multiplications.

The GMRES and the BiCGSTAB are two different Krylov methods that may be used for solving the linear system arising from the vectorial FEM discretization of the RTE. These two methods can be differentiated based on how they use the Krylov space $\mathcal{K}_k(A, r_0)$ to generate the solution vector I_k. On the one hand, the GMRES chooses I_k by minimizing the Euclidean norm of the residual $r_k = b - Ax_k$ for x_k in $\mathcal{K}_k(A, r_0)$. It does so in two steps: at first, an orthogonal basis is generated by the Arnoldi procedure, and, as a second step, a least squares problem is solved to compute I_k. The BiCGSTAB, on the other hand, tries to reach convergence by following the mutual orthogonalization of two sequences using the non symmetric Lanczos procedure. More details may be found in [189].

Concerning the stopping criterion, usually, the convergence is assumed to be reached when the norm $\|r_k\|_2 = \|b - Ax_k\|_2$ is sufficiently small. Generally, the total number of iterations needed to reach convergence, k_c, is much lower than m, the order of A. How few iterations are required depends on the eigenspectrum of A, and the nature of this dependence is crucial for understanding Krylov subspace methods [182].

4.3   Discussions via some numerical experiments

In this section, results and discussions for different numerical tests are provided. The convergence for the Krylov subspace solvers is reached when the norm of the relative unpreconditioned residual $\|r_k\|_2 \,/\, \|r_0\|_2$ is lower than 10^{-6}.

The numerical experiments presented in the subsection 4.3.1 were performed on an ordinary laptop (Intel Core i7 with 16 GB of RAM) using 8 MPI processes in parallel, while the numerical experiments presented in the next subsection 4.3.2 were performed using 320 MPI processes on the supercomputer Liger, at ICI supercomputing facility (6,048 cores Intel Xeon cluster) hosted by Central Nantes, France.

In chapter 3, we reported near-linear scaling for the AD and DD methods. Hence, the method characteristics derived using a specific number of MPI processes (320 in this case), should have similar trends at other MPI counts as well because of the optimal scaling. Note also that, among the previously developed angular decomposition and domain decomposition methods, the former is used as the standard solver throughout this section.

4.3.1 Eigenspectrum analysis

Eigenvalue analysis of any problem can give away crucial information regarding the problem. For any particular problem, with eigenspectrum analysis one could judge the conditioning, coupling, convergence, etc. Motivated by this fact, the numerical experiments performed in this subsection are designed to study the eigenspectrum of different radiation problems. The Arnoldi iteration algorithm [187] is applied for calculating the eigenspectrum of the matrices. Note that, though a total of m eigenvalues exist for a matrix of size m, out of all eigenvalues the Arnoldi iteration algorithm only provides us with the $N_{eigen} : N_{eigen} < m$ eigenvalues that are of interest for the Krylov subspace solvers. The Arnoldi iteration algorithm computes the eigenvalues of the Hessenberg matrix $\boldsymbol{H}_n$. The Hessenberg matrix $\boldsymbol{H}_n$, in fact is the orthogonal projection of $\boldsymbol{A}$ onto the Krylov subspace. This incomplete spectrum of eigenvalues cannot be used for complete eigenvalue analysis, however it is intended here only for assisting in understanding the convergence of the Krylov subspace solvers, and for approximating the matrix condition numbers.

For the numerical tests in this subsection, we used a 1 cm^3 cubic-shaped participating medium impinged with a top hat-type collimated external radiative source on its left face:

$$\hat{I}(\boldsymbol{x}, \boldsymbol{s}) = I_0 \mathbb{1}_{\left[(y-y_0)^2 + (z-z_0)^2 < r_b^2, \, x=0, \text{ and } \boldsymbol{s}=\boldsymbol{s}_{\text{in}}\right]}, \tag{4.13}$$

where $I_0 = 100$ W cm^{-2}sr^{-1}, $y_0 = 0.5$ cm, $z_0 = 0.5$ cm, and $r_b = 0.2$ cm represent the strength of the source, the center coordinates, and the impinging radius, respectively. $\mathbb{1}$ is the Heaviside step function such that $\mathbb{1}_{[\text{condition}]} = 1$ if the condition is true, and $\mathbb{1}_{[\text{condition}]} = 0$ otherwise. The impinging direction of this source is $\boldsymbol{s}_{\text{in}} = \left[\frac{-1}{\sqrt{2}} \; \frac{-1}{\sqrt{2}} \; 0\right]^T$. A schematic representation of this inflow boundary condition is shown in figure 4.1a. Further, a 10,000 nodes tetrahedral mesh and a 80 directions refined icosahedron were used for the spatial and the angular meshes, respectively.

(a) Tests in section 4.3.1.

(b) Tests in section 4.3.2.
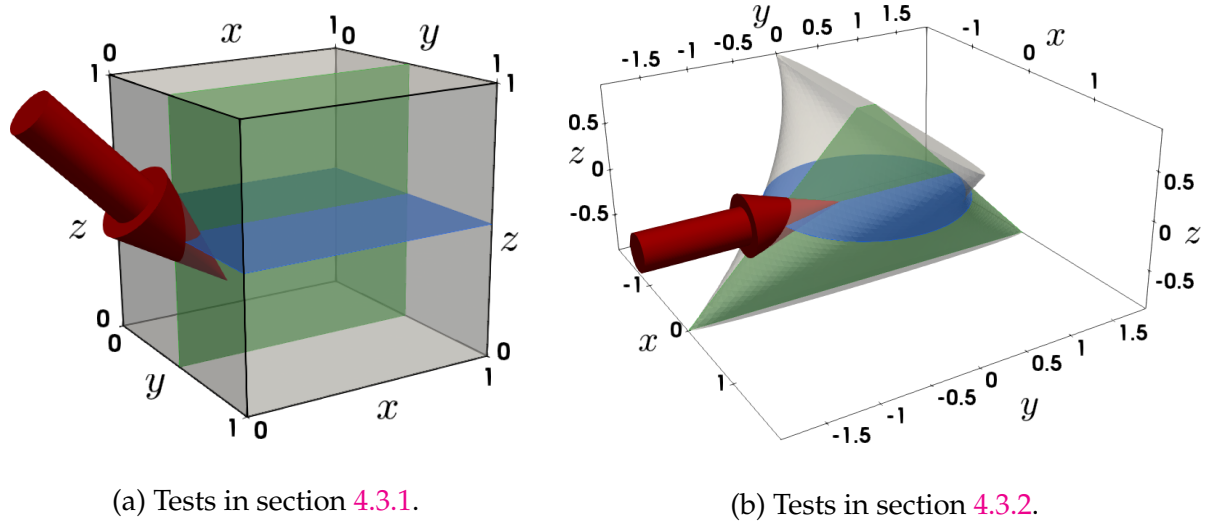
Figure 4.1: Inflow boundary conditions and the geometry used for the tests in section 4.3. External radiation source is shown impinging the different media.

The media are considered homogenized with $\Phi(\boldsymbol{s}_m, \boldsymbol{s}_n)$ modeled using the Henyey–Greenstein phase function [163], with the anisotropy factor $g = 0.5$. Based on this geometry and boundary condition, eight tests (1A to 1H) are formulated with the different radiation parameters summarized in table 4.1.

Test	κ	σ_s	n	Comments
1A	ϵ	ϵ	1	Transparent medium without reflection
1B	5	ϵ	1	Highly absorbing medium without reflection
1C	1	1	1	Semi-transparent medium without reflection
1D	ϵ	5	1	Highly scattering medium without reflection
1E	ϵ	ϵ	2.5	Transparent medium with reflection
1F	5	ϵ	2.5	Highly absorbing medium with reflection
1G	1	1	2.5	Semi-transparent medium with reflection
1H	ϵ	5	2.5	Highly scattering medium with reflection

Table 4.1: Radiative properties for tests 1A to 1H used in section 4.3.1: absorption coefficient κ is given in cm^{-1}, scattering coefficient σ_s is given in cm^{-1}, and n is the index of refraction of the medium. The small value ϵ is set to 10^{-6}.

Figure 4.2a presents the eigenspectrum for test 1A, which considers a non-reflecting transparent medium. The linear system conditioning in this case is dominated by the transport matrix A^T, as $A^S \approx 0$, $A^E \approx 0$, and $A^R = 0$. As such, the linear system is diagonally dominant. Based on the highest and the lowest eigenvalues (marked with filled black and blue circles in the plot of figure 4.2a, respectively), we get an approximate condition number $\text{cond}_2(A) = \max |\lambda(A)| / \min |\lambda(A)| \approx 921$.
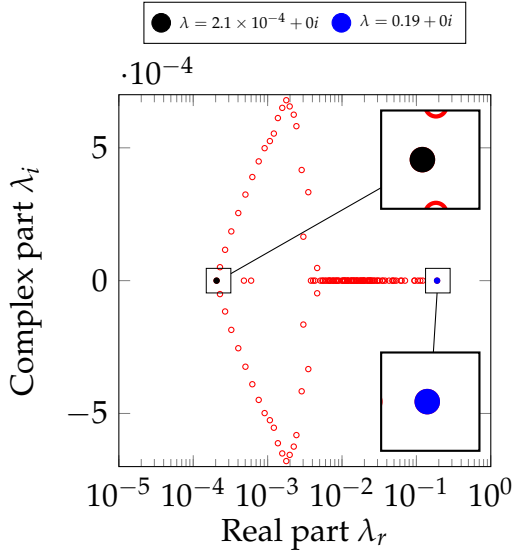
(a) Fully transparent medium, test 1A.
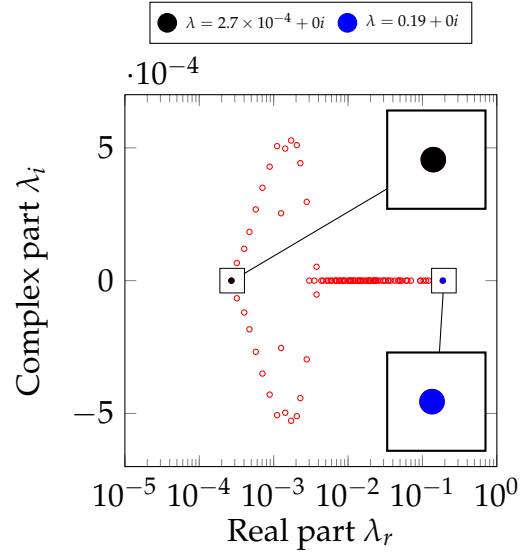
(b) Highly absorbing medium, test 1B.
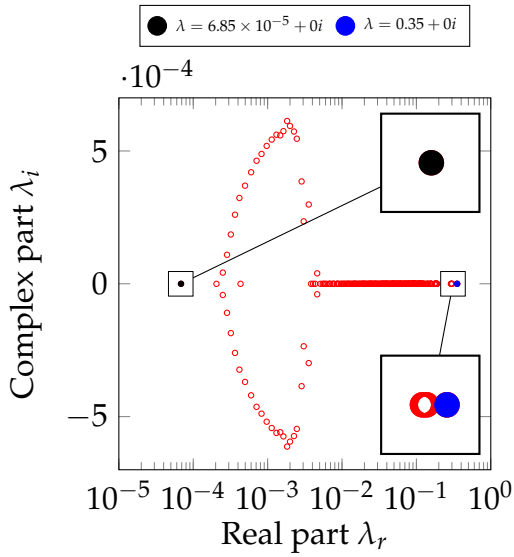
(c) Semi-transparent medium, test 1C.
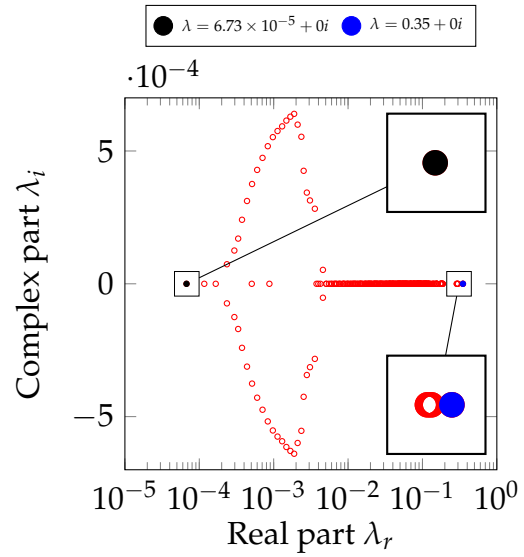
(d) Highly scattering medium, test 1D.

Figure 4.2: Eigenspectra for the transparent (pure transport) medium (test 1A), for the highly absorbing (optically thick) medium (test 1B), for the semi-transparent medium (test 1C), and for the highly scattering medium (test 1D). For this whole set of tests, the refractive index n was set to 1 (non-reflecting media).

Figure 4.2b presents the eigenspectrum for test 1B, which considers a non-reflecting optically thick medium (strong absorption). The linear system conditioning in this case is dominated by both the transport A^T and the extinction A^E, as $A^S \approx 0$ and $A^R = 0$. As weights are added to the diagonal matrices, we expect a better conditioning than for the transparent test 1A. This is proved by a reduction of the condition number $\mathrm{cond}_2(A) \approx 695$. Comparing to test 1A, there is a 30 % smaller value. The Krylov subspace methods may be expected to converge in fewer iterations. Next, for tests 1C and 1D, cases that involve scattering, the eigenspectra are presented in figures 4.2c and 4.2d, respectively. Notice the drift of minimal eigenvalues towards the origin, in comparison to the transparent and absorption test cases. $\min |\lambda|$ are observed to be approximately four times smaller compared to the previous tests. The highest eigenvalues $\max |\lambda|$ are also observed to increase in magnitude, however by a factor two only. Overall, these drifts of eigenvalues result in increasing the condition numbers. We determined $\mathrm{cond}_2(\mathbb{A}) \approx 5155$ for test 1C and $\mathrm{cond}_2(\mathbb{A}) \approx 5197$ for test 1D. Hence, it is likely that a larger Krylov subspace (in dimension) would be needed for solving the scattering media problems.

Another perspective to understand the increase in $\mathrm{cond}_2(\mathbb{A})$ for tests 1C and 1D is that, due to the presence of the scattering phenomenon ($\sigma_s \geq 0$), the N_d discrete PDEs in (4.1) become strongly coupled, hence the global system is more difficult to solve. More specifically, now the solver has to deal with $A = A^T + A^E + A^S$. Unlike matrices A^T and A^E, which just contain diagonal blocks, the scattering matrix A^S contains both diagonal and off-diagonal blocks, cf. equations (4.5) and (4.6). Indeed, it is the presence of A^S which causes the strong coupling and the increase of the condition number.

Tests 1E, 1F, 1G, and 1H are similar to tests 1A, 1B, 1C, and 1D, respectively, except that for these tests, specular reflection is allowed at the boundaries. The corresponding spectra for the tests 1E to 1H are presented in figures 4.3a to 4.3d, respectively. Observe that the eigenspectrum for test 1F (figure 4.3b) is almost similar to its corresponding non-reflecting test 1B (figure 4.2b). More precisely, we report that $\mathrm{cond}_2(\mathbb{A}) \approx 699$ for test 1F, which is almost similar to what was reported for test 1B, where $\mathrm{cond}_2(\mathbb{A}) \approx 695$. Due to such a similarity between the systems, ideally both tests 1B and 1F should converge almost with similar rates. The reason for this similarity is that, due to the strong absorption coefficient for test 1F, the impinging radiation is not able to reach any other boundary of the medium. The impinging radiation, in fact, would be absorbed as soon as it enters the medium, hence not allowing for reflection
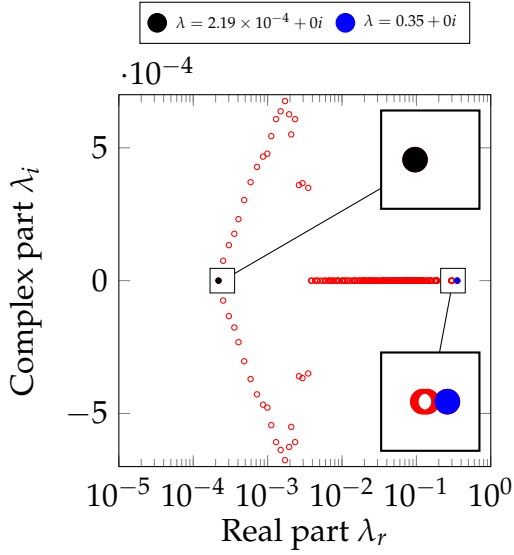
(a) Fully transparent medium, test 1E.
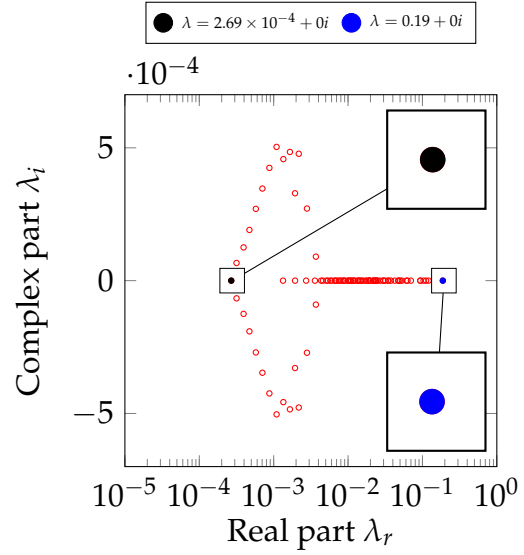
(b) Highly absorbing medium, test 1F.
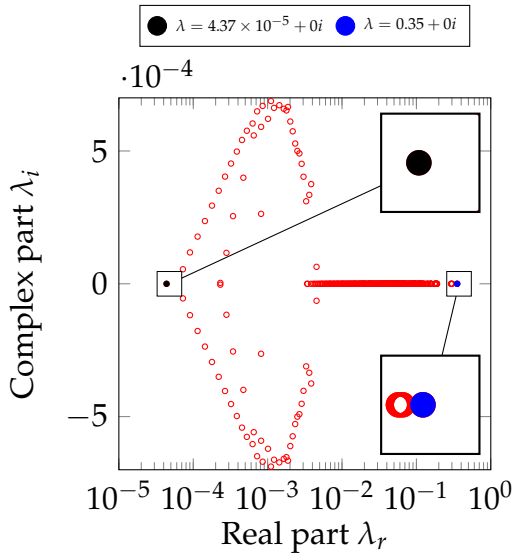
(c) Semi-transparent medium, test 1G.
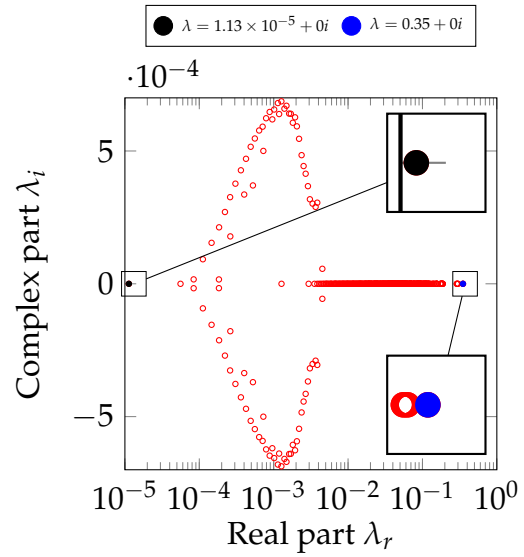
(d) Highly scattering medium, test 1H.

Figure 4.3: Eigenspectra for the transparent (pure transport) medium (test 1E), for the highly absorbing (optically thick) medium (test 1F), for the semi-transparent medium (test 1G), and for the highly scattering medium (test 1H). For this whole set of tests, the refractive index n was set to 2.5 (highly reflective borders).

physics to occur. Thereby, we could say that, even though the physics of reflection is present in test 1F, its eigenspectrum is still mostly controlled by the transport A^T and the extinction A^E.

From the eigenspectrum of test 1E, which considers a transparent medium with reflection at boundaries, it is seen that adding reflection alone to the transport can lead to a change of the matrix condition number. In particular, the greatest eigenvalue was observed to increase (by a factor of two in comparison to the pure transport case), while the smaller eigenvalue remained stable. Overall, $\text{cond}_2(\mathbb{A}) \approx 1598$, which is 1.7 times greater than that of the non-reflecting transparent medium case (test 1A).

Coming to the scattering tests with reflection, tests 1G and 1H, we observe a drift of low eigenvalues towards the origin when compared to their counterpart tests 1C and 1D. In particular, the smallest eigenvalue was 1.6 and 6 times smaller for tests 1G and 1H, respectively, than what was observed for scattering tests without reflection. However the highest eigenvalue remains stable, indicating that it is not influenced by the presence of reflection. Overall, the $\text{cond}_2(\mathbb{A}) \approx 8046$ and 30973 for tests 1G and 1H, respectively. Comparing to other problems in this subsection, the condition number observed for the highly scattering problem involving reflection (test 1H) is the highest in magnitude. Hence, it is likely that a larger Krylov subspace (in dimension) would be needed for solving this problem.

To explain in more details the reflecting tests, physically dealing with specular reflection can be tricky because, at the reflecting border, the energy carried by the impinging direction i is assigned to the reflecting direction(s) j. The reflecting direction(s) j depends both on the surface normal $\boldsymbol{n}$ and on the direction of incidence. For geometries with complex boundaries (many distinct normals) the probability of i getting reflected to many arbitrary directions j is high. Owing to this physics, the reflecting matrix $\mathbb{A}^R$ contains an arbitrary weighted structure which is contrary to the uniform weighted structure of other matrices present in expression (4.4). In other words, the coupling between the N_d PDEs (4.1) becomes less structured, hence more difficult to handle.

4.3.2 Krylov solver analysis for different radiation problems

Based on the eigenspectrum analysis carried out in the previous subsection, it was revealed that the absorbing media problems are well-conditioned (low condition number), the condition number increases when scattering is involved, and becomes

even higher when the medium is both scattering and reflecting. For this reason, in this subsection, we analyze five physics-wise different radiation problems, tests 2A to 2E, solved with the GMRES and the BiCGSTAB, with and without preconditioning. In particular, two classic preconditioners, the standard Jacobi and the block Jacobi (with incomplete LU factorizations with zero level of fill-in as block solvers) applied on the right, are used to enhance the efficiency of the two Krylov subspace methods.

For the tests of this subsection, a berlingot-shaped medium (see figure 4.1b) is used as the standard geometry. The non-convex geometry resembles a tetrahedron which is used to assimilate the cross-section between two struts of an open-cell foam, as used in concentrated solar power applications [78]. The surface topology $\partial \Omega(u, v)$ of the berlingot is parameterized by the following [190],

$$\partial \Omega(u, v) = \begin{cases} x = ab(1 + u) \cos v \\ y = ab(1 - u) \sin v \\ z = au \end{cases} \quad a, b \in \mathbb{R}, \ u \in [-1, 1], \text{ and } v \in [0, 2\pi],$$

in which a and b define the height and the width of the geometry, respectively. We have chosen $a = b = 1$, this corresponds to a berlingot-shaped medium which is 4 cm $\times$ 4 cm $\times$ 2 cm in dimensions.

Much like the boundary conditions used in the previous subsection, in this subsection the collimated top hat-type radiative source follows the same equation (4.13), but with the following parameters: $I_0 = 1$ W cm^{-2}sr^{-1}, $y_0 = 0.0$ cm, $z_0 = 0.0$ cm, $r_b = 0.2$ cm, and $s_{\text{in}} = [0\,1\,0]^T$, i.e., the source enters the geometry with its direction parallel to the y-axis. Figure 4.1b presents an isometric view of the berlingot-shaped medium and its corresponding inflow boundary condition. The figure also contains internal cross-sections of the geometry in order to detail the berlingot's complex shape.

Further, a 57,000 nodes tetrahedral mesh and the 320 directions refined icosahedron were used as the spatial and angular meshes, respectively. In this subsection, we would be dealing with problems involving reflection, to capture the physics more accurately such high count of directions ($N_d = 320$) was used, as recommended in [4]. Just like the tests in the previous subsection, the media are considered homogenized with $\Phi(s_m, s_n)$ modeled using the Henyey–Greenstein phase function, with the anisotropy factor $g = 0.5$. The five tests in this subsection, tests 2A to 2E, are formulated with the different radiation parameters summarized in table 4.2.

(a) Test 2A, transparent medium without reflection.

(b) Test 2B, highly absorbing medium without reflection.

(c) Test 2C, highly scattering medium without reflection.

(d) Test 2D, transparent medium with reflection.

(e) Test 2E, highly scattering medium with reflection.
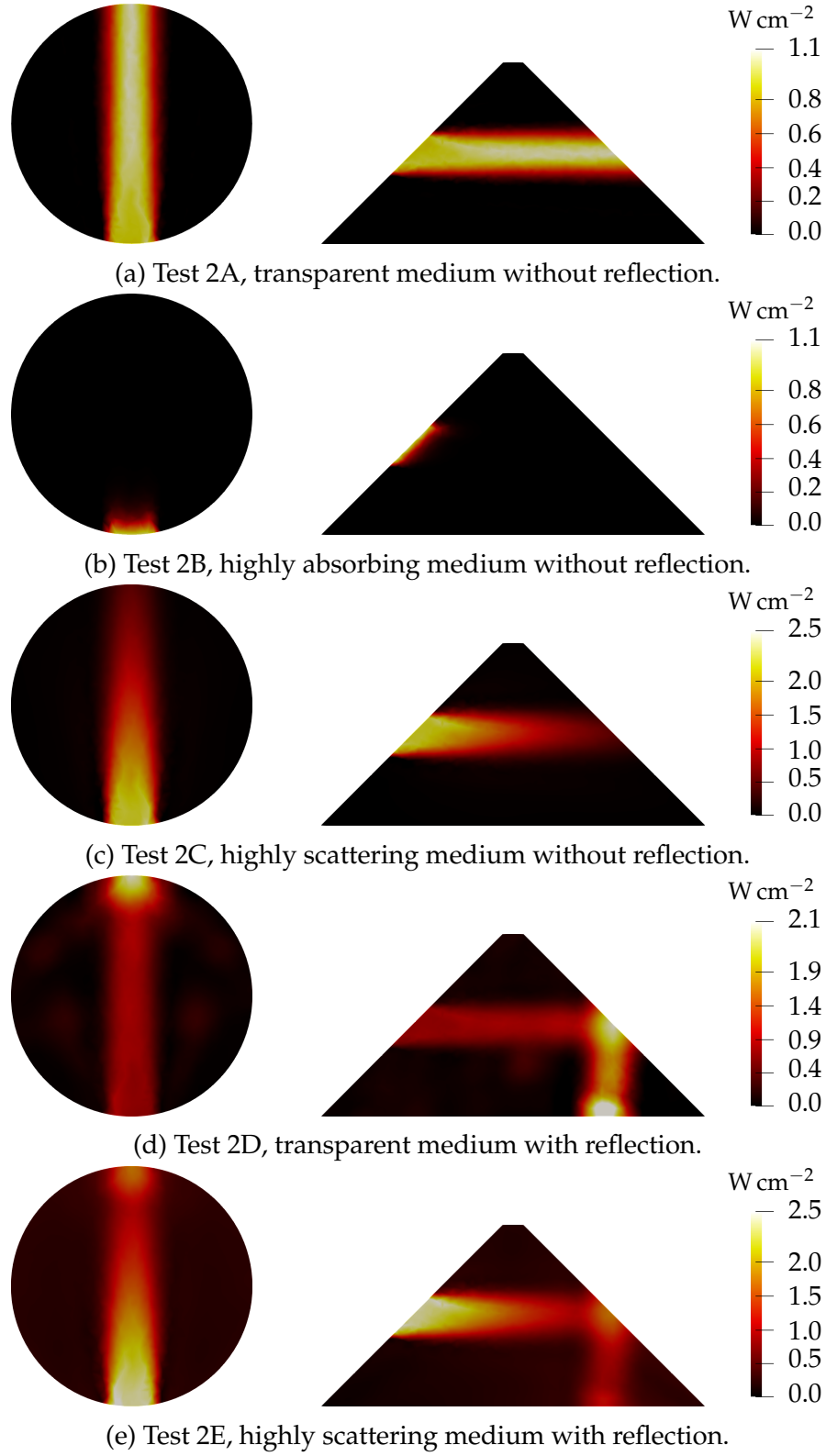
Figure 4.4: Radiation density cross-sections for the berlingot-shaped medium tests.

Test	κ	σ_s	n	Comments
2A	ϵ	ϵ	1	Transparent medium without reflection
2B	5	ϵ	1	Highly absorbing medium without reflection
2C	ϵ	5	1	Highly scattering without reflection
2D	ϵ	ϵ	2.5	Transparent medium with reflection
2E	ϵ	5	2.5	Highly scattering with reflection

Table 4.2: Radiative properties for tests 2A to 2E used in section 4.3.2: the absorption coefficient κ is given in cm^{-1}, the scattering coefficient σ_s is given in cm^{-1}, and n is the index of refraction of the medium. The small value ϵ is set to 10^{-6}.

Figures 4.4 shows two cross-sections (xy-plane at $z = 0$ and yz-plane at $x = 0$) of the photon density fields, $G(\boldsymbol{x}) = \sum_{m=1}^{N_d} I(\boldsymbol{x})_m \omega_m$, within the berlingot-shaped medium of the tests 2A to 2E. Adhering to the physics we can clearly notice, in the provided cross-sections, pure transport, absorption dominance, scattering dominance, and reflection dominance, for the respective tests.

Figures 4.5 to 4.9 present the convergence history of the GMRES and the BiCGSTAB used for solving tests 2A to 2E. For each case we have used the Krylov subspace solvers with and without preconditioners. From all these figures one can clearly draw a conclusion that the BiCGSTAB outperforms the GMRES in all cases. However, the BiCGSTAB is observed to show erratic behaviors of convergence ($\|\boldsymbol{r}_k\|_2$ grows several order in magnitude) which is classic to this method. Axelsson [191] claims that Lanczos-based methods, such as the BiCGSTAB, not based on minimization principles, are susceptible to erratic convergence behaviors. Such erratic behaviors were also reported in [90, 192]. These convergence outbursts are in fact caused by the near failure of the mutual orthogonalization process of the BiCGSTAB. We further show that these outbursts have less impact (almost negligent) for absorbing medium problems due to their lower condition numbers, while these are frequently present in other problems that are not absorption dominant. The outbursts in problems involving reflections are highest in number due to their weak conditioning. As it may occur, the BiCGSTAB may fail once in a while due to its delicate orthogonalization, hence its chances of failure for problems involving reflections are higher than for other problems. On the contrary, the GMRES smoothly converges to the desired solutions, however with slower rates of convergence than the BiCGSTAB. Apart from the faster convergence rates of the BiCGSTAB, it should also be noted that, the BiCGSTAB uses less memory than the GMRES. This is because 30 additional auxiliary vectors (the maximum dimension of the Krylov subspace generated by the Arnoldi procedure

before a restart occurs) need to be stored for the GMRES compared to the BiCGSTAB which uses a short recurrence and only requires 8 auxiliary vectors.
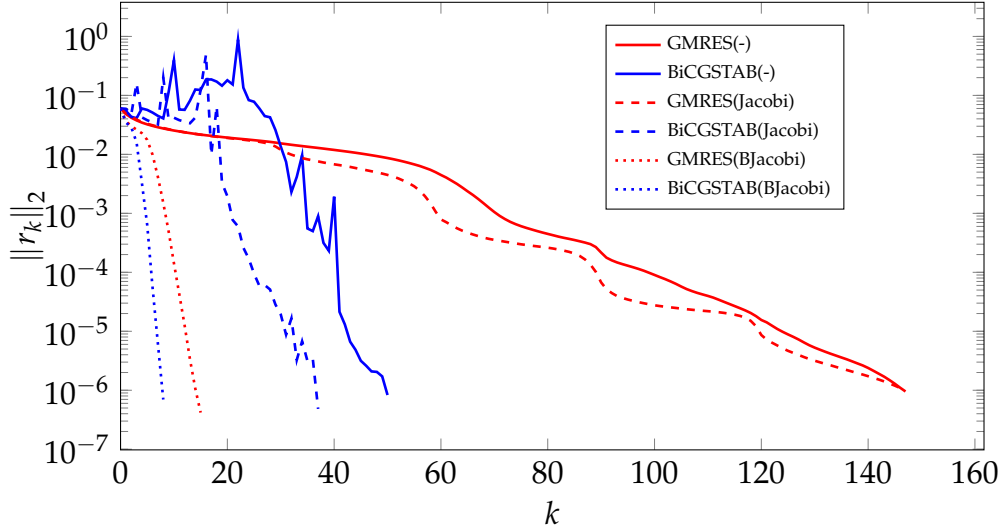
Figure 4.5: Logarithmic convergence history for the GMRES and the BiCGSTAB methods used for solving the transparent medium problem without reflection, test 2A. Block Jacobi is abbreviated as BJacobi.
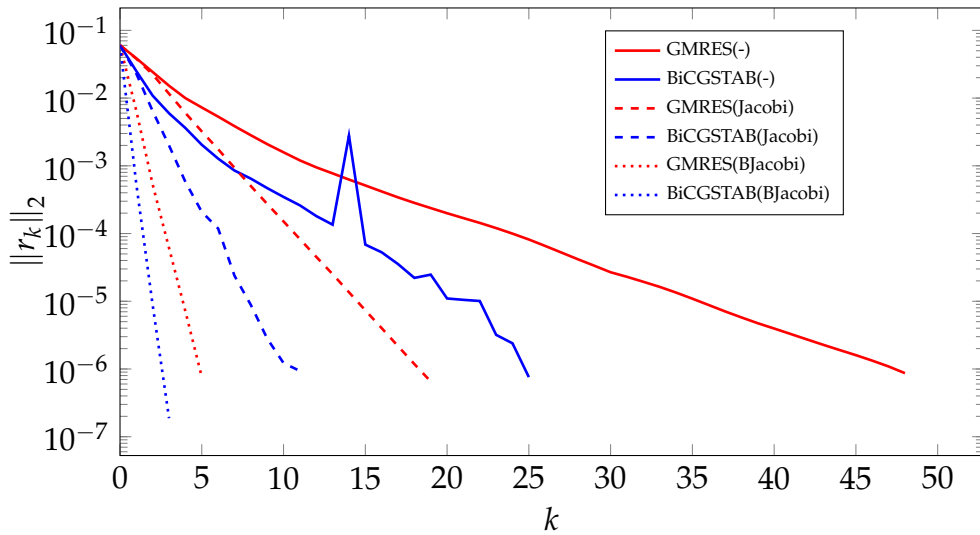
Figure 4.6: Logarithmic convergence history for the GMRES and the BiCGSTAB methods used for solving the absorbing medium problem without reflection, test 2B. Block Jacobi is abbreviated as BJacobi.

In all convergence history plots, it is clear that both Jacobi and block Jacobi preconditioners reduce the total iteration counts for both Krylov subspace methods. It
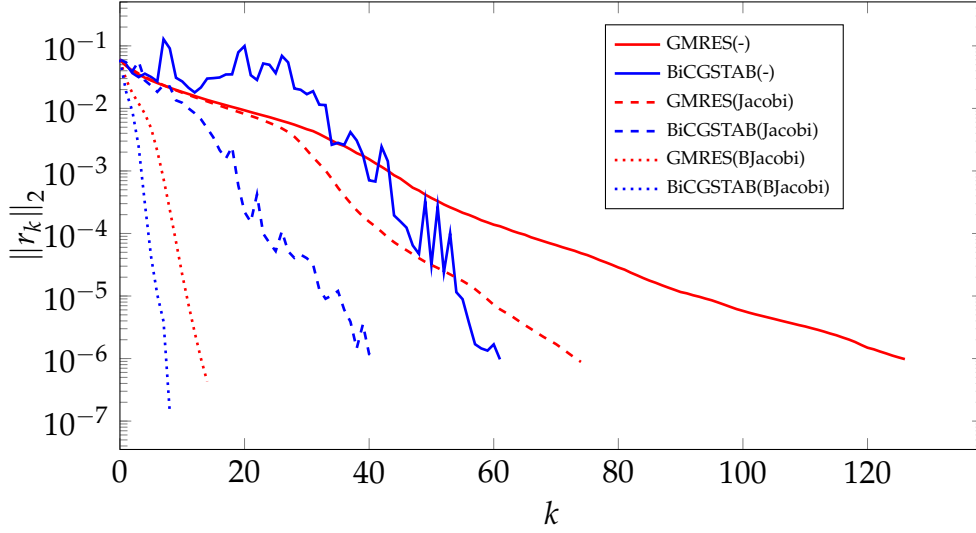
Figure 4.7: Logarithmic convergence history for the GMRES and the BiCGSTAB methods used for solving the scattering medium problem without reflection, test 2C. Block Jacobi is abbreviated as BJacobi.
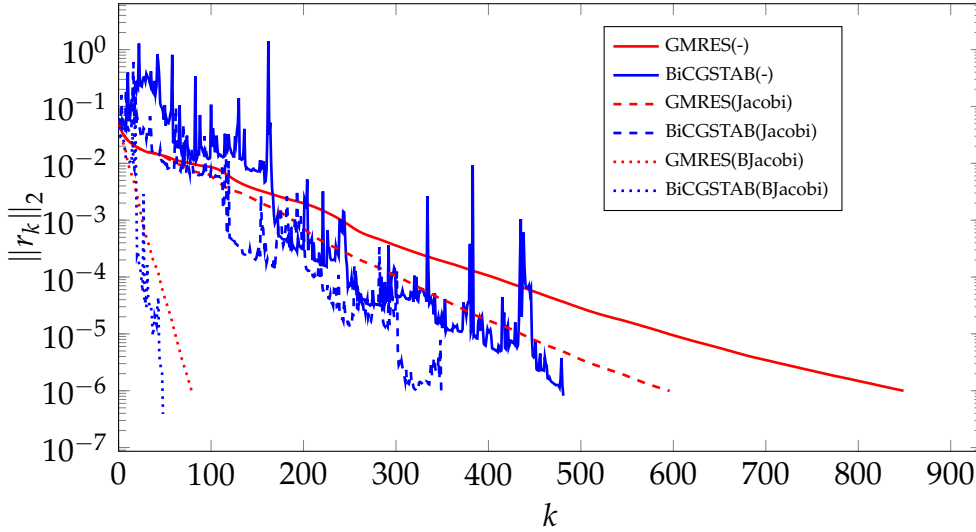
Figure 4.8: Logarithmic convergence history for the GMRES and the BiCGSTAB methods used for solving the transparent problem with reflection, test 2D. Block Jacobi is abbreviated as BJacobi.
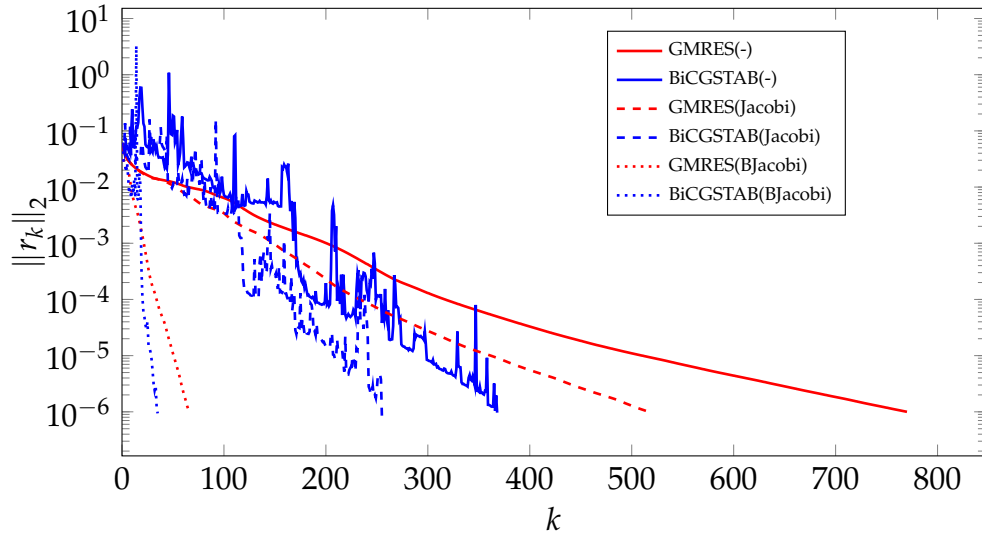
Figure 4.9: Logarithmic convergence history for the GMRES and the BiCGSTAB methods used for solving the scattering medium problem with reflection, test 2E. Block Jacobi is abbreviated as BJacobi.

can also be observed that preconditioning in case of the BiCGSTAB not only leads to faster convergences but also stabilizes the method.

In table 4.3 we provide the total number of iterations to converge k_c and the respective times to solution t_s for tests 2A to 2E. The reported times t_s correspond to the time spent in setting up the preconditioner plus the time spent for reaching convergence. The table displays that much more work is required for solving the problems involving reflection. All expect one result are adhering to the eigenvalue analysis carried out in the previous section. The result that does not agree with the previous eigenvalue analysis is the transparent case with reflection, test 2D. The higher iteration count (compared to other tests in this subsection), may mean that this test has a worst eigenspectrum distribution than the others. While this was not the case for the cubic-shaped test case. We observed such a behavior because, unlike the cubic-shaped media that has six unique normals, the berlingot-shaped media has 455 unique normals at the boundary (mesh dependent). Because of the transparency, no resistance is offered to the incoming radiation ($\kappa = \sigma_s \approx 0$), this implies that radiation will remain trapped in the medium for a longer period and each time it hits any surface different directions (intensities I_m) get coupled with each other. Hence, the coupling is arbitrary and much more complex compared to the cubic-shaped reflection cases.

Overall, in this subsection, the BiCGSTAB was seen to outrun the GMRES,

Test	GMRES						BiCGSTAB					
	None		Jacobi		BJacobi		None		Jacobi		BJacobi	
	k_c	t_s	k_c	t_s	k_c	t_s	k_c	t_s	k_c	t_s	k_c	t_s
2A	147	88.1	147	84.17	15	9.2	50	56.5	37	41.6	8	9.8
2B	48	34.5	19	10.9	5	4.0	25	27.3	11	6.0	3	2.0
2C	126	70.8	74	60.1	14	8.1	61	50.7	41	44.9	9	4.0
2D	849	496.10	596	366.47	79	45.1	481	369.7	349	260.4	48	41.01
2E	770	445.6	517	292.2	66	57.1	368	310.4	255	200.8	35	34.01

Table 4.3: Performance in terms of iterations to converge (k_c) and solving time (t_s, in seconds), for the GMRES and the BiCGSTAB with/without preconditioners.

for solving different problems of radiation, in terms of convergence rates, total solving times, and memory requirements.

4.4 Conclusion

This chapter was dedicated to the analysis of Krylov subspace methods for solving different multi-dimensional radiative transfer problems. The linear systems for these different multi-dimensional radiative transfer problems were built following the angular decomposition (with vectorial finite elements) discretization of the discrete ordinates radiative transfer equation.

Based on different physics, radiation in transparent, absorbing, scattering, and reflecting media were analyzed. An eigenspectrum analysis was set up on these different problems in order to study the effect of each physics on the condition number of the problem. It is concluded that: absorbing/transparent media problems are well conditioned with low value of condition numbers, including scattering increases the condition number of the discretized system, condition numbers for absorbing media with reflecting surfaces do not change, and conditioning deteriorates heavily (highest value of condition number) when reflection is involved within transparent/scattering medium problems.

Two Krylov subspace solvers, the GMRES and the BiCGSTAB, with and

without preconditioning, were investigated for solving the above mentioned radiative transfer problems. In conclusion, the BiCGSTAB outran the GMRES for all cases, with lower iteration count, solving times, and memory requirements. However, typical to the BiCGSTAB, erratic convergences were sometimes observed in comparison to the smooth convergence curves for the GMRES. These erratic behaviors were more prominent for the cases with reflecting media. Concerning preconditioners, as expected, it was established that preconditioning systems with the block Jacobi method (with incomplete LU factorizations with zero level of fill-in as block solvers) leads to faster convergence. Moreover, preconditioning also reduced drastically the outbursts of the BiCGSTAB.

CHAPTER

5

APPLICATION

P revious chapters were dedicated towards description and development of the vectorial FEM for solving the RTE. In the current chapter some numerical experiments will be conducted for analyzing some complex large scale problems of radiative transfer. However, before that, the proposed strategy is verified and validated, both numerically and experimentally.

5.1   Numerical verification and validation tests

In order to use the proposed vectorial FEM to predict outcomes from previously unforeseen situations in radiative transfer, it is important to build trust in the methods reliability. In other words, it is important to validate and verify the proposed method. This can be done by asserting whether the vectorial FEM is able to reproduce analytical or experimental observations for certain radiative transfer problems. Another way is to compare against results of certain benchmark problems solved with other numerical tools, hence performing cross-validation. Before progressing further, let us interpret what validation and verification means in the context of numerical modeling. Assuming the mathematical model for a given physics is accurate, *verification* investigate if an accurate numerical solution to the given mathematical model can be obtained via the numerical method which is being verified. By the process of verification the order of accuracy for the numerical methods can also be calculated. Whereas *validation* asserts if an appropriate mathematical model has been chosen to describe the physical

phenomenon. More elaborate discussions on the process of validation and verification of numerical tools can be found in [193].

5.1.1 Verification tests with the method of manufactured solutions

The best possibility for verifying a numerical tool is to choose a problem that has an exact analytical solution and use this exact solution as a benchmark. However, for the RTE, analytical solutions do not exist when one considers emitting, absorbing, and scattering media (semi-transparent) with complex boundary conditions. To salvage verification process for scenarios like this, one turns to the method of manufactured solutions. The method of manufactured solutions is used by many numerical communities for solver (code) verification, see for example [194, 195]. Concerning the RTE solvers, studies such as [35, 130, 196, 197] used the method of manufactured solutions for solver verification.

In the method of manufactured solutions, we start with an assumed explicit expression for the solution field (manufactured solution). Then, the solution is substituted in the concerned PDE model. This leads to a consistent set of source terms and/or initial conditions and/or boundary conditions. These terms are then used to solve the equation numerically, with the method (solver) that needs to be verified. Finally, by analyzing the error between the numerical solution and the assumed solution, one can verify if the numerical method works. In addition, by analyzing how the error decreases when finer numerical discretization is considered, one can obtain the order of convergence for the numerical method.

5.1.1.1 Test 1: two-dimensional case

The proposed vectorial FEM approach for solving the RTE depends on two discretizations: the DOM and the vectorial SUPG-FEM. Since dual discretization is followed, both angular and spatial discretizations should be verified.

Let us assume a hypothetical participating medium with interdependent radiative properties $\sigma_s = 2\kappa$. The anisotropic phase function $\Phi(s, s')$ for the medium is given by the expression

$$\Phi(s, s') = \frac{1}{2\pi} \frac{2 + s \cdot s'}{2}. \tag{5.1}$$

Let us further assume the exact radiative intensity is given by,

$$\widehat{I}(x) = 1 + \sin(2\kappa \pi x) \sin(2\sigma_s \pi y). \tag{5.2}$$
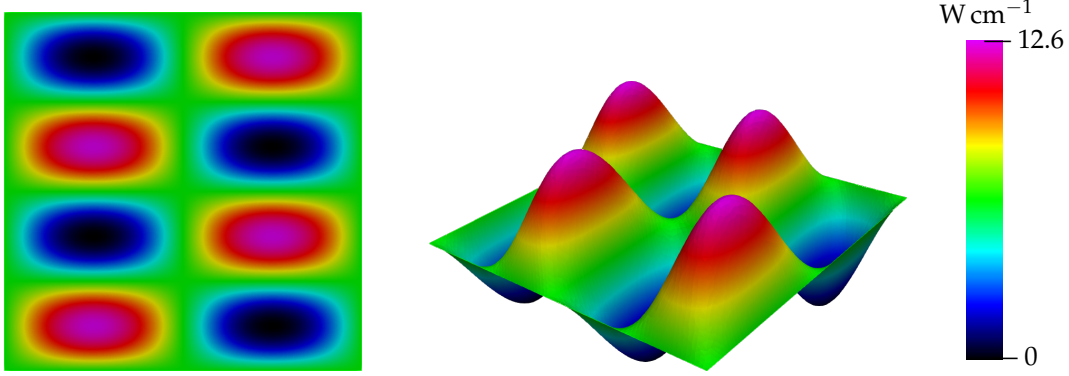
Figure 5.1: Manufactured radiative density field $\widehat{G}(x)$. Left: simple 2D view of the density field, and right: warped density field.

The verification is based on the exact radiative density $\widehat{G}(x)$ (in other words the explicit manufactured solution), given by

$$\widehat{G}(x) = \oint_{\mathcal{S}} \widehat{I}(x) \, ds = 2\pi\big(1 + \sin(2\kappa\pi x)\sin(2\sigma_s\pi y)\big) \tag{5.3}$$

This equation (5.3) is our manufactured solution (exact radiative density).

The corresponding source term is next determined by substituting equation (5.2) into the RTE (1.18) and then following some mathematical simplifications, so that,

$$\kappa I_b(x) = \cos(\theta)2\kappa\pi\cos(2\kappa\pi x)\sin(2\sigma_s\pi y) + \sin(\theta)2\sigma_s\pi\sin(2\kappa\pi x)\cos(2\sigma_s\pi y)$$
$$+ \kappa(1 + \sin(2\kappa\pi x)\sin(2\sigma_s\pi y)). \tag{5.4}$$

-	coarsest	coarse	fine	finest
Spatial mesh				
N_v	162	551	2037	7,931
N_e	278	1,016	3,908	15,536
h_x	0.08	0.04	0.02	0.01
Angular mesh				
N_d	4	8	16	32
h_s	1.57	0.78	0.39	0.19

Table 5.1: Angular and spatial mesh characteristics. h_s denotes the size of the angular mesh which is in fact the average weight of the unit-sphere discretization. With each refinement the spatial and angular mesh sizes are halved.

With the given source term (equation (5.4)), the RTE can now be solved numerically by using the proposed vectorial FEM. With the numerically obtained intensities, the numerical radiative density $G(x)$ is calculated next. Assuming the domain of interest to be a unit centimeteric square, with given $\kappa = 1$ cm^{-1} and $\sigma_s = 2$ cm^{-1}, the exact density field has been shown in the figure 5.1. The RTE was solved numerically several times for four levels of angular and spatial meshes. Table 5.1 summarizes some characteristics about these meshes. Further, to avoid numerical error discrepancies from the linear solver, the GMRES was stopped when the relative unpreconditioned residual was lower than 10^{-13}.

Starting from the coarsest discretizations with each simulation the spatial or/and angular mesh was refined. After each simulation, the error for the numerical density was calculated. For calculating the error of discretization against the exact radiative density, the $L_2(\Omega^h)$ relative error norm $e(G)$ was used. This error is defined as

$$e(G) = \frac{||G - \widehat{G}||_{L_2(\Omega^h)}}{||\widehat{G}||_{L_2(\Omega^h)}} \quad \text{with} \quad ||G||_{L_2(\Omega^h)} = \left(\int_{\Omega^h} G^2(x) \, dx \right)^{1/2}. \quad (5.5)$$
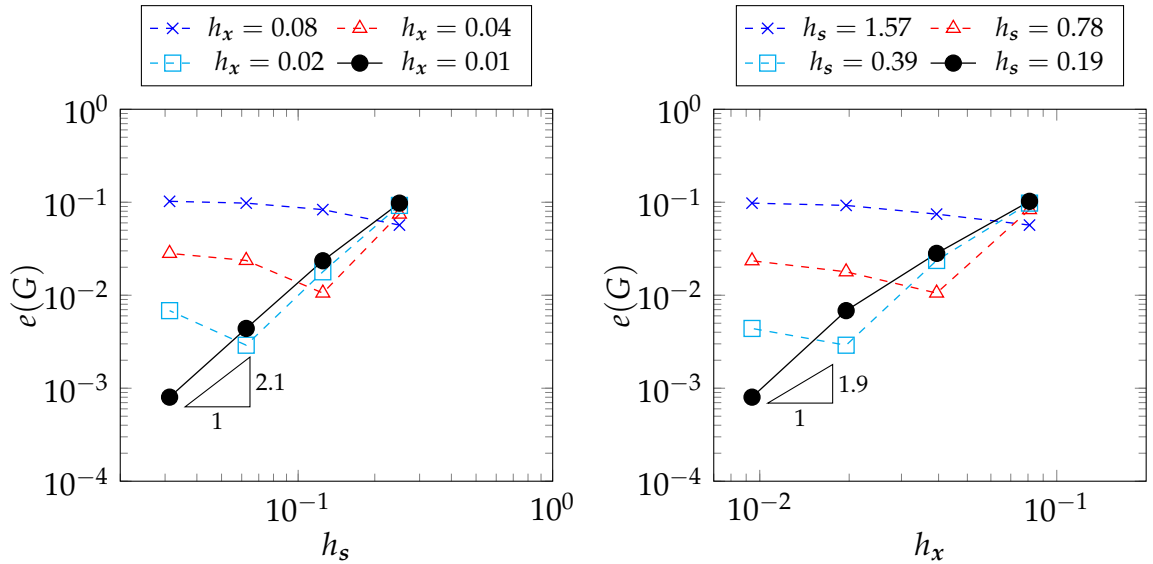
(a) Convergence for angular discretization. (b) Convergence for spatial discretization.

Figure 5.2: Error $e(G)$ on radiative density: comparing the manufactured exact solution to the numerically solved one.

The error $e(G)$ plotted against angular and spatial mesh refinements is presented in figure 5.2. The effect of uniform angular mesh refinement in figure 5.2a

shows that the chosen angular discretization is second order accurate (2.1 to be precise, see figure 5.2a), for the error on the radiative density $e(G)$. Using spatial mesh refinement, spatial discretization was also found out to be almost second order accurate (1.9 to be precise, see figure 5.2b), for the same error on the radiative density. Similar orders of convergence have been reported in [130]. Also note in the figure that such convergences were only obtained with fine spatial and angular meshes. For other cases involving coarse meshes, we observed convergence plateaus, also observed in [78, 86]. Thus, it is best to combine fine meshes for both angles and space to achieve low numerical errors.

5.1.1.2 Test 2: two- and three-dimensional case

A second verification test based on the method of manufactured solutions is performed in order to build further trust on the reliability of results obtained via the vectorial FEM. Moreover, the tests in this subsection are performed in two and three dimensions.

The manufactured radiative intensity for the two tests in this subsection reads

$$\widehat{I}(\boldsymbol{x}) = e^{-a(x+y+z)}(1 + b\cos\theta), \tag{5.6}$$

where a and b are constants dependent on radiative properties, given by $a = \kappa/3$ and $b = \kappa/(\kappa + 6\sigma_s)$ for the 3D test and $a = \kappa/6$ and $b = \kappa/(6\sigma_s)$ for the 2D test. Further, in 2D the coordinate z is chosen to be zero. These particular tests were originally proposed in Gao et al. [35], and later reused in Le Hardy et al. [130].

The manufactured radiative density is constructed by substituting equation (5.6) into equation (5.3) and performing the angular integration:

$$\widehat{G}(\boldsymbol{x}) = \oint_{\mathcal{S}} \widehat{I}(\boldsymbol{x}) \, \mathrm{d}\boldsymbol{s} = \begin{cases} 4\pi e^{-a(x+y)} & \text{in 2D,} \\ 4\pi e^{-a(x+y+z)} & \text{in 3D.} \end{cases} \tag{5.7}$$

An homogeneous participating medium is assumed, with in-scattering being controlled by the anisotropic phase function given by

$$\Phi(\boldsymbol{s}, \boldsymbol{s}') = \begin{cases} \dfrac{1}{2\pi}\dfrac{2 + \boldsymbol{s} \cdot \boldsymbol{s}'}{2} & \text{in 2D,} \\[2ex] \dfrac{3}{16\pi}\dfrac{2 + \boldsymbol{s} \cdot \boldsymbol{s}'}{2} & \text{in 3D.} \end{cases} \tag{5.8}$$

Substituting the manufactured radiative intensities from equation (5.6) in the RTE (1.18), and following mathematical simplifications:

$$\kappa I_b = \{(\kappa - a\sin\theta\cos\phi - a\sin\theta\sin\phi)(1 + b\cos\theta)$$
$$+ \frac{3}{4}\sigma_s b\cos\theta\}e^{-a(x+y)} \quad \text{for 2D test,} \tag{5.9}$$

$$\kappa I_b = \{(\kappa - a\sin\theta\cos\phi - a\sin\theta\sin\phi - a\cos\theta)(1 + b\cos\theta)$$
$$+ \frac{1}{2}\sigma_s b\cos\theta\}e^{-a(x+y+z)} \quad \text{for 3D test.} \tag{5.10}$$

Equations (5.9) and (5.10) are the mathematical manufactured source terms. Using these source terms, the RTE is again numerically solved using the vectorial FEM. In 2D, a unit centimeteric square enclosure forms the domain of interest, while a cubic enclosure with side length 1 cm is assumed in 3D. Again, the discretization error based on the L_2-norm is evaluated to express the vectorial FEM accuracy and efficiency, equation (5.5).
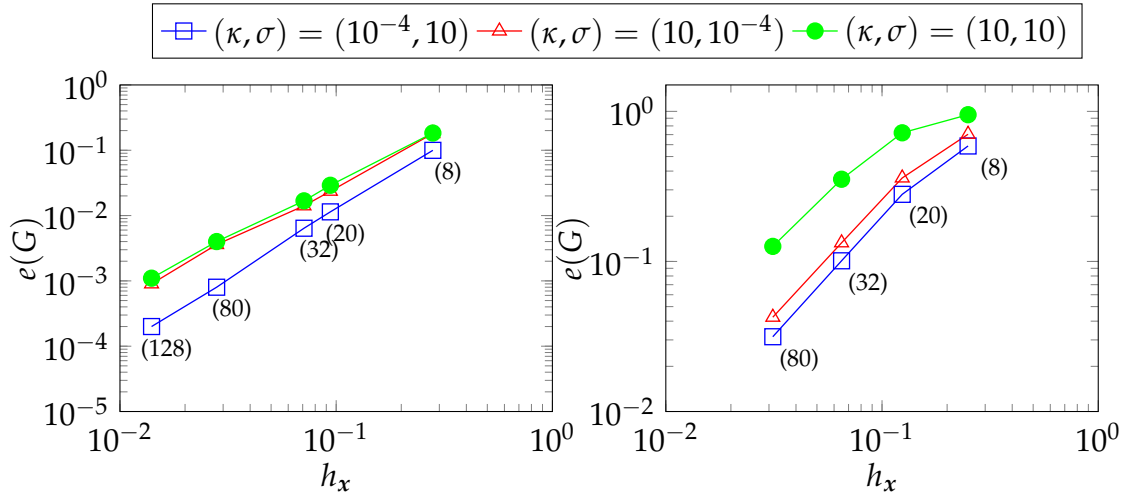
Figure 5.3: Spatio-angular mesh convergence for the vectorial FEM. Left: 2D test, right: 3D test. The numbers in the braces are the number of directions N_d used for each test.

The decrease of $e(G)$ while refining the spatial and angular meshes simultaneously again proves that the vectorial FEM solution tends towards the exact solution with each refinement. This decrease in errors is plotted in figure 5.3. Note that for the tests in this subsection the spatial and angular meshes are simultaneously refined, contrary to tests in the previous subsection. This is done in order to avoid the convergence

(a) Exact solution. (b) Vectorial FEM solution.
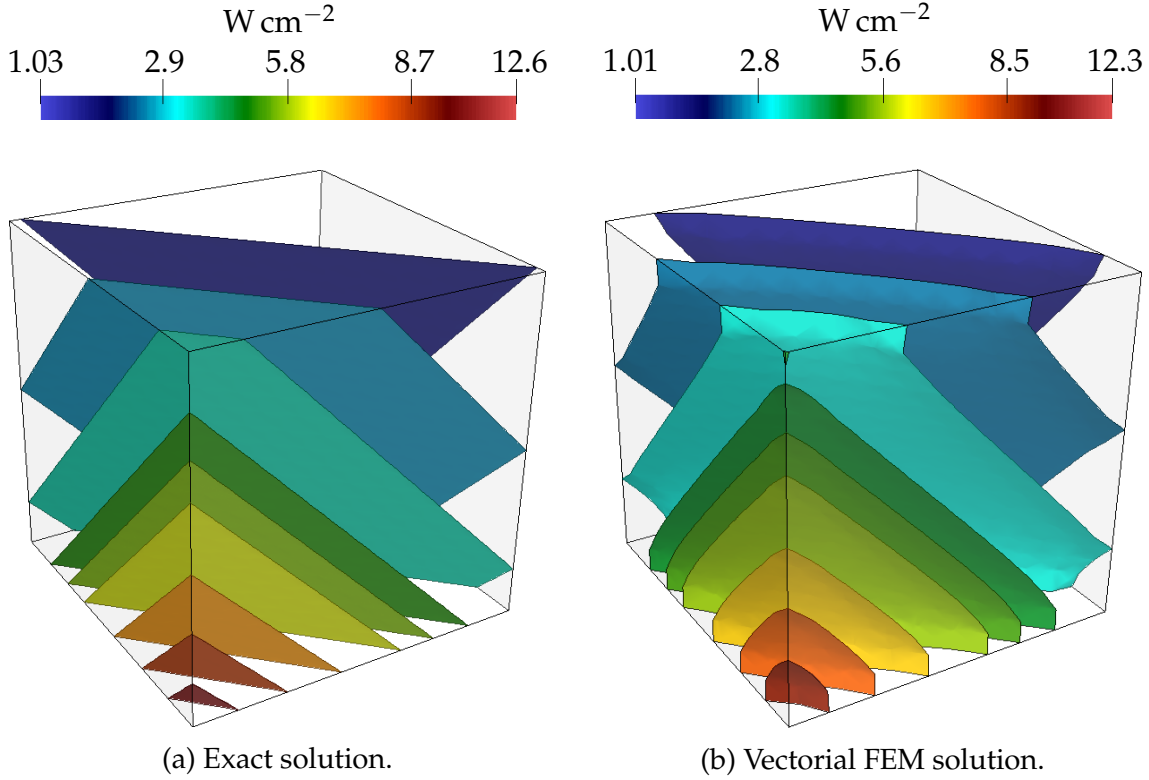
Figure 5.4: Comparing the 3D exact and vectorial FEM ($h_x = 0.125$, $N_d = 20$) radiative density contours within the medium, with radiative properties $(\kappa, \sigma_s) = (10^{-4} \text{ cm}^{-1}, 10 \text{ cm}^{-1})$.

plateaus observed previously and to avoid the ray effect and the false scattering interactions which could have degraded the solutions [88, 89]. The simulations refinement lets us judge the convergence rates for the combined spatio-angular discretization.

Curve fit to the error plots in figure 5.3 again reveals second-order convergence rates for both tests. For angular mesh refinements, alternate meshes between octahedral and icosahedral refinements were used. Thus, the tests were performed using 8, 20, 32, and 80 directions.

To assert the robustness of the proposed method further, the verification was performed for different values of κ and σ_s spanning five orders of magnitude, from 10^{-4} cm^{-1} to 10 cm^{-1}. The different sets of chosen (κ, σ_s) were $(10^{-4}, 10)$, $(10, 10^{-4})$, and $(10, 10)$, all these properties being expressed in cm^{-1}. All of these tests again reported second-order convergence. In figure 5.4, the radiative density contours for the exact and coarse spatio-angular ($h_x = 0.125$, $N_d = 20$) three-dimensional numerical solution from the vectorial FEM have been presented.

To summarize, the method of manufactured solutions verification tests, it is concluded that a reliable solution can be obtained using the vectorial FEM by choosing an appropriate spatio-angular mesh resolution.

5.1.2 Cross-validation test with a benchmark from literature

In this subsection we cross-validate the vectorial FEM solution procedure to some reference solutions available in the literature. The test consists of a two-dimensional unit square enclosure with black walls. The emissive power of the top wall is 1, while other walls have zero emissivity The considered medium is non-absorbing, non-emitting, and isotropically scattering with $\sigma_s = 1$ cm^{-1}. This particular problem is difficult to solve as it is known to enhance errors caused due to ray effect and false scattering, cf. [89, 88].

To compute the solution, while minimizing the ray effects and false scattering interactions, a fine angular discretization from the third refinement of octahedron ($2 \times 256 = 512$ directions) and a fine unstructured spatial mesh with 12,560 nodes were used. Figure 5.5a presents the density distribution $G(\boldsymbol{x})$ inside the medium and figure 5.5b presents the incident radiative heat flux $Q_r^+(\boldsymbol{x}_w)$ plotted on the bottom wall of the medium. Additionally, in figure 5.5b, the proposed vectorial FEM solution is compared to two reference solutions. The first reference solution is a quasi-exact solution presented by Crosbie et al. [198], who used an approach based on removing the singularity from the integral form of the RTE to solve this particular test case. The second reference solution is the one presented by Coelho [89], who used the modified DOM-FVM (MDOM-FVM) method to solve this problem. Apart from the presented reference solutions, this particular test has also been solved using the FEM-FVM [84], the unstructured FVM [99], and the angular FEM [85], to cite but a few.

The considered medium within the enclosure being scattering, figure 5.5a shows the diffusion (scattering) of radiation from the top wall towards other parts of the medium. From figure 5.5b it can be clearly observed that the proposed vectorial FEM solution is in good agreement with both the quasi-exact and the MDOM-FVM reference solutions. Note, the slight oscillations observed in figure 5.5b are classical to this test case, and are caused due to the ray effect and the false scattering interactions.

(a) Density field distribution.

(b) Radiative heat flux on the bottom wall.
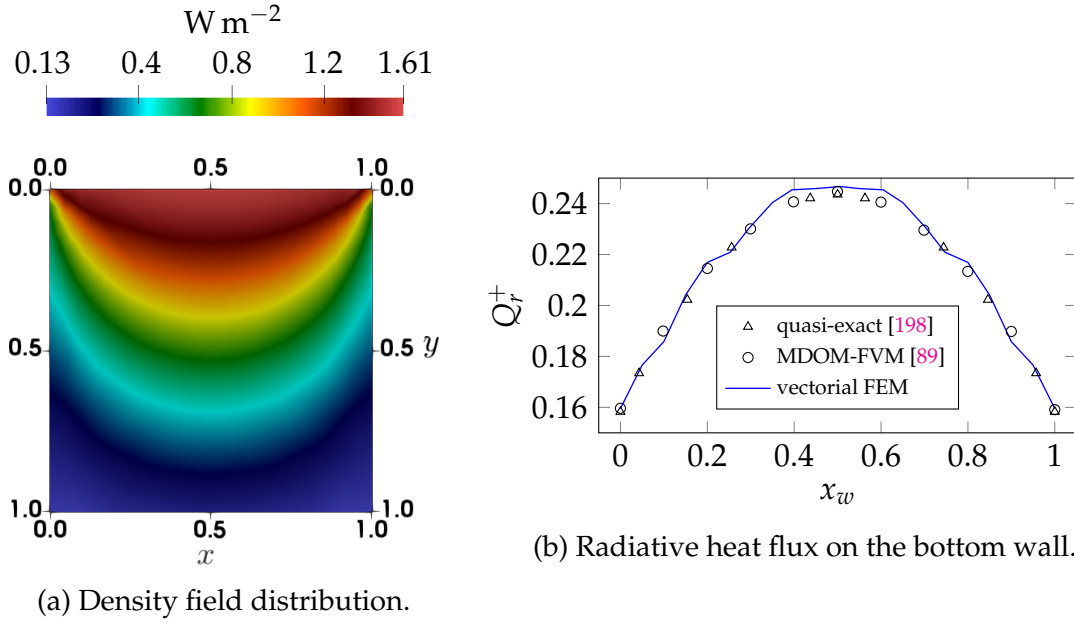
Figure 5.5: Comparison of vectorial FEM solution to other reference solutions.

5.1.3 Validation by using the Monte–Carlo reference solutions

Another approach to validate a numerical tool is to compare simulation results with experimental data. In radiative transfer, in the absence of experimental data the results from Monte–Carlo simulations are often used for validation, we can call them pseudo-experimental data. The Monte–Carlo simulations replicate all elementary level physical processes of radiation, hence, these are often used as reference. Comparing the vectorial FEM solutions to the Monte–Carlo simulations, we are in fact combining validation and verification in one step, this is sometimes called *qualification*. A good match between the numerical solutions obtained via the proposed vectorial FEM against the Monte–Carlo reference data should vouch for the validity of the proposed model.

The Monte–Carlo solver used in the tests to follow is an in-house FORTRAN based solver developed during the masters thesis of Ms. Ketaki Mishra [199]. This solver is capable of solving radiative exchanges within participating media for square and cubic enclosures. The integrated scalar quantities of transmittance T_{NH} and reflectance R_{NH} (normal hemispheric) are chosen for comparing the vectorial FEM to the Monte–Carlo method. Without doubt the Monte–Carlo method is one of the most powerful methods to calculate the chosen integrated quantities.

Let us first define T_{NH} and R_{NH}. Consider an incident photon flux traveling in s_0 and entering an enclosure from the boundary $\partial \Omega_0$ with normal vector n_0. The

109

normal hemispheric transmittance and reflectance are calculated on boundary $\partial\Omega_1$ with normal $\boldsymbol{n}_1$, and the expressions for T_{NH} and R_{NH} read:

$$T_{\mathrm{NH}} = \frac{\displaystyle\int_{\partial\Omega_1} Q_r^-(\boldsymbol{x})\,\mathrm{d}\boldsymbol{x}}{\displaystyle\int_{\partial\Omega_0} Q_r^+(\boldsymbol{x})\,\mathrm{d}\boldsymbol{x}}, \qquad R_{\mathrm{NH}} = \frac{\displaystyle\int_{\partial\Omega_0} Q_r^-(\boldsymbol{x})\,\mathrm{d}\boldsymbol{x}}{\displaystyle\int_{\partial\Omega_0} Q_r^+(\boldsymbol{x})\,\mathrm{d}\boldsymbol{x}} + \rho^s(\boldsymbol{s}_0,\boldsymbol{n}_0). \tag{5.11}$$

here, Q_r^- and Q_r^+ are the radiative heat influx and efflux, defined in equations (1.6) and (1.7).

Further the Monte–Carlo method calculates the normal hemispheric transmittance and reflectance $T_{\mathrm{NH}}^{\mathrm{MC}}$ and $R_{\mathrm{NH}}^{\mathrm{MC}}$ as

$$\begin{aligned} T_{\mathrm{NH}}^{\mathrm{MC}} &= \frac{\text{Number of photons exiting the boundary } \partial\Omega_1}{\text{Number of photons entering in from the boundary } \partial\Omega_0} = \frac{N_{P-T}}{N_{P-E}}, \\ R_{\mathrm{NH}}^{\mathrm{MC}} &= \frac{\text{Number of photons reflected from the boundary } \partial\Omega_1}{\text{Number of photons entering in from the boundary } \partial\Omega_0} = \frac{N_{P-R}}{N_{P-E}}. \end{aligned} \tag{5.12}$$

here, N_{P-E}, N_{P-T}, and N_{P-R} are the total number of photons emitted, transmitted, and reflected respectively. While N_{P-T} and N_{P-R} are photon counts at enclosure surface $\partial\Omega_1$, N_{P-E} is the photon count at $\partial\Omega_0$.

For the vectorial FEM T_{NH} and R_{NH} are calculated again using the discrete ordinates philosophy of replacing the integrals by weighted summation:

$$\begin{aligned} T_{\mathrm{NH}}^{\mathrm{DOM\text{-}FEM}} &= \frac{\sum_{m=1}^{N_d} \displaystyle\int_{\substack{\partial\Omega_1 \\ \boldsymbol{s}_m\cdot\boldsymbol{n}_1>0}} I_m(\boldsymbol{x})\boldsymbol{s}_m\cdot\boldsymbol{n}_1\,\mathrm{d}\boldsymbol{x}}{|\boldsymbol{s}_0\cdot\boldsymbol{n}_0|\displaystyle\int_{\partial\Omega_0} I_{\mathrm{in}}(\boldsymbol{x})\,\mathrm{d}\boldsymbol{x}}, \\[2em] R_{\mathrm{NH}}^{\mathrm{DOM\text{-}FEM}} &= \frac{\sum_{m=1}^{N_d} \displaystyle\int_{\substack{\partial\Omega_0 \\ \boldsymbol{s}_m\cdot\boldsymbol{n}_0>0}} I_m(\boldsymbol{x})\boldsymbol{s}_m\cdot\boldsymbol{n}_1\,\mathrm{d}\boldsymbol{x}}{|\boldsymbol{s}_0\cdot\boldsymbol{n}_0|\displaystyle\int_{\partial\Omega_0} I_{\mathrm{in}}(\boldsymbol{x})\,\mathrm{d}\boldsymbol{x}} + \rho^s(\boldsymbol{s}_0\cdot\boldsymbol{n}_0). \end{aligned} \tag{5.13}$$

Note that such validation has already been performed in the PhD thesis [22] for validation of the standard FEM DOM solver, here, however, the tests are performed to validate the vectorial solver.

The first validation test performed is for a two-dimensional absorbing and isotropically scattering media. The system consists of a square medium 2×2 cm^2
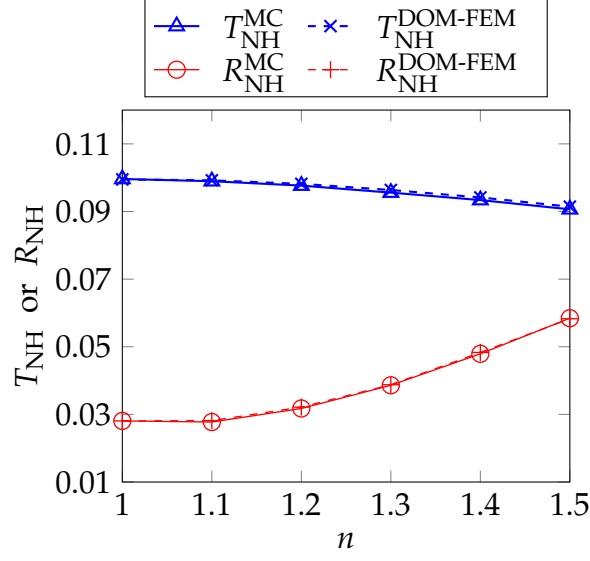
Figure 5.6: Normal hemispherical transmittance and reflectance for 2D test cases with $(\kappa, \sigma) = (1.0, 0.2)$ cm^{-1} and $n \in [1, 1.5]$.

and bounded within specularly reflecting walls. The absorption and the scattering coefficients of the medium are given by $(\kappa, \sigma_s) = (1$ cm$^{-1}, 0.2$ cm$^{-1})$. Further six simulation runs are compared, for each run specular reflectivity power of the boundary is changed, i.e., for the wall $\partial \Omega_1$ the index of refraction n is increased form 1 to 1.5 with an increment of 0.1. For the Monte-Carlo runs, 1 million photos are launched and bombarded onto the wall $\partial \Omega_0$ in $s_0 = [1, 0, 0]$. And for the vectorial FEM runs a fine angular and spatial mesh $(N_d, N_v) = (40, 6500)$ has been used.

Figure 5.6 presents the comparative plots for transmittance and reflectance against changing refractive index. We observe a good agreement between the Monte–Carlo and the proposed vectorial FEM. To quantify, the maximum difference observed in reflectance is 7.79×10^{-4} and that in transmittance is 3.94×10^{-4}. For another two-dimensional case with $(n, \kappa, \sigma_s) = (1.4, 1.0$ cm$^{-1}, 1.0$ cm$^{-1})$, the Monte-Carlo simulation compared to the vectorial FEM reported maximum differences in reflectance and transmittance as 5.82×10^{-5} and 9.13×10^{-5}, respectively.

Next, comparative tests in three dimensional media are performed. The domain of interest is now a cube with 1 cm side lengths. In the first set of tests the index of refraction $n \in [1, 3]$, and $(\kappa, \sigma) = (0.5$ cm$^{-1}, 1$ cm$^{-1})$. Again a million photons are used for the Monte–Carlo run, and for running the vectorial FEM, $(N_d, N_v) = (80, 20000)$. The results obtained for this test are plotted in figure 5.7a. Further, another

(a) Test with $(\kappa, \sigma_s) = (1 \text{ cm}^{-1}, 0.2 \text{ cm}^{-1})$, and $n \in [1, 3]$.

(b) Test with $(\kappa, n) = (0.5 \text{ cm}^{-1}, 1.4)$, and $\sigma_s \in [0, 2] \text{ cm}^{-1}$.
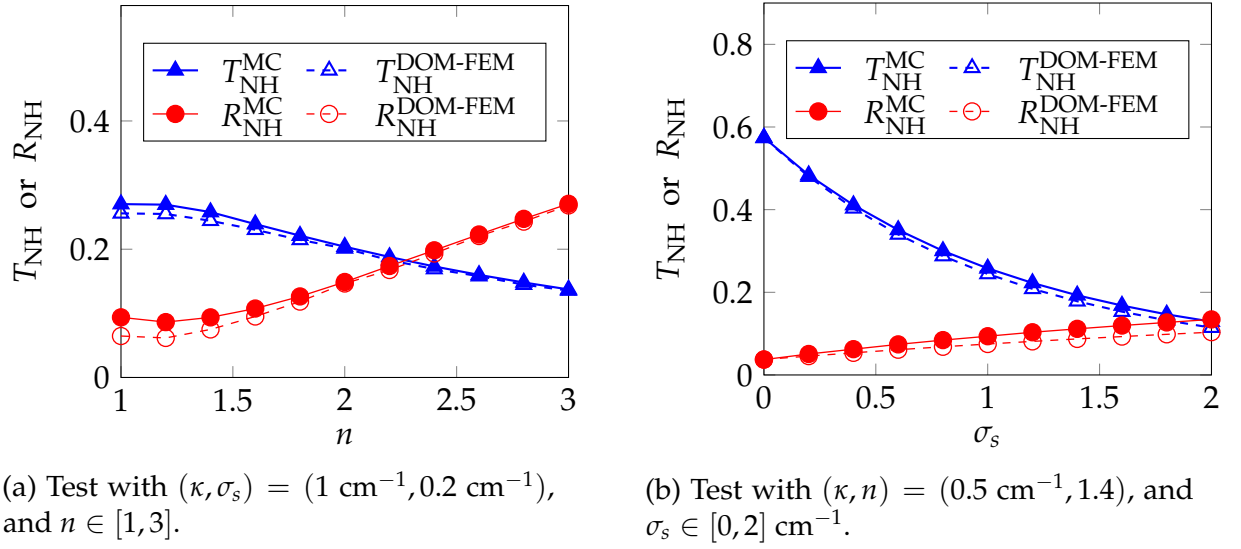
Figure 5.7: Normal hemispheric transmittance and reflectance for 3D test cases.

set of tests is performed for the same cubic geometry, this time however, $n = 1.5$, $\kappa = 0.5 \text{ cm}^{-1}$, and $\sigma_s \in [0, 2] \text{ cm}^{-1}$. The results obtained for this test are plotted in figure 5.7b. Again, for both these 3D cases a very good agreement between the Monte–Carlo and the vectorial FEM simulations are observed.

5.1.4 Experimental validation with laser flash experiments

In this subsection we first show how to perform coupling of the proposed vectorial FEM based radiative transfer solver to a FEM based conduction solver. As a validation test for this coupled conductive-radiative solver, we perform the numerical laser flash analysis on semi-transparent media, and compare the results to experimental ones from the literature.

The aim is to reproduce a thermogram (temperature vs. time curve) obtained in a laser flash experimental apparatus [200] for participating media. The laser flash tests are usually performed to determine the thermal diffusivity, the heat capacity, and the effective thermal conductivity of a material. In this method, the front face of a material is irradiated with a collimated laser source which then results in heat transfer in the medium. The change in temperature with time is observed on the back face of the sample, and using this temperature history the radiative properties like the scattering coefficient and the absorption coefficient can also be estimated, cf. [201, 202]. Although in this subsection the numerical flash analysis serves as a validation test case, one could view these tests as a potential application test case for the coupled

solver.

Vast amount of research has been conducted in the past that deals with numerical strategies for solving the coupled conduction and radiation problem of laser flash method. Most of these works involve reduction of the problem with lots of assumptions in order to reduce the complexity and hence the computation time. For example, the use of simplified 1D radiation physics [203], using analytical expressions for approximating the physics of radiation [204], using semi-empirical formulations to solve the combined heat transfer [205], considering the media either totally black or transparent so that optically-thin or optically-thick approximations of radiation can be applied, etc. Using such assumptions may lead to over or under estimation of correct physics. Using the three-flux model for radiative transfer within the flash experiments, Hahan et al. [206] show that classical laser flash measurements may lead to overestimation of thermal parameters for heterogeneous semi-transparent media at high temperatures. The overestimation error was attributed to negligence in considering the right model for radiative contribution. This shows that in the coupled conduction and radiation problem of laser flash analysis, radiative transfer plays a key role. Hence, this particular test is a good contender for validating a radiative transfer solver.

Before carrying out the tests, in the next subsection mathematical preliminaries for coupling the vectorial FEM radiation model to a FEM based conduction model is explained.

5.1.4.1 Coupling heat conduction with the RTE

The transient heat transfer equation including radiation and conduction contributions reads,

$$\rho C_p \frac{\partial T}{\partial t} = -[\nabla \cdot Q_r + \nabla \cdot Q_c],$$ (5.14)

here, $\nabla \cdot Q_c$, $\nabla \cdot Q_r$, ρ, and C_p are the volumetric conductive source, the volumetric radiative source, the material density, and the specific heat for the system, respectively. From the Fourier's law $\nabla \cdot Q_c = \nabla(-k_c \nabla T)$, with k_c being the effective thermal conductivity. The divergence of the radiative flux $\nabla \cdot Q_r$, is the term that couples the heat equation and the RTE. It embeds the complete physics of the radiative transfer. Following [20], the radiative source term can be expressed as

$$\nabla \cdot Q_r = \kappa 4\pi I_b - \kappa G,$$ (5.15)

here, $G = G(x)$ is the radiative density which one gets after solving the RTE and $I_b = I_b(T, \lambda)$ is the black body source term.

To begin the finite element discretization for equation (5.14), we start by multiplying the equation by a test function q^h and further integrating it over the computational domain Ω^h, such that

$$\int_{\Omega^h} \rho C_p \frac{\partial T^h}{\partial t} q^h \, \mathrm{d}x = \int_{\Omega^h} (k_c \Delta T^h) q^h \, \mathrm{d}x - \int_{\Omega^h} \left(\kappa 4\pi I_b - \kappa G \right) q^h \, \mathrm{d}x, \qquad (5.16)$$

here, T^h and q^h are the finite element trial and the test functions, respectively. These are built using the first order Lagrange polynomial basis $\mathbb{P}_1$ over the mesh Ω^h.

To introduce the boundary condition of interest for the flash test analysis, an integration by parts is performed on the first term on the right hand side of equation (5.16). The weak formulation then reads,

$$\int_{\Omega^h} \rho C_p \frac{\partial T^h}{\partial t} q^h \, \mathrm{d}x + \int_{\Omega^h} k_c \nabla T^h \cdot \nabla q^h \, \mathrm{d}x = \int_{\partial \Omega^h} k_c \frac{\partial T^h}{\partial n} q^h \, \mathrm{d}x$$
$$- \int_{\Omega^h} \left(\kappa 4\pi I_b - \kappa G \right) q^h \, \mathrm{d}x. \qquad (5.17)$$

The first order implicit Euler scheme is used to deal with the time derivative. Moreover, at a given time step $N + 1$, the divergence of the flux $\nabla \cdot Q_r$ is calculated with the help of previous T^N, i.e, the temperature at the previous time step N. The weak formulation then reformulates to,

$$\int_{\Omega^h} \left(\frac{T^{N+1}}{\delta t} q + \alpha \nabla T^{N+1} \cdot \nabla q \right) \mathrm{d}x + \int_{\partial \Omega^h} \frac{\alpha h}{k_c} T^{N+1} q \, \mathrm{d}x = \int_{\partial \Omega^h} \frac{\alpha h}{k_c} T_e q \, \mathrm{d}x$$
$$+ \int_{\Omega^h} \left(\frac{T^N}{\delta t} q - (\kappa 4\pi I_b - \kappa G) q \right) \mathrm{d}x, \qquad (5.18)$$

here, $\alpha = k_c / \rho C_p$ and h are the thermal diffusivity coefficient, and convection coefficient, respectively. Further, T_e is the external temperature and δt is the Euler time step for time discretization. Note that the superscript h for trial and test functions in equation (5.18) have been dropped for readability considerations.

In order to build an algorithm that can numerically simulate the laser flash experiment, let us first understand the procedure of laser flash experiment.

- First, the front face of a sample under investigation is irradiated with a collimated laser flash of intensity I_c, for a short pulse duration t_p. The font face is
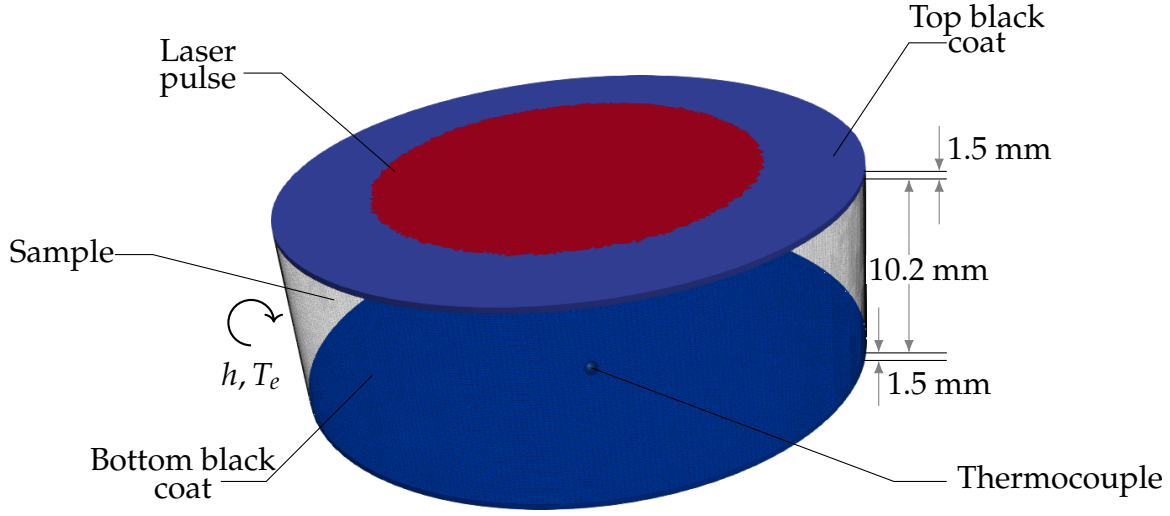
Figure 5.8: Laser flash cylindrical sample with coating (in blue) being irradiated with a flash (in red).

generally coated with a black material (non reflective). The coating has a certain infinitesimal thickness, enough to make sure that it is optically thick to the applied irradiation.

- Naturally, the incident radiation heats up the coating. The heat then starts to flow towards the back face of the sample. These tests take place in a furnace which is held at temperature T_e, since the sample is at local thermal equilibrium with the surroundings the sample is also held at temperature T_e.

- As we are interested in high temperature T_e, both radiation and conduction physics play a key role in the overall heat transfer within the samples bulk. Due to the combined effect of radiation and conduction, there occurs a transfer of energy and hence a non-linear change in temperature across the sample towards the back face.

- from all the outer surfaces of the sample, small amount of convective and radiative loss can be observed.

- Once the heat is transferred across the sample layer the change in temperature on the back face is then measured. Measurements are performed using a thermocouple which is embedded within the back face coat.

Numerically the conductive-radiative transfer coupling is established by solving the heat equation and radiative transfer equation in an iterative manner. Even

---

Algorithm 3: Numerical algorithm for thermogram calculation

---

    input T_e, t_{stop}, t_{p} δt, I_c , properties   ▷ δt-`Euler time step`, t_{stop}-`stopping time`

    load meshes: $\{\Omega_i^h\}_{i=1}^{N_p}$ and $\mathcal{S}^{N_d}$

    define finite element variables: $\mathbb{I}^h$, $\mathbb{W}^h$, T_{N+1}, T_N, T_{nl}, q

    $T_N = T_e$

    for $(t < t_{stop}$: $t = t + \delta t)$ ▷ `this is the time loop`

    do

      | $T_{nl} = T_N$

      | **for** $(i < i_{max} : i = i+1)$ ▷ `this is the nonlinear loop for` T

      | **do**

      | | use Planks law to calculate $I_b = I_b(T_{nl})$ ▷ `equation` (1.8)

      | | **if** $(t \leq t_p)$ **then**

      | | | **solve** RTE with $I_{\text{in}} = I_c$ + source term I_b **return** $\mathbb{I}^h$ ▷ `equation` (3.1)

      | | **end**

      | | **if** $(t > t_p)$ **then**

      | | | **solve** RTE only with source term I_b **return** $\mathbb{I}^h$ ▷ `equation` (3.1)

      | | **end**

      | | using $\mathbb{I}^h$ and I_b calculate $\nabla \cdot Q_r$ ▷ `equation` (5.15)

      | | **solve** conduction equation using T_N and $\nabla \cdot Q_r$ **return** T_{N+1} ▷ `equation` (5.18)

      | | $Er = ||T_{nl} - T_{N+1}||_{\text{inf}}$

      | | $T_{nl} = T_{N+1}$

      | | **if** $(Er < 1.e^{-4})$ **then**

      | | | **break**   ▷ `Nonlinear` T `has converged go to` $t = t + dt$

      | | **end**

      | **end**

      | $T_N = T_{N+1}$

    end

---

though the problem of solving radiative transfer equation has been greatly simplified by using the vectorial FEM, the coupled system is still nonlinear and closed form of solutions are not possible. Hence a non linear iteration loop needs to be setup between the RTE and the heat transfer equation solutions. The full iteration procedure for deriving the total temperature vs. time curve (thermogram) has been reported in algorithm 3.

5.1.4.2   Numerical vs. experimental thermograms for semi-transparent open-cell foams

In this subsection, by using the proposed coupling method from previous subsection, we numerically simulate a laser flash experiment from [201]. This paper experimentally and numerically studied the coupled conductive and radiative heat transfer in

metal and ceramic foams (semi-transparent materials). Although a two dimensional axisymmetric radiative transfer model was use by the authors for solving the radiation, we would however, use full three-dimensional radiative transfer model for solving the radiation physics in the laser flash numerical experiments.

-	ρ	C_p	k_c	σ_s	κ	p
Coat	1000	1200	3.30	0	3000	-
NiCrAl	537	501	0.30	185.3	200.7	93.7
FeCrAl	230	487	0.29	97.4	389.6	96.8

Table 5.2: Thermal properties for the two foam samples and the black coating. The properties are given in the following units: density ρ in $\mathrm{kg\,m^{-3}}$, specific heat C_p in $\mathrm{J\,kg^{-1}\,K^{-1}}$, thermal conductivity k_c in $\mathrm{W\,m^{-1}\,K^{-1}}$, scattering coefficient σ_s in $\mathrm{m^{-1}}$, absorption coefficient κ in $\mathrm{m^{-1}}$, and porosity of the foams p is in %.

The numerical flash analysis for the NiCrAl foam sample and the FeCrAL foam sample was performed at $T_e = 673$ K. The foam sample were cylindrical in shape, with 30 mm diameter and height of 10.2 mm, further the black coating of 3 mm width was used, see figure 5.8. The collimated laser of diameter 2 mm was flashed onto the top surface. For the convective loss outside the furnace convection coefficient of $h = 5.004$ $\mathrm{W\,m^{-2}\,K^{-1}}$. Other physical data pertaining the tests are given in table 5.2. It should be noted that the sample used in these tests have homogenized properties.

Since FEM was used as the standard numerical technique for solving the conduction and the radiation equation, hence we could share the computational grid between the two solvers. Domain decomposition parallelization was used to enhance computational speeds.

Figure 5.9 compares the experimental and the numerical thermograms that were reproduced in this study. It can be observed that the proposed coupled radiative-conductive algorithm is very well able to match the given physics. This validation test is an indication that the radiative source term $\nabla \cdot Q_r$ that depends on solution from the RTE is correctly predicted within the bulk of the media.

Now that the solver has been thoroughly validated and verified in the next section we look into a potential application of the solver.
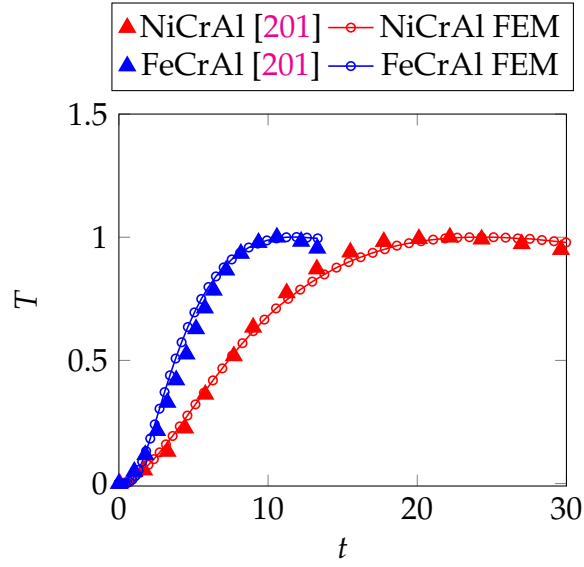
Figure 5.9: Experimental vs. numerical thermogram for a NiCrAl and FeCrAl foams.
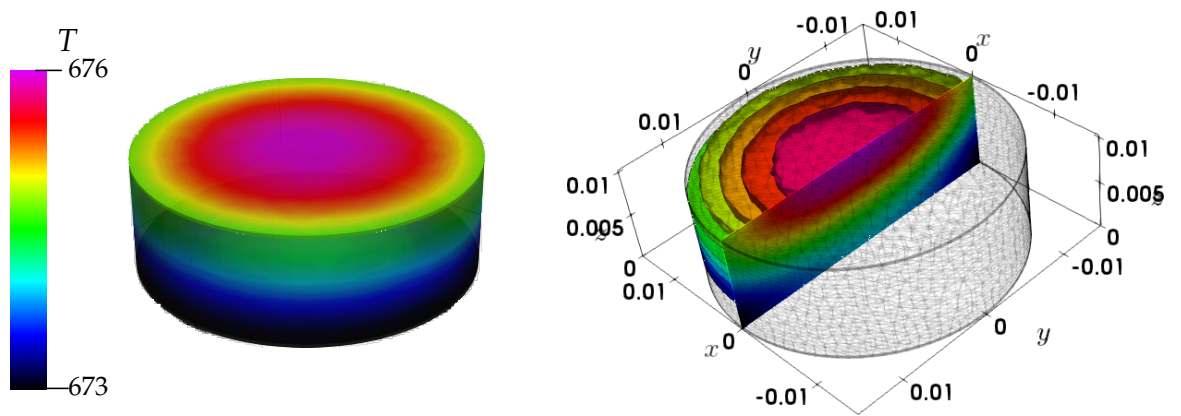
Figure 5.10: Temperature fields for the NiCrAl foam sample under flash. Left: simple isometric view, and right: sliced contours of the temperature field.

5.2 Application test cases: open-cell foam radiation

In several porous media applications, heat transfer via radiation is involved. For instance, porous burners [207], volumetric solar receivers [208], thermo-chemical reactors [209], high temperature heat exchangers [210], etc., are few real world application examples of porous media where the radiative transfer plays a propitious role. Thereby, designing and optimizing such porous systems can be leveraged by appropriate prediction of the radiative fields within the volume of these media. Motivated by this fact, the current section deals with radiative transfer modeling in open-cell foams.
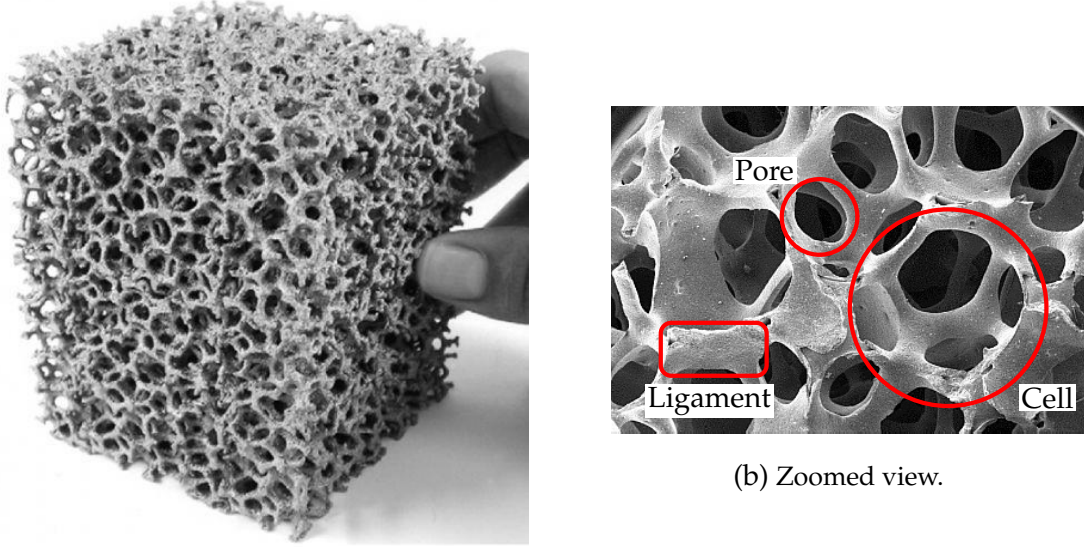
(a) A metallic open cell foam [211].

(b) Zoomed view.

Figure 5.11: Open cell foam example.

An open-cell foam is composed of two phases: the solid phase (ligament network) and the fluid phase (formed by the air spaced between the ligament network, often dubbed as pores), see figure 5.11. Radiative transfer, by definition, is characterized by energy exchange that occurs while a stream of photons traverse through a medium. Since photons have the capability to travel within the solid and fluid phase of the foams, thereby, foam radiation is a complex (topology-wise) bi-phasic radiative transfer problem.

In a numerical framework, conventionally, foam radiation problems are tackled by solving the analytical equations that are formulated after consolidating series of experimental/numerical data. For example, a recent work by Cunsolo et al. [212] proposed some simplified analytical correlations for predicting the extinction coefficient of a foams. Another, conventional approach consists in converting the bi-phasic participating medium to a single phase participating medium, i.e, performing homogenization[1]. The RTE is then solved within a homogenized medium. As such, the RTE is solved with volume averaged radiative properties [214, 215]. One of the primary reasons that motivates the use of these methods is their low computational cost. Moreover, the topological complexity of a real foam problem is also avoided. Undoubtedly, these methods can predict very well the overall radiative transfer behavior for

---

[1]Homogenization can only be performed for a foam sample if the total volume of the foam (pore phase plus the solid phase) is greater than the representative elementary volume [213].

foams (transmittance, absorptance, etc.). However, calculation of exact radiative fields within the foams volume is beyond the capabilities of these methods. It may lead to misunderstanding the real role played by the solid network in terms of volume of radiation propagation. One may also argue that these approaches are only applicable for a specific set of foams.

The discrete-scale numerical approach, the one used in the current section, is an alternative method that can be applied in order to more accurately predict the radiative fields within the foam volumes [216, 217, 218]. This kind of approach involves direct pore scale simulations, while using the realistic topological data of the foam skeleton. Both solid and fluid phase radiative properties are used to solve the RTE. Appealingly, these methods can provide critical information on the energy localization zones within the foam volume. Currently, the method has been drawing considerable attention, however, a major bottleneck for the approach is its computational requirements. Hybrid approaches, combining the discrete-scale and continuous-scale (homogenized) numerical approaches, also exist [219].

Generally handling the discrete-scale numerical approach poses many challenges: i) complex geometries often contain non convex boundaries, radiation propagating in certain directions may re-enter the computational domain leading to numerical complexities. ii) Detailing complex geometries accurately requires a mesh with a huge number of degrees of freedom, causing problems of computer resource management. iii) Many of these problems involve heterogeneous properties, hence the derived matrix systems can be difficult to solve. Moreover in the bi-phasic problem, the semi-transparent media gets coupled to almost transparent media (air), such coupling is not trivial to handle. iv) Exact knowledge of the radiative properties of the heterogeneous media (wavelength, temperature, direction) is also an important issue.

In order to investigate on the complete behavior of radiation within the open cell foam, we divide the problem in three stages. First, we employ the developed RTE solver to study the radiative transfer behavior within a single ligament, this is presented in the next subsection 5.2.1. Next, in subsection 5.2.2, the problem is scaled up and the single foam cells modeled with the Kelvin-cell (tetrakaidecahedron) are solved. The Kelvin-cell is composed of 24 ligaments. Finally, the problem is scaled up further in subsection 5.2.3, and we solve the $5 \times 5 \times 5$ Kelvin-cell based open-cell foam problems. Naturally, as the scales rise the global problem becomes larger and more difficult to handle. Indeed, the problems of foam radiation are good contenders for

testing the previously developed vectorial FEM algorithm.

5.2.1 Modeling the radiative transfer within foam ligaments

Investigating the foam ligaments is gaining popularity among researchers involved in designing foams with controlled macroscopic radiative properties. Recently, Guevelou et al. [213] performed infrared microscopy reflectivity measurement on the ligaments of a silicon carbide open-cell foams. The aim was to determine the effective complex index of refraction. Analytical radiation models based on an effective medium law was used by the authors in order to avoid treating directly the effect played the ligaments surface roughness. In [220] it was shown that the use of realistic tomographied representations can facilitate a better agreement with experimental measurements. It was also recently underlined in [221] that the ligament geometries influence the determination of the radiative properties for the metallic foams. Hence, precise characterization of the radiative transfer within the ligament, either opaque or semitransparent, can provide critical information for developing high-quality experiments. Moreover, the previously mentioned motivation holds as well, i.e., the knowledge of localized radiative fields within the ligaments can be crucial for improving efficiency of the overall foams.

(a) Surface mesh of the ligament.

(b) The ligament geometry.
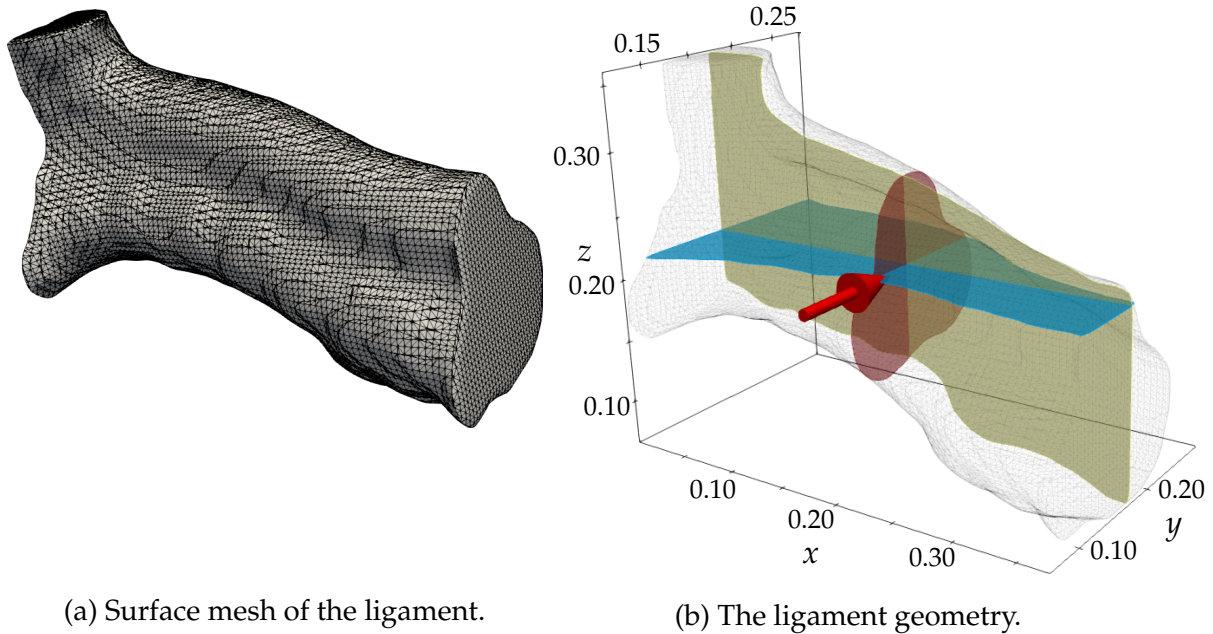
Figure 5.12: Ligament mesh reconstructed using X-ray tomography. The arrow on the right figure represents the collimated input direction $s_{\text{in}} = [0, 1, 0]^\top$.

The numerical investigations, in this subsection, are performed on the three dimensional digitalized ligament obtained from a real ceramic foam. This particular
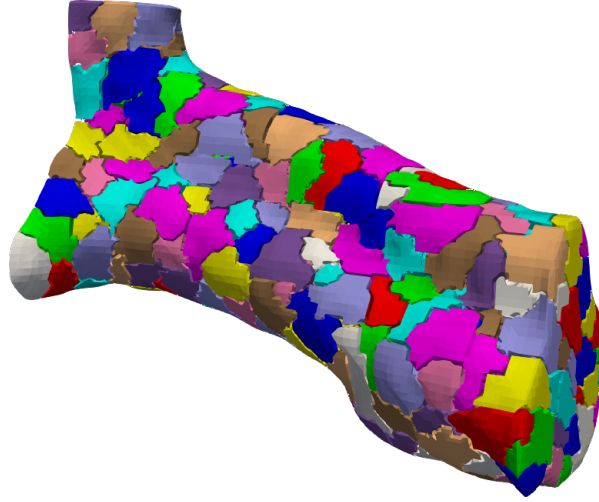
Figure 5.13: Partitioned ligament mesh $\{\Omega_i^h\}_{i=1}^{500}$.

foam was elaborated with the replication method [222]. Numerical tests with this foam geometry has also been presented in [22, 4], however with a different set of boundary conditions and lesser spatial and angular mesh resolutions. The reason to revisit the test, here, is to emphasize on effect of complex ligament topology on radiative prorogation. To acquire the digitized ligament, an X-ray tomography experiment[2] was performed on a cylindrical silicon carbide (SiC) based open-cell foam (diameter=10 mm, thickness=10 mm). Then, by using the marching cube algorithm [223], the external surface mesh of the ligament containing 27,916 triangles was constructed. This surface mesh was then refined and used to create the required volumetric tetrahedral mesh of the ligament, with approximately 0.15 million vertices. The volumetric meshing was performed using the open source mesher Gmsh [160]. The surfasic mesh of the ligament and the ligament geometry are presented in figure 5.12. It can be noticed that the ligament length is approximately twice the size of its lateral dimensions. In figure 5.12b three orthogonal slice planes have been represented within the ligament geometry, these slice planes are used later in the subsection for presenting the solution fields. Further, notice that the topology of the ligament is far from being simple.

Using the ligament from figure 5.12, two test cases are formulated, these are distinguished by the radiative properties chosen, see table 5.3. Properties provided in

---

[2]The X-ray tomography experiments were performed at the European Synchrotron Radiation Facilities (Grenoble, France) on the ID19 beamline. More details about the X-ray tomography experiment are presented in [4]. The acquired ligament surface meshes are courtesy of Sylvain Chupin and Denis Rochais from Commissariat l'Energie Atomique et aux Energies Alternatives (CEA)/Le Ripault, BP 16, 37260 Monts, France.

-	κ	σ_s	n	Φ	Medium
Al$_2$O$_3$	3	90	1.7	Isotropic	Semi-transparent
SiC	250	25	2.4	Isotropic	Opaque

Table 5.3: Radiative properties for the two different materials that compose the ligaments. The properties were recorded at 2 µm wavelength and are given in the following units: absorption coefficient κ in cm^{-1}, scattering coefficient σ_s in cm^{-1}, and n is the refractive index.

table 5.3 have been extracted from the work of Makino et al. [224], who determined the volumetric radiative properties of low porous refractory ceramics for wavelengths ranging from 0.4 to 33.3 µm and at temperatures going from 290 to 700 K. By choosing alumina (Al$_2$O$_3$) and silicon carbide (SiC) as the test materials, a particular attention is paid to select media that are able to illustrate either a semitransparent behavior (Al$_2$O$_3$) or an opaque behavior (SiC) for the same thickness of propagation within the ligament.

For the two tests we assume a collimated beam impinging the ligament on one of its lateral side with the direction $s_{\text{in}} = [0, 1, 0]^\top$, see figure 5.12b. It is worth notifying that the side-to-side distance propagation is 135 µm. The beam size is of radius $r = 25$ µm and has a Gaussian shape, defined by :

$$I_{\text{in}}(x, s_{\text{in}}) = \tilde{I}_0 e^{-10^{9.5}\left[(x-x_0)^2+(z-z_0)^2\right]} \mathbb{1}_{[(x-x_0)^2+(z-z_0)^2<r^2]}, \tag{5.19}$$

where $x_0 = 187.5$ µm and $z_0 = 200$ µm represent the position of the center of the beam. Also, $\tilde{I}_0$ denotes the amplitude of the incident beam radiative intensity, which has been chosen to be 500 W m^{-2} sr^{-1} in following simulations.

_	SiC (opaque)			Al$_2$O$_3$ (semi-transparent)		
	32	128	512	32	128	512
d.o.f.	48.3×10^5	19.3×10^6	77.2×10^6	48.3×10^5	19.3×10^6	77.2×10^6
nnz	6.9×10^7	2.7×10^8	1.1×10^9	6.9×10^7	2.7×10^8	1.1×10^9
k	147	375	463	242	806	885
t_s	35.3	266.5	820.9	61.7	631.3	1569.3

Table 5.4: Solution phase details for the ligament tests. t_s denotes the total time, i.e., matrix building plus solving time in seconds, and k convergence iteration number. 32, 128, and 512 in the table header represent the directions N_d.

In order to solve the two test cases, the given spatial mesh of the ligament was used alongside angular meshes coming from the first three refinements of the

octahedron ($N_d = 32, 128$, and 512). The solved model consist specular reflections, for which the reflectivity coefficient ρ^s was estimated with the partitioning method [78]. All problems were solved on the supercomputer Liger, and 500 MPI processes were used for each problem. Further, the DD parallel algorithm was used with the GMRES solver, the partitioned spatial mesh of the ligament is presented in figure 5.13. For detecting the GMRES convergence, the relative iterative tolerance was set to 10^{-8}. Additional computational details of the tests are tabulated in 5.4.

First thing that one should notice from table 5.4 is that for a particular direction, irrespective of the ligament material, the total number of degrees of freedom (d.o.f.) and the total number of non-zeros (nnz) remain the same. This is because both SiC and Al_2O_3 media have non zero values for κ and σ_s, hence the sparsity of the overall matrix system remains the same. For a particular direction, although the sparsity is the same, the condition numbers, however, for the two cases will be different. Adhering to the discussions made in section 4.3.1, as the SiC ligament is opaque and the Al_2O_3 ligament is semi-transparent by nature, condition number of Al_2O_3 ligament test case should be more than the SiC ligament case. This is asserted by the rise in iteration count and total solving time for the Al_2O_3 ligament test cases in comparison to the SiC ligament cases. If the solver was not parallelized, the most time taking problem in this subsection (Al_2O_3 ligament case with $N_d = 512$) which took 26 minutes to solve, it would have taken over 9 days (($26 \times 500)/(60 \times 24) = 9.03$) to solve this particular problem with a serial solver. This example emphasizes the need of parallelization for solving complex radiative transfer problem. Overall, even though the geometry was complex and specular reflections were involved, the developed RTE solver was able to easily converge.

The radiative density profiles obtained from the semi-transparent Al_2O_3 ligament simulations have been presented in figure 5.14. The radiative density fields within the ligaments volumes are represented on the three orthogonal sliced planes. Further, the effect of increasing the number of the DOM directions for the overall radiative field solutions has also been highlighted in the figure. The solution obtained with the 32 directions is clearly different than the other two. It can also be observed that the solution fields obtained with $N_d = 128$ tend towards the ones obtained with 512 directions, even though some differences remain. One can realize, between the two cases of $N_d = 128$ and 512, the main propagation direction has almost converged. More precisely, the radiative density amplitude with 128 directions is overestimated in comparison to the 512 directions, see figure 5.15. Figure 5.15, which presents a one
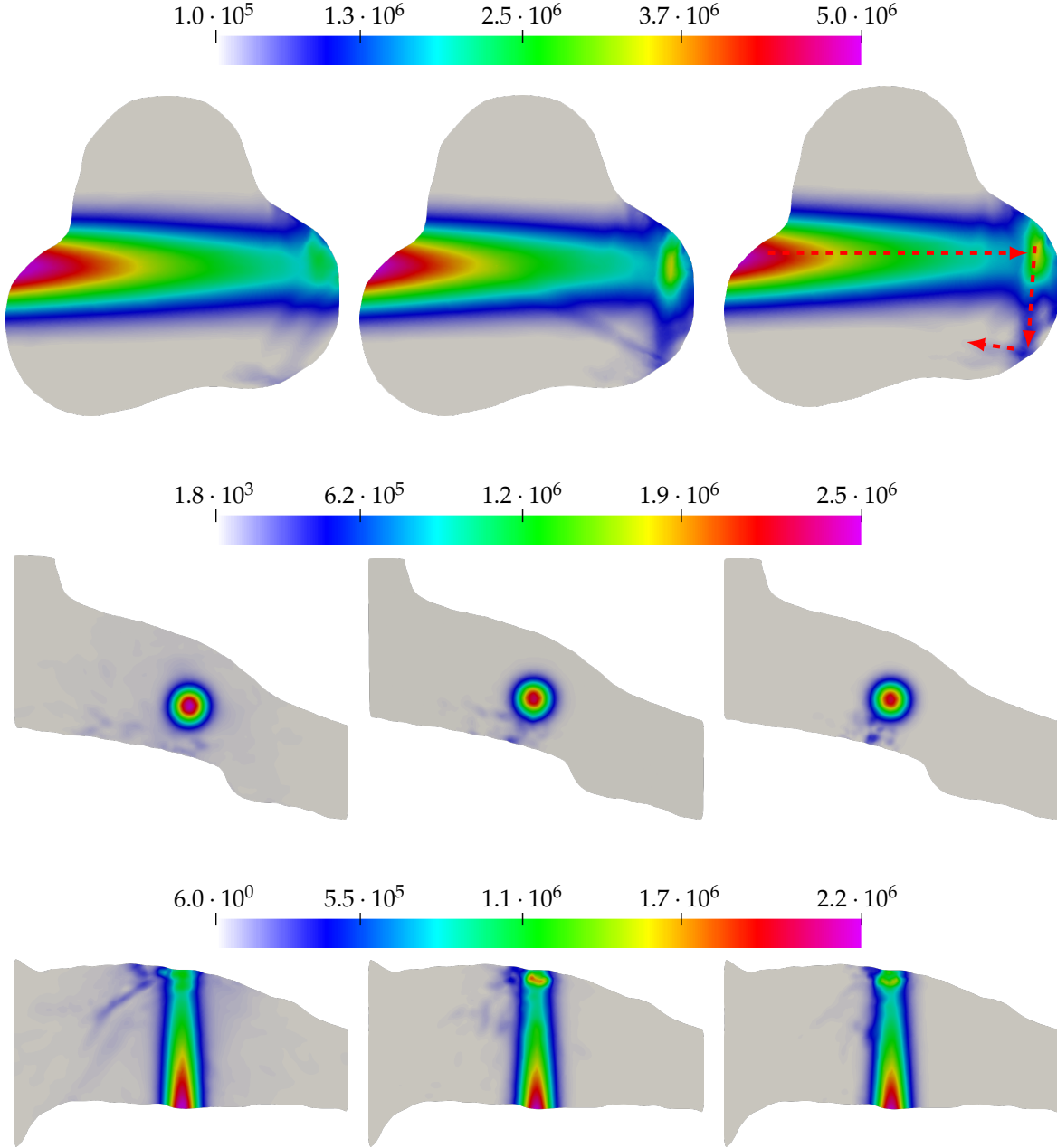
Figure 5.14: Radiative density fields $G(x)$ within the Al$_2$O$_3$ ligament presented on the three orthogonal cross sections. Left column: $N_d = 32$, middle column: $N_d = 128$, and right column: $N_d = 512$. $G(x)$ is given in W cm^{-2}.
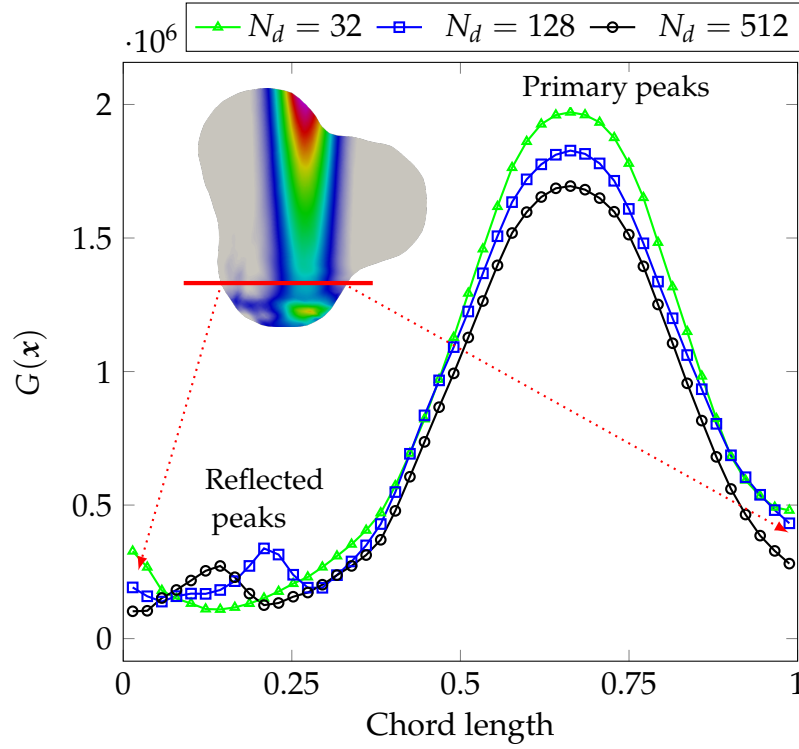
Figure 5.15: One dimensional radiative density plot for the Al$_2$O$_3$ ligament simulated using different directions. $G(x)$ is given in W cm^{-2} and the chord length is normalized from 0 to 1.

dimensional radiative density plot for the Al$_2$O$_3$ ligament simulated using different directions, quantifies the radiative density amplitude over a line that intersects one of the three orthogonal planes near the far end boundary of the ligament. The difference in the density amplitudes appear due to scattering effect. Further, this particular difference is not observed with SiC ligament case, since it is opaque and absorption dominates. Most certainly, 128 directions are not enough to realize the physic with high accuracy, higher direction counts are needed. Note, for the radiative transfer problems within simple cubic geometries, while 80 directions which are more commonly used in the literature might be enough, with scattering and complex topologies 80 directions may not be enough.

Another feature that distinguishes the semi-transparent simulation case of the 512 directions Al$_2$O$_3$ ligament, is reflections. It appears that, as the radiative energy from the main propagation direction reaches the boundary, due to reflection some energy takes a u-turn back into the ligament. This has been highlighted in the top right subfigure of the figure 5.14. This characteristic of reflections is more precisely captured
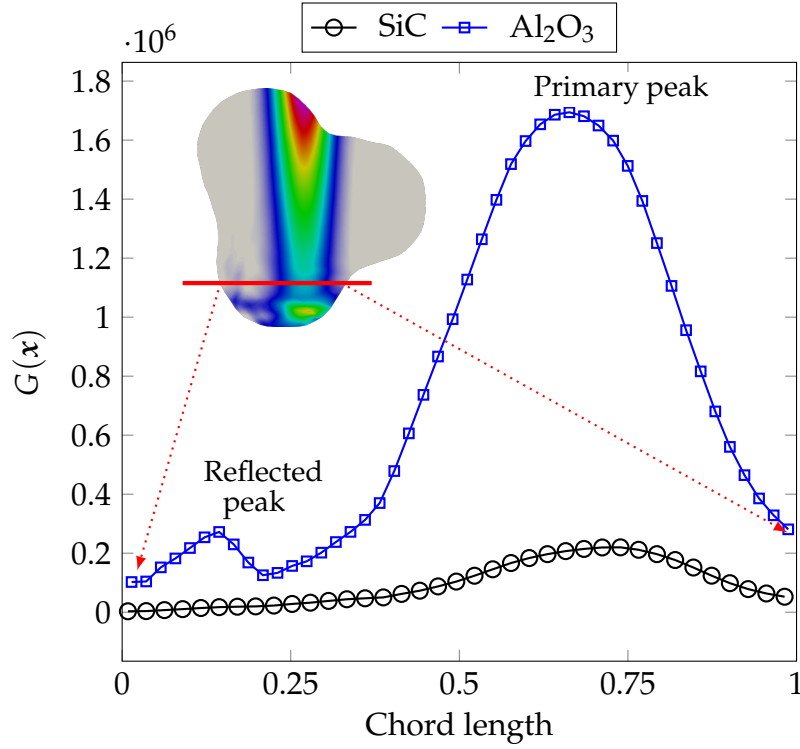
Figure 5.16: One dimensional radiative density plot comparing the SiC ligament to the Al_2O_3 ligament. $G(x)$ is given in $W\,cm^{-2}$ and the chord length is normalized from 0 to 1.

in the one dimensional radiative density plot presented in figure 5.15. In the plot one observes two distinct peaks, a large and a smaller one. The larger peak is around the main propagation direction, the reflected peak which is displaced to the left of the primary peak is smaller in magnitude. The radiative density magnitude of the reflected peak, as expected, is lower due to the fact that some radiative energy is lost to the surroundings at the reflecting boundaries. Also, observe the location of the reflected peaks for the three direction (32, 128, and 512) cases are different. This again suggests that high direction counts are needed for capturing such physics precisely. What can also be observed a high radiative energy zone just before the reflecting boundary. As the shape of the boundary were reflections are taking place resemble to that of a parabolic trough solar collector, such a zone is expected. Within parabolic toughs by using the principles of reflection one can localize the radiative energy almost in the same manner as is observed for the Al_2O_3 ligament, cf. [78, 85]. This localized energy zone has been highlighted within the contoured density fields presented in figure 5.17.

In figures 5.16 and 5.17 the major differences in the radiation propagation be-
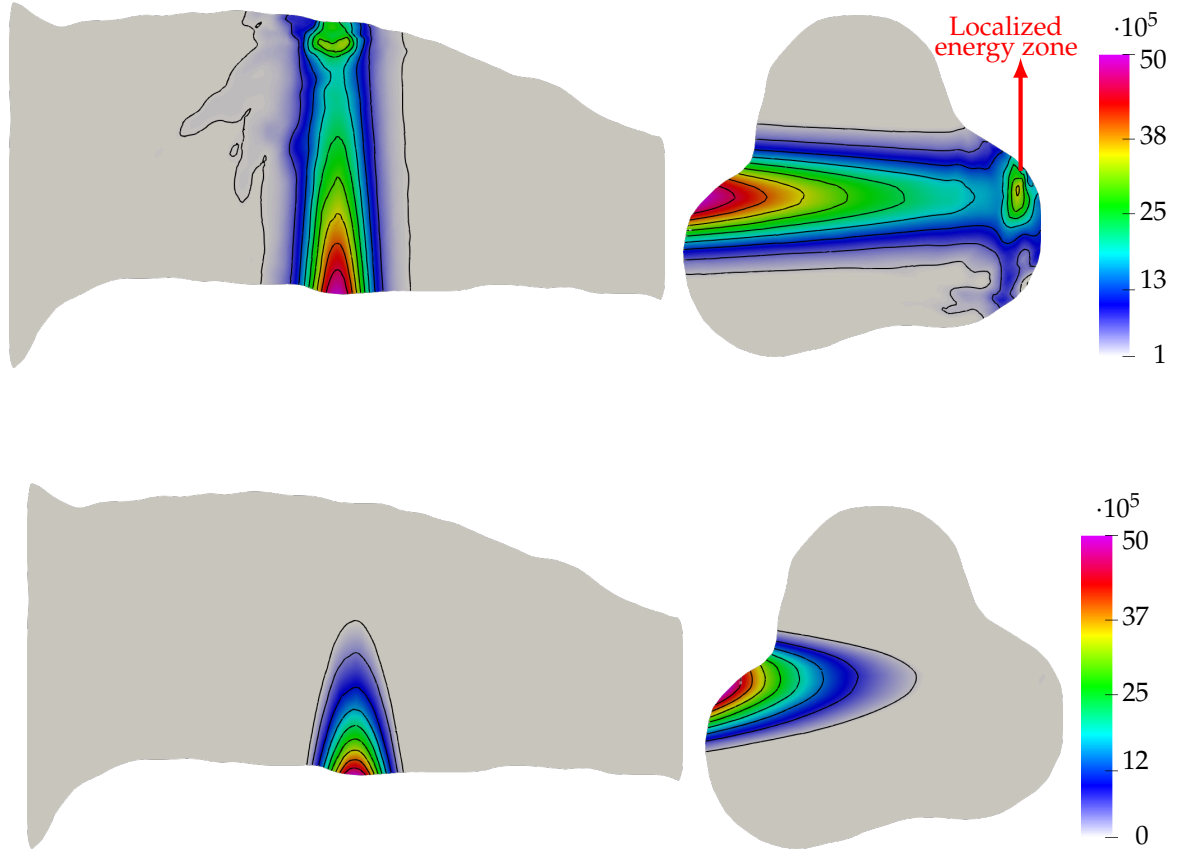
Figure 5.17: Radiative density fields $G(x)$ within the Al$_2$O$_3$ ligament (top row) and the SiC ligament (bottom row) presented on the two orthogonal cross sections. $G(x)$ is given in W cm^{-2}.

havior within the bulk of the SiC ligament and the Al$_2$O$_3$ ligament has been compared. Via the contoured radiative density fields plotted on the two orthogonal slices within the ligaments, figure 5.17 highlights that the Al$_2$O$_3$ ligament being semi-transparent allows the radiation to escape out of the ligament. On the other hand, the SiC ligament being opaque can be seen extinguishing fully the radiation energy within the bulk of the medium. The reflections phenomena can be clearly observed to occur for the Al$_2$O$_3$ ligament case, while the same is not true for the SiC ligament case. This being true, one does not observe any reflected peak (due to u-turn of radiation) within the SiC ligament case, see figure 5.16.

5.2.2   Modeling the radiative transfer within the Kelvin-cell

Next, we scale up the problem and analyze a single Kelvin-cell under radiation. The Kelvin-cell or the tetrakaidecahedron is a polyhedron with 14 faces: 6 quadrilateral

and 8 hexagonal, and is composed of 24 edges, see figure 5.18. Three dimensional packing of the Kelvin-cell is often used as a model for structured open-cell foams. In the numerical test cases appearing in this subsection, the semi-transparent and the opaque Kelvin-cell skeletons are irradiated with collimated radiative intensities. Like the previous subsection, for the opaque and the semi-transparent test materials the SiC and the Al_2O_3 were chosen. Further, in this subsection, the numerical investigations will be explained in three phases: pre-processing, solving phase, and post processing.

(a) The tetrakaidecahedron.   (b) The Kelvin-cell .
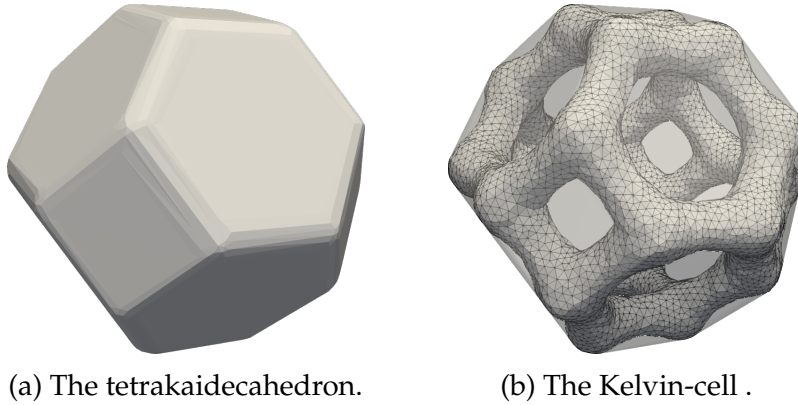
Figure 5.18: Tetrakaidecahedron to the Kelvin-cell geometry.

5.2.2.1 Pre-processing

Most of the studies carried out in the literature, construct the Kelvin-cell ligaments with standard shapes, such as cylinders, parallelepipeds, prisms, etc., cf. [225, 226, 212]. However, elaborating real foam cells out of such ideal shapes is difficult. For this reason, the Kelvin-cell topology constructed in this section does not contain an idealistic shapes for the forming ligaments. This realistic topology of the Kelvin-cell is generated using an in-house software genMat [227, 213], a C++ and Qt based framework to synthesize realistic cellular materials. The genMat makes use of the marching cubes algorithm [223] to accurately generate the surface mesh triangulation of the cell sample. Further, a desired feature of genMat is that the generated ligament shapes can be controlled using different diameters within the ligament. Ligaments are created with bulky ends and a thin mid sections, 1 : 1.6 ratio is maintained for all the ligaments, see figure 5.19c.

The generated surface mesh triangulation from the marching cubes algorithm contains sharp edges and a huge number of degrees of freedom. This surface mesh cannot be directly used to create the finite element volumetric mesh. As a pre-processing step, we reconstruct a smooth surface mesh from this initial surface mesh. This is done

(a) Marching cube surface mesh.

(b) Re-meshed surface mesh.

(c) Zoomed remeshed surface mesh.

(d) Zoomed marching cube surface mesh.
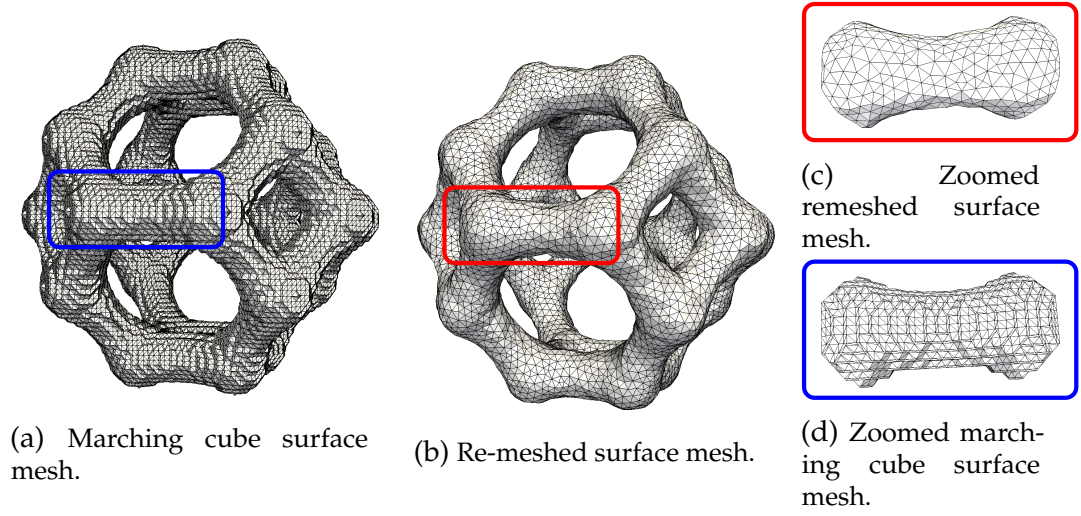
Figure 5.19: Pre-processing step of surface remeshing for the Kelvin-cell.

(a) Immersed mesh domain with a 1000 $\mathrm{W\,cm^{-2}\,sr^{-1}}$ collimated source in x direction.

(b) Three possible pathways (arrows) in which the incoming radiation can cross the Kelvin-cell.
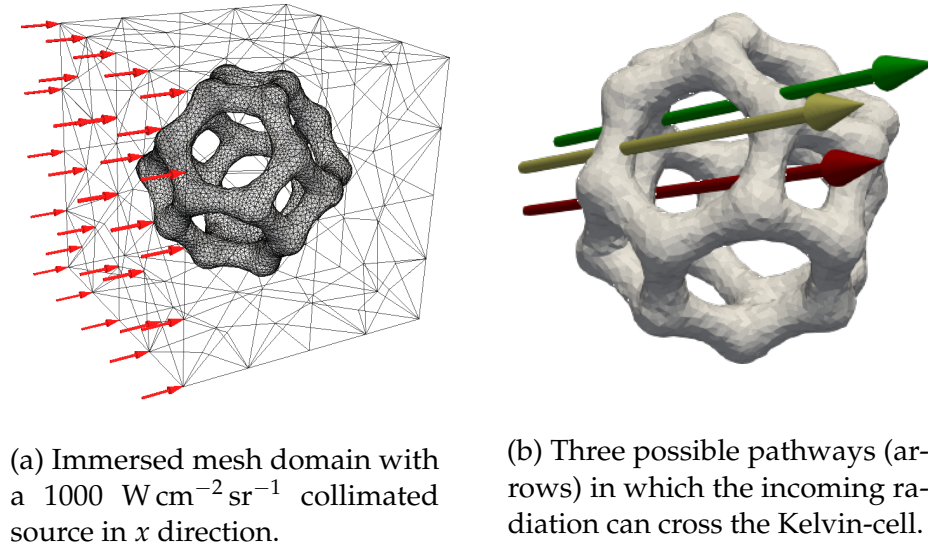
Figure 5.20: Immersed Kelvin-cell domain and the possible pathways for radiation within the cell domain. Red arrow represents pathway 1: radiation directly escapes without any contact with the ligaments, yellow arrow represents pathway 2: radiation comes in contact with one ligament before escaping, and green arrow represents pathway 3, radiation has to traverse through two ligaments before escaping.

by using surface mesh adaption based on a tuned Hausdorff metric value [228, 229]. In figure 5.19, this remeshing step for the Kelvin-cell geometry is presented; notice the overall mesh improvement after remeshing. The initial mesh with 64,271 surface triangles was reconstructed using 16,711 triangles. This reconstructed surface triangulation was then used to generate a tetrahedral volumetric mesh with 1.6 million nodes. The finite element mesh generator Gmsh [230], and the mesh adaptation library mmglib [228, 231] were respectively used as the meshing and the remeshing kernels. The Kelvin-cell produced via this procedure, finally, has an internal diameter of 0.53 cm, the ligament mid sections and ends have diameters of 0.08 cm and 0.12 cm, respectively.

Overall the Kelvin-cell geometry contains non convex boundaries. For the collimated test cases considered in this subsection the propagating radiation needs to re-enter the computational domain. This problem, as such, cannot be solved by considering the Kelvin-cell geometry alone as the computational domain. In order to take into account the re-entry of radiation, a coarse mesh of pure transparent medium is considered to envelop the Kelvin-cell. Hence, it is assumed that the geometry is immersed within a cube of 1 cm^3 pure transparent medium. A pure transparent medium is neither absorbing, nor scattering ($\kappa = \sigma_s = 0$). This property allows us to choose a very coarse mesh for such medium implying minimal additional computational cost, and computationally such medium will not alter with radiation (pure transport), thereby conserving the physical problem description.

Figure 5.20a shows the immersed mesh domain with the inflow boundary source impinging along the x direction, i.e, $\boldsymbol{s}_{\text{in}} = [1, 0, 0]^\top$. Notice, in the figure, a coarse unstructured mesh for the external surrounding domain and a fine unstructured mesh for the immersed Kelvin-cell domain. Generally, solving such problem with steep heterogeneity is difficult to solve using the standard iterative algorithms like the Gauss-Siedel or the source iteration. However, as pointed out earlier, the preconditioned GMRES should be able to handle such complexities. This is one of the reasons that motivates the use of implicit solving techniques for the complex radiative transfer problems. Overall, in this subsection, we are solving problems that are roughly ten folds larger than the ligament cases that were solved in the last subsection. Further, difference comes from the fact that, the interface between the Kelvin-cell boundaries and the external transparent media requires the physics of reflections and refractions, this will not be considered here. The limitation comes from the fact that the Kelvin-cell boundaries are now internal interfaces, as the Kelvin-cell mesh has been immersed.

131

The solver developed within the framework of this thesis does not yet support the physics of reflections and refraction for the internal interfaces, this is one of the future perspectives of the $\mathbb{C}\text{é}f_0\mathcal{PR}$am team to extended the domain of the developed solver. Hence, in this subsection the RTE is just solved with the collimated inflow boundary condition and reflections are avoided.

-	SiC (opaque case)	Al_2O_3 (semi-transparent case)
d.o.f.	79.3×10^7	79.3×10^7
nnz	1.3×10^{10}	1.3×10^{10}
k	44	74
t_s	570.2	966.5

Table 5.5: Solution phase details for the Kelvin-cell tests. t_s denotes the total time, i.e., matrix building plus solving times in seconds, and k denotes the convergence iteration number.

5.2.2.2 Solving

For the solution process, in this subsection, the parallel DD solving algorithm with the GMRES is used. Parallelization with 500 MPI processes was used to solve the test cases on supercomputer Liger. Adhering to the knowledge gained in the previous subsection, we know that more directions are required to capture the physics more precisely. Hence, for these Kelvin-cell tests, only the highest direction count 512 directions was used for all simulations appearing in this subsection. Computational details of the two Kelvin-cell tests performed in this subsection are tabulated in 5.5. From the table we observe that the d.o.f. and the nnz for these test cases are ten folds bigger than the ligament cases in the previous subsection. Also what can be noticed is that the solver takes less time to solve the Kelvin-cell problems in comparison to the ligament test cases from the previous subsection. This is due the fact that reflections were avoided, so the condition number of these problems should be better than the ones in the previous subsection. Additionally, if we compare the SiC Kelvin-cell case to the Al_2O_3 Kelvin-cell case we observe higher number of iterations and time to solve. The reason is scattering, as the Al_2O_3 Kelvin-cell is semi-transparent by nature it is more difficult to solve than the SiC case.

5.2.2.3 Post-processing

Once all the radiative intensities are calculated, we compute the radiative density which represents the energy field of radiation. Figure 5.21 presents the density fields for the SiC and the Al_2O_3 Kelvin-cell cases. Notice that due to radiation shadowing
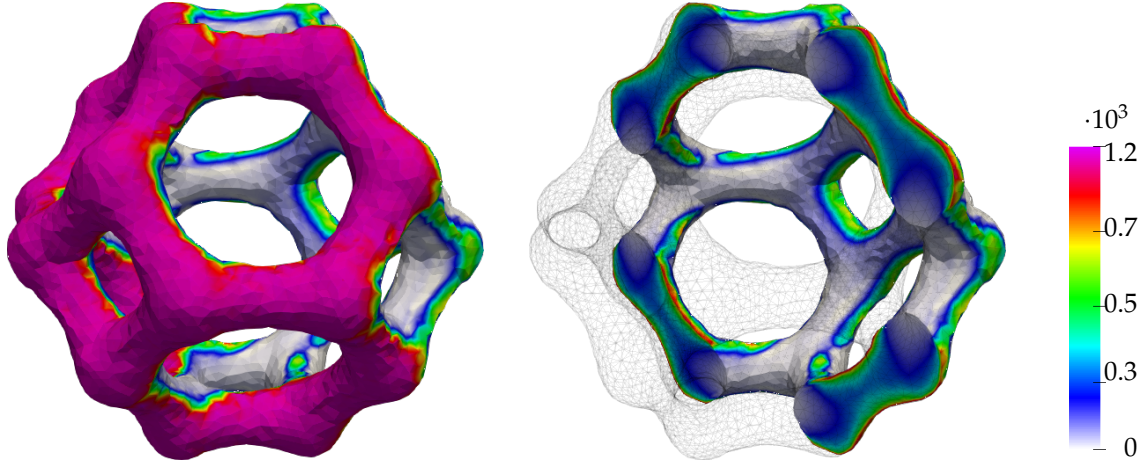
(a) The SiC based Kelvin-cell.
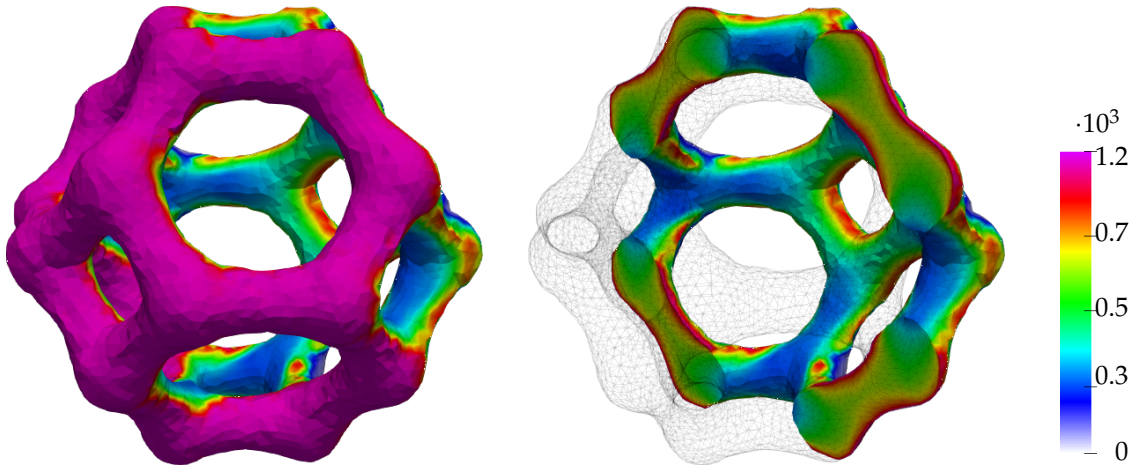
(b) The Al$_2$O$_3$ based Kelvin-cell.

Figure 5.21: Radiative density fields for the SiC and the Al$_2$O$_3$ Kelvin-cell under collimated radiation. Right: clipped section views to visualize density for rear end Kelvin-cell ligaments. Left: full Kelvin-cell density fields on the foams skeleton. Radiative density $G(x)$ is given in W cm^{-2}.

$$0.0 \cdot 10^0 \qquad 0.3 \cdot 10^3 \qquad 0.5 \cdot 10^3 \qquad 0.7 \cdot 10^3 \qquad 1.2 \cdot 10^3$$

(a) The SiC Kelvin-cell.

(b) The Al_2O_3 Kelvin-cell.
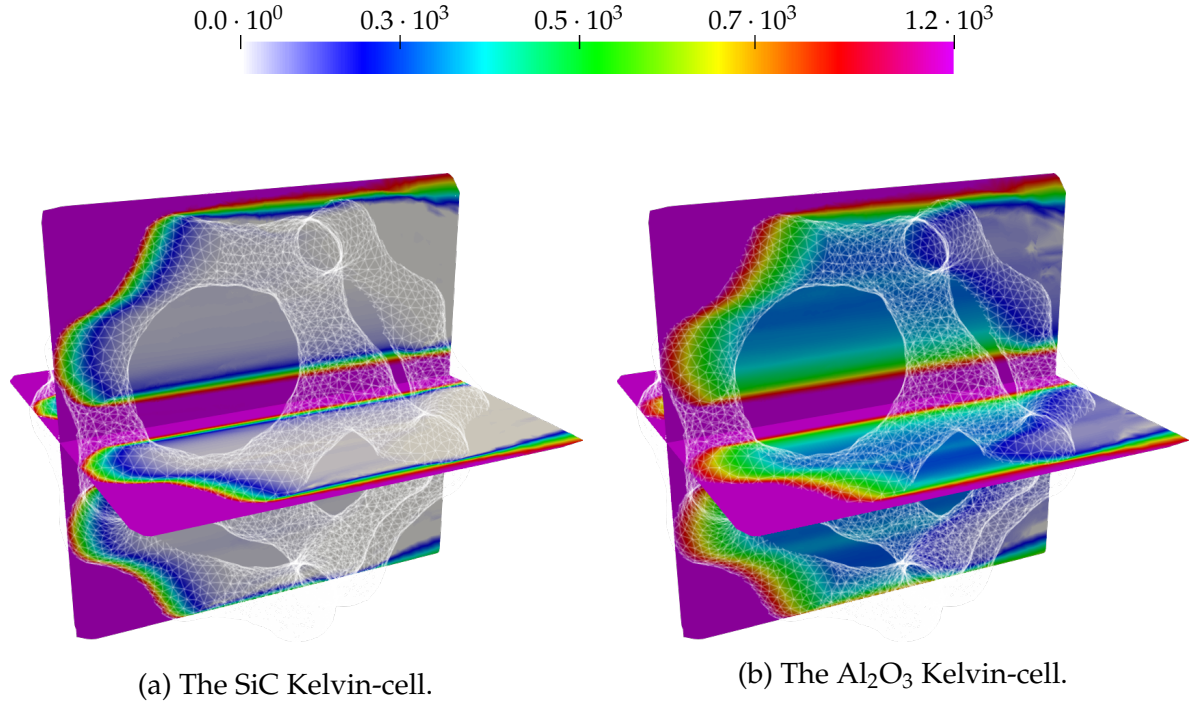
Figure 5.22: Sliced section view of radiative density fields on two orthogonal planes within the SiC and the Al_2O_3 based Kelvin-cells under collimated radiation. Radiative density $G(x)$ is given in $W\,cm^{-2}$.

caused by absorption of radiation, which occurs within the primary ligaments (front facing), the rear end ligaments receive less radiation. The clipped section views of the density fields provided figure 5.21 shows the radiatively cold ligaments at the back of the Kelvin-cell in comparison to the respective front ones. Further it is observed that, the material properties play a vital role in controlling the propagation of radiation. As the SiC Kelvin-cell is absorbing in nature, the material resists propagation of radiation as such impinging radiation is absorbed within the primary ligaments, and we see no propagation of radiation on the rear end ligaments. Contrary to this, the Al_2O_3 Kelvin-cell , is highly scattering and mildly absorbing in nature, the material scatters the impinging radiation. As a result, we notice larger values of radiation imprints on the rear end ligaments in comparison to the SiC Kelvin-cell case. These differences are also highlighted in the sliced section view of radiative density fields on two orthogonal planes within the propagating media that has been presented in figure 5.22.

Within the Kelvin-cell radiation cases, the incoming radiation may escape directly traveling along the pores (pathway 1), the radiation can encounter single ligament before escaping (pathway 2), or the radiation can at-most encounter two
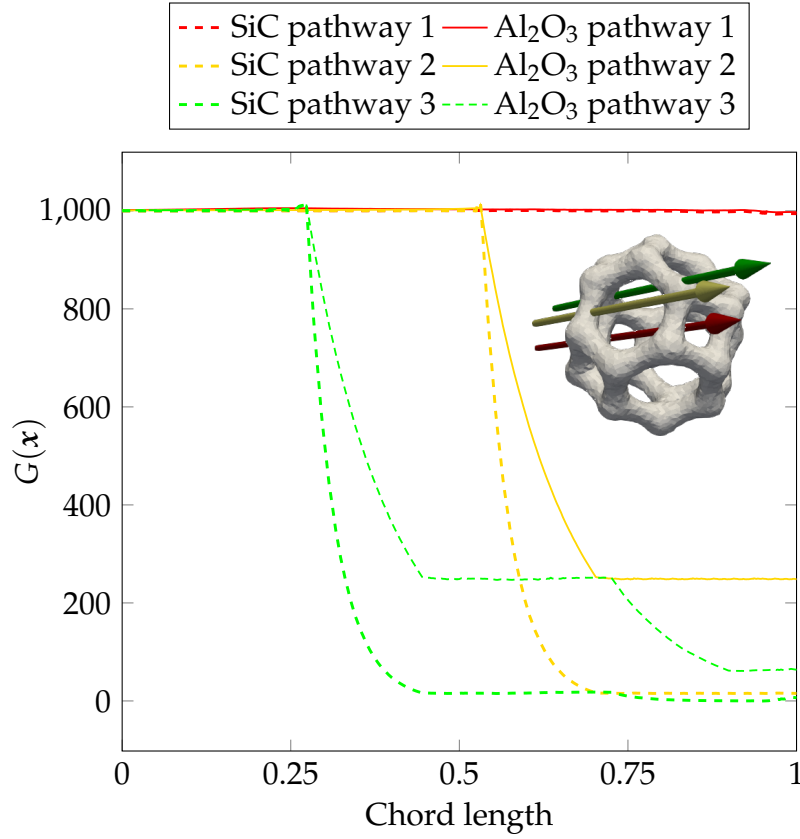
Figure 5.23: One dimensional radiative density plot along three different pathways within the Kelvin-cell for the SiC and the Al$_2$O$_3$ cases. $G(x)$ is given in W cm^{-2} and the chord length is normalized from 0 to 1.

ligaments before escaping (pathway 3). Figure 5.20b highlights these three pathways. For the SiC case, the overall results for the latter two pathways (2 and 3) are almost the same, as the material is highly absorbing energy will never go past the ligaments. The same is not true for the Al$_2$O$_3$ Kelvin-cell case, pathways 2 and 3 will attenuate the radiation by different amounts. The radiative density results for these three different pathways are highlighted in figure 5.23. For the Al$_2$O$_3$ Kelvin-cell case it can be seen that, as the radiation traverses through the first set of ligaments there is exponential drop in radiative energy, next as it encounters the surrounding transparent media the radiation energy then remains constants, and finally as the radiation traverses through the second set of ligaments there is exponential drop of energy again. Observe that the radiative energy, which moves past the first set of ligaments, is high enough to go through second exponential drop in the Al$_2$O$_3$ Kelvin-cell case. The same is not true for the SiC case, notice that, almost all the radiative energy is absorbed by the first set of ligaments.
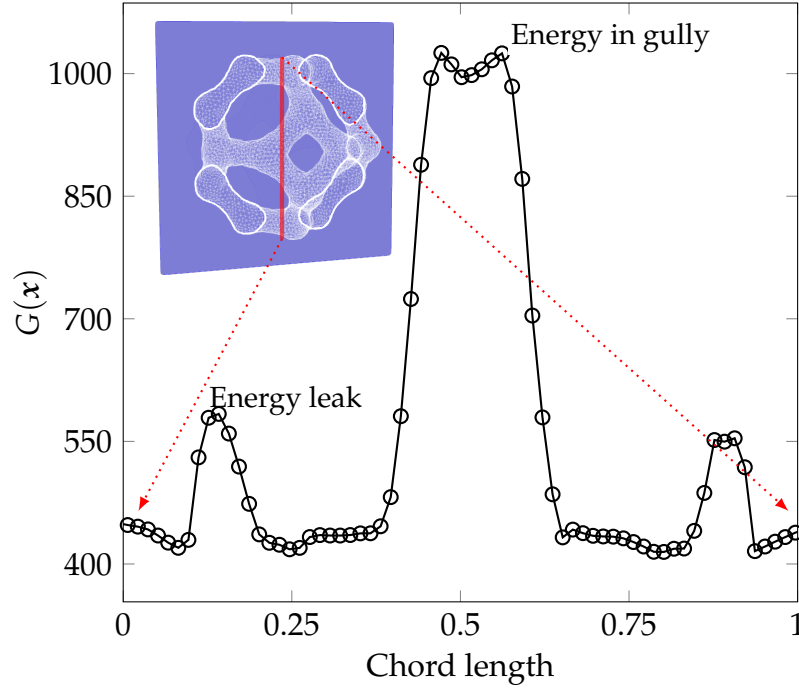
Figure 5.24: One dimensional radiative density plot along a line just after the front ligaments of the Al$_2$O$_3$ Kelvin-cell. $G(x)$ is given in W cm^{-2} and the chord length is normalized from 0 to 1.

Another particular scenario that was observed for the Al$_2$O$_3$ Kelvin-cell case was the radiation leak effect. This is caused due to the irregularly shaped ligaments. Recall, the Kelvin-cell ligaments are tapered, hence they are thinner at the center and bulkier at the ends. Naturally, the optical path that the radiation has to traverse before escaping the ligaments is lower at the center of the ligament than the other parts of the ligament. Consequently, the central parts of the ligament leak more radiation, this can be observed in the figure 5.24. The two distinct peaks that can be seen in the figure 5.24 clearly suggest the radiation energy leak at the central part of the ligament. This case is particular to the Al$_2$O$_3$ ligaments and was not observed for the SiC ligaments. On that matter, it should not be observed for other opaque materials too.

5.2.3 Modeling the radiative transfer within the full foams

After analyzing the ligament alone and the single Kelvin-cell in the two previous subsections, in this subsection we scale up the problem and analyze a cluster of Kelvin-cells under radiation. $5 \times 5 \times 5$ Kelvin-cells are stitched together to form a 125 pored structured open-cell foam. These structured pores compose the solid phase computational domains for the simulations appearing in this subsection. Again the
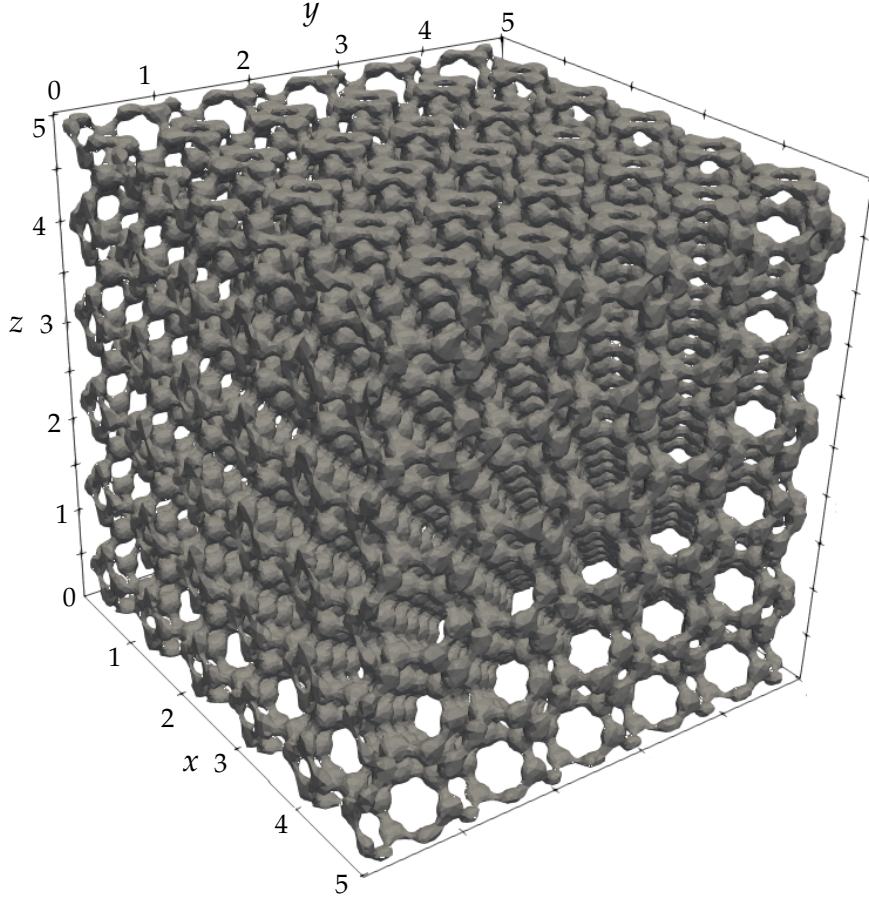
Figure 5.25: Topology of a $5 \times 5 \times 5$ Kelvin-cells based structured open-cell foam after remeshing.

testing conditions remain standard as before, a collimated radiation sources of intensity $1000\,\mathrm{W\,m^{-2}\,sr^{-1}}$ impinges onto the SiC and the Al_2O_3 based open-cell foams.

The same tool, genMat, which was used to construct the Kelvin-cell test case, is now used to construct the topologies of the full open-cell foam. The ligament topologies are tapered as before, and the generated surface meshes are reconstructed with the remesher mmglib. The overall foam geometry is shown in figure 5.25. The mesh now contains roughly 15 million nodes and this is used along with 512 directions for the DOM. Overall, in this subsection, problems with approximately 8 billion unknowns are solved (the highest the solver has so far been tested with). Just like the previous Kelvin-cell test case we do not have an option than to not use reflections, so two test cases of SiC and Al_2O_3 full foams are solved without any reflections and refractions at the internal interfaces. If we observe the SiC case results from the two last subsections, one can be sure that once the radiation enters into the ligaments it

gets absorbed. This lets us formulate a third test case, in which we only simulate the pore phase of the full foam. As the solid phase of the foam is avoided, the solid-pore interface now becomes an external boundary, hence, we can treat reflections at these boundaries, as was done in the ligament test cases. The difference here is that the surroundings (pore space) forms the computational domain, and for the ligament cases it was the opposite, the solid phase formed the computational domain. This third test case helps analyze the effect of reflections with the opaque open cell foams. For handling reflections, the reflection coefficient ρ^s is constructed with the partition method [78]. Simulations, in this subsection, will be performed by following the principles of the previous subsection, i.e., the foam meshes are immersed within a transparent pore space, which is now 125 folds larger than the Kelvin-cell cases. The open cell foams then have approximately 80% porosity.

-	SiC (opaque) no reflections	Al$_2$O$_3$ (semi-transparent) no reflections	SiC (opaque) with reflections
d.o.f	76.7×10^8	76.7×10^8	60.1×10^7
nnz	1.5×10^{11}	1.5×10^{11}	9.03×10^9
k	56	59	340
t_s	405.1	423.4	852.8

Table 5.6: Solution phase details for the full open-cell foam tests. t_s denotes the total time, i.e., matrix building plus solving time in seconds, and k convergence iteration number.

These tests were performed by using 1200 MPI processes and the DD algorithm. The GMRES with a stopping criteria of 10^{-8} was used as the standard solver. The computational details of the three test cases that are solved in this subsection are provided in table 5.6. We notice the standard facts, i.e, reflection case is difficult to solver (more iterations and time), this is followed by non reflection semi-transparent case, and finally the easiest to solve is the non reflecting opaque case. Notice that the total d.o.f. and the nnz for the reflection case is lower than the non-reflecting cases, this is due to the fact that the internal mesh within the ligaments is not considered anymore. However, it should be notified that a finer mesh for pore space was considered in the reflecting case in comparison to the pore space mesh of the non reflecting cases. Although the reflecting case has lesser d.o.f. than the other two cases, it is still the most time consuming problem among the three test cases in this subsection. This again emphasizes on the fact that adding reflections within a transparent media can deteriorate the conditioning of the problem, and make it more difficult to solve. Nevertheless, the reflecting SiC open-cell foam case took approximately 15 minutes to solve, suggesting,

again, the robustness of the developed solver.

The radiative density profiles for the non-reflecting test cases of the SiC and the Al_2O_3 foams are provided in figure 5.26. The radiative densities have been presented on the skeletons of the foams. It is observed that the SiC foams, as expected, do not allow the radiation to pass beyond the first set of ligaments, the Al_2O_3 foam on the contrary allows partial radiative energies to go beyond the first set of ligaments. In figure 5.27 clipped section views of the radiative density fields within the foams volume is presented. Both, the pore phase and the solid phase densities can be clearly seen in the figures. One can observe that due to the free pore space, formed by the 5 inline Kelvin-cells, the radiative energy freely escapes to the surrounding without being attenuated. This free pore space pathway is analogous to pathway 1 of the Kelvin-cell case, that was presented in figure 5.20b. As a result high radiative energy zones, or gullies of radiation energies are formed within these pore space pathways. Next, we observe that radiation gets attenuated with stepped drops as it passes from ligament to ligament within the Al_2O_3 foam case. This stepped drop is plotted in figure 5.28. Within this stair-case type of radiative energy drop the primary ligament attenuation to radiation is the strongest. Almost 80% energy is extinguished by the first rank of Kelvin-cells. Qualitatively similar stair-case drops for structured foams was also observed recently in [232].

For the third test case in this subsection, the clipped radiative density fields within the SiC foam with reflections is presented in figure 5.29. From the figure one observes that the localized high energy zones of radiation are found within the pore spaces that are formed due to the first rank of Kelvin-cell. It can be clearly seen that reflections lead to a overall back scatter effect. If homogenized the SiC open-cell foams are represented by an equivalent back scattering sample. In [233], the homogenized SiC foams were characterized with a back scattering phase function (anisotropy coefficient $g = -0.6$). The density fields observed in figure 5.29 assert the same back scattering behavior. This figure also brings into picture the key role played by reflections within the open cell foams.

To investigate further this reflecting problem, the third test case, figure 5.30 provides the sliced density fields along a pore channel with the SiC based open-cell foam solved with reflections. What is interesting to notice is, how due to reflections, the energy bounces from one ligament surface to another. Due to reflections the pore space behind the ligaments is observed to carry considerable amount of radiative energy

(a) SiC foam sample.

(b) Al$_2$O$_3$ foam sample.
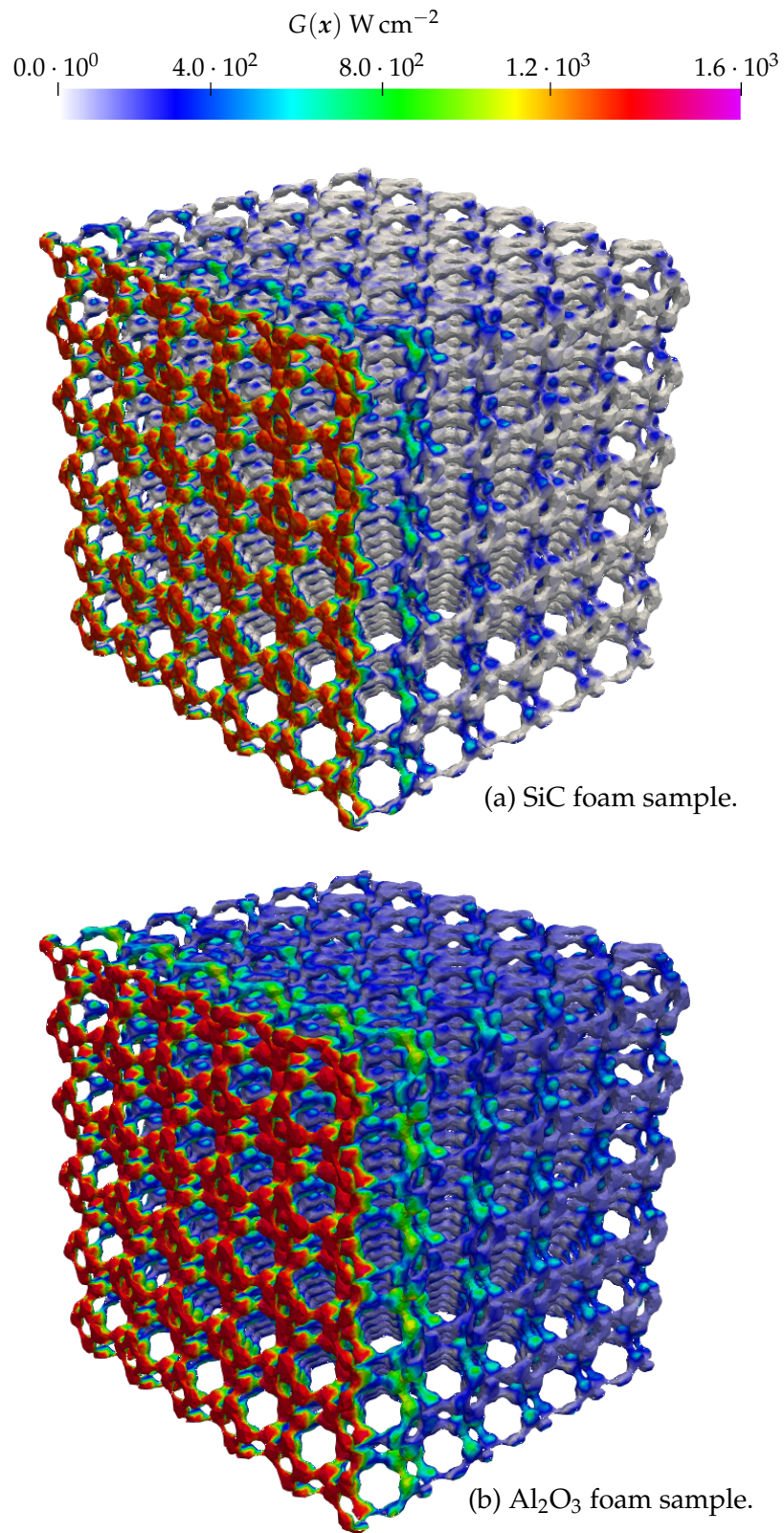
Figure 5.26: Radiative density fields for Kelvin-cell based open-cell foams under collimated radiation.

(a) SiC foam sample.

(b) Al$_2$O$_3$ foam sample.
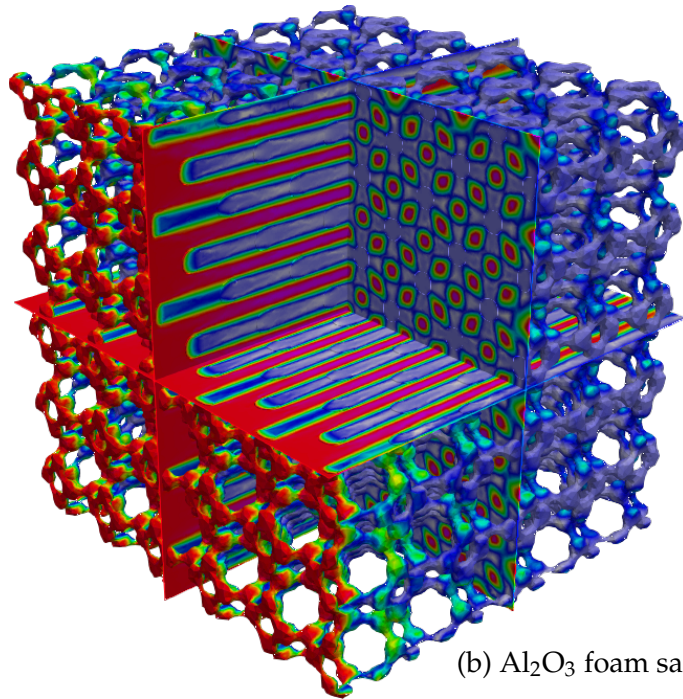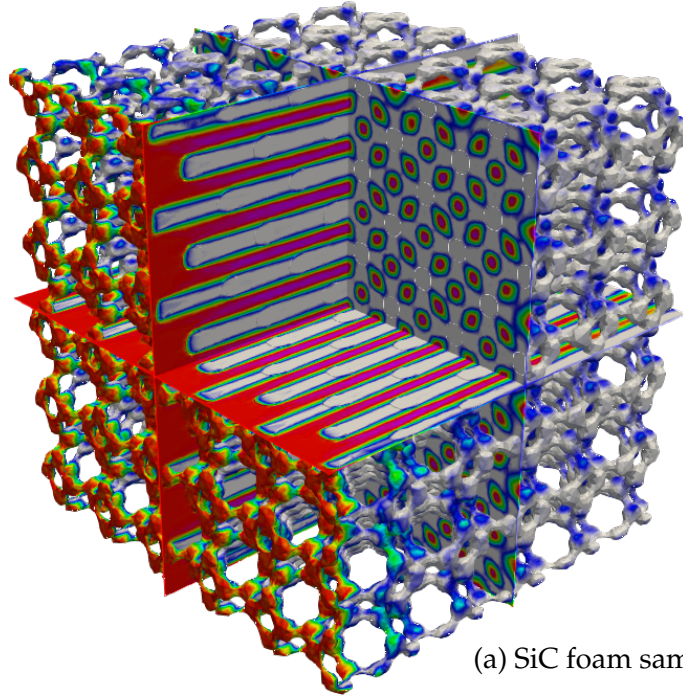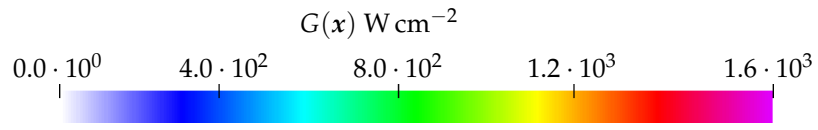
Figure 5.27: Clipped section view of radiative density fields for Kelvin-cell based open-cell foams under collimated radiation.
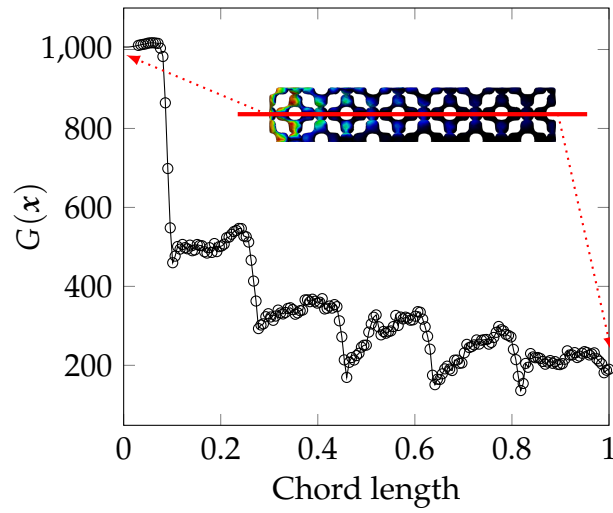
Figure 5.28: One dimensional radiative density plot along the in-line Kelvin-cell ligaments for the Al_2O_3 based open-cell foam. $G(x)$ is given in $W\,cm^{-2}$ and the chord length is normalized from 0 to 1.
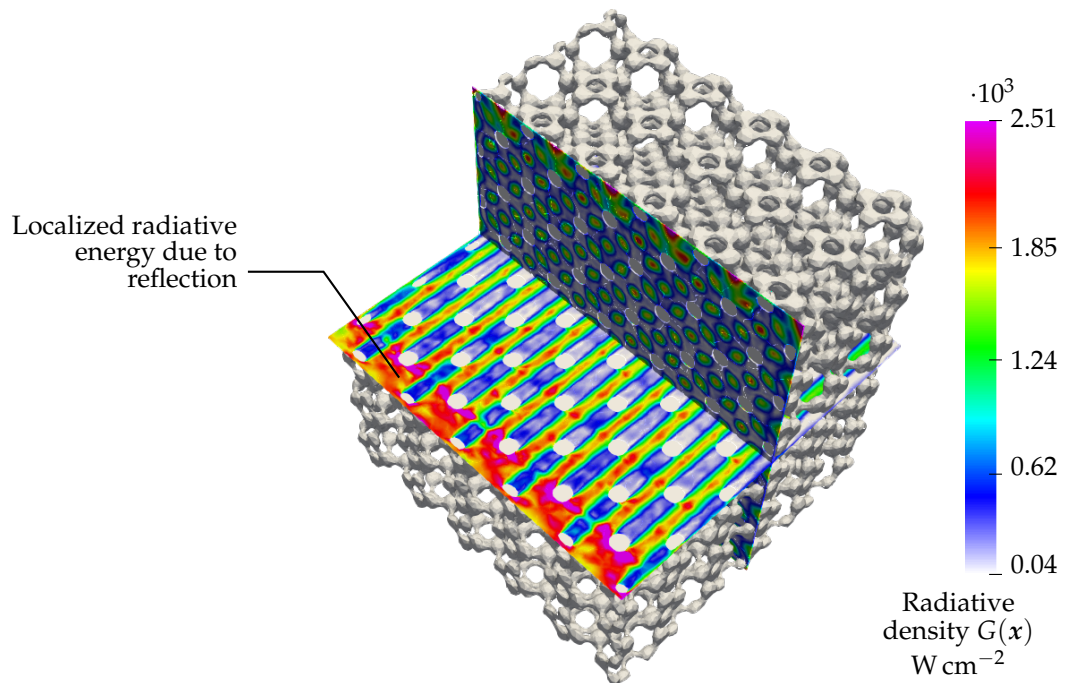
Figure 5.29: Clipped radiative density field within the SiC foam showing a global back scatter due to reflection.
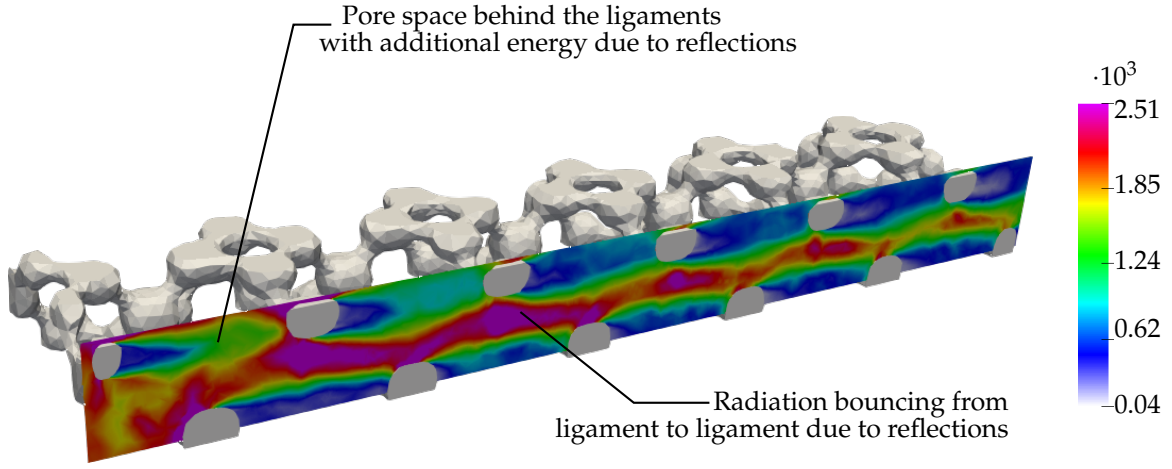
Figure 5.30: Radiative density filed $G(x)$ on a sliced plane along the pore channel for a SiC based open-cell foam. $G(x)$ is given in $W\,cm^{-2}$.

as it receives reflected energy. This would not have been the case if reflections were absent, these pore spaces then would have been with no radiative energy. Figure 5.31 provides the one dimensional radiative density plot along the pore channel for the reflecting SiC open-cell foam case. We observe multiple high energy peaks along the one dimensional line, these are the reflected energies that are propagating from ligament to ligament. Additionally, what can be observed is that these peaks get lower in energy level with a linear decay. This decay is associated to reflection coefficient ρ^s, as with each reflection only a part of energy is reflected back by the surface, while the rest is absorbed by the ligament.

Overall, in the last subsections, the developed vectorial FEM solver was used to perform some very large scale challenging numerical experiments on the open-cell foam geometries. Problems with billions of unknowns were solved on supercomputer Liger within minutes. Thanks to robust Krylov subspace solvers, scaled solutions were obtained with optimal convergences. Additional capability of the solver to solve the transparent semi-transparent material coupling problems was highlighted. The radiative field analysis which were performed for the foams brought into light the volumetric radiation fields within the ligaments, the Kelvin-cells, and the full foams. This brings into picture more accurate and comprehensive knowledge about the localized and overall radiative energy attenuation within foams. This knowledge can be used to design more accurately open-cell foams that are being used within many radiative transfer applications.
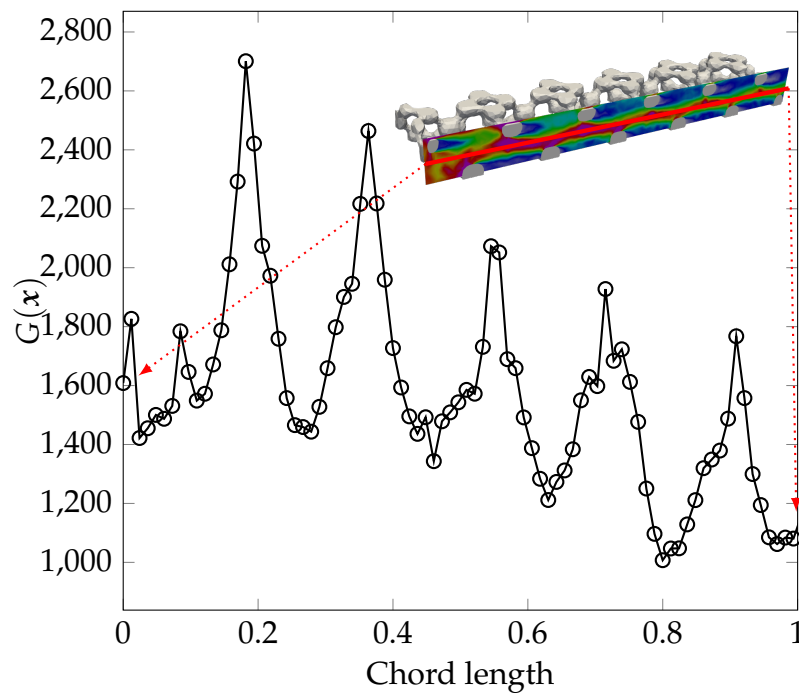
Figure 5.31: One dimensional radiative density plot along the pore channel for the SiC based open-cell foam. $G(x)$ is given in $\mathrm{W\,cm^{-2}}$ and the chord length is normalized from 0 to 1.

The main objective of this thesis was to develop an efficient method for solving the multidimensional monochromatic steady-state radiative transfer problems. It was desired to apply the developments of this thesis for solving radiative transfer problems within topologically complex participating media that included scattering. The integro-differential nature of the radiative transfer equation compelled this work to be numerical. Hence, over the course of five chapters presented in this thesis, several useful strategies for numerically solving the radiative transfer equation were designed. As main ingredients, an advanced finite element technique, high performance computing, and preconditioning were explored. The main highlights of the thesis are enlisted below.

- We started by reviewing the full discretization procedure of the finite element method coupled with the discrete ordinate method which is often used for the spatio-angular discretization of the radiative transfer equation. To improve upon such a discretization technique, instead of using the standard finite elements, the radiative transfer equation was reformulated by using the vectorial finite elements.

- It was shown that the vectorial finite element method for solving the radiative transfer equation lead to linear systems with banded matrices, conversely to the block matrix structure obtained with the standard finite element method.

- As expected, in comparison to the standard finite element method, the proposed vectorial finite element method was proven to be faster and more effective discretization approach, for solving the radiative transfer equation. Faster timings for the linear system assemblies, as well as for the solution phase were observed, when solving the scattering media radiative transfer problems. For the non-scattering media problems, the vectorial finite element method was still faster

145

than the standard finite element method, but only at the linear system assembly phase.

- The developed vectorial finite element method was cross-validated against a benchmark problem of radiation from the literature. Additional cross-validation was performed by using the Monte–Carlo simulation as reference. Further, numerical verification test based on the method of manufactured solutions was performed for asserting the accuracy of the vectorial finite element method. Convergence of the vectorial finite element method solution towards the exact solution could be obtained by concurrent refinement of spatial and angular meshes. In agreement with the literature, the numerical verification tests proved that piecewise linear vectorial finite element method for solving the radiative transfer equation is second-order accurate.

- To take advantage of the modern supercomputers, the vectorial finite element method for solving the radiative transfer equation allows parallelization via two different approaches of angular decomposition and domain decomposition. Both of these techniques were employed separately to obtain two different parallelized solvers, that were also compared to each other. A strong scalability analysis, on thousands of MPI processes, was performed for the two methods and it was established that both possess quasi-linear scaling characteristics. Timing wise, the angular decomposition method performs better than the domain decomposition method.

- A new algebraic technique for efficiently redistributing the matrices obtained with the angular decomposition method was developed. This matrix redistribution technique allows to extend the scope of angular decomposition method. The extended–angular decomposition method can be used with up to $N_d{}^2$ processing elements, while the standard angular decomposition method was limited to N_d processing elements. A direct advantage of this new approach is that we were able to use the angular decomposition method on more than one thousand MPI processes.

- To investigate preconditioning for the Krylov subspace methods for solving different multi-dimensional radiative transfer problems an eigenspectrum analysis was performed. Based on the physics, four distinct problems of radiation in transparent, absorbing, scattering, and reflecting media were analyzed. An eigenspectrum analysis was set up on these different problems in order to study

the effect of each physics on the condition number of the discretized system. It was concluded that:

- Absorbing/transparent media problems are well conditioned, problems with such media have low condition numbers.

- Including scattering or increasing the strength of scattering, leads to increase in the condition number of the discretized system, hence making it more difficult to solve.

- Adding reflections to a highly absorbing medium problem does not effect the conditioning of the problem. Absorbing media problems in general remain well conditioned with low values of condition numbers.

- Conditioning deteriorates heavily when reflection is involved in transparent/scattering media problems. High condition numbers are observed for such cases.

- Two Krylov subspace solvers, the GMRES and the BiCGSTAB, with and without preconditioning, were investigated for solving the above mentioned radiative transfer problems. In conclusion, the BiCGSTAB outran the GMRES for all cases, with lower iteration count, solving times, and memory requirements. However, typical to the BiCGSTAB, erratic convergences were sometimes observed in comparison to the smooth convergence curves for the GMRES. These erratic behaviors were more prominent for the cases including reflecting borders.

- Concerning preconditioners, as expected, it was established that preconditioning systems with the block Jacobi method (with incomplete LU factorizations with zero level of fill-in as block solvers) lead to faster convergence. In particular, the BiCGSTAB with the block Jacobi preconditioning emerged as the faster solution method in comparison to the non-preconditioned BiCGSTAB, the non-preconditioned GMRES, the Jacobi preconditioned BiCGSTAB, the Jacobi preconditioned GMRES, and the block Jacobi preconditioned GMRES. Moreover, preconditioning also reduced drastically the outbursts of the BiCGSTAB.

- As a challenging application test case for the developed solver, some realistic problems of the open-cell foam radiation were solved. Following hierarchy, we investigated the foam ligament, a single foam cell (the Kelvin-cell), and finally the full foam. These were problems with billions of unknowns and involved very complex geometries and transparent semi-transparent media couplings. Using thousands of MPI processes, the solutions were obtained in short times (less than

half an hour for the largest case). The results from these simulations, the volumetric radiation fields, brought into picture a more accurate and comprehensive knowledge about the localized and overall radiative energy attenuation within such foams.

Following are the perspectives for this thesis.

- The proposed vectorial finite element method, used for solving the monochromatic steady-state radiative transfer equation, can be used as a stepping stone for designing a multi-frequency or transient radiative transfer solver.

- Since the vectorial finite elements concentrate different unknown fields into one vectorial space, for coupled problem of radiation-conduction or radiation-conduction-convection it can be interesting to solve all unknowns at once using the concept of vectorial finite elements.

- There are still open issues concerning the definition of a more efficient preconditioner for the domain decomposition distribution. It could also be interesting to lower the memory requirements of the angular decomposition approach by combining domain and angular decomposition approach (hybrid approach). Moreover, since an almost optimal preconditioner for the systems yielded by angular decomposition has been established (block Jacobi with incomplete LU factorizations with zero level of fill-in as block solvers), this could be of importance to design a suitable preconditioner for an hybrid approach.

- In this thesis, the Krylov subspace methods, the GMRES and BiCGSTAB were implemented in the conventional way, full linear system was stored and then solved. This implies large computational memory. However, it is possible to avoid explicit storage of the linear system and still solve the linear system by using a Krylov subspace method. All what is needed is a subroutine (or a law) that can perform a matrix–vector multiplication without storing the full linear system. This is the principle of matrix-free Krylov subspace method, exploring such options can help drastically reduce the memory requirements of the vectorial finite elements solver.

- Adaptive mesh refinement that depends on the theory of error estimation is well established in the field of finite element methods. In order to reduce the total

number of spatial or angular degrees of freedom, efforts could be made to plug in the mesh refinement routines for the current vectorial finite element method.

- At the internal interfaces, an integral part of the boundary conditions comes from the physics of refractions and reflections. Efforts could be made to integrate such boundary conditions into the vectorial variational formulation for the RTE.

- In the fields of inverse radiative transfer, e.g., diffused optical tomography, it may be required to solve the RTE many times in a loop leading to long overall solution times. Inverse radiative transfer was one of the previous research direction of the $\mathbb{C}\text{é}f_0\mathcal{PR}$am team. Since the parallelized vectorial finite element method is now able to solve the RTE quickly, this can drastically reduce the overall solution times for an inverse computation. Hence, it could be interesting for the $\mathbb{C}\text{é}f_0\mathcal{PR}$am team to re-explore this field of inverse radiative transfer.

- In the context of open-cell foam radiation problems, a single ligament shape with two different materials was explored. A parametric study on different ligament shapes, sizes, materials, boundary conditions, etc., could be set up and analyzed to bring into picture the real role of radiative transfer within these systems. The same could be followed for other radiative transfer problems, like the full foam radiative transfer problems, the laser heating problems of material manufacturing, etc.

[1]   M. A. Badri, P. Jolivet, B. Rousseau, S. Le Corre, H. Digonnet, and Y. Favennec, "Vectorial finite elements for solving the radiative transfer equation," *Journal of Quantitative Spectroscopy and Radiative Transfer*, vol. 212, pp. 59–74, 2018.

[2]   M. A. Badri, P. Jolivet, B. Rousseau, and Y. Favennec, "High performance computation of radiative transfer equation using the finite element method," *Journal of Computational Physics*, vol. 360, pp. 74–92, 2018.

[3]   M. A. Badri, P. Jolivet, B. Rousseau, and Y. Favennec, "Preconditioned Krylov subspace methods for solving radiative transfer problems with scattering and reflection," *Computers and Mathematics with Applications*, 2018.

[4]   D. Le Hardy, M. A. Badri, B. Rousseau, S. Chupin, D. Rochais, and Y. Favennec, "3D numerical modelling of the propagation of radiative intensity through a X-ray tomographied ligament," *Journal of Quantitative Spectroscopy and Radiative Transfer*, vol. 194, pp. 86–97, 2017.

[5]   M. A. Badri, A. Biallais, G. Domingues, Y. Favennec, G. Fugallo, A. M. Monthe, and B. Rousseau, "Combining micro- meso- and macro-scopic numerical methods for multiscale radiative transfer modeling of sic-based foams up to very high temperatures," in *Proceedings of the 16th International Heat Transfer Conference*, IHTC 16. Beijing, China, August 10–15, 2018.

[6]   M. A. Badri, Y. Favennec, P. Jolivet, S. Le Corre, and B. Rousseau, "A parallel implicit mixed-fem solution for complex domain radiative trasfer problems using immersed meshes," in *Proceedings of Computational Thermal Radiation in Participating Media VI Eurotherm Seminar No. 110*, CTRPM VI, Lisbon, Portugal, April 11–13, 2018.

[7]   Y. Favennec, M. A. Badri, T. Mathew, and B. Rousseau, "Angular adaptivity with finite elements on ball-triangulation for efficient numerical solutions of radiative transfer equation," in *Proceedings of Computational Thermal Radiation*

151

in Participating Media VI Eurotherm Seminar No. 110, CTRPM VI, Lisbon, Portugal, April 11–13, 2018.

[8]   M. A. Badri, Y. Favennec, P. Jolivet, D. Le Hardy, S. Le Corre, and B. Rousseau, "Spatial versus angular parallelization for solution of radiative transfer equation in participating media," in *ICHMT DIGITAL LIBRARY ONLINE*, Begel House Inc., 2017.

[9]   M. A. Badri, Y. Favennec, P. Jolivet, S. Le Corre, A. Biallais, and B. Rousseau, "Discrete-scale numerical radiative transfer analysis of porous participating medias," in *French Interpore Conference on Porous Media*, JEMP 2018, Nantes, France, Oct. 8–10, 2018 (Presentation).

[10] B. Rousseau, A. Biallais, M. A. Badri, Y. Favennec, T. Fey, M. Stumpf, and J. Vicente, "Numerical design of cellular ceramics with prescribed effective thermal radiative properties," in *Computational Thermal Radiation in Participating Media VI Eurotherm Seminar No. 110*, CTRPM VI, Lisbon, Portugal, April 11–13, 2018 (Poster).

[11] S. Lal, M. A. Badri, Y. Favennec, and B. Rousseau, "Towards development of a robust 3D numerical method to interpret thermograms of cellular ceramics acquired by the Laser Flash method," in *42nd International Conference and Expo on Advanced Ceramics and Composites*, ICACC2018, Daytona Beach, USA, Jan. 21–26, 2018 (Presentation).

[12] M. A. Badri, Y. Favennec, S. Le Corre, and B. Rousseau, "Implicit parallel radiative transfer equation solver with application to complex semi-transparent media," in *11émes Journées d'Etudes en Rayonnement Thermique*, JERT2017, Orléans, France, Nov. 23–24, 2017 (Presentation).

[13] M. A. Badri, Y. Favennec, H. Digionnet, S. Le Corre, and B. Rousseau, "Mixed finite element solution of radiative transfer equation ," in *7th International Conference on Advanced COmputational Methods in ENgineering*, ACOMEN2017, Ghent, Belgium, Sept. 18–22, 2017 (Presentation).

[14] C. Stokes-Griffin and P. Compston, "A combined optical-thermal model for near-infrared laser heating of thermoplastic composites in an automated tape placement process," *Composites Part A: Applied Science and Manufacturing*, vol. 75, pp. 104–115, 2015.

[15] A. C. Terracciano, S. De Oliveira, D. Vazquez-Molina, F. J. Uribe-Romo, S. S. Vasu, and N. Orlovskaya, "Thermal and Acoustic Performance of Al2O3,

MgO–ZrO2, and SiC Porous Media in a Flow-Stabilized Heterogeneous Combustor," *Energy & Fuels*, vol. 31, no. 7, pp. 7552–7561, 2017.

[16] M. Schweiger and S. R. Arridge, "The Toast++ software suite for forward and inverse modeling in optical tomography," *Journal of biomedical optics*, vol. 19, no. 4, p. 040801, 2014.

[17] "Plastic Thermpforming." http://www.primepacktech.com/technology/thermoforming.html.
Accessed: 2016-09-30.

[18] R. Dickes, V. Lemort, and S. Quoilin, "Semi-empirical correlation to model heat losses along solar parabolic trough collectors," *Proceedings of ECOS 2015*, 2015.

[19] "Outgoing longwave radiation." https://climatesciences.jpl.nasa.gov/projects/enso/.
Accessed: 2018-04-15.

[20] M. F. Modest, *Radiative heat transfer*.
Academic press, 2013.

[21] G. Kanschat, E. Meinköhn, R. Rannacher, and R. Wehrse, *Numerical methods in multidimensional radiative transfer*.
Springer, 2009.

[22] D. Le Hardy, *Traitement des conditions aux limites spéculaires pour l'étude du transport radiatif dans des matériaux à géométrie complexe*.
PhD thesis, University of Nantes, 2015.

[23] P. Coelho, "Lecture notes on solution methods of the radiative transfer equation," Summer school Ecole Thématique CNRS, ETR2017, May 2017.

[24] J. Oxenius, *Kinetic theory of particles and photons: theoretical foundations of non-LTE plasma spectroscopy*, vol. 20.
Springer Science & Business Media, 2012.

[25] W. von Waldenfels, "Stochastic properties of the radiative transfer equation," in *Numerical Methods in Multidimensional Radiative Transfer* (G. Kanschat, E. Meinköhn, R. Rannacher, and R. Wehrse, eds.), (Berlin, Heidelberg), pp. 19–25, Springer Berlin Heidelberg, 2009.

[26] S. Chandrasekhar, "Radiative transfer," *Oxford, Clarendon Press*, 1950.

[27] B. J. Choudhury and P. Pampaloni, *Passive Microwave Remote Sensing of Land–Atmosphere Interactions*.

Vsp, 1995.

[28] E. E. Salpeter and H. A. Bethe, "A relativistic equation for bound-state problems," *Physical Review*, vol. 84, no. 6, p. 1232, 1951.

[29] S. Durant, *Propagation de la lumière en milieu aléatoire. Rôle de l'absorption, de la diffusion dépendante et du couplage surface-volume.* PhD thesis, Ecole Centrale Paris, 2003.

[30] J. R. Howell, M. P. Menguc, and R. Siegel, *Thermal radiation heat transfer.* CRC press, 2010.

[31] L. P. Kourganoff V., "Basic methods in transfer problems," *Ciel et Terre*, vol. 69, p. 215, 1953.

[32] W. Fiveland, "Discrete-ordinates solutions of the radiative transport equation for rectangular enclosures," *Journal of Heat Transfer*, vol. 106, no. 4, pp. 699–706, 1984.

[33] J. Chai and S. Patankar, "Finite-volume method for radiation heat transfer," *Advances in Numerical Heat Transfer*, vol. 2, pp. 109–141, 2000.

[34] S. Richling, E. Meinköhn, N. Kryzhevoi, and G. Kanschat, "Radiative transfer with finite elements-I. Basic method and tests," *Astronomy & Astrophysics*, vol. 380, no. 02, pp. 776–788, 2001.

[35] H. Gao and H. Zhao, "A fast-forward solver of radiative transfer equation," *Transport Theory and Statistical Physics*, vol. 38, no. 3, pp. 149–192, 2009.

[36] L. Liu and L. Liu, "Discontinuous finite element method for radiative heat transfer in semitransparent graded index medium," *Journal of Quantitative Spectroscopy and Radiative Transfer*, vol. 105, no. 3, pp. 377–387, 2007.

[37] J. Spanier and E. Gelbard, "Monte Carlo principles and neutron transport problems," 1969.

[38] E. E. Lewis and W. F. Miller, *Computational methods of neutron transport.* John Wiley and Sons, Inc., New York, NY, 1984.

[39] I. Lux and L. Koblinger, *Monte Carlo particle transport methods: neutron and photon calculations*, vol. 102. Citeseer, 1991.

[40] J. Wood and M. Williams, "Recent progress in the application of the finite element method to the neutron transport equation," *Progress in Nuclear Energy*, vol. 14, no. 1, pp. 21–40, 1984.

[41] C. De Oliveira, "An arbitrary geometry finite element method for multigroup neutron transport with anisotropic scattering," *Progress in Nuclear Energy*, vol. 18, no. 1-2, pp. 227–236, 1986.

[42] G. S. Abdoulaev and A. H. Hielscher, "Three-dimensional optical tomography with the equation of radiative transfer," *Journal of Electronic Imaging*, vol. 12, no. 4, pp. 594–601, 2003.

[43] T. Tarvainen, M. Vauhkonen, and S. Arridge, "Gauss–Newton reconstruction method for optical tomography using the finite element solution of the radiative transfer equation," *Journal of Quantitative Spectroscopy and Radiative Transfer*, vol. 109, no. 17, pp. 2767–2778, 2008.

[44] A. H. Hielscher, R. E. Alcouffe, and R. L. Barbour, "Comparison of finite-difference transport and diffusion calculations for photon migration in homogeneous and heterogeneous tissues," *Physics in medicine and biology*, vol. 43, no. 5, p. 1285, 1998.

[45] H. K. Kim and A. Charette, "Frequency domain optical tomography using a conjugate gradient method without line search," *Journal of Quantitative Spectroscopy and Radiative Transfer*, vol. 104, no. 2, pp. 248–256, 2007.

[46] J. R. Howell and M. Perlmutter, "Monte Carlo solution of thermal transfer through radiant media between gray walls," *Journal of heat transfer*, vol. 86, no. 1, pp. 116–122, 1964.

[47] M. Cherkaoui, J.-L. Dufresne, R. Fournier, J.-Y. Grandpeix, and A. Lahellec, "Monte carlo simulation of radiation in gases with a narrow-band model and a net-exchange formulation," *Journal of Heat Transfer*, vol. 118, no. 2, pp. 401–407, 1996.

[48] J. T. Farmer and J. R. Howell, "Comparison of monte carlo strategies for radiative transfer in participating media," in *Advances in heat transfer*, vol. 31, pp. 333–429, Elsevier, 1998.

[49] E. W. Larsen and B. Mercer, "Analysis of a monte carlo method for nonlinear radiative transfer," *Journal of Computational Physics*, vol. 71, no. 1, pp. 50–64, 1987.

[50] M. F. Modest, "Backward Monte Carlo simulations in radiative heat transfer," *Journal of heat transfer*, vol. 125, no. 1, pp. 57–62, 2003.

[51]   R. Kong, M. Ambrose, and J. Spanier, "Efficient, automated Monte Carlo methods for radiation transport," *Journal of Computational Physics*, vol. 227, no. 22, pp. 9463–9476, 2008.

[52]   M. R. Hogerheijde and F. F. van der Tak, "An accelerated Monte Carlo method to solve two-dimensional radiative transfer and molecular excitation," *arXiv preprint astro-ph/0008169*, 2000.

[53]   A. Badal, F. Zafar, H. Dong, and A. Badano, "A real-time radiation dose monitoring system for patients and staff during interventional fluoroscopy using a GPU-accelerated Monte Carlo simulator and an automatic 3D localization system based on a depth camera," in *Medical Imaging 2013: Physics of Medical Imaging*, vol. 8668, p. 866828, International Society for Optics and Photonics, 2013.

[54]   T. M. Evans, S. W. Mosher, S. R. Slattery, and S. P. Hamilton, "A Monte Carlo synthetic-acceleration method for solving the thermal radiation diffusion equation," *Journal of Computational Physics*, vol. 258, 2014.

[55]   A. Sawetprawichkul, P. F. Hsu, and K. Mitra, "Parallel computing of three-dimensional Monte Carlo simulation of transient radiative transfer in participating media," in *8th AIAA/ASME Joint Thermophysics and Heat Transfer Conference*, p. 2901, 2002.

[56]   X. Jia, X. Gu, J. Sempau, D. Choi, A. Majumdar, and S. B. Jiang, "Development of a GPU-based Monte Carlo dose calculation code for coupled electron–photon transport," *Physics in Medicine & Biology*, vol. 55, no. 11, p. 3077, 2010.

[57]   J. H. Jean, "The equation of radiative transfer of energy," *Monthly Notices Royal Astronomical Society*, vol. 78, pp. 28–36, 1917.

[58]   Y. Bayazitoilu and J. Higenyi, "Higher-order differential equations of radiative transfer: P3 approximation," *AiAA Journal*, vol. 17, no. 4, pp. 424–431, 1979.

[59]   M. Mengüç and R. Viskanta, "Radiative transfer in three-dimensional rectangular enclosures containing inhomogeneous, anisotropically scattering media," *Journal of Quantitative Spectroscopy and Radiative Transfer*, vol. 33, no. 6, pp. 533–549, 1985.

[60]   Ricardo and Modest, "Implementation of High-Order Spherical Harmonics Methods for Radiative Heat Transfer on OPENFOAM," *Journal of Heat Transfer*, vol. 137, no. 5, p. 052701, 2015.

[61] H. Park, R. Ahluwalia, and K. Im, "Three-dimensional radiation in absorbing-emitting-scattering media using the modified differential approximation," *International Journal of Heat and Mass Transfer*, vol. 36, no. 5, pp. 1181–1189, 1993.

[62] M. Krook, "On the solution of equations of transfer.," *The Astrophysical Journal*, vol. 122, p. 488, 1955.

[63] J. J. Derby, S. Brandon, and A. G. Salinger, "The diffusion and P1 approximations for modeling buoyant flow of an optically thick fluid," *International Journal of Heat and Mass Transfer*, vol. 41, no. 11, pp. 1405–1415, 1998.

[64] K. F. Evans, "The spherical harmonics discrete ordinate method for three-dimensional atmospheric radiative transfer," *Journal of the Atmospheric Sciences*, vol. 55, no. 3, pp. 429–446, 1998.

[65] P. S. Brantley and E. W. Larsen, "The simplified P3 approximation," *Nuclear Science and Engineering*, vol. 134, no. 1, pp. 1–21, 2000.

[66] E. W. Larsen, J. Morel, and J. M. McGhee, "Asymptotic derivation of the multi-group P1 and simplified PN equations with anisotropic scattering," *Nuclear science and engineering*, vol. 123, no. 3, pp. 328–342, 1996.

[67] E. W. Larsen, G. Thömmes, A. Klar, M. Seaıd, and T. Götz, "Simplified PN approximations to the equations of radiative heat transfer and applications," *Journal of Computational Physics*, vol. 183, no. 2, pp. 652–675, 2002.

[68] F. Lockwood and N. Shah, "A new radiation solution method for incorporation in general combustion prediction procedures," in *Symposium (international) on combustion*, vol. 18, pp. 1405–1414, Elsevier, 1981.

[69] P. Coelho and M. Carvalho, "A conservative formulation of the discrete transfer method," *Journal of Heat Transfer*, vol. 119, no. 1, pp. 118–128, 1997.

[70] H. Nirgudkar, S. Kumar, and A. Srivastava, "Solution of radiative transfer equation using discrete transfer method for two-dimensional participating medium," *International Communications in Heat and Mass Transfer*, vol. 61, pp. 88–95, 2015.

[71] J. C. Henson and W. Malalasekera, "Comparison of the discrete transfer and Monte Carlo methods for radiative heat transfer in three-dimensional nonhomogeneous scattering media," *Numerical Heat Transfer, Part A Applications*, vol. 32, no. 1, pp. 19–36, 1997.

[72] J. Y. Murthy and D. Choudhury, "Computation of participating radiation in complex geometries," *Developments in Radiative Heat Transfer*, vol. 203, no. 1, pp. 153–166, 1992.

[73] A. Haidekker, A. Charette, and Y. Kocaefe, "Application of the hybrid zone/Monte Carlo method to 3-D curvilinear grids in radiative heat transfer," *International journal for numerical methods in engineering*, vol. 37, no. 2, pp. 203–216, 1994.

[74] G. Raithby and E. Chui, "A finite-volume method for predicting a radiant heat transfer in enclosures with participating media," *Journal of Heat Transfer*, vol. 112, no. 2, pp. 415–423, 1990.

[75] W. Fiveland and J. Jessee, "Finite element formulation of the discrete-ordinates method for multidimensional geometries," *Journal of thermophysics and heat transfer*, vol. 8, no. 3, pp. 426–433, 1994.

[76] S. T. Thynell, "Discrete-ordinates method in radiative heat transfer," *International journal of engineering science*, vol. 36, no. 12, pp. 1651–1675, 1998.

[77] D. Balsara, "Fast and accurate discrete ordinates methods for multidimensional radiative transfer. Part I, basic methods," *Journal of Quantitative Spectroscopy and Radiative Transfer*, vol. 69, no. 6, pp. 671–707, 2001.

[78] D. Le Hardy, Y. Favennec, and B. Rousseau, "Iterative and FEM methods to solve the 2- D Radiative Transfer Equation with specular reflexion," in *Journal of Physics: Conference Series*, vol. 676, IOP Publishing, 2016.

[79] P. J. Coelho, "Advances in the discrete ordinates and finite volume methods for the solution of radiative heat transfer problems in participating media," *Journal of Quantitative spectroscopy and Radiative transfer*, vol. 145, pp. 121–146, 2014.

[80] V. I. Lebedev, "Quadratures on a sphere," *USSR Computational Mathematics and Mathematical Physics*, vol. 16, no. 2, pp. 10–24, 1976.

[81] W. Fiveland, "Three-dimensional radiative heat-transfer solutions by the discrete-ordinates method," *Journal of Thermophysics and Heat Transfer*, vol. 2, no. 4, pp. 309–316, 1988.

[82] A. F. Woodrow, "The selection of discrete ordinate quadrature sets for anisotropic scattering," *Fundamentals of Radiation Heat Transfer*, vol. 160, pp. 89–96, 1991.

[83] C. Thurgood, A. Pollard, and H. Becker, "The TN quadrature set for the discrete ordinates method," *Journal of heat transfer*, vol. 117, no. 4, pp. 1068–1070, 1995.

[84] P. J. Coelho, "A hybrid finite volume/finite element discretization method for the solution of the radiative heat transfer equation," *Journal of Quantitative Spectroscopy and Radiative Transfer*, vol. 93, no. 1-3, pp. 89–101, 2005.

[85] R. O. Castro and J. P. Trelles, "Spatial and angular finite element method for radiative transfer in participating media," *Journal of Quantitative Spectroscopy and Radiative Transfer*, vol. 157, pp. 81–105, 2015.

[86] J. Kóphází and D. Lathouwers, "A space–angle DGFEM approach for the Boltzmann radiation transport equation with local angular refinement," *Journal of Computational Physics*, vol. 297, pp. 637–668, 2015.

[87] G. Raithby, "Evaluation of discretization errors in finite-volume radiant heat transfer predictions," *Numerical Heat Transfer: Part B: Fundamentals*, vol. 36, no. 3, pp. 241–264, 1999.

[88] J. C. Chai, H. S. Lee, and S. V. Patankar, "Ray effect and false scattering in the discrete ordinates method," *Numerical Heat Transfer, Part B Fundamentals*, vol. 24, no. 4, pp. 373–389, 1993.

[89] P. Coelho, "The role of ray effects and false scattering on the accuracy of the standard and modified discrete ordinates methods," *Journal of Quantitative Spectroscopy and Radiative Transfer*, vol. 73, no. 2-5, pp. 231–238, 2002.

[90] S. Turek, "An efficient solution technique for the radiative transfer equation," *Impact of computing in science and engineering*, vol. 5, no. 3, pp. 201–214, 1993.

[91] M. L. Adams and E. W. Larsen, "Fast iterative methods for discrete-ordinates particle transport calculations," *Progress in nuclear energy*, vol. 40, no. 1, pp. 3–159, 2002.

[92] M. Seaïd and A. Klar, "Efficient preconditioning of linear systems arising from the discretization of radiative transfer equation," in *Challenges in Scientific Computing-CISC 2002*, pp. 211–236, Springer, 2003.

[93] G. Longoni, *Advanced quadrature sets, acceleration and preconditioning techniques for the discrete ordinates method in parallel computing environments*. University of Florida Gainsville, 2004.

[94] J. Goncalves and P. Coelho, "Parallelization of the discrete ordinates method," *Numerical Heat Transfer*, vol. 32, no. 2, pp. 151–173, 1997.

[95] G. Krishnamoorthy, R. Rawat, and P. J. Smith, "Parallel computations of radiative heat transfer using the discrete ordinates method," *Numerical Heat Transfer*, vol. 47, no. 1, pp. 19–38, 2004.

[96] C. Gong, J. Liu, L. Chi, H. Huang, J. Fang, and Z. Gong, "GPU accelerated simulations of 3D deterministic particle transport using discrete ordinates method," *Journal of Computational Physics*, vol. 230, no. 15, pp. 6010–6022, 2011.

[97] G. Raithby and E. Chui, "A Finite-Volume Method for predicting a radiant heat transfer in enclosures with participating media," *Journal of Heat Transfer*, vol. 112, no. 2, pp. 415–423, 1990.

[98] J. C. Chai, H. S. Lee, and S. V. Patankar, "Finite volume method for radiation heat transfer," *Journal of thermophysics and heat transfer*, vol. 8, no. 3, pp. 419–425, 1994.

[99] J. Murthy and S. Mathur, "Finite volume method for radiative heat transfer using unstructured meshes," *Journal of Thermophysics and Heat Transfer*, vol. 12, no. 3, pp. 313–321, 1998.

[100] P. Coelho and J. Gonçalves, "Parallelization of the finite volume method for radiation heat transfer," *International Journal of Numerical Methods for Heat & Fluid Flow*, vol. 9, no. 4, pp. 388–406, 1999.

[101] G. Raithby, "Discussion of the finite-volume method for radiation, and its application using 3D unstructured meshes," *Numerical Heat Transfer: Part B: Fundamentals*, vol. 35, no. 4, pp. 389–405, 1999.

[102] L. Matthews, R. Viskanta, and F. Incropera, "Combined conduction and radiation heat transfer in porous materials heated by intense solar radiation," *Journal of Solar Energy Engineering*, vol. 107, no. 1, pp. 29–34, 1985.

[103] C. Spuckler and R. Siegel, "Two-flux and diffusion methods for radiative transfer in composite layers," *Journal of heat transfer*, vol. 118, no. 1, 1996.

[104] L. Dombrovsky, J. Randrianalisoa, and D. Baillis, "Modified two-flux approximation for identification of radiative properties of absorbing and scattering media from directional-hemispherical measurements," *JOSA A*, vol. 23, no. 1, pp. 91–98, 2006.

[105] W. E. Vargas, "Generalized four-flux radiative transfer model," *Applied optics*, vol. 37, no. 13, pp. 2615–2623, 1998.

[106] R. Siddall and N. Selcuk, "Evaluation of a new six-flux model for radiative transfer in rectangular enclosures," *Trans. Inst. Chem. Eng*, vol. 57, pp. 163–169, 1979.

[107] H. Hottel and A. Sarofim, "Radiative transport," *McCravv Hill, New York*, 1965.

[108] R. G. Deissler, "Diffusion approximation for thermal radiation in gases with jump boundary condition," *Journal of Heat Transfer*, vol. 86, no. 2, pp. 240–245, 1964.

[109] C. Bardos, F. Golse, and B. Perthame, "The Rosseland approximation for the radiative transfer equations," *Communications on Pure and Applied Mathematics*, vol. 40, no. 6, pp. 691–721, 1987.

[110] P. Coelho, O. Teerling, and D. Roekaerts, "Spectral radiative effects and turbulence/radiation interaction in a non-luminous turbulent jet diffusion flame," *Combustion and Flame*, vol. 133, no. 1-2, pp. 75–91, 2003.

[111] L. Stenholm, H. Störzer, and R. Wehrse, "An efficient method for the solution of 3D radiative transfer problems," *Journal of Quantitative Spectroscopy and Radiative Transfer*, vol. 45, no. 1, pp. 47–56, 1991.

[112] Y. Qiao, H. Qi, Q. Chen, L. Ruan, and H. Tan, "Multi-start iterative reconstruction of the radiative parameter distributions in participating media based on the transient radiative transfer equation," *Optics Communications*, vol. 351, pp. 75–84, 2015.

[113] D. Mihalas, L. Auer, and B. Mihalas, "Two-dimensional radiative transfer. I-Planar geometry," *The Astrophysical Journal*, vol. 220, pp. 1001–1023, 1978.

[114] R. Wehrse and W. Kalkofen, "Advances in radiative transfer," *The Astronomy and Astrophysics Review*, vol. 13, no. 1-2, pp. 3–29, 2006.

[115] A. D. Klose and A. H. Hielscher, "Iterative reconstruction scheme for optical tomography based on the equation of radiative transfer," *Medical physics*, vol. 26, no. 8, pp. 1698–1707, 1999.

[116] C. Dullemond and R. Turolla, "An efficient algorithm for two-dimensional radiative transfer in axisymmetric circumstellar envelopes and disks," *arXiv preprint astro-ph/0003456*, 2000.

[117] E. Meinköhn, "A general-purpose finite element method for 3D radiative transfer problems," in *Numerical Methods in Multidimensional Radiative Transfer*, pp. 99–173, Springer, 2009.

[118] K. Ren, G. Bal, and A. H. Hielscher, "Frequency domain optical tomography based on the equation of radiative transfer," *SIAM Journal on Scientific Computing*, vol. 28, no. 4, pp. 1463–1489, 2006.

[119] L. Liu, "Finite volume method for radiation heat transfer in graded index medium," *Journal of Thermophysics and Heat Transfer*, vol. 20, no. 1, pp. 59–66, 2006.

[120] M. R. Charest, C. P. Groth, and Ö. L. Gülder, "Solution of the equation of radiative transfer using a Newton–Krylov approach and adaptive mesh refinement," *Journal of Computational Physics*, vol. 231, no. 8, pp. 3023–3040, 2012.

[121] P. J. Coelho, "Advances in the discrete ordinates and finite volume methods for the solution of radiative heat transfer problems in participating media," *Journal of Quantitative Spectroscopy and Radiative Transfer*, vol. 145, pp. 121–146, 2014.

[122] G. Krishnamoorthy, R. Rawat, and P. J. Smith, "Parallelization of the P-1 radiation model," *Numerical Heat Transfer, Part B: Fundamentals*, vol. 49, no. 1, pp. 1–17, 2006.

[123] G. Pal, A. Gupta, M. F. Modest, and D. C. Haworth, "Comparison of accuracy and computational expense of radiation models in simulation of non-premixed turbulent jet flames," *Combustion and Flame*, vol. 162, no. 6, pp. 2487 – 2495, 2015.

[124] J. Reddy and V. Murty, "Finite-element solution of integral equations arising in radiative heat transfer and laminar boundary-layer theory," *Numerical Heat Transfer, Part B: Fundamentals*, vol. 1, no. 3, pp. 389–401, 1978.

[125] I. Anteby, I. Shai, and A. Arbel, "Numerical calculations for combined conduction and radiation transient heat transfer in a semitransparent medium," *Numerical Heat Transfer: Part A: Applications*, vol. 37, no. 4, pp. 359–371, 2000.

[126] P. Furmanski and J. Banaszek, "Finite element analysis of concurrent radiation and conduction in participating media," *Journal of Quantitative Spectroscopy and Radiative Transfer*, vol. 84, no. 4, pp. 563–573, 2004.

[127] S. Richling, "Radiative transfer with finite elements: Application to the Lyα emission of high-redshift galaxies," in *Numerical Methods in Multidimensional Radiative Transfer*, pp. 279–287, Springer, 2009.

[128] W. An, L. Ruan, H. Qi, and L. Liu, "Finite element method for radiative heat transfer in absorbing and anisotropic scattering media," *Journal of Quantitative Spectroscopy and Radiative Transfer*, vol. 96, no. 3, pp. 409–422, 2005.

[129] L. Ruan, M. Xie, H. Qi, W. An, and H. Tan, "Development of a finite element model for coupled radiative and conductive heat transfer in participating

media," *Journal of Quantitative Spectroscopy and Radiative Transfer*, vol. 102, no. 2, pp. 190–202, 2006.

[130] D. Le Hardy, Y. Favennec, and B. Rousseau, "Solution of the 2-D steady-state radiative transfer equation in participating media with specular reflections using SUPG and DG finite elements," *Journal of Quantitative Spectroscopy and Radiative Transfer*, vol. 179, pp. 149–164, 2016.

[131] S. D. Pautz, "An algorithm for parallel S_n sweeps on unstructured meshes," *Nuclear Science and Engineering*, vol. 140, no. 2, pp. 111–136, 2002.

[132] S. Van Criekingen, F. Nataf, and P. Havé, "PARAFISH: A parallel FE–P_N neutron transport solver based on domain decomposition," *Annals of nuclear energy*, vol. 38, no. 1, pp. 145–150, 2011.

[133] O. Balima, T. Pierre, A. Charette, and D. Marceau, "A least square finite element formulation of the collimated irradiation in frequency domain for optical tomography applications," *Journal of Quantitative Spectroscopy and Radiative Transfer*, vol. 111, no. 2, pp. 280–286, 2010.

[134] G. Kanschat, *A robust finite element discretization for radiative transfer problems with scattering*.
Citeseer, 1998.

[135] M. Avila, R. Codina, and J. Principe, "Spatial approximation of the radiation transport equation using a subgrid-scale finite element method," *Computer Methods in Applied Mechanics and Engineering*, vol. 200, no. 5, pp. 425–438, 2011.

[136] J. Pontaza and J. Reddy, "Least-squares finite element formulations for one-dimensional radiative transfer," *Journal of Quantitative Spectroscopy and Radiative Transfer*, vol. 95, no. 3, pp. 387–406, 2005.

[137] L. Ruan, W. An, H. Tan, and H. Qi, "Least-squares finite-element method of multidimensional radiative heat transfer in absorbing and scattering media," *Numerical Heat Transfer, Part A: Applications*, vol. 51, no. 7, pp. 657–677, 2007.

[138] L. Liu, "Least-squares finite element method for radiation heat transfer in graded index medium," *Journal of Quantitative Spectroscopy and Radiative Transfer*, vol. 103, no. 3, pp. 536–544, 2007.

[139] F. Hecht, "New development in FreeFem++," *Journal of Numerical Mathematics*, vol. 20, no. 3-4, pp. 251–266, 2012.

[140] W. Bangerth, R. Hartmann, and G. Kanschat, "deal. II–a general-purpose object-oriented finite element library," *ACM Transactions on Mathematical Software (TOMS)*, vol. 33, no. 4, p. 24, 2007.

[141] B. Patzák, "OOFEM–an object-oriented simulation tool for advanced modeling of materials and structures," *Acta Polytechnica*, vol. 52, no. 6, 2012.

[142] E. Meinköhn and S. Richling, "Radiative transfer with finite elements-II. Ly α line transfer in moving media," *Astronomy & Astrophysics*, vol. 392, no. 3, pp. 827–839, 2002.

[143] T. J. Hughes, L. P. Franca, and G. M. Hulbert, "A new finite element formulation for computational fluid dynamics: VIII. The Galerkin/least-squares method for advective-diffusive equations," *Computer methods in applied mechanics and engineering*, vol. 73, no. 2, pp. 173–189, 1989.

[144] M. L. Adams and E. W. Larsen, "Fast iterative methods for discrete-ordinates particle transport calculations," *Progress in nuclear energy*, vol. 40, no. 1, pp. 3–159, 2002.

[145] Y. Saad and M. H. Schultz, "GMRES: A generalized minimal residual algorithm for solving nonsymmetric linear systems," *SIAM Journal on scientific and statistical computing*, vol. 7, no. 3, pp. 856–869, 1986.

[146] H. A. Van der Vorst, "Bi-CGSTAB: A fast and smoothly converging variant of Bi-CG for the solution of nonsymmetric linear systems," *SIAM Journal on scientific and Statistical Computing*, vol. 13, no. 2, pp. 631–644, 1992.

[147] G. Kanschat, "Solution of multi-dimensional radiative transfer problems on parallel computers," in *Parallel Solution of Partial Differential Equations*, pp. 85–96, Springer, 2000.

[148] L. R. Herrmann, "Finite-element bending analysis for plates," *Journal of the Engineering Mechanics Division*, vol. 93, no. 5, pp. 13–26, 1967.

[149] B. Darlow, R. E. Ewing, M. Wheeler, *et al.*, "Mixed finite element method for miscible displacement problems in porous media," *Society of Petroleum Engineers Journal*, vol. 24, no. 04, pp. 391–398, 1984.

[150] V. Girault and P. A. Raviart, *Finite element methods for Navier–Stokes equations: theory and algorithms*, vol. 5.
Springer Science & Business Media, 2012.

[151] A. Bossavit, "Mixed finite elements and the complex of whitney forms," *The mathematics of finite elements and applications VI*, pp. 137–144, 1988.

[152] R. Huber and R. Helmig, "Multiphase flow in heterogeneous porous media: A classical finite element method versus an implicit pressure–explicit saturation-based mixed finite element–finite volume approach," *International Journal for Numerical Methods in Fluids*, vol. 29, no. 8, pp. 899–920, 1999.

[153] L. Chounet, D. Hilhorst, C. Jouron, Y. Kelanemer, and P. Nicolas, "Simulation of water flow and heat transfer in soils by means of a mixed finite element method," *Advances in water resources*, vol. 22, no. 5, pp. 445–460, 1999.

[154] D. Boffi, F. Brezzi, and M. Fortin, "Mixed finite element methods and applications, volume 44 of Springer Series in Computational Mathematics," 2013.

[155] D. S. Malkus and T. J. Hughes, "Mixed finite element methods-reduced and selective integration techniques: a unification of concepts," *Computer Methods in Applied Mechanics and Engineering*, vol. 15, no. 1, pp. 63–81, 1978.

[156] C. R. Drumm and J. Lorenz, "Parallel FE approximation of the even/odd-parity form of the linear Boltzmann equation," *Mathematical and Computer Modelling*, vol. 31, no. 2-3, pp. 55–71, 2000.

[157] M. Seaıd, M. Frank, A. Klar, R. Pinnau, and G. Thömmes, "Efficient numerical methods for radiation in gas turbines," *Journal of Computational and Applied Mathematics*, vol. 170, no. 1, pp. 217–239, 2004.

[158] L. O. Mafteiu-Scai, "The bandwidths of a matrix. A survey of algorithms," *Annals of West University of Timisoara-Mathematics*, vol. 52, no. 2, pp. 183–223, 2014.

[159] E. Cuthill and J. McKee, "Reducing the bandwidth of sparse symmetric matrices," in *Proceedings of the 1969 24th national conference*, pp. 157–172, ACM, 1969.

[160] C. Geuzaine and J. F. Remacle, "Gmsh: A 3-D finite element mesh generator with built-in pre-and post-processing facilities," *International journal for numerical methods in engineering*, vol. 79, no. 11, pp. 1309–1331, 2009.

[161] S. Balay, S. Abhyankar, M. F. Adams, J. Brown, P. Brune, K. Buschelman, L. Dalcin, V. Eijkhout, W. D. Gropp, D. Kaushik, M. G. Knepley, L. C. McInnes, K. Rupp, B. F. Smith, S. Zampini, H. Zhang, and H. Zhang, "PETSc web page," 2017.

[162] J. Ahrens, B. Geveci, C. Law, C. Hansen, and C. Johnson, "36-ParaView: An end-user tool for large-data visualization," *The visualization handbook*, vol. 717, 2005.

[163] L. G. Henyey and J. L. Greenstein, "Diffuse radiation in the galaxy," *The Astrophysical Journal*, vol. 93, pp. 70–83, 1941.

[164] G. Krishnamoorthy, R. Rawat, and P. J. Smith, "Parallel computations of radiative heat transfer using the discrete ordinates method," *Numerical Heat Transfer*, vol. 47, no. 1, pp. 19–38, 2004.

[165] J. Goncalves and P. Coelho, "Parallelization of the discrete ordinates method," *Numerical Heat Transfer*, vol. 32, no. 2, pp. 151–173, 1997.

[166] P. Coelho and J. Gonçalves, "Parallelization of the finite volume method for radiation heat transfer," *International Journal of Numerical Methods for Heat & Fluid Flow*, vol. 9, no. 4, pp. 388–406, 1999.

[167] L. H. Howell, "A parallel AMR implementation of the discrete ordinates method for radiation transport," in *Adaptive Mesh Refinement-Theory and Applications*, pp. 255–270, Springer, 2005.

[168] M. R. Charest, C. P. Groth, and Ö. L. Gülder, "Solution of the equation of radiative transfer using a Newton–Krylov approach and adaptive mesh refinement," *Journal of Computational Physics*, vol. 231, no. 8, pp. 3023–3040, 2012.

[169] J. W. Fischer and Y. Azmy, "Comparison via parallel performance models of angular and spatial domain decompositions for solving neutral particle transport problems," *Progress in Nuclear Energy*, vol. 49, no. 1, pp. 37–60, 2007.

[170] M. P. Adams, M. L. Adams, W. D. Hawkins, T. Smith, L. Rauchwerger, N. M. Amato, T. S. Bailey, and R. D. Falgout, "Provably optimal parallel transport sweeps on regular grids," tech. rep., Lawrence Livermore National Laboratory (LLNL), Livermore, CA, 2013.

[171] Y. Y. Azmy, "Multiprocessing for neutron diffusion and deterministic transport methods," *Progress in Nuclear Energy*, vol. 31, no. 3, pp. 317–368, 1997.

[172] S. P. Burns and M. A. Christen, "Spatial domain-based parallelism in large-scale, participating-media, radiative transport applications," *Numerical Heat Transfer*, vol. 31, no. 4, pp. 401–421, 1997.

[173] H. Schwarz, "Ueber einige abbildungsaufgaben.," *Journal fur die reine und angewandte Mathematik*, vol. 70, pp. 105–120, 1869.

[174] G. Karypis and V. Kumar, "METIS: Unstructured Graph Partitioning and Sparse Matrix Ordering System, Version 4.0," 2009.

[175] G. Karypis, K. Schloegel, and V. Kumar, "Parmetis," *Parallel graph partitioning and sparse matrix ordering library. Version*, vol. 2, 2003.

[176] F. Pellegrini, "Scotch and Libscotch 6.0 User's guide," *Bacchus team, INRIA Bordeaux Sud-Ouest Technical Report: CNRS*, vol. 5800, 2012.

[177] F. Bellet, E. Chalopin, F. Fichot, E. Iacona, and J. Taine, "RDFI determination of anisotropic and scattering dependent radiative conductivity tensors in porous media: Application to rod bundles," *International Journal of Heat and Mass Transfer*, vol. 52, no. 5, pp. 1544–1551, 2009.

[178] P. R. Amestoy, I. S. Duff, J.-Y. L'Excellent, and J. Koster, "MUMPS: a general purpose distributed memory sparse solver," in *International Workshop on Applied Parallel Computing*, pp. 121–130, Springer, 2000.

[179] J. Liu, H. Shang, and Y. Chen, "Parallel simulation of radiative heat transfer using an unstructured finite-volume method," *Numerical Heat Transfer: Part B: Fundamentals*, vol. 36, no. 2, pp. 115–137, 1999.

[180] D. Mihalas, "Stellar atmospheres," *San Francisco, WH Freeman and Co., 1978. 650 p.*, 1978.

[181] E. W. Larsen, "Transport acceleration methods as two-level multigrid algorithms," *Operator Theory: Advances and Applications*, vol. 51, pp. p34–47, 1991.

[182] I. C. Ipsen and C. D. Meyer, "The idea behind Krylov methods," *American Mathematical Monthly*, pp. 889–899, 1998.

[183] S. Turek, "A generalized mean intensity approach for the numerical solution of the radiative transfer equation," *Computing*, vol. 54, no. 1, pp. 27–38, 1995.

[184] B. W. Patton and J. P. Holloway, "Application of preconditioned GMRES to the numerical solution of the neutron transport equation," *Annals of Nuclear Energy*, vol. 29, no. 2, pp. 109–136, 2002.

[185] W. F. Godoy and P. E. DesJardin, "On the use of flux limiters in the discrete ordinates method for 3D radiation calculations in absorbing and scattering media," *Journal of Computational Physics*, vol. 229, no. 9, pp. 3189–3213, 2010.

[186] M. A. Heroux, R. A. Bartlett, V. E. Howle, R. J. Hoekstra, J. J. Hu, T. G. Kolda, R. B. Lehoucq, K. R. Long, R. P. Pawlowski, E. T. Phipps, *et al.*, "An overview of the Trilinos project," *ACM Transactions on Mathematical Software (TOMS)*, vol. 31, no. 3, pp. 397–423, 2005.

[187] W. E. Arnoldi, "The principle of minimized iterations in the solution of the matrix eigenvalue problem," *Quarterly of applied mathematics*, vol. 9, no. 1, pp. 17–29, 1951.

[188] W. H. Reed, "New difference schemes for the neutron transport equation," *Nuclear Science and Engineering*, vol. 46, no. 2, pp. 309–314, 1971.

[189] Y. Saad, *Iterative methods for sparse linear systems*.
SIAM, 2003.

[190] F. Robert and E. Alain, "Berlingot." http://www.mathcurve.com/surfaces/berlingot/berlingot.shtml, 2017.
Accessed: 2017-12-05.

[191] O. Axelsson, *Iterative solution methods*.
Cambridge university press, 1996.

[192] G. Kanschat, "Solution of radiative transfer problems with finite elements," in *Numerical methods in multidimensional radiative transfer*, pp. 49–98, Springer, 2009.

[193] W. L. Oberkampf, T. G. Trucano, and C. Hirsch, "Verification, validation, and predictive capability in computational engineering and physics," *Applied Mechanics Reviews*, vol. 57, no. 5, pp. 345–384, 2004.

[194] P. J. Roache, "Verification of codes and calculations," *AIAA journal*, vol. 36, no. 5, pp. 696–702, 1998.

[195] L. Eça, M. Hoekstra, A. Hay, and D. Pelletier, "Verification of RANS solvers with manufactured solutions," *Engineering with computers*, vol. 23, no. 4, pp. 253–270, 2007.

[196] Y. Wang, "The method of manufactured solutions for RattleSnake a SN radiation transport solver inside the MOOSE framework," tech. rep., Idaho National Laboratory (INL), 2012.

[197] S. D. Pautz, "Verification of transport codes by the method of manufactured solutions: the ATTILA experience," tech. rep., Los Alamos National Lab., NM (US), 2001.

[198] A. L. Crosbie and R. Schrenker, "Radiative transfer in a two-dimensional rectangular medium exposed to diffuse radiation," *Journal of Quantitative Spectroscopy and Radiative Transfer*, vol. 31, no. 4, pp. 339–372, 1984.

[199] M. K, "Developing a 3D numerical tool for modeling the transport of thermal radiation in order to identify reflectance and transmittance of a semitransparent material," Master's thesis, University of Nantes, Nantes, France, 2015.

[200] W. Parker, R. Jenkins, C. Butler, and G. Abbott, "Flash method of determining thermal diffusivity, heat capacity, and thermal conductivity," *Journal of applied physics*, vol. 32, no. 9, pp. 1679–1684, 1961.

[201] R. Coquard, D. Rochais, and D. Baillis, "Experimental investigations of the coupled conductive and radiative heat transfer in metallic/ceramic foams," *International Journal of Heat and Mass Transfer*, vol. 52, no. 21-22, pp. 4907–4918, 2009.

[202] H. Qi, C.-Y. Niu, S. Gong, Y.-T. Ren, and L.-M. Ruan, "Application of the hybrid particle swarm optimization algorithms for simultaneous estimation of multi-parameters in a transient conduction–radiation problem," *International Journal of Heat and Mass Transfer*, vol. 83, pp. 428–440, 2015.

[203] S. Andre and A. Degiovanni, "A new way of solving transient radiative-conductive heat transfer problems," *Journal of Heat Transfer*, vol. 120, no. 4, pp. 943–955, 1998.

[204] T. Lu and C. Chen, "Thermal transport and fire retardance properties of cellular aluminium alloys," *Acta Materialia*, vol. 47, no. 5, pp. 1469–1485, 1999.

[205] M. Lazard, S. André, and D. Maillet, "Diffusivity measurement of semi-transparent media: model of the coupled transient heat transfer and experiments on glass, silica glass and zinc selenide," *International Journal of Heat and Mass Transfer*, vol. 47, no. 3, pp. 477–487, 2004.

[206] O. Hahn, F. Raether, M. Arduini-Schuster, and J. Fricke, "Transient coupled conductive/radiative heat transfer in absorbing, emitting and scattering media: application to laser-flash measurements on ceramic materials," *International Journal of Heat and Mass Transfer*, vol. 40, no. 3, pp. 689–698, 1997.

[207] Y. Huang, C. Y. H. Chao, and P. Cheng, "Effects of preheating and operation conditions on combustion in a porous medium," *International Journal of Heat and Mass Transfer*, vol. 45, no. 21, pp. 4315–4324, 2002.

[208] A. Kribus, Y. Gray, M. Grijnevich, G. Mittelman, S. Mey-Cloutier, and C. Caliot, "The promise and challenge of solar volumetric absorbers," *Solar Energy*, vol. 110, pp. 463–481, 2014.

[209] W. Fuqiang, C. Ziming, T. Jianyu, Z. Jiaqi, L. Yu, and L. Linhua, "Energy storage efficiency analyses of co2 reforming of methane in metal foam solar thermochemical reactor," *Applied Thermal Engineering*, vol. 111, pp. 1091–1100, 2017.

[210] A. Amiri and K. Vafai, "Analysis of dispersion effects and non-thermal equilibrium, non-darcian, variable porosity incompressible flow through porous media," *International Journal of Heat and Mass Transfer*, vol. 37, no. 6, pp. 939–954, 1994.

[211] N. Guo and M. C. Leu, "Additive manufacturing: technology, applications and research needs," *Frontiers of Mechanical Engineering*, vol. 8, no. 3, pp. 215–243, 2013.

[212] S. Cunsolo, R. Coquard, D. Baillis, W. K. Chiu, and N. Bianco, "Radiative properties of irregular open cell solid foams," *International Journal of Thermal Sciences*, vol. 117, pp. 77–89, 2017.

[213] S. Guévelou, B. Rousseau, G. Domingues, J. Vicente, and C. Caliot, "Representative elementary volumes required to characterize the normal spectral emittance of silicon carbide foams used as volumetric solar absorbers," *International Journal of Heat and Mass Transfer*, vol. 93, pp. 118–129, 2016.

[214] W. Lipiński, D. Keene, S. Haussener, and J. Petrasch, "Continuum radiative heat transfer modeling in media consisting of optically distinct components in the limit of geometrical optics," *Journal of Quantitative Spectroscopy and Radiative Transfer*, vol. 111, no. 16, pp. 2474–2480, 2010.

[215] R. Coquard, D. Baillis, and J. Randrianalisoa, "Homogeneous phase and multiphase approaches for modeling radiative transfer in foams," *International Journal of Thermal Sciences*, vol. 50, no. 9, pp. 1648–1663, 2011.

[216] A. Akolkar and J. Petrasch, "Tomography based pore-level optimization of radiative transfer in porous media," *International Journal of Heat and Mass Transfer*, vol. 54, no. 23-24, pp. 4775–4783, 2011.

[217] B. Rousseau, J. Rolland, P. Echegut, E. Brun, and J. Vicente, "Numerical prediction of the radiative behavior of metallic foams from the microscopic to macroscopic scale," in *Journal of Physics: Conference Series*, vol. 369, p. 012003, IOP Publishing, 2012.

[218] Y. Li, X.-L. Xia, Q. Ai, C. Sun, and H.-P. Tan, "Pore-level determination of spectral reflection behaviors of high-porosity metal foam sheets," *Infrared Physics & Technology*, vol. 89, pp. 77–87, 2018.

[219] X.-L. Xia, Y. Li, C. Sun, Q. Ai, and H.-P. Tan, "Integrated simulation of continuous-scale and discrete-scale radiative transfer in metal foams," *Journal of Quantitative Spectroscopy and Radiative Transfer*, vol. 212, pp. 128–138, 2018.

[220] M. Loretz, E. Maire, and D. Baillis, "Analytical modelling of the radiative properties of metallic foams: Contribution of x-ray tomography," *Advanced engineering materials*, vol. 10, no. 4, pp. 352–360, 2008.

[221] S. Cunsolo, D. Baillis, N. Bianco, V. Naso, and M. Oliviero, "Effects of ligaments shape on radiative heat transfer in metal foams," *International Journal of Numerical Methods for Heat & Fluid Flow*, vol. 26, no. 2, pp. 477–488, 2016.

[222] A. Füssel, D. Böttge, J. Adler, F. Marschallek, and A. Michaelis, "Cellular ceramics in combustion environments," *Advanced Engineering Materials*, vol. 13, no. 11, pp. 1008–1014, 2011.

[223] W. E. Lorensen and H. E. Cline, "Marching cubes: A high resolution 3d surface construction algorithm," in *ACM siggraph computer graphics*, vol. 21, pp. 163–169, ACM, 1987.

[224] T. Makino, T. Kunitomo, I. Sakai, and H. Kinoshita, "Thermal radiation properties of ceramic materials," *Heat Transfer-Japanese Research,(ISSN 0096-0802)*, vol. 13, pp. 33–50, 1984.

[225] G. Contento, M. Oliviero, N. Bianco, and V. Naso, "The prediction of radiation heat transfer in open cell metal foams by a model based on the lord kelvin representation," *International Journal of Heat and Mass Transfer*, vol. 76, pp. 499–508, 2014.

[226] P. Kumar, F. Topin, and J. Vicente, "Determination of effective thermal conductivity from geometrical properties: application to open cell foams," *International Journal of Thermal Sciences*, vol. 81, pp. 13–28, 2014.

[227] S. Guévelou, B. Rousseau, G. Domingues, and J. Vicente, "A simple expression for the normal spectral emittance of open-cell foams composed of optically thick and smooth struts," *Journal of Quantitative Spectroscopy and Radiative Transfer*, vol. 189, pp. 329–338, 2017.

[228] C. Dobrzynski and P. Frey, "Anisotropic delaunay mesh adaptation for unsteady simulations," in *Proceedings of the 17th international Meshing Roundtable*, pp. 177–194, Springer, 2008.

[229] N. Aspert, D. Santa-Cruz, and T. Ebrahimi, "Mesh: Measuring errors between surfaces using the hausdorff distance," in *Multimedia and Expo, 2002. ICME'02. Proceedings. 2002 IEEE International Conference on*, vol. 1, pp. 705–708, IEEE, 2002.

[230] C. Geuzaine and J.-F. Remacle, "Gmsh: A 3D finite element mesh generator with built-in pre-and post-processing facilities," *International Journal for Numerical Methods in Engineering*, vol. 79, no. 11, pp. 1309–1331, 2009.

[231] C. Dapogny, C. Dobrzynski, and P. Frey, "Three-dimensional adaptive domain remeshing, implicit domain meshing, and applications to free and moving boundary problems," *Journal of computational physics*, vol. 262, pp. 358–378, 2014.

[232] F. Gomez-Garcia, J. Gonzalez-Aguilar, S. Tamayo-Pacheco, G. Olalde, and M. Romero, "Numerical analysis of radiation propagation in a multi-layer volumetric solar absorber composed of a stack of square grids," *Solar Energy*, vol. 121, pp. 94–102, 2015.

[233] S. Guévelou, *Caractérisation des propriétés thermo-radiatives de mousses à structure numériquement contrôlée: vers le design d'absorbeurs solaires*.
PhD thesis, University of Nantes, 2015.

LIST OF FIGURES

LIST OF TABLES

Titre : Stratégies éléments finis pour l'équation de transfert radiatif

Mots clés : Transfert radiatif, éléments finis vectoriels, méthode des ordonnées discrètes, parallélisation

La méthode des ordonnées discrètes couplée à la méthode des éléments finis est souvent utilisée pour résoudre numériquement l'équation de transfert radiatif. L'objectif principal de cette thèse est d'améliorer cette technique numérique. Au lieu d'utiliser des éléments finis standards, cette thèse reformule l'équation de transfert radiatif en utilisant des éléments finis vectoriels. Par rapport aux éléments finis standards, cette reformulation donne des temps plus courts pour la phase d'assemblage des systèmes linéaires, et surtout pour la phase de résolution. Des méthodes itératives de sous-espaces de Krylov préconditionnées, comme le GMRES et le BiCGSTAB, sont employées pour résoudre les systèmes linéaires résultant de la discrétisation par éléments finis. La

méthode développée a été validée par rapport à des problèmes de référence. Pour résoudre de gros problèmes de rayonnement sur des calculateurs parallèles, la méthode des éléments finis vectoriels est parallélisée en utilisant des approches de décomposition de domaine et de décomposition angulaire. Les méthodes parallèles proposées possèdent des capacités de mise à l'échelle quasi-linéaires sur un grand nombre de processeurs. Les solveurs parallèles développés sont utilisés pour effectuer des simulations numériques à grande échelle avec des milliards d'inconnues. Dans l'ensemble, il est montré comment effectuer des simulations numériques complexes de rayonnement à des échelles auparavant inaccessibles pour les solveurs de transfert radiatif standard.

Title : Efficient finite element strategies for solving the radiative transfer equation

Keywords : Radiative transfer, vectorial finite elements, discrete ordinates method, parallelization

The discrete ordinate method coupled with the finite element method is often used for numerically solving the radiative transfer equation. The main goal of this thesis is to improve upon such numerical technique. Instead of using standard finite elements, this thesis reformulates the radiative transfer equation using vectorial finite elements. In comparison to standard finite elements, this reformulation yields faster timings for the linear system assemblies, as well as for the solution phase when solving scattering media problems. Preconditioned Krylov subspace methods like the GMRES and the BiCGSTAB are employed for solving the linear systems arising from the proposed vectorial finite element discretization. The developed methods

are validated against benchmark problems available in literature. In addition, the method of manufactured solutions is used for verifying the proposed method. For solving large problems of radiation on parallel computers, the vectorial finite element method is parallelized using domain decomposition and angular decomposition approaches. The proposed parallel methods possess quasi-linear scaling capabilities on a large number of processes. The developed parallel solvers are used to perform large scale numerical simulations with billions of unknowns. Overall it is shown how to perform complex numerical simulations of radiation at scales that were previously unattainable by standard radiative transfer equation solvers.